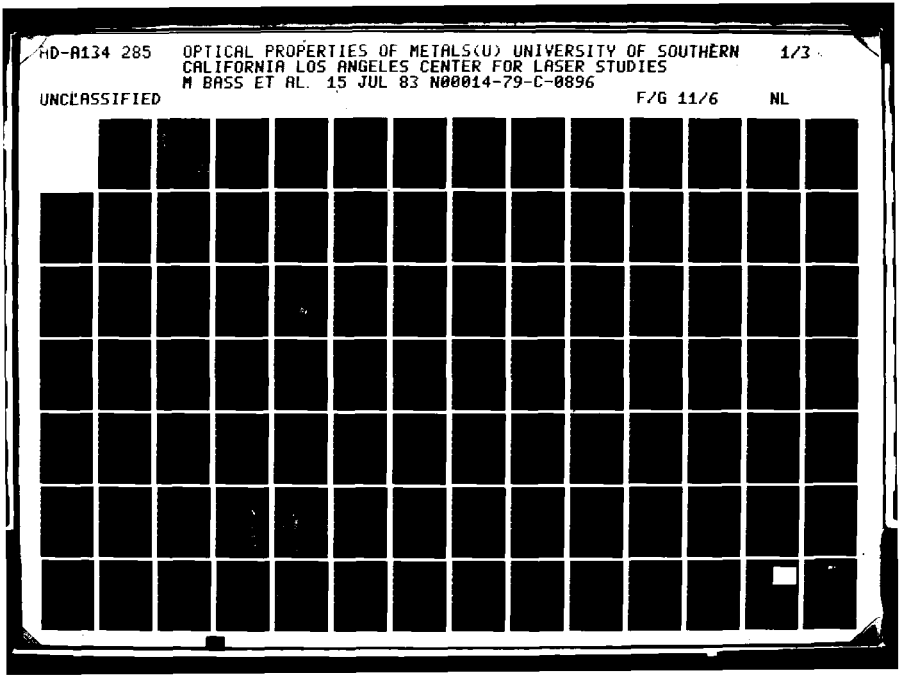
AD-A134 285 OPTICAL PROPERTIES OF METALS(U) UNIVERSITY OF SOUTHERN 1/3
CALIFORNIA LOS ANGELES CENTER FOR LASER STUDIES
M BASS ET AL. 15 JUL 83 N00014-79-C-0896
UNCLASSIFIED F/G 11/6 NL

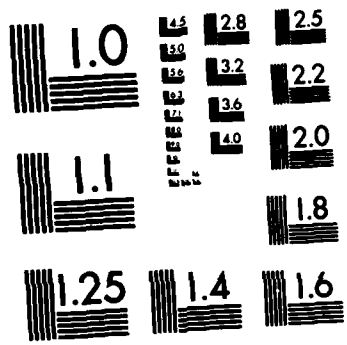

SRO-01

OPTICAL PROPERTIES OF METALS

Annual Report No. 3
ONR SRO Research Grant No.
N0014-79-C-0896
Center for Laser Studies, USC
and Naval Weapons Center
11-1-81 - 10-30-82

ANNUAL REPORT NO. 3

ONR SRO Research Grant No. N00014-79-C-0896

Optical Properties of Metals

A Joint Research Project of

Center for Laser Studies
University of Southern California
University Park
Los Angeles, CA 90089-1112

and

Naval Weapons Center
China Lake, CA 93555

Principal Investigator at U.S.C.: Michael Bass

Principal Investigator at N.W.C.: Jean Bennett

Period Covered in this Report

11/1/81 - 10/30/82

Report Date
July 15, 1983

Table of Contents

Chapter 1

Introduction

The study of the optical properties of metals jointly by U.S.C. and N.W.C. is described in this third annual report of work performed under and O.N.R. Selected Research Opportunities program. The research was divided into several categories including;

1. Mechanisms of Absorption,

2. Optical Properties of Dielectric-Metal Interfaces,

3. Intensity Dependent Absorption Processes,

4. Laser Induced Failure of Metal Surfaces,

5. Optical Properties of Finely Structured Metals, and

6. Laser Surface Desorption.

This report is composed of the several papers published or presented as a result of research conducted in this program. Included are papers on single and multiple pulse laser induced damage to diamond turned mirrors, the role of roughness in determining metal surface absorption and damage, a model for multiple pulse damage based on the accumulation of plastic stress, infrared laser stimulated desorption, thin film on metal absorption, cryogenic metal mirror operation and scattering on molybdenum surfaces. In addition, material is included which is descriptive of the two Ph. D. theses which were finished during the final year of this program.

The highlights of the third year's work are described below:

1. Single and multiple pulse laser damage studies were carried out at 10600,1064, and 532 nm. The samples studied included diamond turned bulk Cu and diamond turned electrodeposited Ag. The single pulse threshold decreases or remains constant with increasing spot size. On the other hand, the multiple pulse threshold increases with increasing spot size. The difference in their behavior suggests that the two phenomena are the result of different mechanisms. Localized surface defects and impurities appear to be responsible for single pulse damage, while for

multiple pulse damage a model is proposed based on the cumulative effect of plastic deformation induced by thermal stresses.

2. Intensity dependent absorption in diamond turned and mechanically polished samples of Cu and Ag revealed that the absorption increased with increasing intensity. This observation could be explained in terms of thermal mechanisms. It was observed that the increase was reversible even though under Nomarski illumination microscopy the surface was altered. Profilimetry revealed that while the height of the altered surface roughness was not very different than unirradiated material the frequency of the roughness profile was significantly higher. Since the altered surface could be damaged more easily than an unirradiated site the presence of the sharp edges is thought to be a contributor the the surface degradation which leads to laser damage in used mirror surfaces.

3. The total absorption of diamond turned Ag and Cu was measured directly by laser calorimetry. These measurements were carried out at wavelengths from 468 to 10600 nm. The data were analyzed with a model which includes the contribution to the absorption due to surface roughness. As a result the effective electron relaxation time was found as a function of frequency. This in turn was used to find the effective conductivity as a function of frequency and inferences concerning the Fermi surface of the metal in the diamond turned surface were drawn.

4. Infrared laser induced surface desorption was demonstrated for water and other contaminants on nominally transparent substrates. In the samples measured to date the desorption is defect dominated for both small and large spot sizes. A clear correlation was found between the desorbed contaminant fluence and the laser damage threshold of the materials studied. Laser cleaned surfaces were dosed with water at temperatures up to 100 deg. C and showed no evidence of readsorbed water in subsequent laser desorption studies. This indicates a passivation of the surface by laser desorption and provides a major reason to continue research in this area.

5. By studying the absorption of dielectric overcoated and bare metal mirrors at temperatures from room temperature down to that of liquid nitrogen it was possible to identify usage conditions for cryogenically cooled mirrors. Little change was observed in the absorption of a multilayer dielectric overcoated enhanced metal mirror. In contrast, cooling a bare metal mirror of Ag, Au or Cu to liquid nitrogen temperature should decrease the absorption from the room temperature value by about one order of magnitude. This was experimentally verified. Additional benefit is to be gained from the increased thermal conductivity at low temperatures. For an Ag mirror these factors should result in an increase in the melt damage threshold by a factor of ~1.5. These

considerations are especially appropriate for space applications of high power density lasers systems where passive cooling can be employed.

6. Laser damage was studied on bare diamond machined Cu at 45 deg. incidence angle. Within the experimental accuracy the threshold for p polarized light was identical to that for normally incident light. The threshold for s polarized light was about a factor of two larger as can be expected from the optical properties of the metal. This experiment provided an excellent cross check on the experimental techniques used to measure damage threshold as well as providing for the first time reliable damage data at non-normal incidence.

Chapter 2

Single and Multiple Pulse Catastrophic Damage in Diamond Turned Cu and Ag Mirrors and 10600, 1064, and 532 nm

N. Koumvakalis, C. S. Lee and M. Bass

Center for Laser Studies
University of Southern California
University Park, DRB-17
Los Angeles, CA 90089-1112

SINGLE AND MULTIPLE PULSE CATASTROPHIC DAMAGE IN DIAMOND TURNED Cu AND Ag MIRRORS AT 10.6, 1.06 and 0.532 μm

N. Koumvakalis, C. S. Lee, and M. Bass

Center for Laser Studies

University of Southern California

University Park, DRB 17

Los Angeles, CA 90089-1112

Abstract

The results of single and multiple pulse damage studies at 10.6, 1.06 and 0.532 μm in diamond turned bulk Cu and diamond-turned electrodeposits of Ag on Cu are presented. The single pulse damage threshold decreases or remains constant with increasing spot size as previously reported. On the other hand, the multiple pulse threshold increases with increasing spot size. The difference in their behavior suggests that the two phenomena are the result of different mechanisms. Localized surface defects and impurities appear to be responsible for single pulse damage, while for multiple pulse damage a model is proposed based on the cumulative effect of plastic deformation induced by thermal stresses.

Key words: Copper mirror; damage; defect; diamond-turned; multiple pulse; pulsed calorimetry; silver mirror; single pulse; thermal gradient stress.

I. Introduction

The continuous development of high power pulsed lasers has made the question of radiation induced resistance of the optical components employed an important problem. Copper and silver mirrors because of their high reflectivity and good thermal conductivity are used extensively in laser applications. Theses mirrors must withstand high-intensity, short-pulse irradiation in multiple as well as in single pulse operation. Last year [1] we presented data for Cu mirrors, where, at 1.06 μm the multiple pulse damage threshold increased with increasing beam size. The effect was attributed to stress developed during the pulse with no further analysis.

The scope of the present work is to analyze the observed behavior of Cu and Ag mirrors under 10.6 μm, 1.06 μm and 0.532 μm multiple and single pulse irradiation and present a model to explain the damage processes. In the case of multiple pulses, we examine the thermomechanical stress degradation of the metal surface under laser irradiation. As a result we can describe multiple pulse damage in terms of a cumulative process where the damaged medium has a memory of the preceding pulses if the power is more than a certain threshold value. The single pulse damage process is described in terms of a defect triggered breakdown.

II. Experimental

The samples used were OFHC bulk Cu and electrodeposited Ag on Cu substrates diamond turned in the facilities of the

NWC in China Lake. We also used OFHC bulk Cu diamond turned by Intop Corp.

The damage test facilities are depicted in Figure 1 and are in principle the same as those used in previous damage and calorimetry studies [1,2]. An important addition was the use of a SHG crystal in the Molectron Nd:YAG laser which allowed irradiation with 0.532 μm light.

The repetition rate of both lasers - 10Hz for the Nd:YAG at both 1.06 and 0.532 μm and 5/8 Hz for the CO_2 laser - set a limit to the maximum number of shots used for the experiment, the limit being 10^4 shot for the Nd:YAG and 1,500 shots for the CO_2 laser.

The quality and reproducibility of the laser beams is of crucial importance in damage experiments. Therefore their temporal as well as spatial profiles were periodically monitored. For the Nd:YAG laser at 1.06 μm and 0.532 μm we used a fast photodiode to measure the temporal profile and a Reticon diode array to monitor the spatial distribution of the laser beam. For the CO_2 laser we used a photon drag detector to monitor the temporal waveform while the spatial profile was determined by beam scans.

The sample was positioned in a calorimetric chamber evacuated to ~100 mTorr (see Figure 1). A site was then selected on the sample's surface and irradiated with many pulses of constant energy. Damage would occur instantly or after a number of pulses. For the 10.6 μm and 1.06 μm irrad-

iation damage was monitored by using laser calorimetry. As described previously [1,2] upon damage the behavior of the heating curve displayed in real time would change dramatically while at the same time one could observe a flash or spark. Due to the increased absorption of Cu and Ag at 0.532 μm detection of damage with laser calorimetry presented serious technical problems. Therefore, a photomultiplier with appropriate filtering was used which detected the increased scattering which accompanied damage as well as the broad spectrums of wavelengths produced by the intense plasma formed during the catastrophic damage process.

After damage, the number of pulses required to cause failure N, and the corresponding intensity I_N, were recorded. Then a new site was selected and irradiated at a lower intensity, where more pulses were required to produce damage until an intensity was reached showing no evidence of causing failure after 1,500 pulses at 10.6 μm and 10,000 pulses at 1.06 and 0.532 μm.

The same experiment was then repeated for several beam sizes in order to determine the multiple as well as the single pulse damage intensity as a function of the beam size. (In this work beam size is given as the radius of the beam where the intensity is $1/e^2$ of the axis intensity).

III. Results

Figure 2 shows a plot of the log of the number of shots N vs intensity for diamond turned Cu at 10.6 μm, 1.06 μm and

0.532 μm, while Figure 3 shows the same plot for diamong turned Ag. One notices that as the intensity is reduced more pulses are required for damage.

Figure 4 shows a plot of the multiple pulse damage intensity for a certain number of shots (open circles) as well as the single pulse damage (solid circles) as a function of beam radius for diamond turned Cu at 10.6, 1.06 and 0.532 μm. Figure 5 shows the same plot for diamond turned Ag. The single pulse damage threshold decreases or remains constant as the beam size increases. In contrast the multiple pulse damage threshold increases with increasing beam size in a linear fashion.

An examination of the damage morphology with a Nomarski microscope reveals that single pulse damage generally occurs at localized defect sizes. On the other hand, in multiple pulse damage, prior to catastrophic failure (i.e. before a flash or spark were observed), the irradiated sites become roughened and the degree of roughness increased with increasing number of pulses. The results for Cu are shown in reference 2. Figure 6 shows the results for Ag at 0.532 μm. In Figure 6a, the site was irradiated for 1,500 pulses, while in Figure 6b, the site was irradiated for 5,000 pulses. Catastrophic failure was not observed in either case. We were able to detect the increased scattering due to surface roughening at 0.532 μm with the photomultiplier before catastrophic failure occurred.

IV. Discussion

The observed beam-size dependence for single pulse damage is similar to the one observed for damage to thin films and surfaces of transparent media [3,4,5]. The model suggested in that work, which seems also to be valid for metal mirrors, assumes that the nature and distribution of surface defects determine the beam size dependence. As a result the probability of the laser beam striking a defect will be greater for larger beam sizes. If the beam size is larger than the mean distance between defects so that the beam area striking the sample encompasses several of them, the damage threshold will be invariant with spot size increase. Apparently the range of beam sizes used in the present experiment (r_{1/e^2} between 50 and 250 μm) satisfies the condition. There is recent evidence [6] that multiple pulse damage in dielectric reflectors follows the same trend in its beam size dependence as the single pulse damage, namely the laser damage intensity decreases or remains constant for increasing beam size. Damage following the above trend can be characterized as extrinsic.

An entirely different description applies to the multiple shot damage we observed in Cu and Ag. The sample surface morphology before catastrophic damage occurred was indicative of an accumulation process suggested before [7]. To explain the accumulation of deformation leading to catastrophic damage as well as the unexpected spot-size dependence of the multiple pulse damage threshold we considered the generation of stress

by a local temperature gradient associated with a non-uniform temperature field.

The temperature distribution produced by a Gaussian beam at the end of a square pulse of duration τ_p, assuming that the thermal diffusion length is negligible in comparison to the beam dimension, is given by:

$$T(r) = \frac{AI_0\sqrt{\tau_p}}{\rho C\sqrt{\pi\kappa}} \exp(-r^2/w^2) \qquad (1)$$

for $w >> \sqrt{4\kappa\tau_p}$

where:

A = absorptance

I_0 = peak intensity

ρ = material density

C = specific heat

κ = thermal diffusivity

w = spot radius at $1/e^2$

τ_p = pulse duration

The shear stress of a plane metal surface subjected to heating is proportional to the temperature gradient introduced, so that the maximum shear stress (occurring where the temperature gradient is maximum) is given by:

$$\sigma_s^{max} = \frac{AI_0\alpha E\tau_p}{\sqrt{2e}(1-\nu)\rho C}\,\frac{1}{\nu} \qquad (2)$$

where the additional parameters are:

E = Young's modulus

α = coefficient of thermal expansion

ν = Poisson's ratio

When the shear stress exceeds the yield stress σ_y of the material, the metal deforms plastically. The onset of plastic deformation is defined when:

$$\sigma_s \geq \sigma_y$$

Substituting σ_s from (2) and solving for the critical now intensity I_y

$$I_y(w) = \frac{\sqrt{2e}\ (1-\nu)\ \rho C \sigma_y}{AE\tau_p}\ w$$

According to Porteus et al [8], the most dominant damage mechanism on clean and carefully prepared surfaces, as is our case, is slip bands resulting from thermal stresses and having a threshold significantly lower than the one required for catastrophic damage. The slip bands and the other plastic deformations occurring when the yield strength of the surface is exceeded during each pulse, will manifest themselves an increase in surface roughness. Repetitive pulse illumination will cause an accumulation of plastic deformation and a continuous increase in surface roughness until catastrophic damage occurs.

V. Conclusion

The single as well as the multiple pulse damage behavior of Cu and Ag diamond turned mirrors at 0.532 μm, 1.06 μm and 10.6 μm as a function of He laser beam size have been examined. For the single shot damage, a probabilistic model can be applied in which the nature and distribution of defects are responsible for the observed behavior. Such a damage process can be characterized as extrinsic. In the case of

multiple pulse damage, a cumulative process triggered by thermal stresses leads to the observed spot size dependence and demonstrates that multiple pulse damage is dominated by an intrinsic process.

The authors express their thanks to Dr. D. Decker from the NWC in China Lake and P. Engstrom from INTOP Corporation for kindly supplying the crystals. They also want to thank Dr. L. Merkle for helpful discussions. This work was sponsored by ONR-SRO Research Grant No. N00014-70-C-0896.

References

1. N. Koumvakalis, C.S. Lee and M. Bass, Proceedings of the 13th Symposium on Laser Induced Damage in Optical Materials, Boulder, Colorado, Nov. 1981 and to be published by the National Bureau of Standards.
2. C.S. Lee, N. Koumvakalis, and M. Bass, Appl. Phys. Lett. 41 (7), 1982.
3. L.G. DeShazer, B.E. Newnam and K.M. Leung, Appl. Phys. Lett. 23, 707 (1973).
4. V. Wang, C.R. Giuliano and B. Garcia, NBS Special Publication No. 435, 1973, p. 216.
5. J.R. Bettis, R.A. House II and A.H. Guenther, NBS Special Publication No. 462, 1976, p. 338.
6. S.R. Foltyn, L.J. Jolin and B.E. Newnam, Proceedings of the 14th Symposium on Laser Induced Damage in Optical Materials, Boulder, Colorado, Nov. 1982 and to be published by the National Bureau of Standards.
7. H.M. Musal, Jr., NBS Special Publication No. 568, 1979, p. 159.
8. J.O. Porteus, D.L. Decker, J.L. Jernigan, W.N. Faith and M. Bass, IEEE J. Quantum Electr. QE-14, 776 (1978).

Figure Captions

Figure 1. Schematic of experimental apparatus.

Figure 2. Measured log N vs I_N for diamond-turned OFHC Cu irradiated at a) 0.532 μm b) 1.06 μm c) 10.6 μm.

Figure 3. Measured log N vs I_N for diamond-turned electroplated Ag irradiated at a) 0.532 μm b) 1.06 μm c) 10.6 μm.

Figure 4. I_N vs W for diamond turned OFHC Cu irradiated at a) 0.532 μm b) 1.06 μm c) 10.6 μm. $N = 10^3$ shots.

Figure 5. I_N vs W for diamond turned electroplated Ag irradiated at a) 0.532 μm 6) 1.06 μm c) 10.6 μm $N = 10^3$ shots.

Figure 6. Nomarski micrograph of laser-induced surface roughening in diamond turned electroplated Ag at constant intensity for two different numbers of pulses. a) N = 1,500 b) N = 5,000.

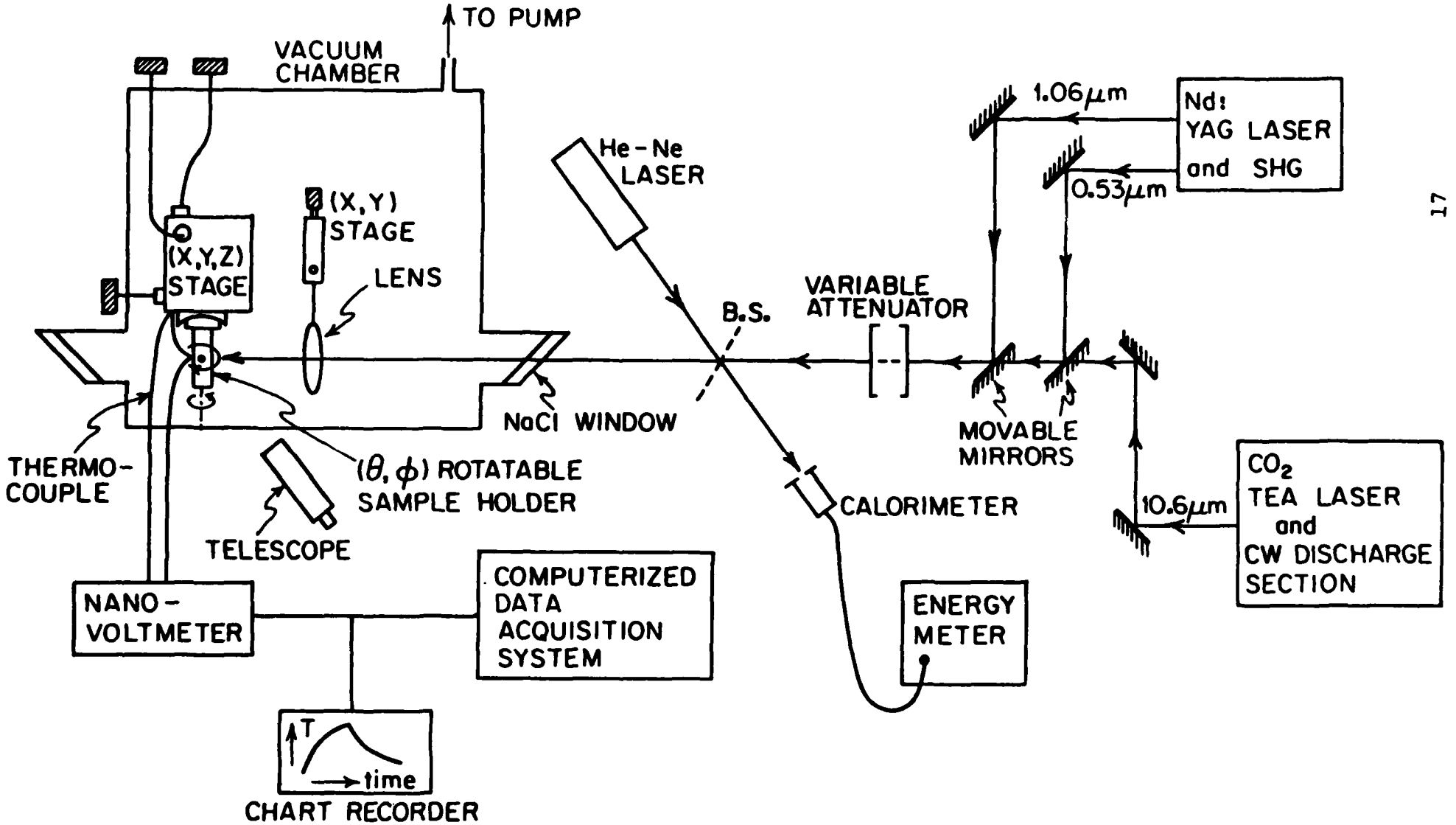
TO PUMP
VACUUM CHAMBER
1.06μm
Nd: YAG LASER and SHG
0.53μm
He-Ne LASER
(X,Y) STAGE
(X,Y,Z) STAGE
LENS
VARIABLE ATTENUATOR
B.S.
NaCl WINDOW
MOVABLE MIRRORS
THERMO-COUPLE
(θ, φ) ROTATABLE SAMPLE HOLDER
CALORIMETER
10.6μm
CO2 TEA LASER and CW DISCHARGE SECTION
TELESCOPE
NANO-VOLTMETER
COMPUTERIZED DATA ACQUISITION SYSTEM
ENERGY METER
T
time
CHART RECORDER

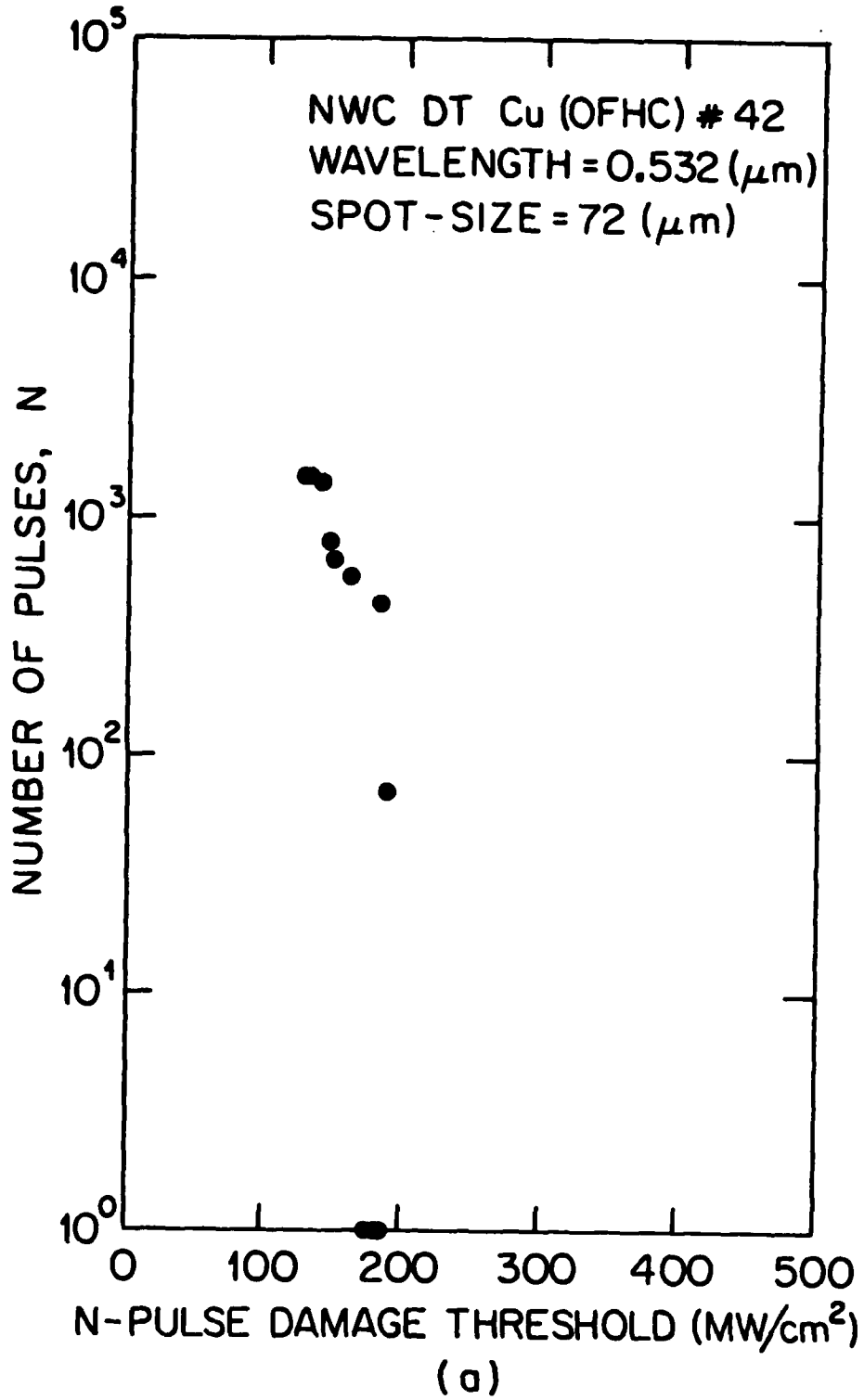
NWC DT Cu (OFHC) # 42
WAVELENGTH = 0.532 (μm)
SPOT-SIZE = 72 (μm)
NUMBER OF PULSES, N
10^5
10^4
10^3
10^2
10^1
10^0
0
100
200
300
400
500
N-PULSE DAMAGE THRESHOLD (MW/cm^2)

(a)

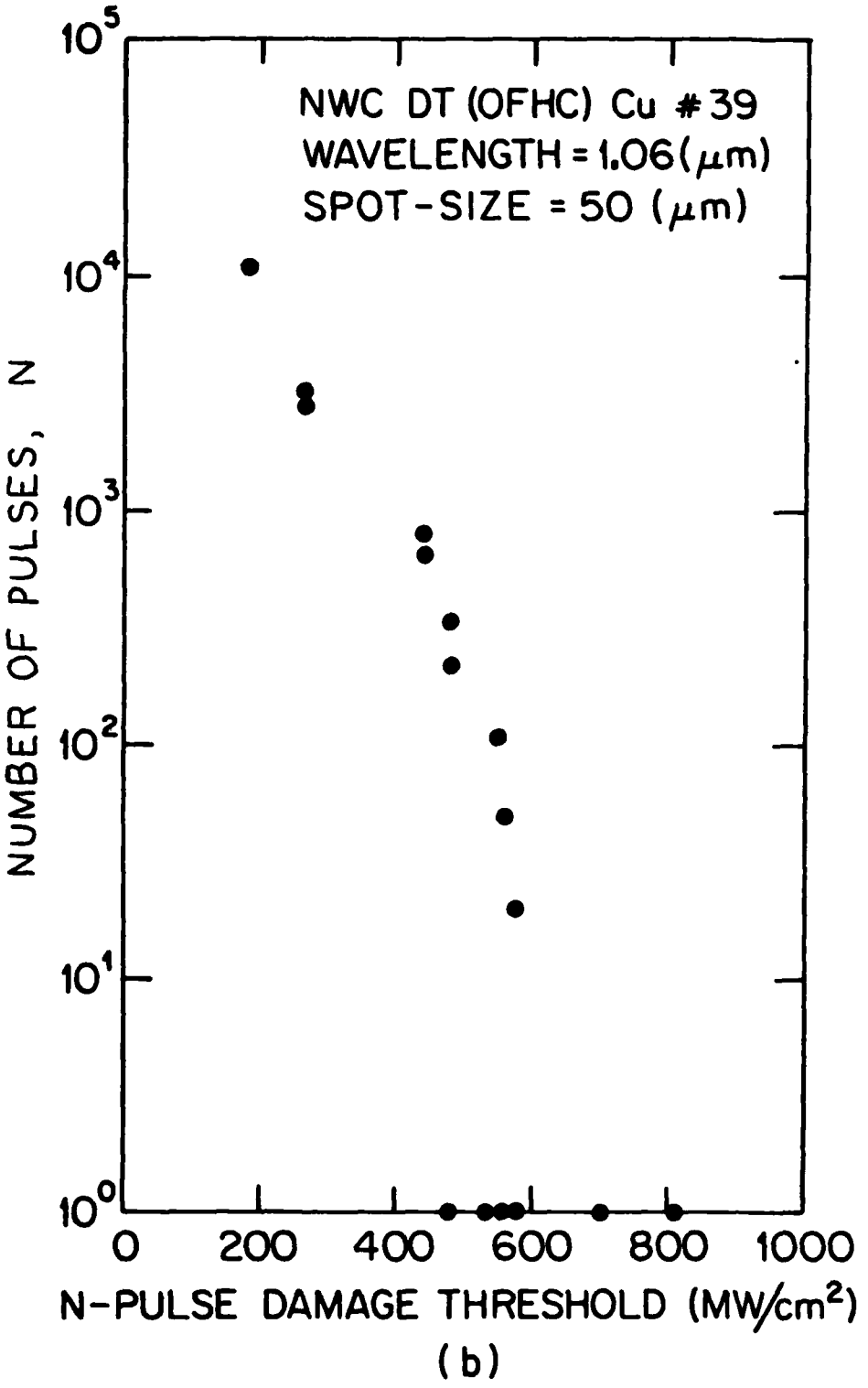
NWC DT (OFHC) Cu #39
WAVELENGTH = 1.06 (μm)
SPOT-SIZE = 50 (μm)
NUMBER OF PULSES, N
10^5
10^4
10^3
10^2
10^1
10^0
0
200
400
600
800
1000
N-PULSE DAMAGE THRESHOLD (MW/cm^2)

(b)

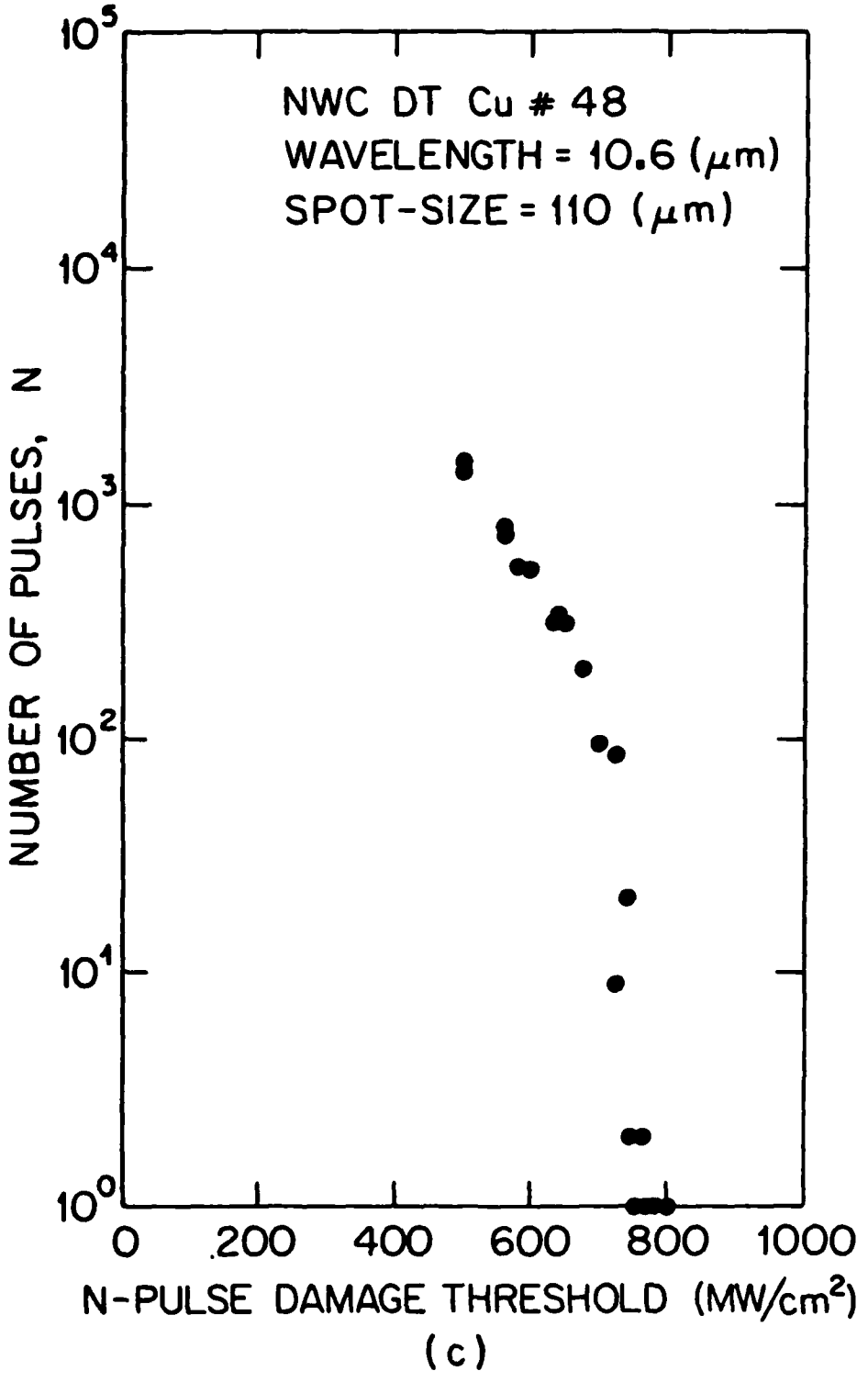
NWC DT Cu # 48
WAVELENGTH = 10.6 (μm)
SPOT-SIZE = 110 (μm)
NUMBER OF PULSES, N
10^5
10^4
10^3
10^2
10^1
10^0
0
200
400
600
800
1000
N-PULSE DAMAGE THRESHOLD (MW/cm^2)

(c)

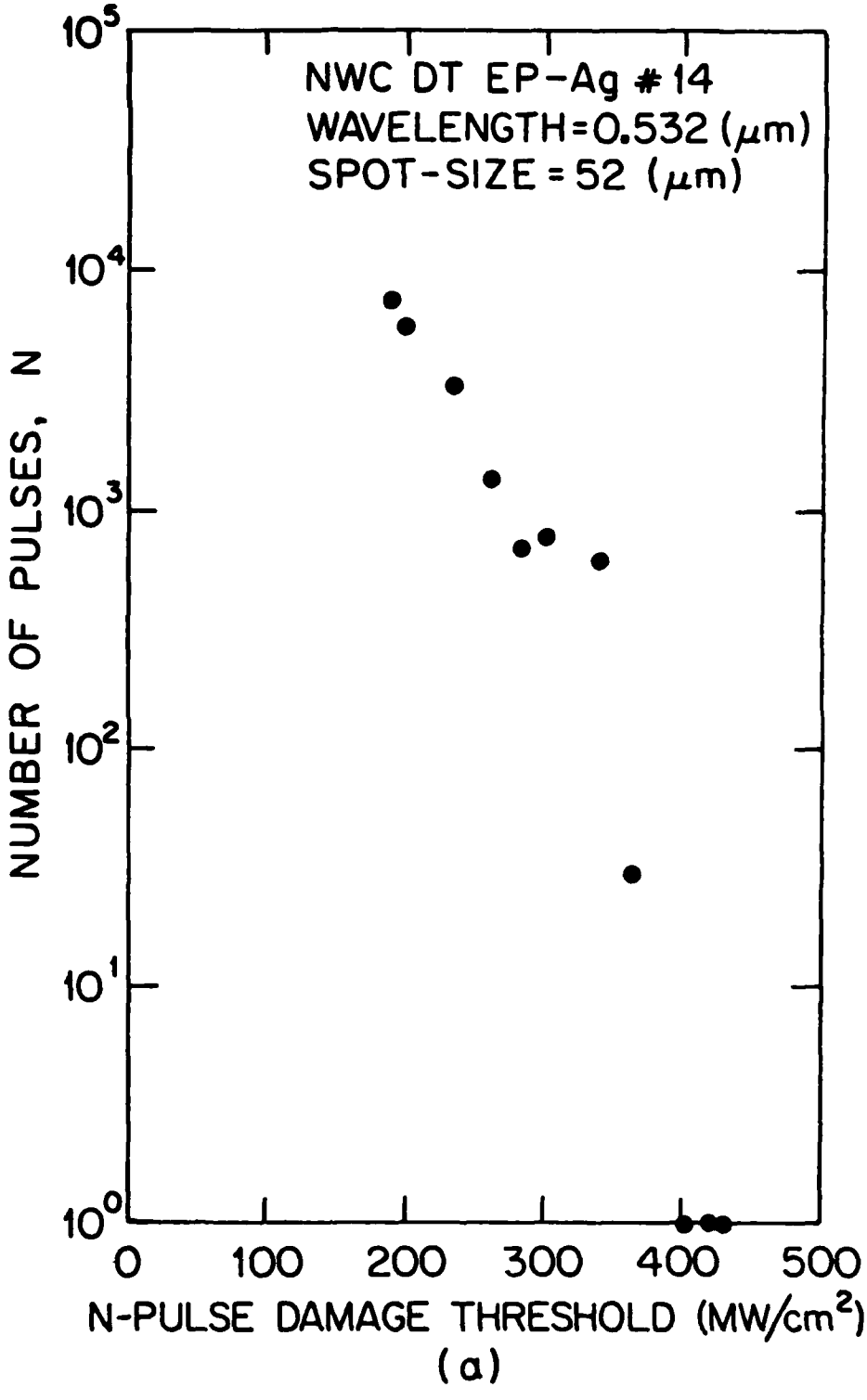
NWC DT EP-Ag #14
WAVELENGTH=0.532 (μm)
SPOT-SIZE = 52 (μm)
NUMBER OF PULSES, N
10^5
10^4
10^3
10^2
10^1
10^0
0
100
200
300
400
500
N-PULSE DAMAGE THRESHOLD (MW/cm^2)
(a)

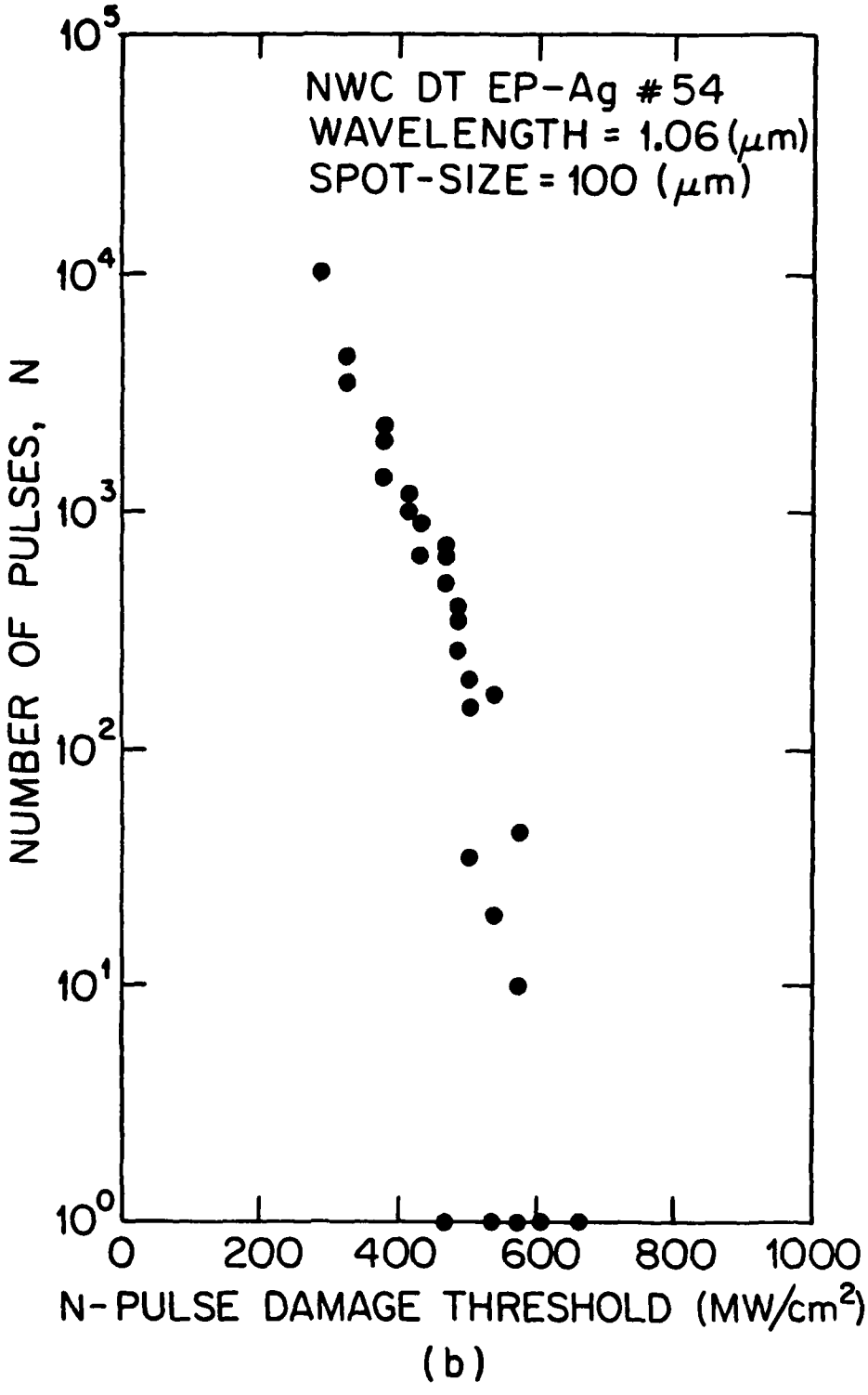
NWC DT EP-Ag #54
WAVELENGTH = 1.06 (μm)
SPOT-SIZE = 100 (μm)
NUMBER OF PULSES, N
10^5
10^4
10^3
10^2
10^1
10^0
0
200
400
600
800
1000
N-PULSE DAMAGE THRESHOLD (MW/cm^2)

(b)

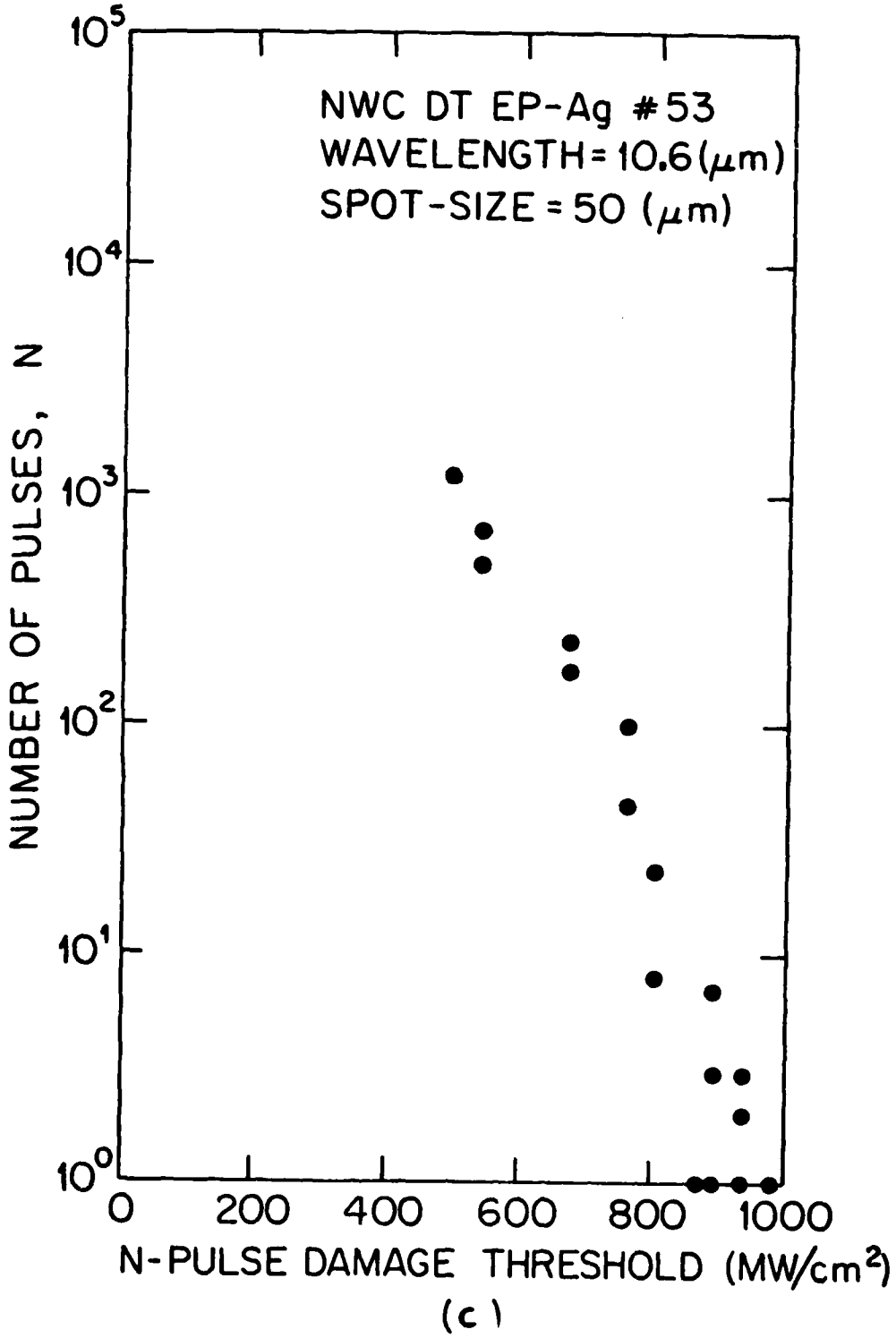
NWC DT EP-Ag #53
WAVELENGTH = 10.6 (μm)
SPOT-SIZE = 50 (μm)
NUMBER OF PULSES, N
10^5
10^4
10^3
10^2
10^1
10^0
0
200
400
600
800
1000
N-PULSE DAMAGE THRESHOLD (MW/cm²)

(c)

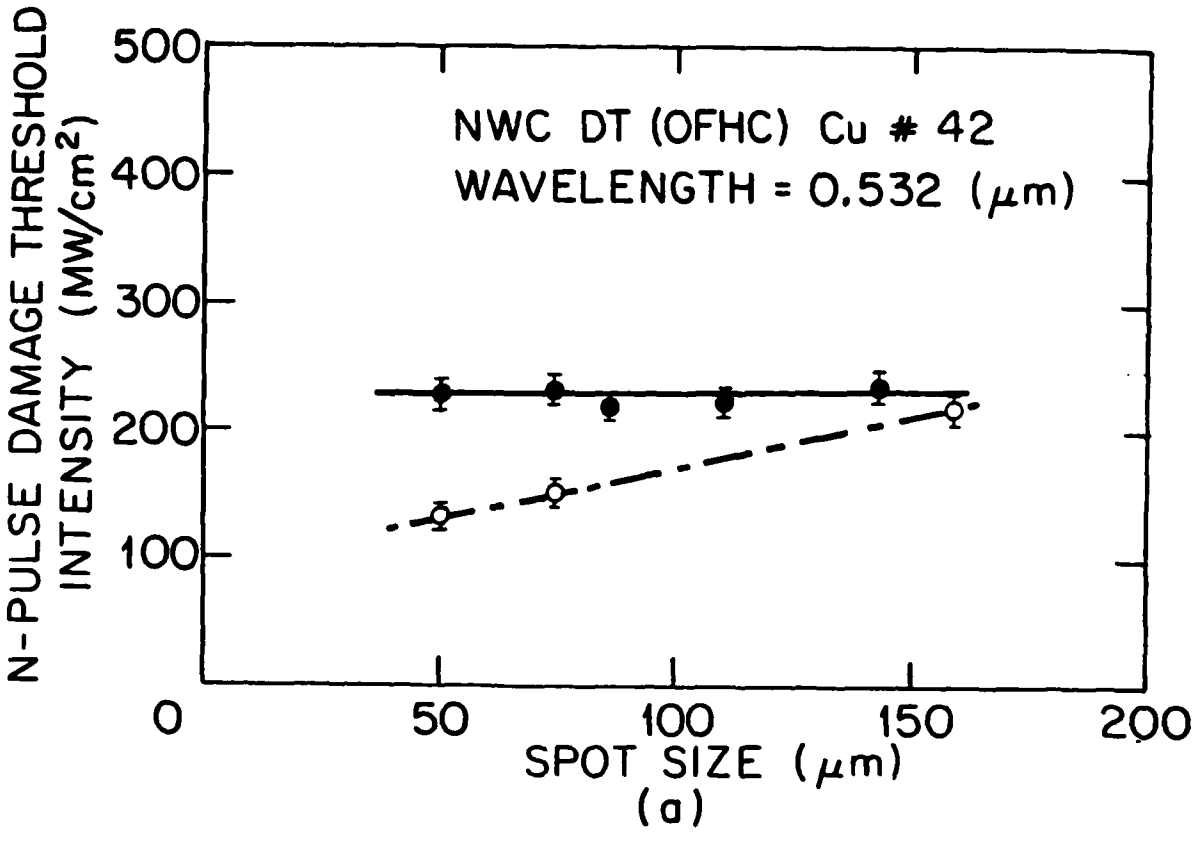
N-PULSE DAMAGE THRESHOLD INTENSITY (MW/cm²)
500
400
300
200
100
0
50
100
150
200
SPOT SIZE (μm)
NWC DT (OFHC) Cu # 42
WAVELENGTH = 0.532 (μm)

(a)

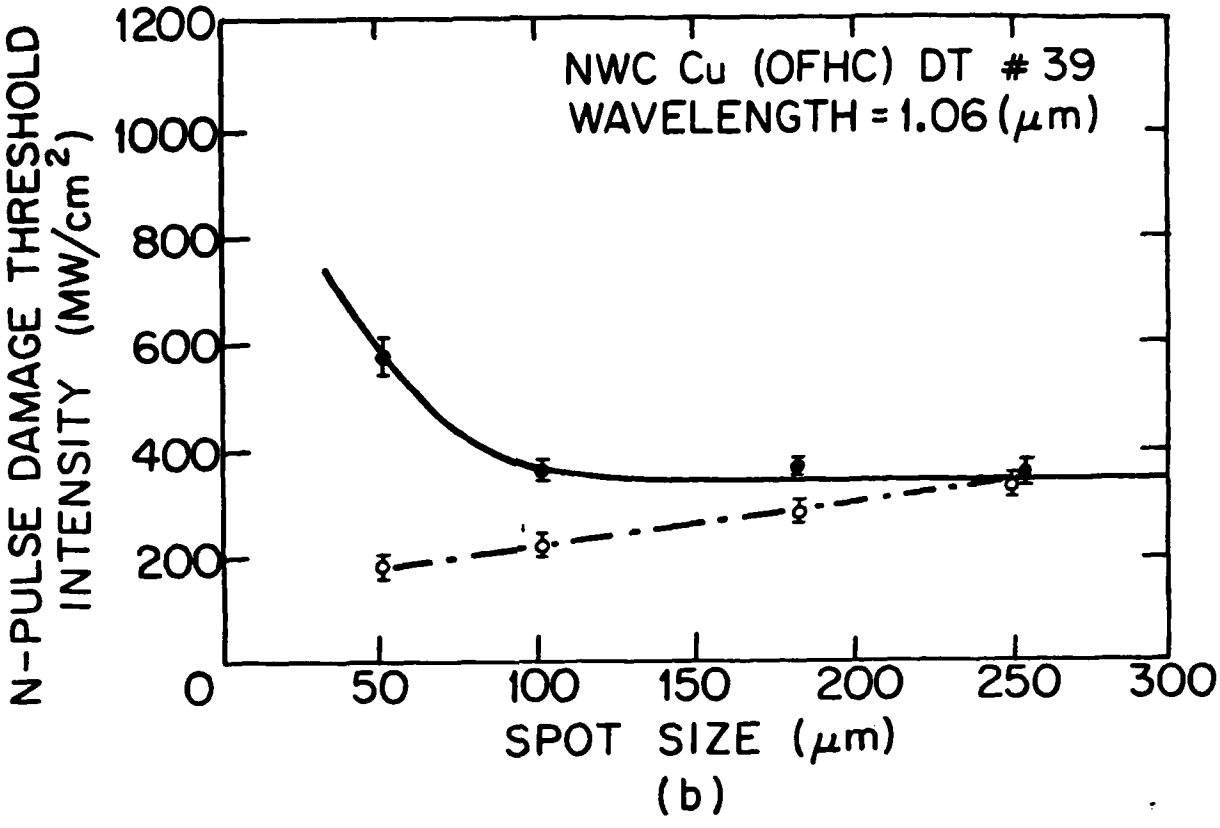
NWC Cu (OFHC) DT # 39
WAVELENGTH = 1.06 (μm)
N-PULSE DAMAGE THRESHOLD INTENSITY (MW/cm²)
1200
1000
800
600
400
200
0
50
100
150
200
250
300
SPOT SIZE (μm)

(b)

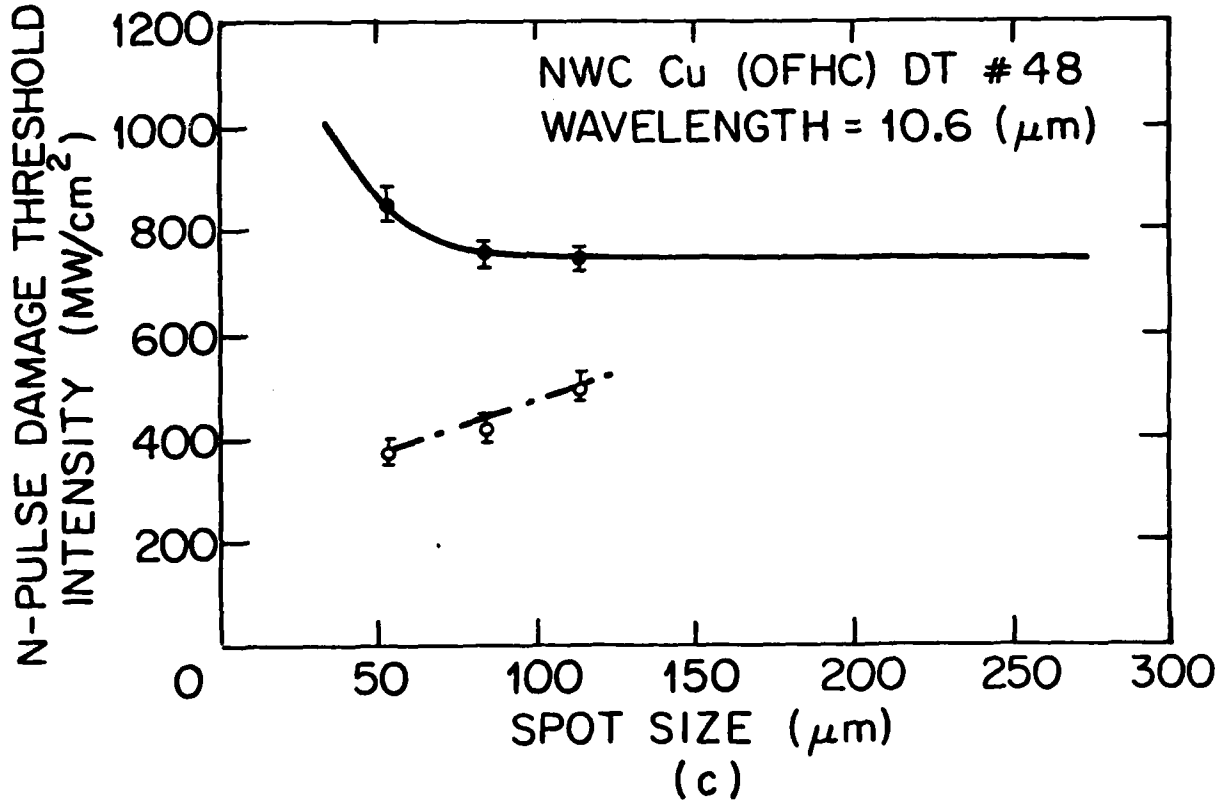
NWC Cu (OFHC) DT # 48
WAVELENGTH = 10.6 (μm)
N-PULSE DAMAGE THRESHOLD INTENSITY (MW/cm²)
1200
1000
800
600
400
200
0
50
100
150
200
250
300
SPOT SIZE (μm)

(c)

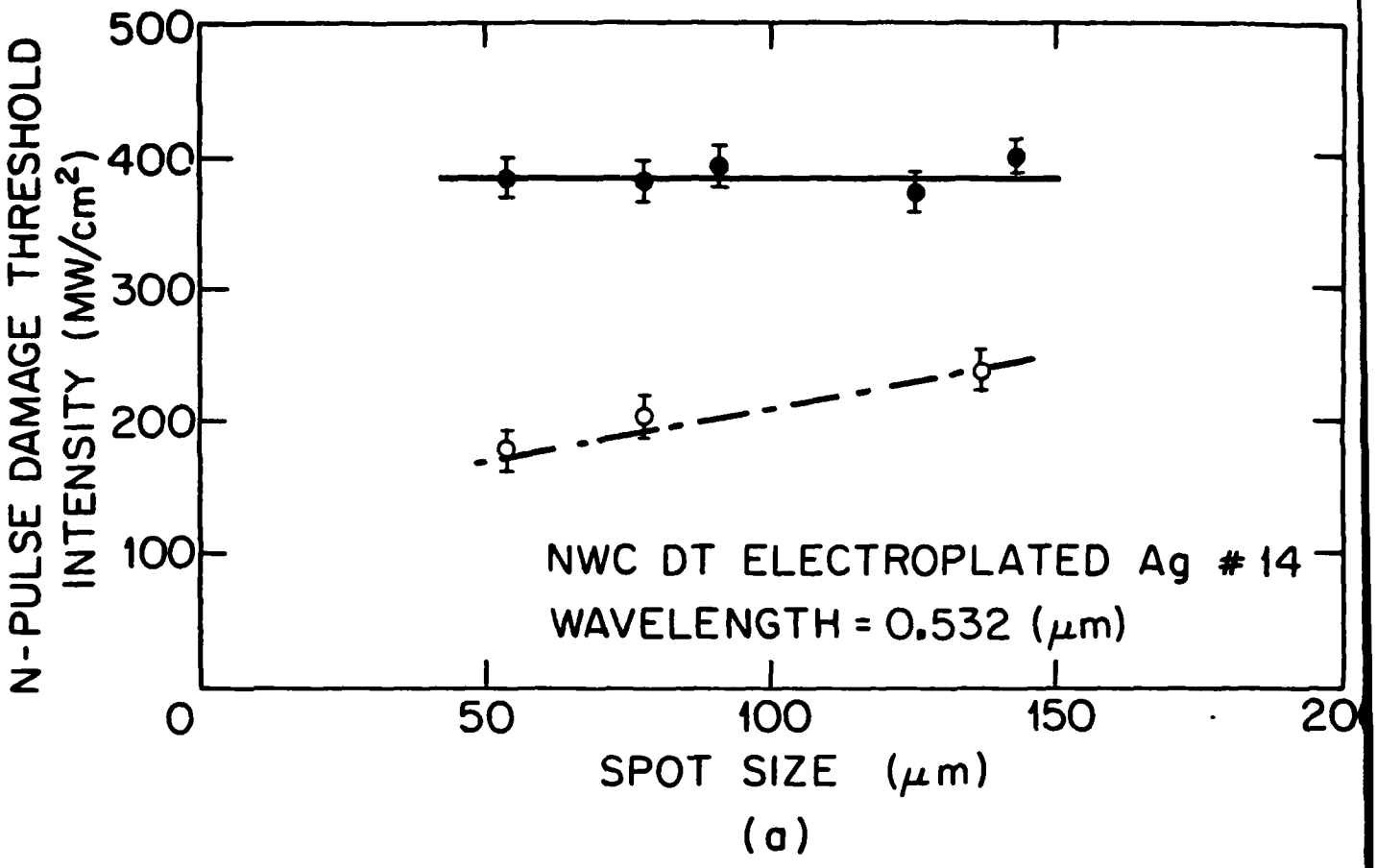
N-PULSE DAMAGE THRESHOLD INTENSITY (MW/cm²)
500
400
300
200
100
0
50
100
150
20
SPOT SIZE (μm)
NWC DT ELECTROPLATED Ag #14
WAVELENGTH = 0.532 (μm)

(a)

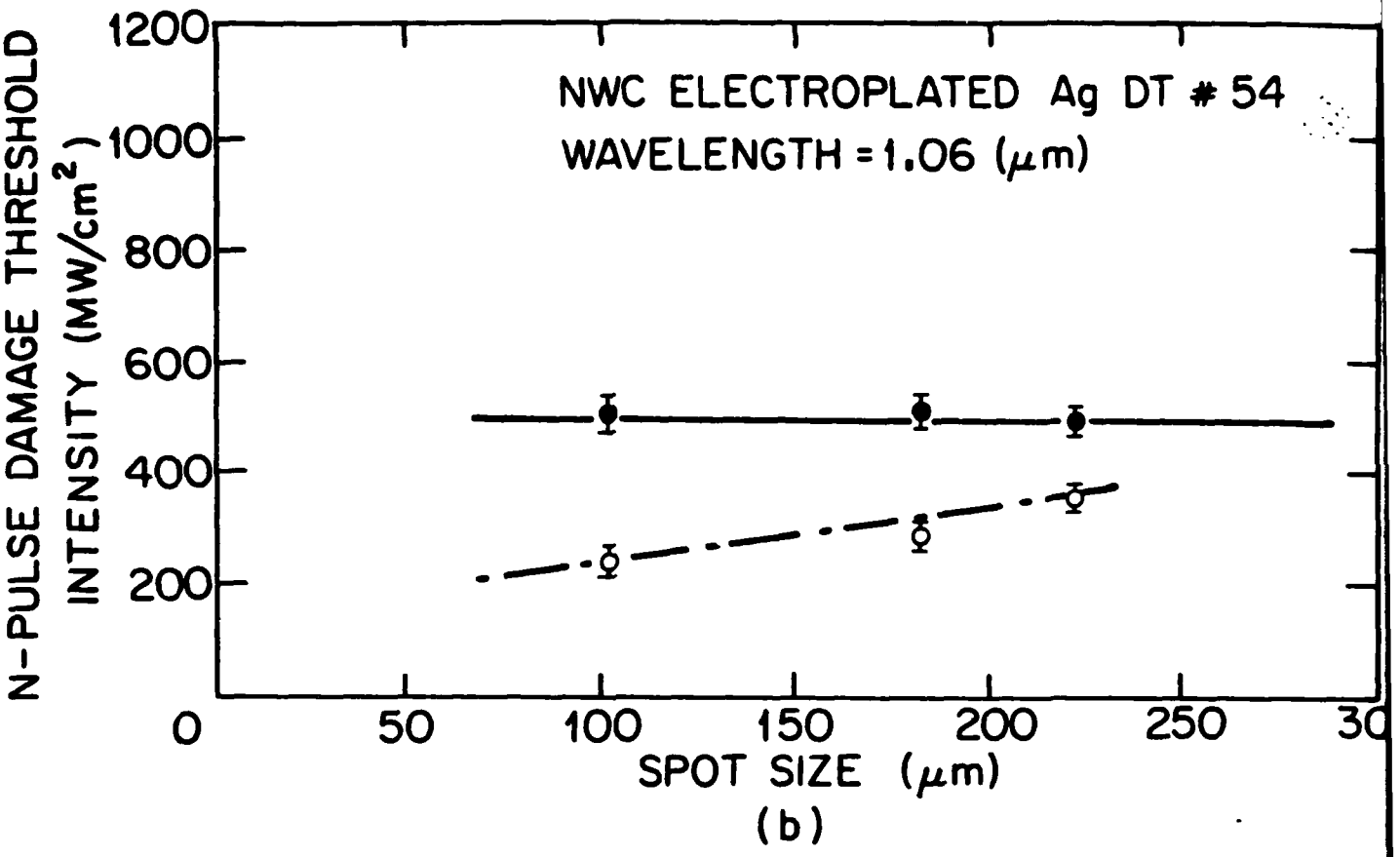
NWC ELECTROPLATED Ag DT # 54
WAVELENGTH = 1.06 (μm)
N-PULSE DAMAGE THRESHOLD INTENSITY (MW/cm²)
1200
1000
800
600
400
200
0
50
100
150
200
250
SPOT SIZE (μm)

(b)

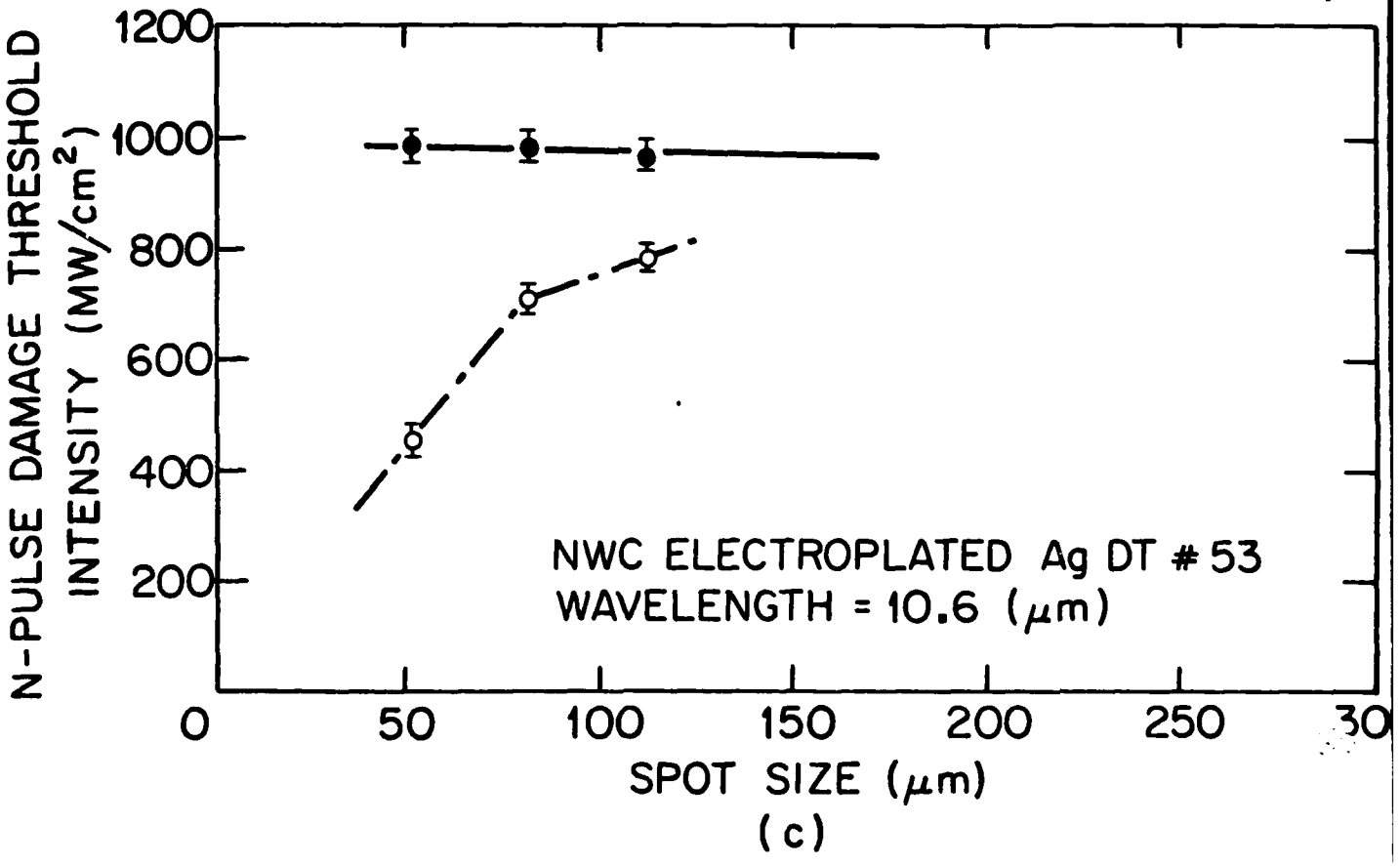
NWC ELECTROPLATED Ag DT # 53
WAVELENGTH = 10.6 (μm)
N-PULSE DAMAGE THRESHOLD INTENSITY (MW/cm²)
1200
1000
800
600
400
200
0
50
100
150
200
250
SPOT SIZE (μm)

(c)

NWC DT Cu # 42

inadiation $\lambda = 0.53$ [illegible]

210 um

a)

NWC DT Cu # 42

$\lambda = 0.532$ [illegible]

210 um

b)

Chapter 3

A Theoretical Model for Multiple Pulse Laser Induced Damage to Metal Mirrors

C. S. Lee, N. Koumvakalis and M. Bass

Center for Laser Studies
University of Southern California
University Park, DRB-17
Los Angeles, CA 90089-1112

A THEORETICAL MODEL FOR MULTIPLE - PULSE LASER - INDUCED DAMAGE TO METAL MIRRORS

C. S. Lee, N. Koumvakalis and M. Bass
Center for Laser Studies
University of Southern California
University Park,
Los Angeles, California 90089-1112

Abstract

In this paper, we present a phenomenological model based on laser-induced thermoelasticity, which shows that the threshold intensity required to initiate plastic deformation of metal surfaces increases with laser beam size for spots larger than the thermal diffusion length during the pulse. The results are consistent with previous experimental observations.

I. Introduction

In recent years there has been a growing interest in utilizing metal optics for high power laser applications at infrared wavelengths. This interest stems from their high reflectivity and good thermal conductivity, as well as from recent advances in precision metal optical machining[1]. However, laser - induced damage to active laser materials and other optical components generally determines the limit of useful laser performance. Accordingly, it is of great importance to understand the mechanisms of damage and subsequently reduce the susceptibility of optical elements to damage.

Single - pulse damage studies provide only part of the information needed for accurate prediction of laser system operation. There is evidence[2,3] that a material may exhibit a certain damage resistance under single pulse exposure but behave quite differently when incorporated in multiple - pulse operation. Several investingations of multiple - pulse damage on metal surfaces have been reported in the literature[4,5]. A significant reduction in damage threshold over the single pulse value was observed. This was attributed either to an increase in temperature which accumulated during the course of irradiation or to the build - up of an absorbing vapor or a micro-plasma near the surface due to repetitive irradiation by short laser pulses.[4] In these interpretations the interpulse interval(or repetition rate) of the laser pulses played a major role. The accumulation of temperature(or micro-plasma) depends on the time for heat(or plasma)

diffusion over a distance of the order of the beam spot-size compared to the interpulse period.

Recently, we reported the spot-size dependence of multiple pulse damage threshold for Cu, Ag and Au metal mirrors at several wavelengths[6,7]. In that work we attributed the increase of the damage threshold with increasing beam size to thermal stresses induced by a temperature gradient resulting from nonuniform laser heating. The purpose of this paper is to present a phenomenological model based on a linearized thermoelastic theory and an analysis of the observed spot-size dependence of the multiple-pulse damage threshold of metal mirrors.

II. Data

The experimental set-up and procedure used in measuring the damage threshold of metal mirrors were described in previous work.[6] The results are summarized in Tables I, II and III. An examination of the data indicates that the multiple-pulse damage fluxes show opposite trends in spot-size dependence to that of single-pulse damage threshold. The decreasing trend in single pulse damage threshold with increasing spot size was explained by a model based on defect-triggered mechanisms.[9] However, the observed result of multiple pulse damage experiments cannot be explained either by the temperature or the micro-plasma accumulation model discussed above.

III. Theory

Plastic deformation due to pulsed laser-induced thermal stress as the mechanism of multiple-pulse damage to metal mirrors

was initially suggested by Wang in 1972[8]. Later, this mechanism was reconsidered in more detail by Musal[9] following the observation of slip deformation by Porteus, Fountain, Jernigan, Faith and Bennett[10]. These researchers studied Cu surfaces irradiated with a single CO_2 laser pulse attenuated to below the melting threshold. According to Musal[9], repetitive pulse irradiation will cause an accumulation of plastic deformation providing the yield strength of the surface is exceeded during each pulse. Furthermore, such cumulative effects may progressively deteriorate the surface quality and eventually lead to catastrophic failure. The uniform illumination used in Musal's model[9], eliminated any spot-size effects. The unexpected spot-size dependence of the N-pulse damage threshold reported in our previous work[6] and expanded on in this paper is thought to be the result of the peaked Gaussian spatial distribution.

A. Metal Surface Heating

The problem of laser-induced heating of solids has been explored by many workers[11-13]. The temperature distribution at the end of the laser pulse depends on the thermal diffusion length for the laser pulse duration[13]. In our experiments the thermal diffusion length, defined as

$$d \equiv (4\kappa\tau_\rho)^{\frac{1}{2}}$$

where κ is the thermal diffusivity of the metal and τ_ρ is the pulse duration, is 3μm. This is much larger than the optical skin depth which is of the order of few hundred Angstroms and so we can use a surface heating model[13]. An analytical solution for the temperature increase at the end of a square pulse of duration τ_ρ is[13]

$$\theta(r,z) \equiv T(r,z) - T_o = \frac{A I_o w^2 \tau_p}{\rho C (\pi \kappa \tau_p)^{\frac{1}{2}} (4\kappa\tau_p + w^2)} \exp\left[- \frac{z^2}{4\kappa\tau_p} - \frac{r^2}{(4\kappa\tau_p + w^2)} \right] \quad (1)$$

where T_o, A, ρ, C, and are respectively the initial temperature, the optical absorptance, the material density, the specific heat and the thermal diffusivity. I_o is the peak intensity of a Gaussian beam, w is the beam waist at $1/e^2$ intensity and τ_p is the pulse duration(FWHM). Such a temperature distribution may cause differential thermal expansion of the metal and subsequent thermal stresses.

B. Thermomechanical Response

The thermal stresses developed when the surface of a metal is subject to nonuniform heating relax to nearly zero in the direction normal to the surface. On the other hand, they can be very large in the direction parallel to the surface since displacement(strain) in that direction is inhibited by the unheated region of the surrounding material. If the stresses exceed the elastic limit of the metal, the surface will suffer plastic deformation. Repeated pulse irradiation will create a succession of heating and cooling cycles. The subsequent compressive (heating) and tensile(cooling) plastic strains will accumulate and will finally manifest themselves as surface roughening and intrusion-extrusion hillocks where slip planes interest the free surface. Such effects were initially considered by Musal[9] who assumed a spatially uniform laser irradiation. In this paper the non-uniform nature of the laser distribution is taken into account.

Table I. Single and multiple pulse damage thresholds at 10.6 μm[a]

sample	spot coverage w μm	I_1 {MW/cm^2}	I_N {MW/cm^2}[b]
OFHC Cu	50	825 ± 25 (5%)	400 ± 10 (5%)
DT #48	80	728 ± 28 (6%)	475 ± 12 (5%)
(NWC)	110	760 ± 5 (3%)	540 ± 14 (5%)
OFHC Cu	50	847 ± 45 (7%)	380 ± 19 (7%)
DT #8	80	818 ± 52 (8%)	522 ± 21 (6%)
(INTOP)	120	778 ± 36 (7%)	713 ± 18 (5%)
EP Ag	50	903 ± 34 (6%)	475 ± 19 (6%)
DT #53	80	906 ± 70 (9%)	662 ± 20 (5%)
(NWC)	110	903 ± 56 (6%)	761 ± 23 (5%)

a. Pulse duration at this wavelength is 200 nsec at FWHM.

b. A value of 10^3 is selected for N.

Table II. Single and multiple pulse damage thresholds at 1.06 μm[a]

sample	spot radius w(μm)	I_1 {MW/cm^2}	I_N {MW/cm^2}[b]
OFHC Cu	50	528 ± 48 (9%)	180 ± 5 (5%)
DT #39	100	333 ± 13 (4%)	234 ± 7 (3%)
(NWC)	180	348 ± 10 (4%)	330 ± 10 (3%)
	250	345 ± 10 (4%)	330 ± 10 (3%)
OFHC Cu	100	449 ± 44 (10%)	287 ± 29 (10%)
DT #10	195	457 ± 16 (5%)	351 ± 11 (5%)
(INTOP)	225	447 ± 10 (4%)	409 ± 12 (5%)
EP Ag	100	518 ± 54 (10%)	285 ± 29 (10%)
DT #54	180	506 ± 15 (3%)	293 ± 18 (6%)
(NWC)	225	472 ± 6 (3%)	347 ± 10 (3%)
OFHC Cu	100	209 ± 6 (3%)	
DT #91	195	228 ± 7 (3%)	
(INTOP)	250	197 ± 6 (3%)	
OFHC Cu	95	289 ± 32 (11%)	176 ± 9 (5%)
MP #3	135	242 ± 44 (18%)	175 ± 9 (5%)
(NORTHROP)	250	301 ± 9 (3%)	220 ± 7 (3%)
EP Au	56	509 ± 18 (4%)	231 ± 9 (4%)
DT #2	118	457 ± 13 (3%)	249 ± 11 (5%)
	255	467 ± 10 (2%)	345 ± 8 (3%)

a. Pulse duration at this wavelength is 22 nsec at FWHM.

b. Here, a value of 10^4 is selected for N.

Table III. Single and multiple pulse damage thresholds at 0.53 μm[a]

sample	spot radius W (μm)	I_1 {MW/cm^2}	I_N {MW/cm^2}[b]
OFHC Cu	49	231[c]	136[c]
DT #42	73	237	153
(NWC)	85	220	---
	108	222	---
	140	239	---
	158	---	217
EP Ag	52	373	180
DT #14	77	372	200
(NWC)	92	383	---
	124	368	---
	134	---	236
	140	393	---
EP Au	85	183	101
DT #1	134	185	119
	164	180	136

a. Pulse duration at this wavelength is 15 nsec at FWHM.

b. A value of 10^3 is selected for N.

c. The uncertainty of damage is about $\pm$ 7%.

In general, two types of thermal stresses can be generated in an elastic medium by laser irradiation. These are 1) transient(or dynamic) stress induced by sudden changes in temperature which occur when the duration of the laser pulse is sufficiently short(of the order of nsec), and 2) steady(or quasi-static) stress arising from a temperature gradient, which becomes significant as the heating is highly localized. Dynamic stresses will relax by launching an elastic (stress) wave which will propagate at the speed of acoustic waves. On the other hand, steady stresses will be relieved by the process of thermal diffusion which is relatively slow compared to dynamic stress relaxation.

In the quasi-static formulation the problem of determining stresses in a half-space irradiated with an axisymmetric radiant flux can be described by the following strain-stress relations (14,15).

$$\sigma_{rr} = \lambda\Delta + 2G\,(du/dr) - \beta\Theta \tag{2}$$

$$\sigma_{\theta\theta} = \lambda\Delta + 2G\,(u/r) - \beta\Theta \tag{3}$$

$$\sigma_{zz} = \lambda\Delta + 2G\,(dv/dr) - \beta\Theta \tag{4}$$

$$\sigma_{rz} = G\Sigma_{rz} = G\,(du/dz + dv/dr) \tag{5}$$

where $$\Delta = \frac{du}{dr} + \frac{u}{r} + \frac{dv}{dz} = \varepsilon_{rr} + \varepsilon_{\theta\theta} + \varepsilon_{zz} \tag{6}$$

$$\lambda = \frac{\nu E}{(1+\nu)\ (1-2\nu)} \tag{7}$$

$$\beta = (3\lambda + 2G)\ \alpha \tag{8}$$

and σ_{rr} (ε_{rr}), $\sigma_{\theta\theta}$($\varepsilon_{\theta\theta}$), σ_{zz} (ε_{zz}), and σ_{rz} (ε_{rz}) are respectively radial, hoop, axial and shear stresses (strains); u and v are radial and axial displacements, α is the coefficient of thermal expansion, ν is Poisson's ratio, E is Young's modulus, G is the

modulus of rigidty (shear modulus), and Θ is the local temperature rise (Eq. (1)). With the imposition of transverse constraints (i.e., u=0 and du/dr = 0), Eqs. (2) to (5) reduce to

$$\frac{(1+2\nu)}{E}\sigma_{zz} = \frac{(1-\nu)}{(1+\nu)}\varepsilon_{zz} - \alpha\Theta \tag{9}$$

$$\frac{(1-2\nu)}{E}\sigma_{rr} = \frac{\nu}{(1+\nu)}\varepsilon_{zz} - \alpha\Theta \tag{10}$$

$$\frac{(1-2\nu)}{E}\sigma_{\theta\theta} = \frac{\nu}{(1+\nu)}\varepsilon_{\theta\theta} - \alpha\Theta \tag{11}$$

$$\varepsilon_{zz} = \frac{dv}{dz} \tag{12}$$

$$\sigma_{rz} = G\frac{dv}{dr} \tag{13}$$

This system of partial differential equations can be further simplified by imposing the boundary condition that the normal stress at the free surface is zero. In the near-surface region of the metal the normal stress is relieved in a short time compared to the time required for thermal diffusion to lower the temperature. With this approximation, these governing equations reduce even further to

$$\varepsilon_{zz} = \frac{dv}{dz} \simeq \frac{(1+\nu)}{(1-\nu)}\alpha\Theta \tag{14}$$

$$\sigma_t = -\frac{E}{1-\nu}\alpha\Theta \tag{15}$$

where σ_t is the transverse stress in both orthogonal directions parallel to the free surface, (i.e., σ_{rr} and $\sigma_{\theta\theta}$). Eq. (14) can be integrated to give

$$v(r,o;t) \simeq -\frac{(1+\nu)}{(1-\nu)}\alpha\int_{z=o}^{\infty}\Theta(r,z;t)dz \tag{16}$$

The negative algebraic signs in Eqs. (15) and (16) indicate

compressive stress and displacement of the free surface in the negative z-direction (i.e., expansional), respectively, for a temperature increase.

The expression for the normal displacement of the surface at the end of a temporally rectangular pulse can be obtained by Eq. (16) and Eq. (1). In the near surface region of the metal, the maximum shear stress due to nonuniform surface heating can be obtained from Eq. (5) and is expressed in the form

$$\sigma_{rz}^{max} \approx \left\{ \frac{A\, I_o \alpha E \tau_p w^2}{\sqrt{2e}(1-\nu)\rho C(4\kappa\tau_p + w^2)^{3/2}} \right\} \tag{17}$$

where e is the base of Naperian logarithms. In our experiment the thermal diffusion length for the pulse duration under consideration (i.e., for copper, $(4\kappa\tau_p)^{\frac{1}{2}} = 3\mu m$ for $\tau_p = 22$ nsec) is much smaller than the beam radius (of the order of $10^2 \mu m$.) Therefore, Eq. (17) can be simplified to

$$\sigma_{rz}^{max} \approx \left\{ \frac{A\, I_o\, \alpha E \tau_p}{\sqrt{2e}(1-\nu)\rho C} \right\} \cdot \frac{1}{w} \tag{18}$$

which indicates that in the limit of large spot-sizes compared to the thermal diffusion length the shear stress is proportional to the pulse duration but inversely proportional to the irradiated spot size.

C. Plastic Deformation

When the shear stress exceeds a critical value in the near-surface region given by the yield strength of the material, plas-

tic yielding takes place. For the specific configuration considered in this experiment and discussed in the previous section, the onset of plastic deformation is simply defined by

$$\sigma_{rz}^{max} > \sigma_y \tag{19}$$

As a consequence, the threshold intensity at which plastic yield will first occur at the free surface follows directly from Eqs. (18) and (19) and is given by

$$I_y \simeq \frac{\sqrt{2e}(1-\nu)\ C\sigma_y}{A\alpha E\tau_p}\ w \tag{20}$$

This important result shows that the threshold intensity for plastic deformation is linearly proportional to the irradiated spot size and therefore, that the power density required to initiate plastic deformation is higher for larger than for smaller spot size Gaussian distributions. In a repetitive pulse experiment the effect of cyclic heating and cooling will cause an accumulation of plastic strain. The plastic deformation in the form of an irregular slip pattern, will manifest itself as random roughness on the free surface. The surface roughening previously observed[6] is therefore related to plastic strain accumulation. The degree of surface roughness induced by multiple-pulse illumination increases as the number of pulses increases[6]. The importance of slip deformation as a damage mode to a metal mirror is that it roughens the surface and the accumulation of roughness will gradually deteriorate the mirror. The catastrophic failure observed in the current experiments following multiple pulse irradiation is related to optical field enhancement at the micro-

irregularities. This leads to the observed lower optical breakdown threshold[6].

E. Theoretical - Experimental Correlation

Fig. 1 shows a typical plot of the number of pulses required to cause failure, N vs. the corresponding intensity[6]. This plot, characteristic of repetitively irradiated metallic mirrors, is very similar to a stress, S, vs. number of cycles required to cause mechanical failure, N, relation, characterizing the cumulative damage of mechanical components due to the cyclic action of the applied stress. Fig. 2 shows a characteristic S vs. N relation described by the following equation[16].

$$KN = \frac{1}{S-\sigma_f} - \frac{1}{S(1-c)} \qquad (21)$$

where N is the number of cycles required to cause failure at stress level S, k and c are material constants and σ_f is a fatigue limit equivalent to I_∞ (w) i.e., the intensity in Eq. (20) required to generate thermal stress sufficient for slip initiation. It should be pointed out that whereas in our figures the intensity is the independent variable, i.e. we plot N vs I, in the figure describing the mechanical failure N is the independent variable i.e. the plot is S vs. N. By analogy with Eq. (21) one can use a similar relation to express a phenomenological relation between the number of pulses N, and the intensity, I,

$$K'N = \frac{1}{I-I_\infty(w)} - \frac{1}{I(1-c')} \qquad (22)$$

where k' and c' are material constant.

Fig. 3 is a plot of two N vs. I diagrams based on Eq. (22)

corresponding to two different spot sizes.

Point A and B indicate that the threshold damage intensity leading to fatigue failure on the Nth pulse is higher for larger spot radii, point B, than for smaller ones, point A. Points C and D illustrate the fact that for larger beam radii more pulses are required to cause damage, point D, than for smaller ones, point C. This behavior is very consistent with the experimental observation in multiple-pulse damage experiments for various beam sizes[6].

IV. Discussion

A. Thermal Diffusion

The result shown in Equ. (20) has been obtained under the assumption that thermal diffusion during the pulse duration is negligible. However as the beam radius becomes smaller or the pulse duration longer, the thermal diffusion length will become comparable or larger than the beam radius. In this case, the analytic expression for I_∞ (w) derived from Eq. (17) without neglecting thermal diffusion is given by

$$I_\infty (w) = \frac{\sqrt{2e}(1-\nu)\rho C\sigma_f}{A\alpha E\tau_p}\left\{w\left(1+\frac{4\kappa\tau_p}{w^2}\right)^{3/2}\right\} \tag{23}$$

where the different parameters have been defined previously. In the short pulse, large spot case ($w^2 >> 4\kappa\tau_\rho$), Eq. (24) reduces to Eq. (20). However, for the long-pulse small spot size case $w^2 << 4\kappa\tau_\rho$ and Eq. (24) reduces to

$$I_\infty (w) = \frac{\sqrt{2e}(1-\nu)\ \rho C\sigma_f (4\kappa\tau_p)^{3/2}}{A\alpha E\tau_p}\ \frac{1}{w^2} \tag{24}$$

giving a spot size dependence oposite to that of Eq. (20).

B. Dynamic Stress

It has been briefly discussed in Section III-B that the thermal expansion following the rapid absorption of radiant energy at the surface of an elastic solid will promote a stress wave propagating with the speed of sound in the material, in addition to the quasi-static stress associated with the nonuniform temperature distribution. Although the present work is concerned with the effects of the latter it is worth briefly discussing the former.

Musal[9] has considered the role that dynamic stress may play in the case of transient surface heating of metal mirrors due to short-pulse, large-spot irradiation. He concludes that when the heated region is substantially larger than the distance the stress wave propagates during the pulse dynamic stresses would cause permanent damage. According to this mechanism a metal mirror can tolerate higher incident radiant fluxes for smaller irradiated spot sizes than for larger ones compared to the stress relaxation length. As the irradiated spot size is reduced, stress relaxation reduces the effect of dynamic stress and quasi-static stress becomes more significant, as is our case. After further reduction of the spot size so that it becomes smaller than the thermal diffusion length, the quasi-stress model gives an increasing damage threshold for decreasing spot sizes, indicated by Eq. (25).

Conclusion

The present work and references have provided some insight as to how metal surfaces respond to repetitive irradiation by laser pulses. The model presented explains the dependence of the intensity on spot size where we observe that for increasing spot sizes the damage intensity increases in a linear fashion.

The authors wish to thank Drs. J. O. Porteus and D. L. Decker (NWC, China Lake) for helpful discussions.

This work was sponsored by ONR-SRO Research Grant No. N0014-70-C-0896.

REFERENCES

1. D.L. Decker and D.J. Grandjean, in Laser Induced Damage to Optical Materials, NBS Spec. Pub. No. 462, pp. 145 (1976).
2. M. Bass, in Laser Induced Damage to Optical Materials, NBS Spec. Pub. No. 341, pp. 90 (1970).
3. M. Bass and K.M. Leung, IEEE J. Quantum Elec., JQE-12, pp. 82 (1976).
4. A.B. Callender, in Laser Induced Damage to Optical Materials, NBS Spec. Pub. No. 435, pp. 202 (1975).
5. S.J. Thomas, R.F. Harrison, and J.F. Figueira, Appl. Phys. Lett. 40, pp. 200 (1982).
6. C.S. Lee, N. Koumvakalis, and M. Bass, Appl. Phys. Lett. 41, pp. 625 (1982); C.S. Lee, Ph.D. Thesis, University of Southern California (1982).
7. N. Koumvakalis, C.S. Lee and M. Bass, in Laser Induced Damage to Optical Materials, to be published by the National Bureau of Standards.
8. V. Wang, A.I. Braunstein, M. Braunstein, and J.Y. Wada, in Laser Induced Damage to Optical Materials, NBS Spec. Pub. No. 372, pp. 183 (1972).
9. H.M. Musal, Jr., in Laser Induced Damage to Optical Materials, NBS Spec. Pub. No. 568, pp. 159 (1979).
10. J.O. Porteus, et al., in Laser Induced Damage to Optical Materials, NBS Spec. Pub. No. 509, pp. 204 (1977).
11. H.S. Carslaw and J.C. Jaeger, Conduction of Heat in Solids, (Clarendon, Oxford, 1959).

12. J.H. Bechtel, J. Appl. Phys. 46, pp. 1585 (1975).

13. J.F. Ready, Effects of High Power Laser Radiation, (Academic Press, New York, 1971).

14. J. Parkus, Thermoelasticity, (Springer-Verlag, New York 1976).

15. R. Hoyle, in Thermal Stress, ed. by B.P. Benham and R. Hoyle, (Sir Isaac Pitman & Sons Ltd., London, 1964), pp. 43.

16. R.R. Gatts, ASME Trans. 83D, pp. 529 (1961).

FIGURE CAPTIONS

Fig. 1. Measured log N vs. I_N for diamond-turned OFHC Cu irradiated at 10.6 μm. Solid circles indicate catastrophic failure accompanied by a visible spark. Open circles indicate damage produced with no observable spark. The spot radius was 110 μm for these data. (after Ref. 6).

Fig. 2. Theoretical γ-L curves (nondimensionalized S-N curves) and composite data from constant stress amplitude tests of steels. (after ref. 16).

Fig. 3. Schematic of N vs I curve based on Eq. (22). Curves 1 and 2 correspond to Eq. (22) of two different spot sizes. Δ indicated fatique limits for slip initiation given by Eq. (20). Points A, B, C, and D are explained in the text.

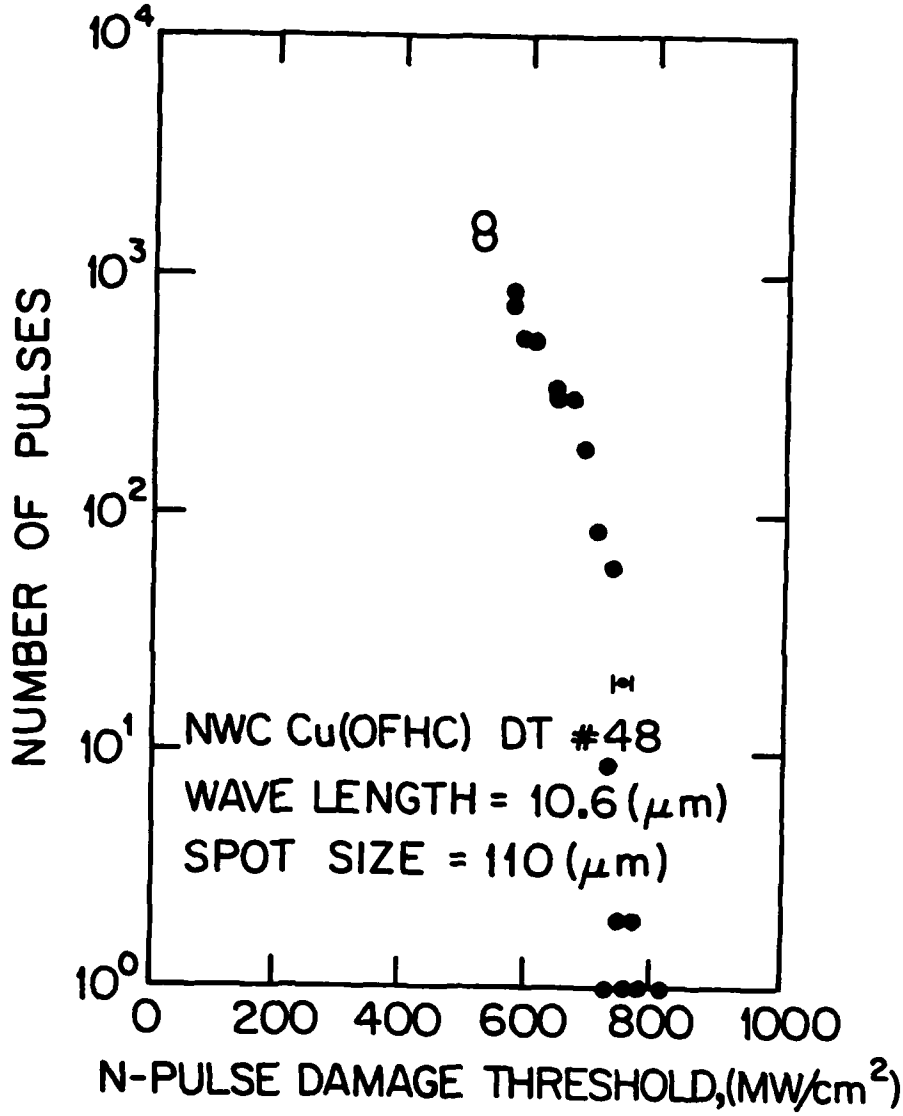
NUMBER OF PULSES
10^4
10^3
10^2
10^1
10^0
8
NWC Cu(OFHC) DT #48
WAVE LENGTH = 10.6 (μm)
SPOT SIZE = 110 (μm)
0
200
400
600
800
1000
N-PULSE DAMAGE THRESHOLD,(MW/cm^2)

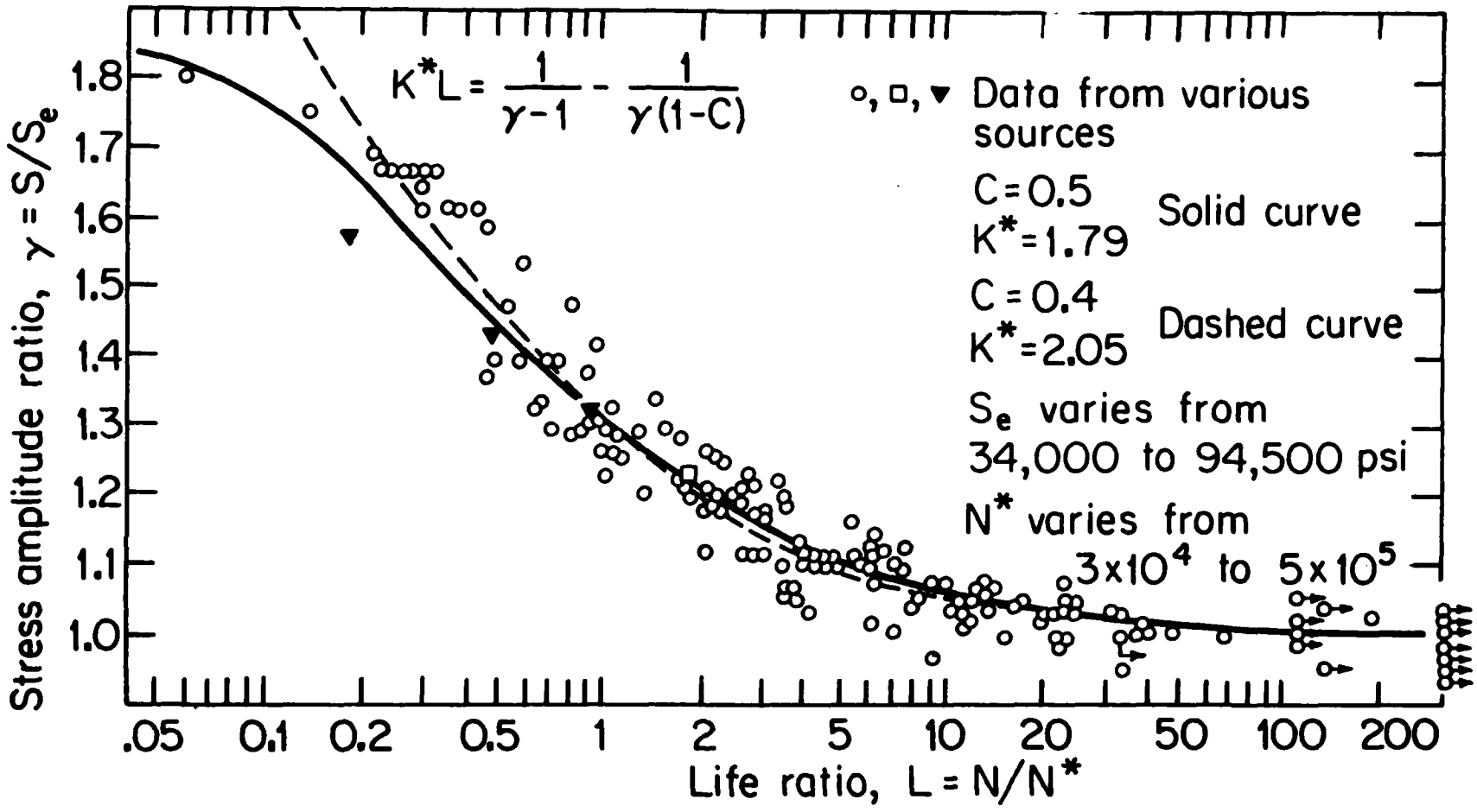
$K^*L = \frac{1}{\gamma-1} - \frac{1}{\gamma(1-C)}$
○, □, ▼ Data from various sources
C = 0.5
K* = 1.79
Solid curve
C = 0.4
K* = 2.05
Dashed curve
S_e varies from 34,000 to 94,500 psi
N* varies from 3×10^4 to 5×10^5
Stress amplitude ratio, $\gamma = S/S_e$
1.8
1.7
1.6
1.5
1.4
1.3
1.2
1.1
1.0
.05
0.1
0.2
0.5
1
2
5
10
20
50
100
200
Life ratio, $L = N/N^*$

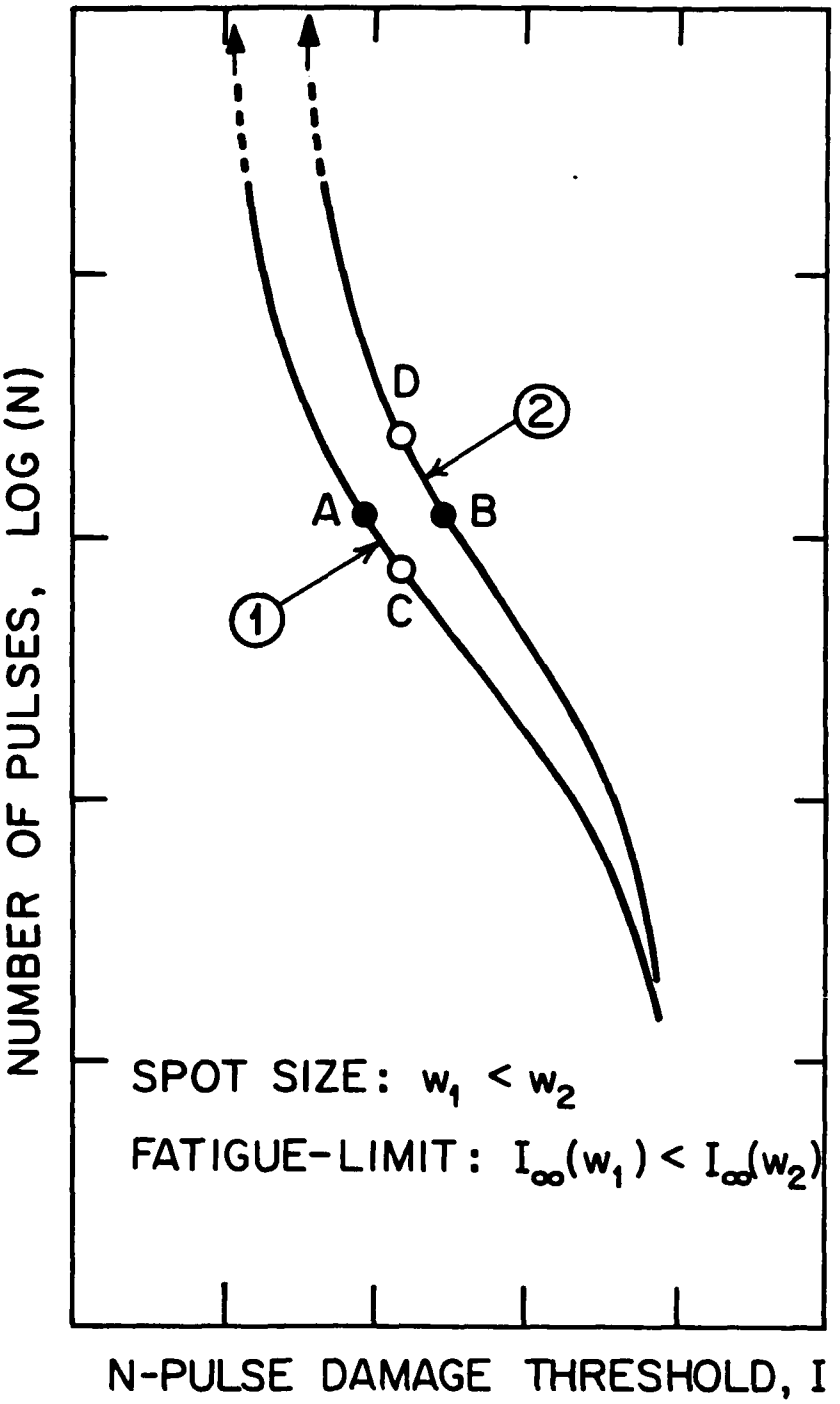
NUMBER OF PULSES, LOG (N)
D
2
A
B
1
C
SPOT SIZE: $w_1 < w_2$
FATIGUE-LIMIT: $I_\infty(w_1) < I_\infty(w_2)$
N-PULSE DAMAGE THRESHOLD, I

Chapter 4

Intensity Dependent Absorption in Cu and Ag Metal Mirrors; The Role of Temperature and Surface Roughness

N. Koumvakalis, C. S. Lee and M. Bass

Center for Laser Studies
University of Southern California
University Park, DRB-17
Los Angeles, CA 90089-1112

INTENSITY DEPENDENT ABSORPTION IN Cu AND Ag METAL MIRRORS: THE ROLE OF TEMPERATURE AND SURFACE ROUGHNESS

N. Koumvakalis, C. S. Lee and M. Bass

Center for Laser Studies

University of Southern California

University Park

Los Angeles, California 90089-1112

Abstract

The intensity dependent absorption in diamond turned Cu and Ag metal mirrors and mechanically polished Cu mirrors was investigated at 1.06 and 0.532 μm. The absorption increased with increasing intensity. The change is explained in terms of thermal mechanisms. The absorption is independent of the surface alterations introduced by irradiation. The observed reduction in damage resistance of the altered material may be caused by the interaction of light with the sharp edges produced by mechanical deformation.

INTENSITY DEPENDENT ABSORPTION IN Cu AND Ag METAL MIRRORS; THE ROLE OF TEMPERATURE AND SURFACE ROUGHNESS

N. Koumvakalis, C. S. Lee and M. Bass

Center for Laser Studies, University of Southern California, University Park, Los Angeles, CA 90089-1112

INTRODUCTION

The advent of high power pulsed lasers has made the observation of non-linear processes feasible in a variety of materials. Multiphoton absorption is commonly observed in semiconductors and is the cause of several interesting effects [1]. Metal mirrors because of their excellent characteristics - very high reflectivity and good thermal conductivity - are very suitable for high power pulsed laser applications particularly in the infra-red. Intensity dependent mechanisms, such as multiphoton absorption could seriously affect their performance, leading eventually to catastrophic damage. Another mechanism which could equally well affect the absorption of metals at high laser powers is the temperature dependence of the absorptance. It has been observed that the absorption of a metal increases with temperature in a quasi-linear fashion [2-5]. As a result of this any temperature variations introduced by the incoming laser beam could change the effective absorption coefficent.

The objective of this work is twofold. In the first part we present repetitively pulsed 1.06μm laser calorimetry studies of diamond turned Cu and Ag electroplated diamond turned Cu mirrors. This work shows an intensity dependent absorption which can be

explained as a result of the temperature dependence of the absorption of the metals. In the second part we examine the surface morphology of diamond turned bulk Cu and Ag and Au electroplated diamond turned Cu mirrors, irradiated with 1.06 and 0.532μm laser intensities up to but not exceeding those which cause catastrophic damage. Catastrophic damage is defined to have occurred when during irradiation there is a visible flash of light from the irradiated material accompanied by a large irreversible increase in its absorption and followed by the observation of a severely disrupted surface. Despite the introduction of laser induced surface alterations such as slip bands the magnitude of the roughness in the irradiated sites before catastrophic damage is comparable to that of the unirradiated sites. Our measurements therefore indicate that the altered surface does not affect the absorptance. The reduced damage resistance of the altered material may be caused by the interaction of the light with sharp edges exposed by the process of slip.

Experimental

The experimental setup and procedure used in measuring intensity dependent absorption and damage in metals are described elsewhere [6,7]. The basic technique was pulsed laser calorimetry. The laser was a Q-switched neodymium yttrium aluminum garnet (Nd:YAG) laser with a second harmonic generator (SHG) so both, 1.06 and 0.532μm were available. This laser operated in a single axial mode at 10 Hz with a pulse duration of 22 nsec at 1.06μm and 18 nsec at 0.532μm (FWHM). The temperature versus time history of the irradiate sample was monitored by laser thermocouple calorimetry and the absorption calculated from the slopes of the heatin and cooling curves. Upon damage the behavior of the heating curve would change dramatically while at the same time one could observe a flash or spark. Due to the increased absorption of Cu and Ag and Au at 0.532μm detection of damage with laser calorimetry presented serious technical problems [7]. Therefore a photomultiplier with appropriate filtering was used which detected the increased scattering accompanying damage.

The morphology of the sample's surface was examined with Nomarski microscopy while the surface roughness profiles were measured with a Talystep profilimeter Model 75-1011 112/1037 M [9]. The samples used were oxygen free high conductivity (OFHC) diamond turned bulk Cu and Ag electroplated diamond turned Cu obtained from the NWC in China Lake, OFHC diamond turned bulk Cu from INTOP Corporation, OFHC bulk Cu mechanically polished by Northrop Corporation and Au electroplated diamond turned Cu from Cohan-Epner Co.

A site on the sample's surface was selected for minimal scattering when illuminated with a HeNe laser beam. It was then irradiated with many pulses of constant energy and the absorptance calculated from the heating and cooling curves. Then a new site was selected, irradiated with a number of pulses of higher power and again the absorption calculated. If catastrophic damage occurred, this intensity provided an upper limit for the experiment. The intensity dependent absorption was measured using 1.06 μm (1.16 ev) irradiation on Cu and Ag samples. Interband transitions in Cu start at ~2.2 eV, so two photon absorption would be a reasonable expectation. In Ag interband transitions do not start until ~3.9 eV so the probability for a multiphoton event is sharply reduced compared to Cu and any indication of intensity dependent absorption would be suggestive of thermal mechanisms. Additional experiments investigating surface deterioration were performed on Au electroplated diamond turned Cu at 0.532 and 1.06 μm.

Figure 1 shows typical plots of absorptance vs. intensity for diamond turned Cu at 1.06 μm. The absorptance increases with increasing intensity, as indicated by the stars, and this increase is completely reversible, that is it decreases with decreasing intensity to the original value as shown by the circles. All the Cu samples examined displayed the same behavior. Figure 1a shows the results for OFHC diamond turned Cu from NWC, figure 1b shows the results for mechanically polished Cu from Northrop Corp., while Fig. 1c presents data for OFHC diamond turned Cu from INTOP. In all the figures the arrows indicate catastrophic damage intensities beyond which the change in absorption is irreversible. There is no dependence of the effect on beam size although as discussed

in previous work [6,7], the damage intensity increases with increasing beam size.

Figure 2 shows a typical plot of the absorptance vs. intensity for Ag at 1.06 μm. The absorptance increases with increasing intensity - stars - and is reversible as indicated by the circles. The arrow indicates catastrophic damage and, as in Cu, after it occurs, the change in the absorptance is irreversible.

Discussion

The temperature dependence of the absorption of a metal is an effect reasonably well established [2-5]. In order to decide whether the heating of the metal surface by the laser pulse was responsible for the observed increase of the absorption, the average temperature excursion at the end of the pulse was calculated [6]. A one dimensional heat transfer model was used based on the following assumptions:

1. The beam dimensions are much larger than the thermal diffusion length $w >> 2[\kappa t_p]^{\frac{1}{2}}$, where w is the beam radius at $1/e^2$ in intensity, κ is the thermal diffusivity and t_p is the pulse length.
2. The thermal properties of the metal and the absorption are independent of temperature. This assumption allows a first order calculation of the irradiation induced temperature changes.
3. The pulse waveform is rectangular (an assumption which causes an over estimate of 10% in ΔT_{av} [8]) and of duration t_p. Under these assumptions the average temperature excursion occurring at the end of the pulse is

$$\Delta T_{av} = \frac{2\ AF}{\pi \kappa t_p^{\frac{1}{2}} \rho C}$$

Table 1

Summary of the intensity dependent absorption measurements on Cu and Ag.

Sample	λ (μm)	Spot-radius (μm, $1/e^2$)	A_{calc} ($x10^{-4}$)	A_{exp} ($x10^{-4}$)
Cu DT 44 (NWC)	1.06	204	86	55
Cu DT 46 (NWC)	1.06	115	85	76
Cu MP 6 (Northrop)	1.06	120	79	72
Cu DT 7 (INTOP)	1.06	320	79	61
Ag DT 13 (NWC)	1.06	170	20	18
Ag DT 13 (NWC)	1.06	290	64	76

where

κ = thermal diffusivity

ρ = density

C = specific heat

A = absorptance

F = fluence in Joules/cm^2

t_p = pulse length

This change in temperature can be used to calculate a first order approximation to the change in the absorptance ΔA since,

$$\Delta A = \frac{dA}{dT} \Delta T \ .$$

The value of dA/dT in Cu calculated from first principles [10] is

$$dA/dT|_{Cu} = 1.56 \times 10^{-5} \ ^\circ C^{-1}$$

while in Ag

$$dA/dT|_{Ag} = 1.6 \times 1.0^{-5} \ ^\circ C^{-1}$$

Experimental evidence obtained by Quimby et.al. [11] gives

$$dA/dT|_{Cu} = (1.5 \pm 0.5) \times 10^{-5} \ ^\circ C^{-1}$$

for the same Cu samples used in this project.

Table I summarizes the intensity dependent absorption measurements on Cu and Ag samples. $A_{calc.}$ is the calculated absorptance based on the model discussed above, while $A_{exp.}$ is the highest value of the absorptance before damage occurs. A comparison between $A_{exp.}$ and $A_{calc.}$ shows close agreement between the theoretical and the experimental results for most of the samples. In all cases, the calculated values are higher than the experimental values. If the increase of the absorption with intesnity is due to mechanisms other than

that due to the temperature change, one would expect an experimental value higher than that calculated.

Surface Morphology

The experiments performed were all multiple pulse experiments, i.e., the chosen site on the sample surface was irradiated for a certain number of pulses until an adequate calorimetric curve for the calculation of absorptance was obtained. Then a new site was selected, irradiated with a different intensity and again an absorptance was calculated. It was observed though that the increase of the absorptance with intensity was not a function of whether the experiment involved several trials on a single site or multiple sites as explained previously.

In multiple site experiments, prior to catastrophic damage (i.e., before the observation of a flash or spark) the irradiated sites become roughened and the degree of roughness increased with increasing number of pulses [6,7]. A catastrophically damaged site has a distinctly different appearance, with a crater dominating the center of the damaged area. As described in the previous section, the increase of the absorptance with intensity is a reversible process despite the physical alterations at the surface of the site studied. The increase in roughness does not introduce any permanent additional absorptance as long as catastrophic damage does not occur.

Figure 3 shows the surface profile of a diamond turned Cu sample (NWC) irradiated with 1.06 μm light. In part a) the surface profile of the roughened area is shown, while part b)

shows the surface profile of the unirradiated area. The increase of surface roughness in the irradiated area is rather small and the changes in absorptance introduced by it are not detectable by laser calorimetry.

In Fig. 4 the surface profile of Au electroplated diamond turned Cu and irradiated with 0.532 μm is presented. Part a) shows the surface profile of a catastrophically damaged area - i.e., the crater - while parts b) and c) show the profiles of the roughened and unirradiated areas respectively. Obviously the roughness change in the crater is significant while the roughness difference between the roughened and unirradiated areas is rather small.

There has been a lot of speculation on the role of roughness in metal mirror damage. In a recent paper [7] we presented a model where multiple pulse damage is due to the cumulative effect of plastic deformation. From the surface profile measurements, it is indicated that in the case of roughened areas, the frequency rather than the amplitude of the roughness has increased. This increased frequency of microirregularities is likely to enhance the local optical electric field strength and precipitate damage in the manner discussed by Bloembergen [12].

Conclusion

Intensity dependent studies on Cu and Ag metal mirrors at 1.06 μm indicate that the intensity dependence of the absorption can be explained in terms of irradiation induced temperature changes. The surface roughness of the irradiated sites does

not affect the absorption measurement but it introduces irregularities sufficient to lower the damage threshold. These irregularities may enhance the local optical electric field strength and thereby reduce the damage resistance of the site.

The authors would like to thank Dr. J. M. Bennett, Michelson Laboratory, Naval Weapons Center for making the surface roughness measurements and Dr. L. M. Merkle for helpful discussions. In addition, they would like to thank Dr. D. M. Decker (NWC), Intop Corp., and Northrop Corp. for providing the samples. This work was sponsored by ONR-SRO Research Grant No. N0014-70-C-0896.

Fig. 1 a) Plot of absorptance vs. intensity for diamond turned OFHC Cu #44 (NWC) at 1.06μm.

b) Plot of absorptance vs. intensity for mechanically polished OFHC Cu #6 (Northrop)

c) Plot of absorptance vs. intensity for diamond turned OFHC Cu #7 (INTOP). The arrows indicate multiple pulsed induced catastrophic damage. The stars (*) indicate absorptance data obtained with increasing intensities, while the circles (0) correspond to absorptance data obtained by reducing the intensity, indicating the reversibility of the process.

Fig. 2 Plot of absorptance vs intensity for Ag electroplated diamond turned OFHC Cu #13 (NWC) at 1.06μm. The arrow indicates multiple pulse induced catastrophic damage. The stars (*) indicate absorptance data obtained with increasing intensities while the circles (0) correspond to absorptance data obtained by reducing the intensity indicating the reversibility of the process.

Fig. 3 Surface profile of diamond turned OFHC, Cu #22 (NWC). Part a) shows the surface profile of the roughened area irradiated with 1.06μm light, while part b) shows the surface profile of the unirradiated area.

Fig. 4 Surface profile of Au electroplated diamond turned Cu. Part a) shows the surface profile of a catastrophically damaged area - i.e. the crater - and part b) shows the surface profile of the roughened area both irradiated with 0.532μm light. Part c) shows the surface profile of the unirradiated area.

REFERENCES

[1]. Y.R. Shen, "Recent Advances in non-linear optics", Rev. of Modern Phys., vol. 48, pp. 1-32, Jan, 1976; and refs. therein.

[2]. S. Roberts, "Optical properties of copper", Phys. Rev., vol. 118, pp. 1509-1518, June 1960.

[3]. P.B. Johnson and R.W. Christy, "Optical constants of copper and nickel as a function of temperature", Phys. Rev. B. vol. 11, pp. 1315-1323, Feb. 1975.

[4]. J.A. Mackay and J.A. Rayne, "Temperature dependence of the infrared absorptivity of the noble metals", Phys. Rev. B., vol. 13, pp. 673-684, Jan. 1976.

[5]. D.L. Decker, V.A. Hodgkin, "Wavelength and Temperature Dependence of the Absolute Reflectance of Metals at Visible and Infrared wavelengths", Nat. Bur. Stand. Spec. Publ., vol. 620, pp. 190-193, 1980.

[6]. N. Koumvakalis, C.S. Lee, and M. Bass, "Intensity Dependent Absorption and Laser Induced Catastrophic Damage in Diamond Turned and Mechanically Polished Cu Mirrors at 1.06μm.", Proceedings of the 13th Symposium on Laser Induced Damage in Optical Materials, Boulder, Colorado, Nov. 1981 and to be published by the National Bureau of Standards.

[7]. C.S. Lee, N. Koumvakalis and M. Bass, "Spot-size dependence of laser-induced damage to diamond turned Cu mirrors", Appl. Phys. Lett., vol. 41, pp. 625-627.

[8]. M. Sparks and E. Loh, Jr., "Temperature dependence of absorptance in laser damage of metallic mirrors: I. Melting", J. Opt. Soc. Am., Vol. 69, pp. 847-858, June 1974.

[9]. J.M. Bennet and J.H.Daney, "Stylus profiling instrument for measuring statistical properties of smooth optical surfaces", Applied Optics, vol. 20, pp. 1785-1802, May 1981.

[10]. Handbook of Chemistry and Physics, 59th ed., (CRC Press 1978).

[11]. R.S. Quimby, M. Bass and L. Liou, "Calorimetric measurement of temperature dependent absorption in copper", Proceedings of the 13th Symposium on Laser Induced Damage in Optical Materials, Boulder, Colorado, Nov. 1981 and to be published by the National Bureau of Standards.

[12]. N. Bloembergen, "Role of Cracks, Pores and Absorbing Inclusions on Laser Induced Damage Threshold at Surfaces of Transparent Dielectrics", Appl. Opt., vol. 12, pp. 661-664, Apr. 1973.

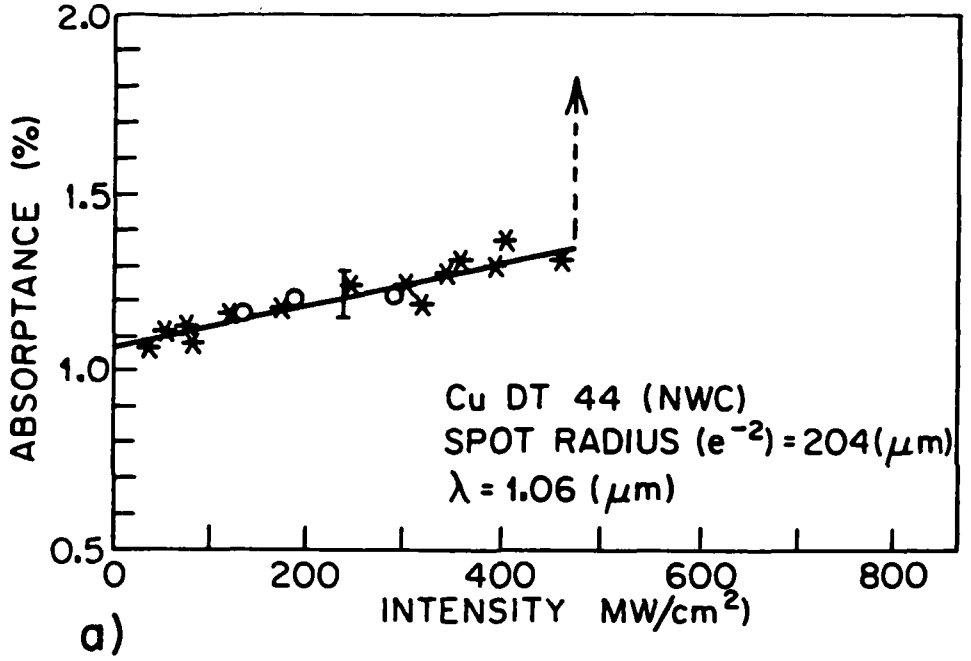
2.0
1.5
1.0
0.5
ABSORPTANCE (%)
Cu DT 44 (NWC)
SPOT RADIUS (e^{-2}) = 204(μm)
λ = 1.06 (μm)
0
200
400
600
800
INTENSITY MW/cm^2)

a)

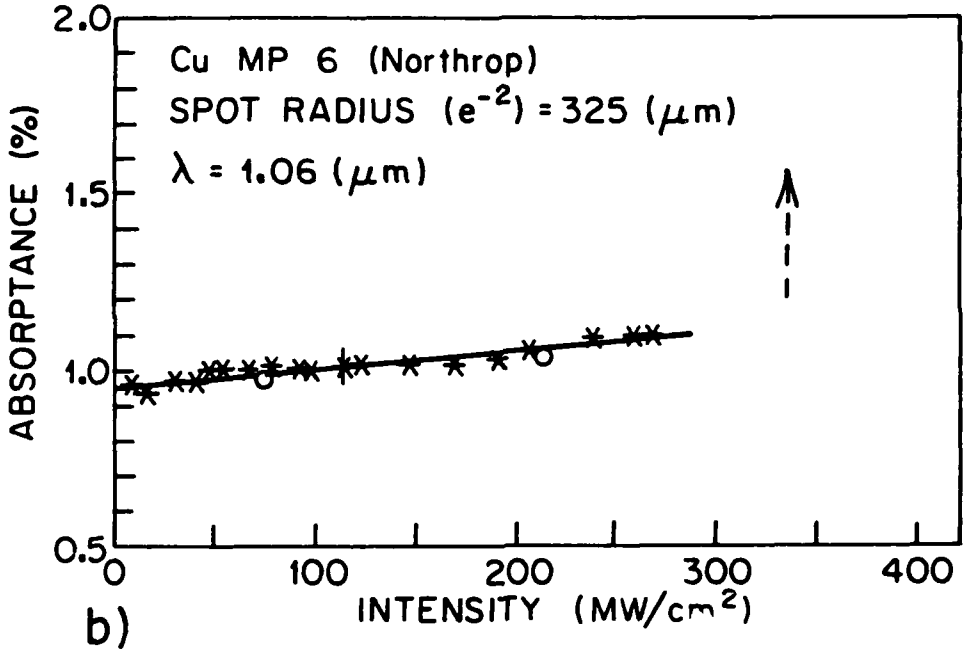
2.0
1.5
1.0
0.5
ABSORPTANCE (%)
Cu MP 6 (Northrop)
SPOT RADIUS (e^{-2}) = 325 (μm)
λ = 1.06 (μm)
0
100
200
300
400
INTENSITY (MW/cm^2)

b)

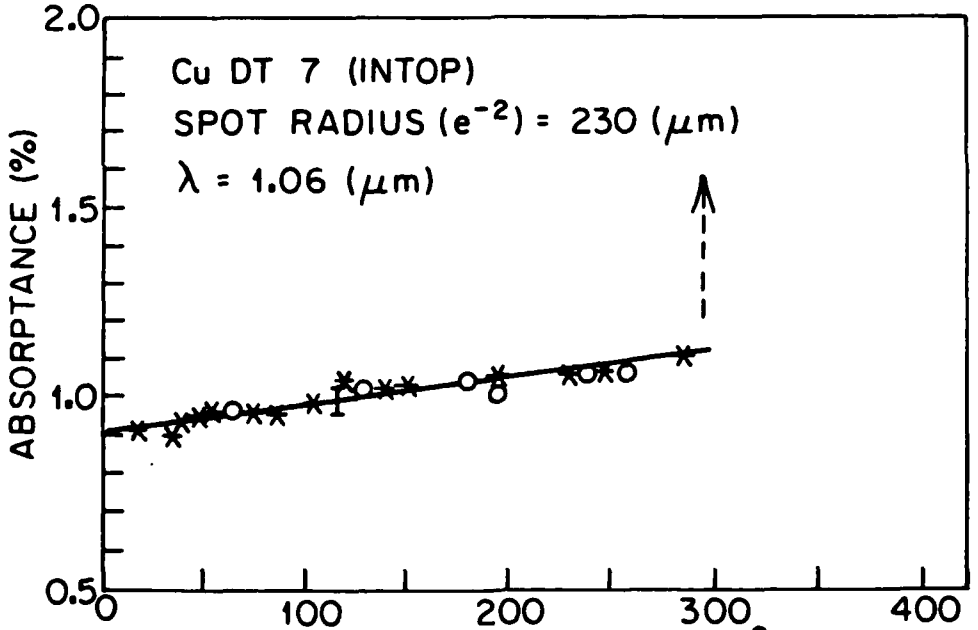
2.0
1.5
1.0
0.5
ABSORPTANCE (%)
Cu DT 7 (INTOP)
SPOT RADIUS (e^{-2}) = 230 (μm)
λ = 1.06 (μm)
0
100
200
300
400

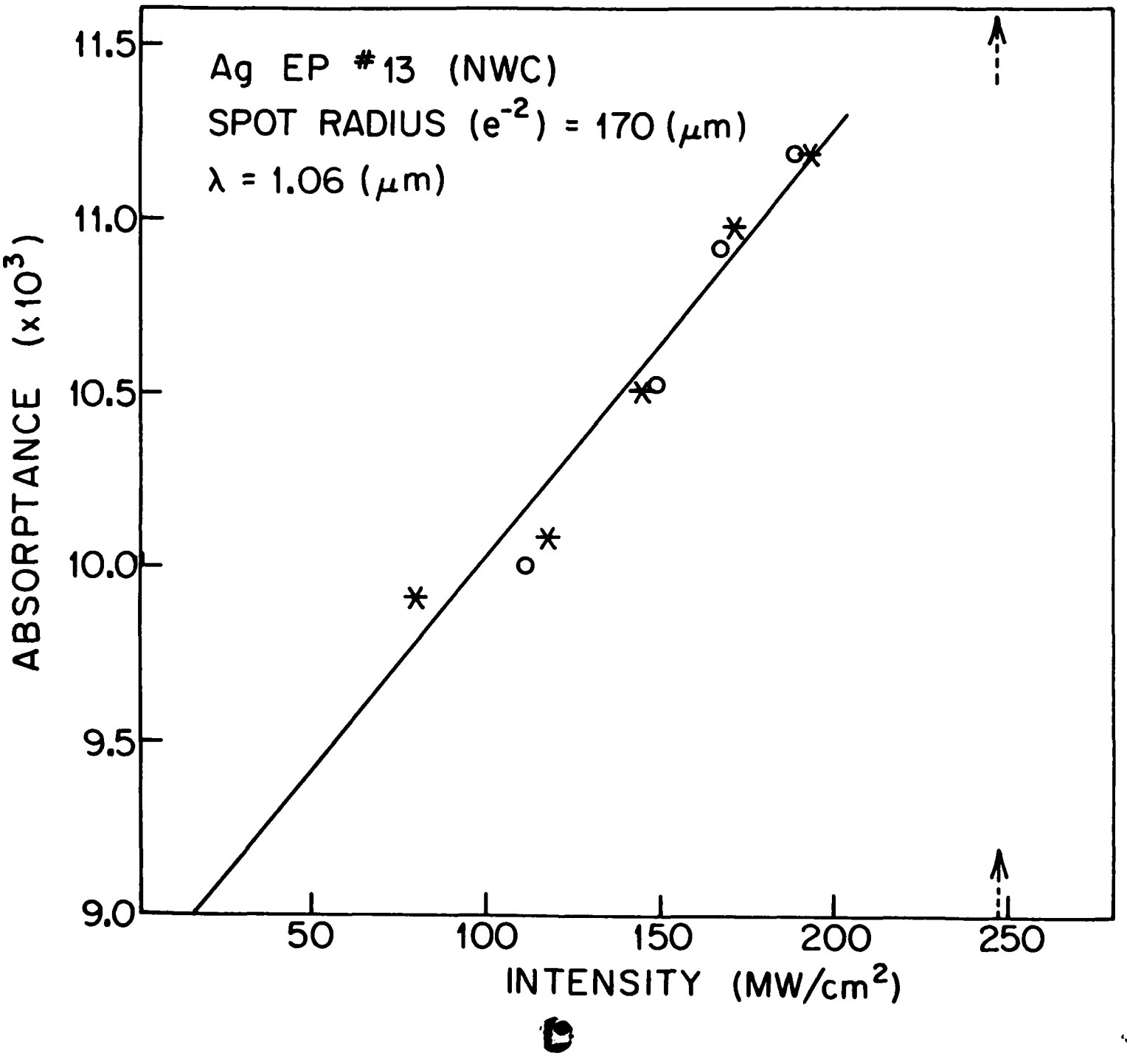
Ag EP #13 (NWC)
SPOT RADIUS (e^{-2}) = 170 (μm)
λ = 1.06 (μm)
ABSORPTANCE ($\times 10^3$)
11.5
11.0
10.5
10.0
9.5
9.0
50
100
150
200
250
INTENSITY (MW/cm^2)

NWC DIAMOND TURNED COPPER, CRATER #22

SURFACE SCANS

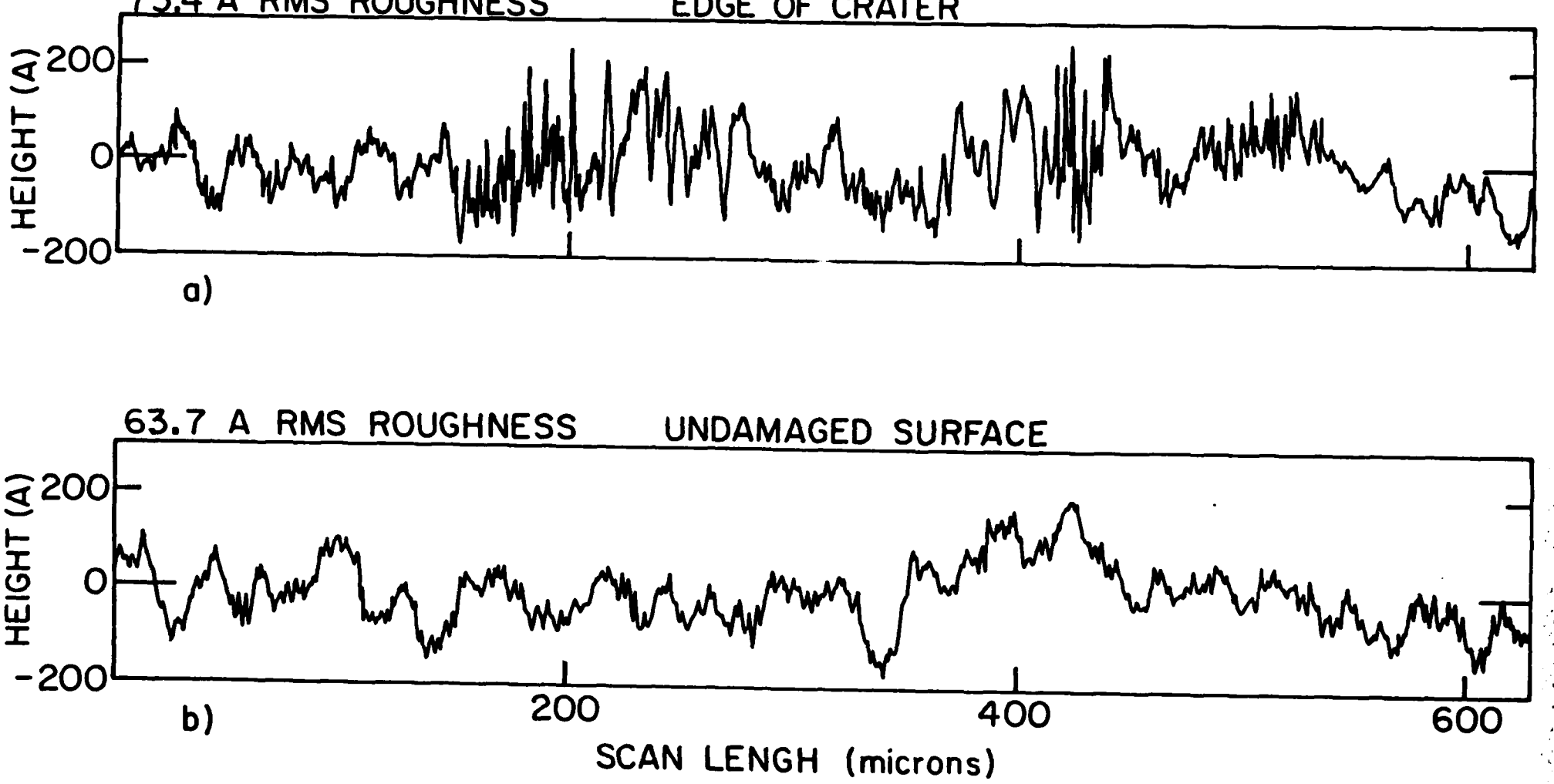

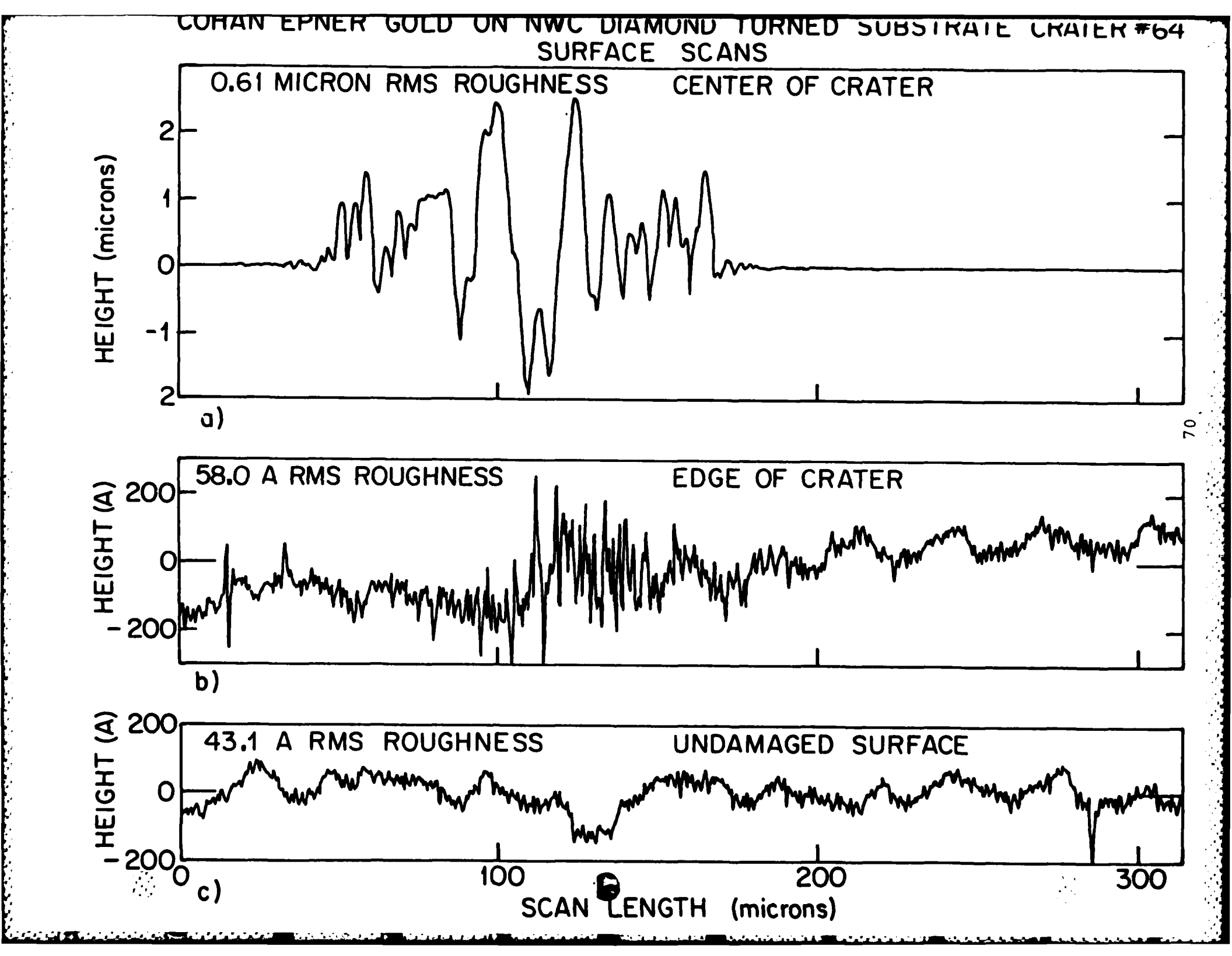
COHAN EPNER GOLD ON NWC DIAMOND TURNED SUBSTRATE CRATER #64
SURFACE SCANS
0.61 MICRON RMS ROUGHNESS
CENTER OF CRATER
HEIGHT (microns)
2
1
0
-1
2
a)
58.0 A RMS ROUGHNESS
EDGE OF CRATER
HEIGHT (A)
200
0
-200
b)
43.1 A RMS ROUGHNESS
UNDAMAGED SURFACE
HEIGHT (A)
200
0
-200
0
100
200
300
c)
SCAN LENGTH (microns)
70

Chapter 5

Calorimetric Studies of Light Absorption by Diamond Turned Ag and Cu Surfaces and Analyses Including Surface Roughness Contributions

M. Bass and L. Liou

Center for Laser Studies
University of Southern California
University Park, DRB-17
Los Angeles, CA 90089-1112

Calorimetric Studies of Light Absorption by Diamond Turned Ag and Cu Surfaces and Analyses Including Surface Roughness Contributions

M. Bass and L. Liou
Center for Laser Studies
University of Southern California
Los Angeles, California 90089-1112

Abstract.

The total absorption of diamond turned Ag and Cu was measured directly by laser calorimetry. These measurements were carried out at wavelengths from 0.468 to 10.6 μm. The data were analyzed with a model which includes the contribution to the absorption due to surface roughness. As a result an effective electron relaxation time was found as a function of frequency. This in turn was used to find the effective conductivity as a function of frequency.

Introduction

The absorption of electromagnetic waves by metals has been studied for many years.[1] Reflectance measurements have been used to determine the absorption but these are sensitive to errors due to scattering from less than ideally smooth surfaces.[2,3,4] In this paper laser calorimetry[5] was used to directly measure the absorption of diamond turned Ag and Cu at several wavelengths. The results are in good agreement with data reported for the reflectance of very smooth deposited Ag and Cu films.[4]

The measured absorption was fit at each frequency to a model which includes Drude, anomalous skin effect and surface roughness contributions.[1] The single fitting parameter is a frequency dependent effective relaxation time for the free electrons. This quantity was then used to determine the effective conductivity as a function of frequency. In the infrared, the effective conductivity reaches a constant value which is less than the dc conductivity. This indicates that the Fermi surface of the material composing the surface of diamond turned metals, is assymetric.[6]

Review of Optical Absorption Mechanisms in Metals

The Drude model for the interaction of free electrons in a metal with electromagnetic waves provides an accurate account of absorption and reflection for low frequency fields.[7] The dielectric constant for a metal as given by the Drude model is

$$\varepsilon(\omega) = 1 - \frac{\omega_p^2}{\omega(\omega + i\,1/\tau)} \tag{1}$$

where ω is the electromagnetic field radian frequency and τ is a phenomenological damping parameter determined by electron collisions with impurities, crystal imperfections and the lattice itself. For pure metals the latter type of collision dominates and τ is the mean time between electron-phonon collisions. The parameter ω_p is the plasma frequency and is given by

$$\omega_p^2 = \frac{4\pi Ne^2}{m^*} \tag{2}$$

Here N is the electron density per unit volume and m* is the effective mass of the electron in the metal. Some of the properties of Ag and Cu relevant to their optical properties are listed in Table I.

If we write

$$\varepsilon(\omega) = \varepsilon_1(\omega) + i\varepsilon_2(\omega) \tag{3}$$

then

$$\varepsilon_1(\omega) = 1 - \frac{(\omega_p\tau)^2}{1 + (\omega\tau)^2} \tag{4}$$

and

Table I

Properties of Ag and Cu Relevant to Optical Absorption*

	Ag	Cu
DC conductivity σ_o (T = 22°C)	$6.22 \times 10^7 \frac{\text{mho}}{\text{m}}$	$5.89 \times 10^7 \frac{\text{mho}}{\text{m}}$
Free electron concentration N	5.86×10^{28} m^{-3}	8.47×10^{28} m^{-3}
Relative effective mass M^*/m_o	1.00	1.45
Plasma frequency ω_p	1.37×10^{16} rad/sec	1.37×10^{16} rad/sec
Fermi velocity v_F	1.57×10^6 m/sec	1.39×10^6 m/sec

*American Institute of Physics Handbook, D.E.Gray, ed., (McGraw-Hill, New York, 1972)

$$\varepsilon_2(\omega) = \frac{(\omega_p\tau)^2}{1+(\omega\tau)^2} \quad \frac{1}{\omega\tau} \tag{5}$$

The complex index of refraction of the metal is

$$\tilde{n} = \sqrt{\varepsilon} = n + i\,k \tag{6}$$

and so the reflectivity for normal incidence is

$$R = \frac{(n-1)^2 + k^2}{(n+1)^2 + k^2} \tag{7}$$

In the Drude model limit $(\omega_p\tau)^2 >> (\omega\tau)^2 >> 1$ and after some manipulation Eq. 7 yields

$$R_D = 1 - \frac{2}{\omega_p\tau} \tag{8}$$

Since whatever is not reflected by the metal must be absorbed, the Drude value for absorption, A_d, is

$$A_0 = 1 - R_D = \frac{2}{\omega_p\tau} \tag{9}$$

Eq. 9 makes it clear that in the limit of low electromagnetic field frequencies, that is in the infrared or at longer wavelengths, the absorption will be independent of frequency assuming τ is a constant. At high frequencies one can model the absorption by assuming that additional processes such as interband transitions give rise to added terms in $\varepsilon_1(\omega)$ and $\varepsilon_2(\omega)$[8] or that $\tau = \tau(\omega)$ at high frequencies. Both of these means of interpreting the data are discussed in this paper. However, in order to do so more correctly for a non-ideal surface

the role of roughness in determining optical absorption must be considered.

The anomalous skin effect may result in modifications to the Drude absorption which can contribute to the infrared absorption.[9-11] This effect is important when the electron mean free path, given by $v_F\tau$, where v_F is the Fermi velocity for the metal, is comparable to the classical skin depth. For room temperature Cu and Ag and wavelengths in the 1-10 μm range, the anomalous skin effect must be taken into account. The absorption due to this phenomenon is given by[9]

$$A_s = \frac{3}{4}\frac{v_F}{c}(1-f) + \frac{\omega_p^2}{2\omega^2}\frac{v_F^3}{c^3} f \qquad (10)$$

where f is the fraction of the electrons which are specularly reflected at the metal's surface. Since f depends upon the quality of the surface finish the contribution of A_s to the total absorption is related to surface roughness. For a very smooth surface $f \simeq 1$ while $f \simeq 0$ for a rough surface. Experimental observation indicate that even for the best surfaces attainable $f \simeq 0$.[11] In this case only the first term in Eq. 10 contributes and A_s is independent of the light freqency.

The total absorption of the metal, assuming the best possible surface finish, is the sum of A_D and A_S where A_D may be modified from the value in Eq. 9 to account for interband transitions at high frequencies. To this quantity it is necessary to add the absorption due to the roughness of the surface. The effect of roughness may be viewed as providing 1) additional surface area 2) parts of the sur-

faces to which the incident beam in not normally incident and 3) possibly providing geometric features in which the light can be trapped and more strongly absorbed. Recently Sari et. al.[12] treated these considerations by using a classical solution to Maxwell's equations at an interface in which the surface roughness was included as a perturbation to the boundary conditions. They assumed the surface to be perfectly smooth in one direction and rough in the other. Assuming that the scale of the roughness is less than the wavelength of the incident light, they give the additional absorption for normally incident linearily polarized light caused by p wave scattering from the roughness is

$$\Delta A_{uc} = 2\varepsilon_2 k_0 |\sqrt{\varepsilon} - 1| \sum_{\vec{k}} \left[|\zeta(\vec{k})|^2 \frac{|\gamma|^2 + K^2}{I_m(\gamma)} \frac{|\alpha|^2}{|\varepsilon\alpha + \gamma|^2} \right] \quad (11)$$

Here k_0 is the wave number of the incident light, $\vec{k}$ is a two dimensional surface wave vector in the surface, and $\zeta(\vec{k})$ is the Fourier transform of the measured surface roughness, $\zeta(R)$, so that

$$\zeta(\vec{k}) = \frac{1}{L^2} \int dR \, e^{-i\vec{K}\cdot\vec{R}} \zeta(R) \quad (12)$$

where L^2 is the surface area normalization parameter. The quantities γ and α are given by

$$\gamma^2 = \varepsilon k_0^2 - K^2 \quad (13)$$

and

$$\alpha^2 = k_0^2 - K^2 \quad . \quad (14)$$

The subscript SP on ΔA_{SP}^{P} is used to indicate that the surface roughness gives rise to the coupling of electromagnetic waves with surface plasmons and it is this interaction which leads to the surface roughness related additional absorption.

The total absorption of a metallic surface which is not ideally smooth is then given by

$$A = A_D + A_S + \Delta A_{SP} \quad . \tag{15}$$

The first term includes the intrinsic properties of the metal at the light frequency (i.e.: $\varepsilon(\omega)$ or $\tau(\omega)$) and the second two terms arise due to the departure of the surface finish from ideality. The contribution due to A_S is frequency independent due to the fact that for most surfaces $p \simeq 0$. The contribution due to ΔA_{SP} depends on frequency through the dependence of ε or τ or ω. If one properly includes the latter two terms in evaluating measurements of optical obsorption then one may obtain estimates of either $\varepsilon(\omega)$ or $\tau(\omega)$. From the latter one may also obtain $\sigma(\omega)$. These estimates are useful in judging the processes responsible for absorption in metals at various frequencies.

Experimental

Laser calorimetry was used to measure the absorption of diamond turned Cu and Ag samples. The samples were oxygen free high conductivity (OFHC) polycrystalline Cu blocks 9.5 x 15.9 x 3.2 mm in dimension. Ag was electroplated onto these blocks and both the bare Cu and plated Ag samples were finished by diamond turning. Diamond turning is a precision machining process which has been employed to form a variety of metal optics surfaces for use in high power laser systems.[13] In this work the silver samples were prepared at the Naval Weapons Center (NWC) and the copper samples at NWC and INTOP Co. The surfaces are shown in micrographs and profilimeter traces in Figs. 1, 2 and 3. Roughness measured by scanning the profilimeter parallel to the DT grooves is called roughness parallel to the grooves and conversely for roughness perpendicular to the grooves.

The experimental configuration employed for the laser calorimetric measurements of absorption is shown schematically in Fig. 4. CW CO_2, b axis Nd:YAP and Kr ion lasers were used to provided normally incident illumination between 10.6 and 0.468 μm. The samples were supported by nylon monofilament threads in a vacuum chamber in order to minimize thermal losses. A differential thermocouple with one junction attached to the sample and the other to a non-irradiated reference thermal mass was used to record the temperature vs. time history of the sample following the start of laser irradiation. Such data is shown in Fig. 5 and along with the incident laser power, the sample's mass and specific heat gives directly the fraction of the incident light absorbed.[5] Table II is a list of the results of these measurements for Cu and Ag. The

Table II

TOTAL ABSORPTION OF DIAMOND TURNED Ag AND Cu
MEASURED BY LASER CALORIMETRY

		PERCENT OF INCIDENT POWER ABSORBED		
rms roughness (Å)		Ag	Cu	Cu
Parallel to grooves		100 ± 20	75 ± 20	115 ± 20
Perpendicular to grooves		100 ± 20	105 ± 20	120 ± 20
λ (μm)	$\omega (10^{15} \frac{rad}{sec})$			
μm	$10^{15} \frac{rad}{sec}$			
10.6	0.178	0.75 ± 0.04	0.74 ± 0.05	0.88 ± 0.03
1.0795	1.746	0.81 ± 0.04	0.81 ± 0.06	1.04 ± 0.04
0.647	2.913	1.42 ± 0.12	3.04 ± 0.42	3.16 ± 0.13
0.568	3.319	1.95 ± 0.24	-----	-----
0.531	3.550	2.44 ± 0.27	-----	-----
0.468	4.028	3.15 ± 0.49	-----	-----

fractional errors indicated are the experimental errors and are smaller at 10.6 and 1.08 μm because more laser power was available to measure these smaller absorptions.

By using laser calorimetry direct measurements of absorption were obtained in the present work. This is in contrast to the more traditional means of estimating absorption as one minus the sum of the measured fraction of the light reflected and scattered. The calorimetrically measured absorptances are not sensitive to errors caused by scattering from a rough surface as are reflectance measurements. Thus it is useful to compare the direct measurements of absolute absorptance for the diamond turned samples with previously published data derived from reflectance measurements for diamond turned and other, so called, near ideal metallic surfaces. In Fig. 6, the results for Ag obtained in the present work are compared to the absolute reflectance data reported by Decker and Hodgkin for diamond turned, sputtered, and UHV evaporated Ag.[4] It is clear that the calorimetrically measured total absorptance data is in excellent agreement with the absolute reflectance data for the best sputtered and UHV deposited samples. This is in contrast to the reflectance data of Decker and Hodgkin for diamond turned Ag. The difference is attributed by Decker and Hodgkin to "a surface roughness effect". In fact this difference may represent the sensitivity of reflectance measurements to surface roughness related scattering. The calorimetric measurements of absorptance are not sensitive to scattering and so give an absorptance value which is nearly equal to one minus the reflectance of the supposed ideally smooth samples at most wavelengths.

Data Analysis

The total absorption given by Eq. 15 was measured in the experiments just described. In order to evaluate these results the first two terms on the right in Eq. 15 will be considered as one term,

$$A_D'(\omega) = 2/\omega_p \tau_{eff}(\omega) \quad . \tag{16}$$

where $\tau_{eff}(\omega)$ is the effective damping time at the particular light frequency in question. In this manner it is possible to account for the changing relative contribution of the anomalous skin effect term and for the contribution to the absorptance due to non-Drude processes (ie: interband transitions) at higher frequencies. Eq. 16 is valid only for $(\omega_p \tau_{eff})^2 >> (\omega\tau_{eff})^2 >> 1$. Using $\tau_{eff}(\omega)$ the real and imaginary parts of the dielectric constant are given from Eqs. 4 and 5 as

$$\varepsilon_1 = 1 - \frac{(\omega_p \tau_{eff}(\omega))^2}{1+(\omega\tau_{eff}(\omega))^2} \tag{17}$$

and

$$\varepsilon_2 = \frac{1}{\omega\tau_{eff}} \quad \frac{(\omega_p \tau_{eff}(\omega))^2}{1+(\omega_p\tau_{eff}(\omega))^2} \quad . \tag{18}$$

Following the definition of τ_{eff} as the effective damping time it is also possible to write the conductivity as a function of frequency,

$$\sigma(\omega) = \frac{Ne^2}{m^*} \tau_{eff}(\omega) \quad . \tag{19}$$

In order to evaluate the third term in Eq. 15 the measured surface roughness (see Figs 1 and 2) in each direction was digitized and a Fourier Transform was performed on an H-P 9825 computer to find $\zeta(\vec{k})$. Since the lasers were polarized parallel to the DT grooves the added absorption due to the roughness found in a profilimeter trace perpendicular to the grooves is the result of s wave scattering. An expression for this case is easily derived from Sari et. al's Eqs. 2.7 and 2.8.[12] We obtain

$$\Delta A_{uc} = 2\, k_o^5\, \varepsilon_2 |\sqrt{\varepsilon} - 1|^2 \sum_{\vec{k}} \frac{|\zeta(\vec{k})|^2}{(I_m(\gamma))\,(|\gamma+\alpha|^2)} \tag{20}$$

for the additional absorption due to s wave scattering from surface roughness for a linearly polarized normally incident beam of light.

The sum of Eqs. 16, 11 and 20 was equated to the measured total absorption and the value of $\tau_{eff}(\omega)$ was adjusted until the best agreement was reached at each frequency. Tables III and IV give the results of these calculations for Ag and Cu respectively. The error in τ_{eff} indicated in these tables derives from the experimental error in the measured absorption and surface roughness. Fig. 6 shows the functional form for $\tau_{eff}(\omega)$ -vs-ω and $\sigma_{eff}(\omega)$ -vs-ω for Ag.

Table III

Properties of Ag Derived from Optical Absorption Data

RMS Roughness: parallel to DT grooves (100 ± 20) Å
perpendicular to DT grooves (100 ± 20) Å

Wavelength (μm)	10.6	1.080	0.647	10.6	0.531	0.468
Frequency (10^{15} rad/sec	0.178	1.746	2.913	3.319	3.550	4.028
Property						
τ_{eff} (10^{-14} sec)	2.90 ± 0.29	2.42 ± 0.24	1.35 ± 0.20	0.98 ± 0.16	0.79 + 0.12	0.6 ± 0.
σ_{eff} (10^{7} mho/m)	4.82 ± 0.48	4.02 ± 0.	2.25 ± 0.32	1.63 ± 0.24	1.31 ± 0.20	1.0 ± 0.20
ϵ_1	-5721	-60.5	-21.1	- 16.0	-14.0	-10.6
ϵ_2	1110	1.46	0.56	0.52	0.53	0.47
A'_D	0.50	0.60	1.09	1.49	1.86	2.38
ΔA^p_{sp}	0.14	0.14	0.27	0.38	0.47	0.63
ΔA^s_{sp}	0.10	0.08	0.04	0.04	0.03	0.03
A_{TOT}	0.74	0.82	1.40	1.91	2.36	3.04

Table IV

Properties of Cu Derived from Optical Absorption Data

	Cu RMS Roughness (Å) Parallel to DT grooves 75 ± 20 Perpendicular to DT grooves 105 ± 20			Cu RMS Roughness (Å) Parallel to DT grooves 115 ± 20 Perpendicular to DT grooves 120 + 20		
Wavelength (μm)	10.6	1.080	0.647	10.6	1.0795	0.647
Frequency (10^{15} rad/sec	0.178	1.746	2.913	0.178	1.746	2.913
Property						
τ_{eff} (10^{-14} sec)	2.7 ± 0.40	2.2 ± 0.30	0.60 ± 0.40	2.7 ± 0.40	2.2 ± 0.30	0.60 ± 0.07
σ_{eff} (10^{7} mho/m)	4.49 ± 0.90	3.65 ± 0.70	1.00 ± 0.20	4.49 ± 0.90	3.65 ± 0.70	1.00 ± 0.20
ϵ_1	-5691	-60.5	-21.0	-5691	-60.5	-21.0
ϵ_2	1186	1.60	1.26	1186	1.60	1.26
A'_D	0.541	0.664	2.433	0.541	0.664	2.433
ΔA^p_{sp}	0.078	0.083	0.314	0.184	0.195	0.743
ΔA^s_{sp}	0.123	0.099	0.105	0.160	0.128	0.138
A_{TOT}	0.742	0.846	2.852	0.885	0.987	3.314

Discussion:

By comparing the calculated total absorption (Tables III and IV) for each sample with the measured value (Table II) it is clear that an effective relaxation time, τ_{eff}, can be defined at each frequency which accounts for the metal's absorption. In the infrared τ_{eff} is nearly independent of frequency as would be expected at frequencies where the Drude model were applicable. At higher frequencies, the contributions of bound electrons to the absorption process result in a decrease in the effective relaxation time. As a result, the shortest wavelength or highest frequency at which the Drude model is sufficient to describe the metal's absorption can be defined as that at which τ_{eff} begins to decrease significantly. For Ag this is ~1 μm as shown in Fig. 6.

A two carrier model has been proposed to explain the frequency dependence of optical absorption by metals.[4] One carrier, type a, sees a perfect lattice since it is within the crystallites and the other, type b, sees a distorted lattice since it is in the areas between the crystallites. Both are considered Drude like free carriers and the resulting dielectric function is shown to be

$$\varepsilon = 1 - \frac{((\omega_p)_a)^2}{\omega^2 + i\ \omega/\tau_a} - \frac{((\omega_p)_b)^2}{\omega^2 + i\ \omega/\tau_b} \qquad (17)$$

where the subscripts a and b refer to the two different carriers. Following the same procedure as outlined above to find Eq. 9 the expression in Eq. 17 leads to an effective relaxation time for the two carrier metal. In the limit where $N_b < N_a$ and $\tau_b < \tau_a$ the

two carrier effective relaxation time is found to vary with frequency as ω^2. The data in Fig. 6 shows that this is experimentally observed in Ag for frequencies corresponding to the visible but it does not apply in the infrared (i.e. for $\lambda \geq 1$ μm).

The effective conductivity of Ag and Cu as shown in Tables III and IV and Fig. 6 reach a nearly constant value at 10.6 μm. The ratio between the dc conductivity and this value may be attributed to the anisotropy of the Fermi surface of the material making up the samples' surfaces. For example, McKay et. al.[6] report a ratio of dc to infrared conductivity of 1.26 ± 0.10 for polycrystalline Ag and 1.3 ± 0.1 for single crystal Cu. The data in Table I and the results in Table III and IV give this ratio as 1.29 ± 0.16 for diamond turned Ag and 1.33 ± 0.26 for diamond turned Cu. The incertainties in these results are due to the surface roughness uncertainty and the experimental errors in the absorption data. Theory indicates that the Fermi surfaces of Ag and Cu should be isotropic and therefore that these ratios should be near unity.[6] In agreement with previous data[6] they are not and the implied anisotropy of the Fermi surface may be due to the presence of finishing induced stresses in the surfaces and the possible presence of surface contaminants.

Conclusions

Direct measurement of the total absorption of a metal by laser calorimetry gives very good agreement with the absorption inferred from reflectance measurement of nearly ideally smooth metallic surfaces. When one accounts for roughness induced absorption, this data can be used to calculated the effective relaxation time of free electrons in the metal when exposed to an electromagnetic field at a given frequency. This phenomenological time then gives the effective conductivity as a function of frequency. In the infrared the effective relaxation time is essentially constant as would be expected at frequencies where the Drude free electron model applies. Above a certain frequency this time decreases with increasing frequency as the contribution to the absorption from bound electrons grows. The dependency of the effective relaxation time on frequency for Ag is in agreement with the two carrier model at frequencies in the visible but not in the infrared. The effective conductivities of Ag and Cu reach constant values at 10.6 μm which are less than their respective dc conductivities. This result indicates that in the surface where optical absorption takes place the Fermi surface of these metals is assymmetric.

REFERENCES

1. There are many texts and review papers in this field. An excellent modern reference is F. Wooten, Optical Properties of Solids (Academic Press, New York, 1972).
2. H.E. Bennett and J.M. Bennett, Optical Properties and Electronic Structure of Metals and Alloys, F. Abeles, ed. (North Holland, Amsterdam, 1966), p. 175.
3. J.M. Bennett and E.J. Ashly, Appl. Opt. 4, 221 (1965).
4. D.L. Decker and V.A. Hodgkin, N.B.S. Special Publication No. 620 (1980).
5. A. Hordvik, Appl. Opt. 16, 2827 (1977).
6. J.A. McKay and J.A. Rayne, Phys. Rev. B 13, 673 (1976).
7. P. Drude, Theory of Optics (Longman, Green, New York, 1922; Dover, New York, 1968).
8. H.Ehrenreich and H.R. Philip, Phys. Rev. 128, 1622 (1962).
9. T. Holstein, Phys. Rev. 88, 1427 (1952); Phys. Rev. 96, 535 (1954).
10. A.B. Pippard, Proc. Roy. Soc. A191, 370 (1947).
11. H.E. Bennett, J.M. Bennett, E.J. Ashley and R.J. Motyka, Phy. Rev. 165, 755 (1968).
12. S.O. Sari, D.K. Cohen and K.D. Scherkoske, Phys. Rev. B 21, 2162 (1980).
13. D.L. Decker and D.J. Grandjean, N.B.S. Special Publication No. 541 (1978), p. 122.

FIGURE CAPTIONS

1. Surface of Ag electroplated on polycrystalline OFHC Cu and diamond turned at N.W.C.:
   (A) Nomarski photomicrograph,
   (B) Profilimeter trace parallel to the diamond turning grooves, and,
   (C) Profilimeter trace perpendicular to the diamond turning grooves.
2. Surface of polycrystalline OFHC Cu diamond turned at N.W.C.:
   (A) Nomarski photomicrograph,
   (B) Profilimeter trace parallel to the diamond turning grooves, and,
   (C) Profilimeter trace perpendicular to the diamond turning grooves.
3. Surface of polycrystalline OFHC Cu diamond turned at INTOP Co.:
   (A) Nomarski photomicrograph,
   (B) Profilimeter trace parallel to the diamond turning grooves, and,
   (C) Profilimeter trace perpendicular to the diamond turning grooves.
4. Schematic diagram of the laser calorimetry experiment.
5. The temperature-time history of an Ag sample irradiated at 10.6 μm.
6. Comparison of the reflectivity derived from the current data with the results of Ref. 4.
   ● current work
   — UHV evaporated (Ref. 4)
   □ Best sputtered (Ref. 4)
   △ Diamond turned (Ref. 4)

(A)
NOMARSKI
PHOTOMICROGRAPH

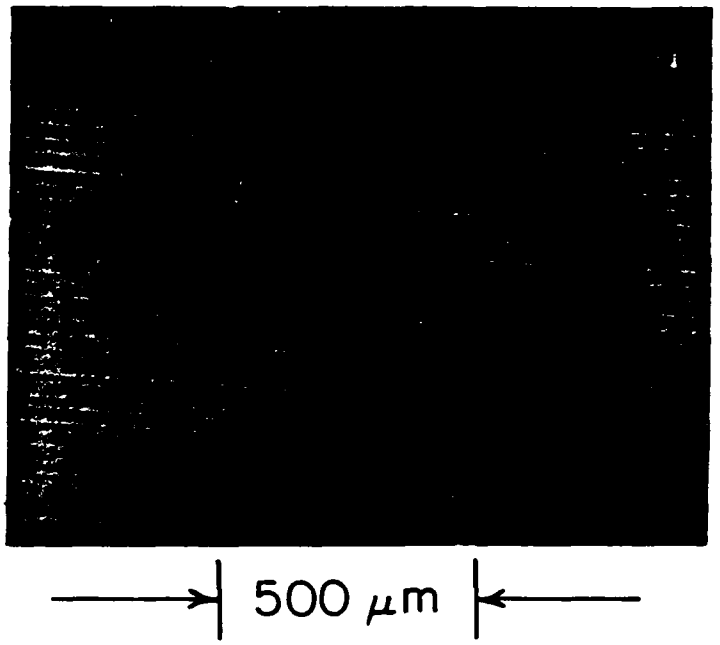

(B)
PROFILIMETER
TRACE
II TO D.T.
GROOVES

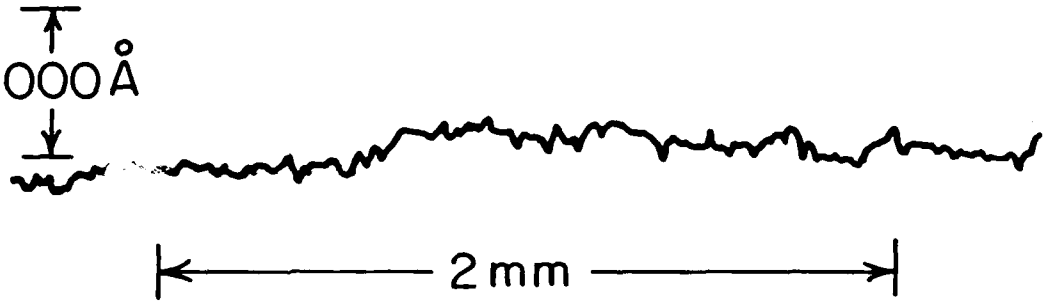

(C)
PROFILIMETER
TRACE
⊥ TO D.T.
GROOVES

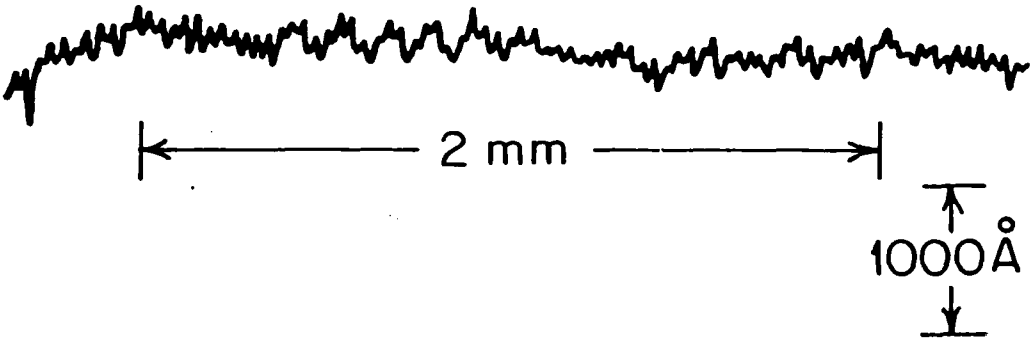

DIAMOND TURNED ELECTROPLATED Ag (N.W.C.)

(A)
NOMARSKI
PHOTOMICROGRAPH

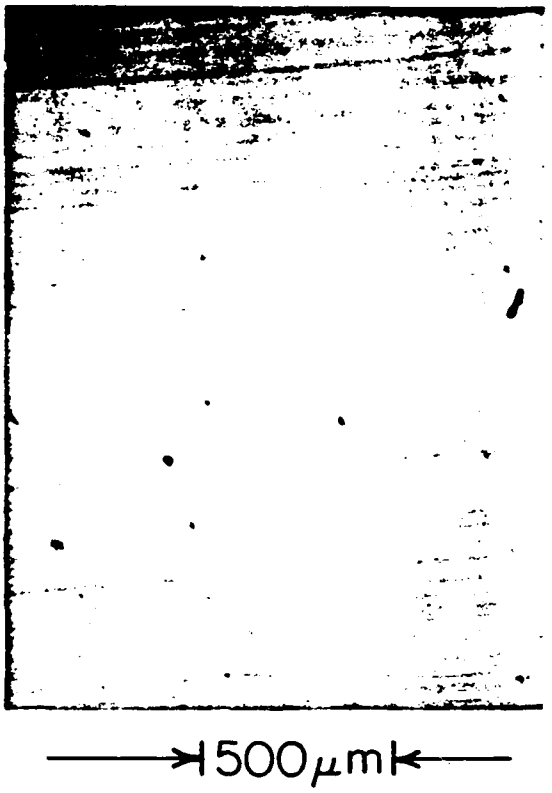

(B)
PROFILIMETER
TRACE
II TO D.T.
GROOVES

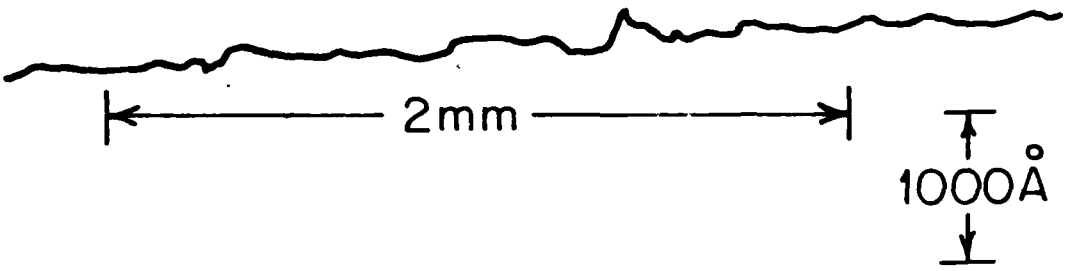

(C)
PROFILIMETER
TRACE
⊥ TO D.T.
GROOVES

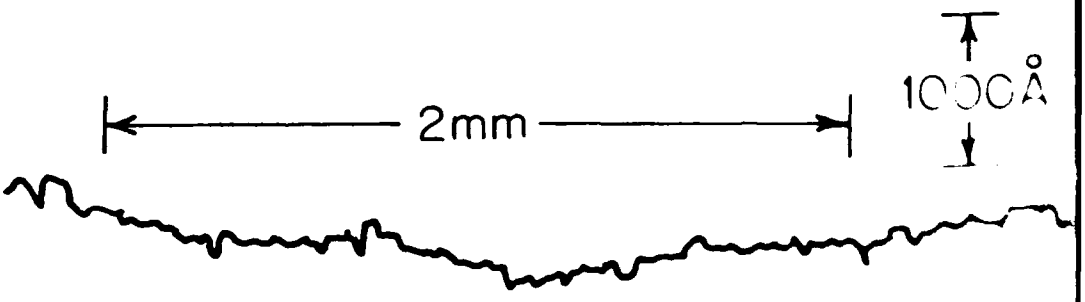

DIAMOND TURNED O.F.H.C. POLYCRYSTA[illegible]

AD-A134 285 OPTICAL PROPERTIES OF METALS(U) UNIVERSITY OF SOUTHERN 2/3
CALIFORNIA LOS ANGELES CENTER FOR LASER STUDIES
M BASS ET AL. 15 JUL 83 N00014-79-C-0896

UNCLASSIFIED F/G 11/6 NL

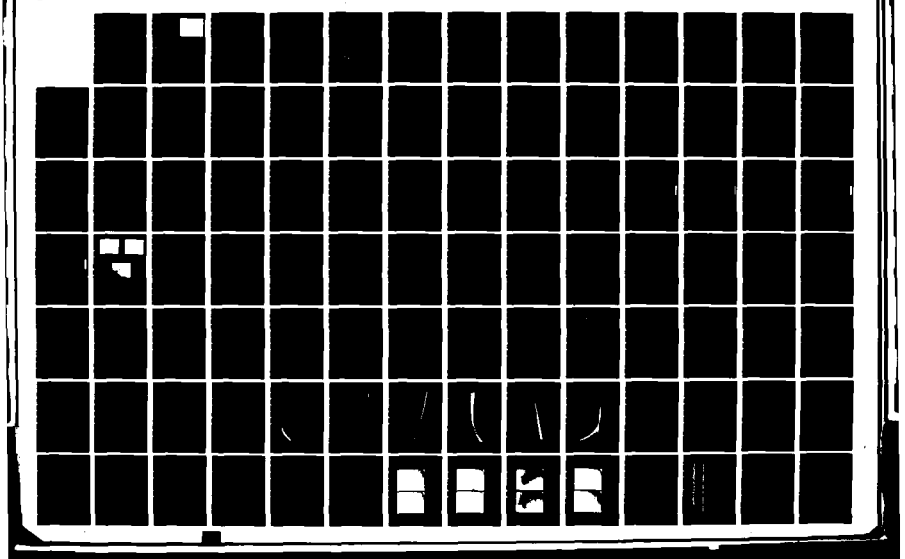

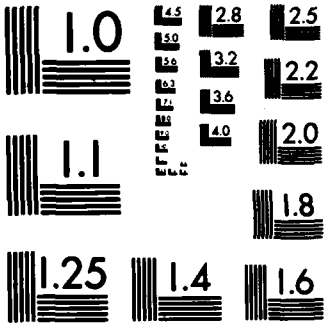

(A)
NOMARSKI
PHOTOMICROGRAPH

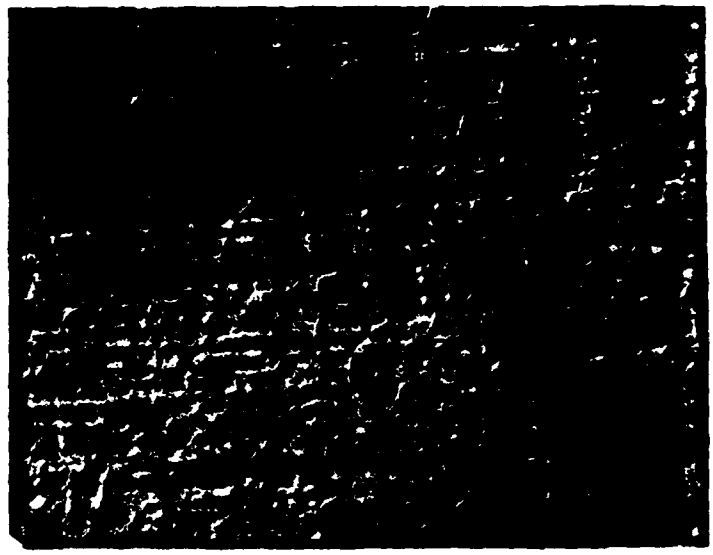

500 μm

(B)
PROFILIMETER
TRACE ∥ TO
D.T. GROOVES

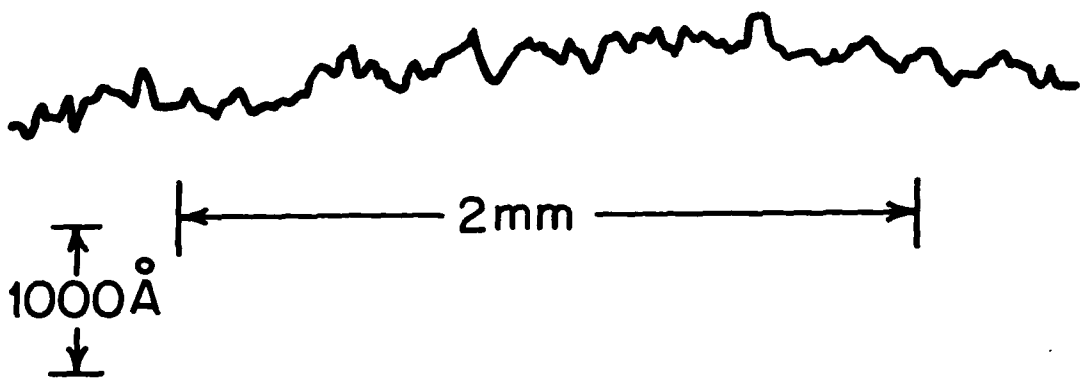

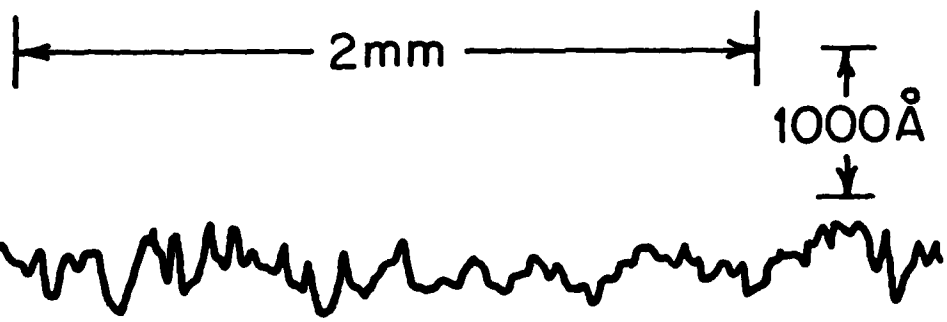

(C)
PROFILIMETER
TRACE ⊥ TO
D.T. GROOVES

DIAMOND TURNED O.F.H.C. POLYCRYSTALLINE Cu (INTOP)

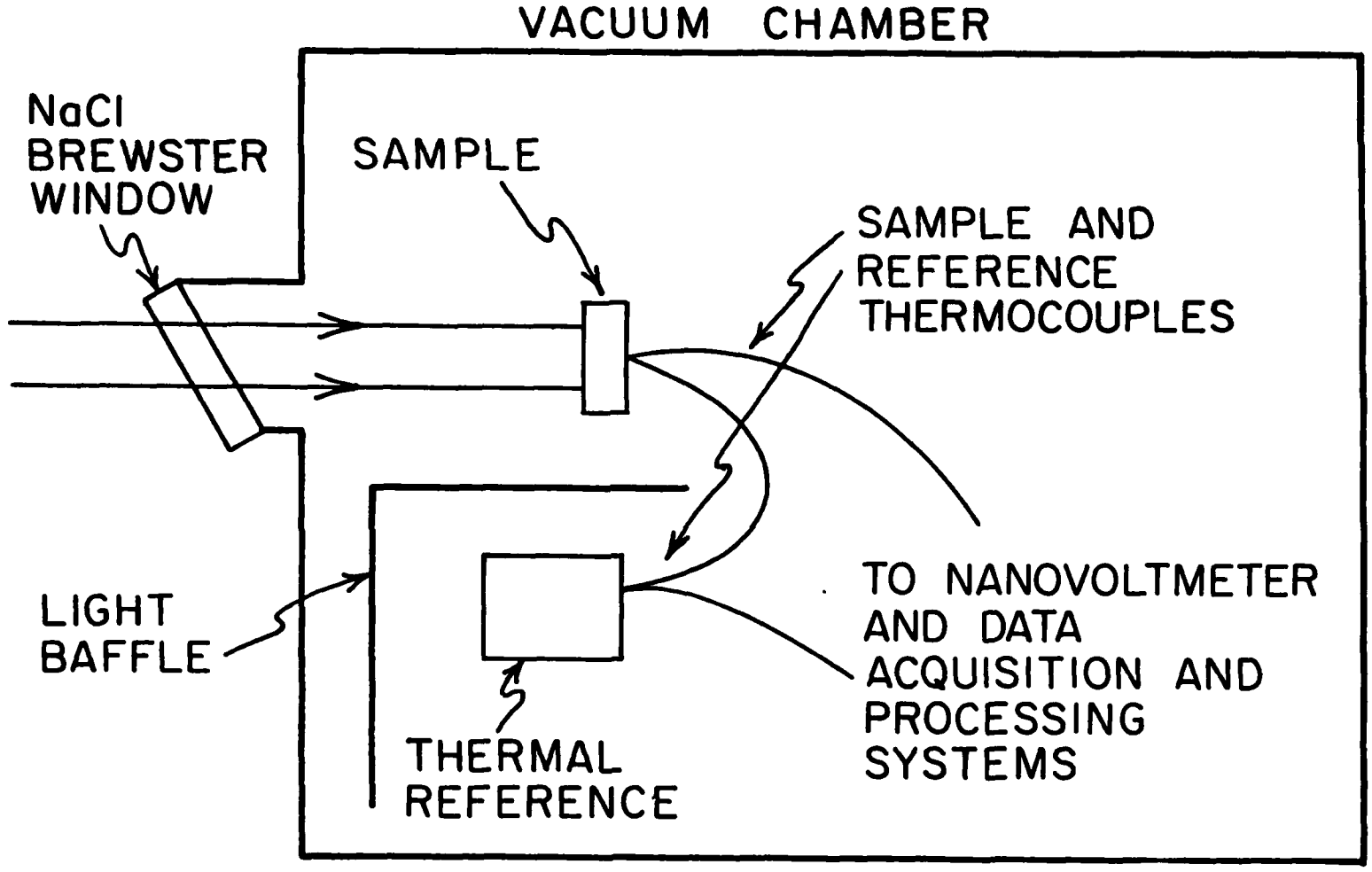
VACUUM CHAMBER
NaCl
BREWSTER
WINDOW
SAMPLE
SAMPLE AND
REFERENCE
THERMOCOUPLES
LIGHT
BAFFLE
THERMAL
REFERENCE
TO NANOVOLTMETER
AND DATA
ACQUISITION AND
PROCESSING
SYSTEMS

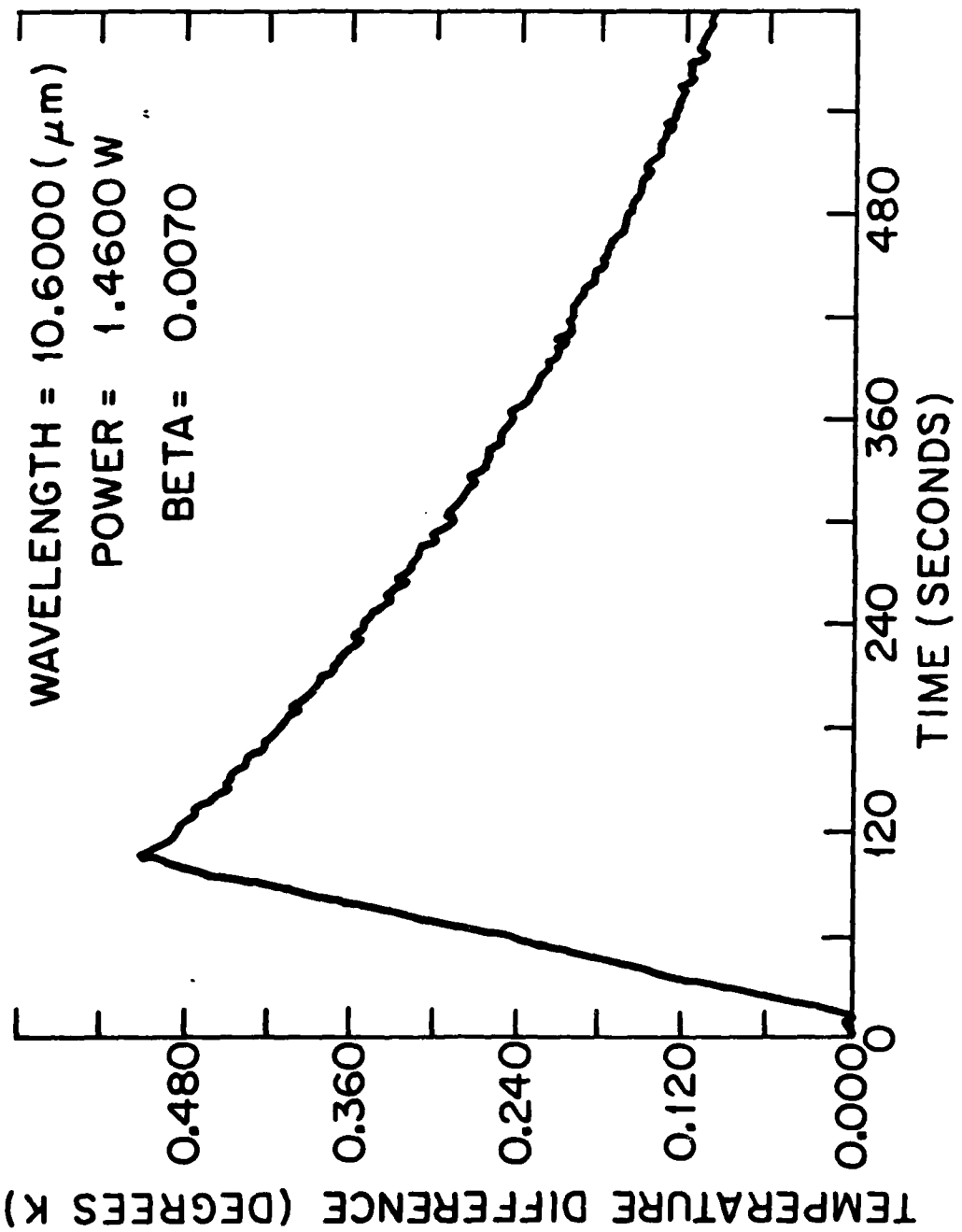
WAVELENGTH = 10.6000 (μm)
POWER = 1.4600 W
BETA = 0.0070
TEMPERATURE DIFFERENCE (DEGREES K)
0.000
0.120
0.240
0.360
0.480
0
120
240
360
480
TIME (SECONDS)

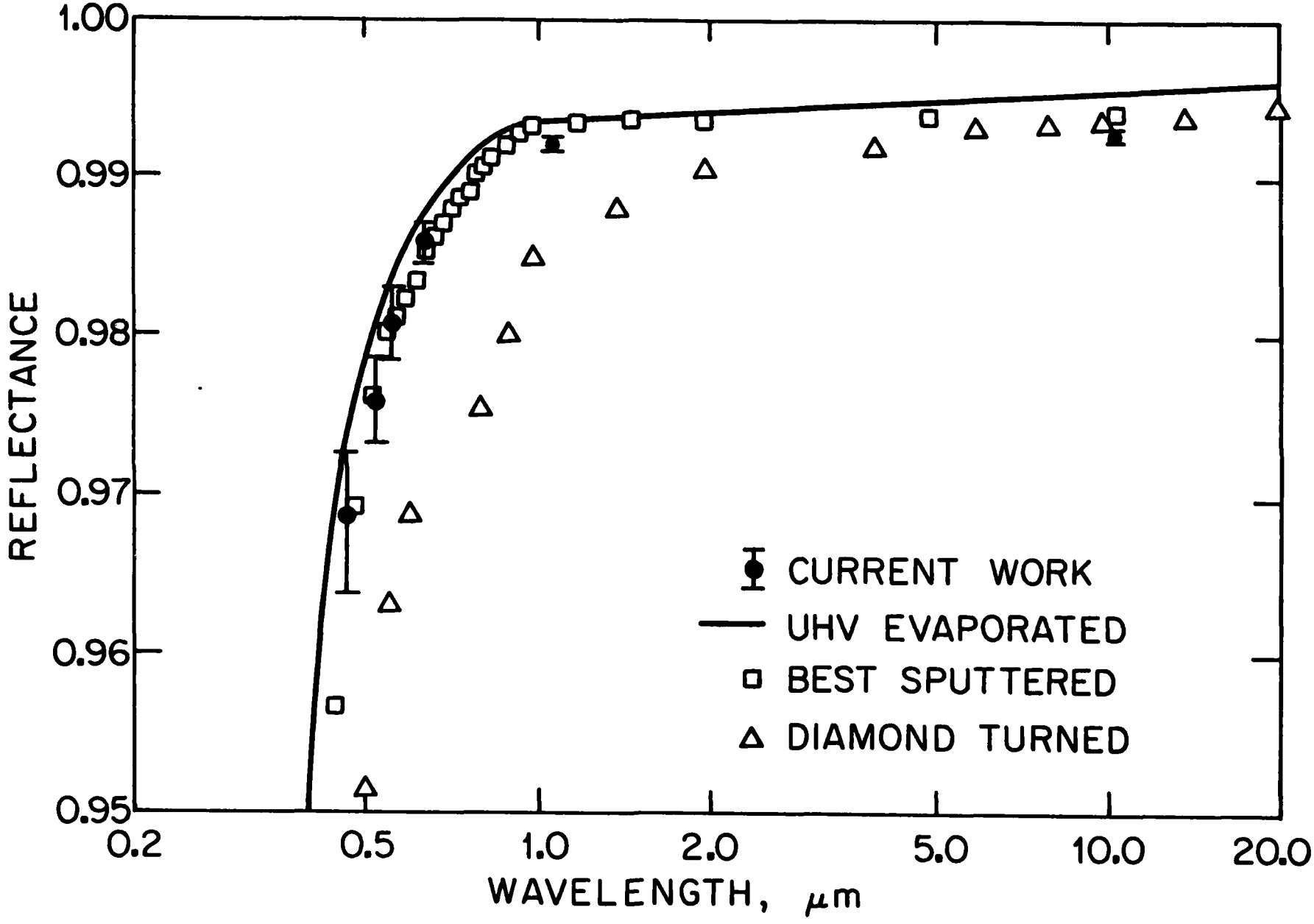
1.00
0.99
0.98
0.97
0.96
0.95
REFLECTANCE
0.2
0.5
1.0
2.0
5.0
10.0
20.0
WAVELENGTH, μm
CURRENT WORK
UHV EVAPORATED
BEST SPUTTERED
DIAMOND TURNED

Chapter 6

Contaminant and Defect Analysis of Optical Surfaces by Infrared Laser-Stimulated Desorption

S. D. Allen

Center for Laser Studies
University of Southern California
University Park, DRB-17
Los Angeles, CA 90089-1112

J. O. Porteus, W. N. Faith and J. B. Franck

Michelson Laboratory, Physics Division
Naval Weapons Center
China Lake, CA 93555

CONTAMINANT AND DEFECT ANALYSIS OF OPTICAL SURFACES BY INFRARED LASER-STIMULATED DESORPTION

S. D. Allen
Center for Laser Studies
University of Southern California, Los Angeles, CA 90089-1112

J. O. Porteus, W. N. Faith, J. B. Franck
Michelson Laboratory, Physics Division
Naval Weapons Center, China Lake, CA 93555

ABSTRACT

Infrared laser induced desorption (LID) has been demonstrated for water and other contaminants on nominally transparent substrates. The apparatus consists of a UHV chamber interfaced with several pulsed IR lasers. Detection of the desorbed fluence is via an ionizer and quadrupole mass analyzer. For the samples measured to date, the LID is defect dominated for both small (120 μm) and large (380 μm) spot sizes. For the larger spot sizes, the data for multiple irradiations of the same site (N/1) can be explained using a simple defect model. The LID fluence of water and other contaminants such as hydrocarbons can vary by orders of magnitude from site to site on the same sample. Similar variations were observed for average values of the desorption signal as a function of sample and substrate finish. The surface damage threshold of these materials correlates with the measured LID fluence of contaminants, i.e., samples and sites with high contaminant fluences damage at low thresholds. Samples investigated include: polished CaF_2 (two vendors), BaF_2, NaCl and etched CaF_2 and NaCl. A comparison of desorbed water and hydrocarbons at 2.8, 3.8

and 10.6 μm suggests that water may not provide the dominant mechanism for localized optical absorption and damage. Laser cleaned surfaces which were dosed with water at - -100°C showed no evidence of readsorbed water on subsequent LID testing, indicating a passivation of the surface.

Introduction

As materials for high power laser optics have improved, it has become increasingly true that failure occurs at surfaces and interfaces in the optical component where contamination is most probable. Last year at this conference we reported initial results from an experiment designed to quantitavely measure such contamination [1]. The experiment consists of an UHV chamber interfaced with a pulsed IR laser. The laser wavelength is chosen such that adsorbed molecules couple strongly to the laser field and absorb sufficient energy to cause desorption. The desorbed molecules are detected with a quadrupole mass analyzer. In most cases, the substrate is highly transparent to the laser wavelength. The advantage of this choice of experimental parameters is that large amounts of energy can be transferred to the adsorbed molecules at intensities significantly below the damage threshold of the substrate. Most other laser induced desorption (LID) experiments are conducted under conditions in which the substrate is highly absorbing [2].

The HF/DF and CO_2 TEA lasers with nominal wavelengths at 2.7, 3.8 and 10.6 μm respectively were used to irradiate samples of CaF_2, BaF_2, NaCl, KCl, Cu, Mo and several coatings. Most measurements were made with the HF laser as it is strongly absorbed by H_2O, a pervasive contaminant. Detected desorbed species include H_2O, OH and hydrocarbon fragments. Detection sensitivity for adsorbed H_2O scales with the laser spot size and is estimated at several percent

of a monolayer using the present experimental geometry. (HF laser, D_{1/e^2} = 380 μm). Initial desorption experiments were carried out on polished and etched samples which had been subjected to an 8 hour bakeout at 250°C, as the tenacity of surface water and hydroxide ions at elevated temperatures is well known [3]. Measurements of desorption fluence as a function of laser energy density showed considerable data scatter which increased for smaller spot sizes $D1/_{e^2}$ = 120 μm. As each data point was taken on a new site (1/1), there appeared to be a large site to site variation on approximately a 100 μm scale. This effect could be due to selective adsorption of contaminants at defect sites such as scratches, cracks, pits and pores.

LID Passivation

In order to overcome this experimental limitation, we used laser induced desorption to clean several "large" areas using multiple overlapping laser irradiations. These areas were then dosed with many Langmuirs of H_2O both at room temperature and -100°C in an attempt to obtain a uniform adsorbed layer. The sample was subsequently re-irradiated and no desorbed H_2O was detected. It was clear from the thermal desorption that occurred as the samples warmed, that water was deposited on the substrate at approximately -100°C, but none was detectable once the substrate had warmed up to slightly below room temperature. Unfortunately, we were unable with the current experimental apparatus to maintain the sample at reduced temperatures during the laser

induced desorption. We can conclude from these results for CaF_2 (100) and (111), BaF_2 (111) and NaCl(100), that laser induced desorption causes changes in the surface which inhibit H_2O adsorption at room temperature. Similar surface passivation effects have been observed for chemically etched KCl surfaces [4]. SEM examination of such single crystal etched surfaces shows an essentially featureless surface with an occasional low angle grain boundary. A reasonable explanation, therefore, is that adsorption of H_2O takes place predominantly at defect sites and that LID somehow removes these sites. These results have obvious applications to surface preparation of high power laser optics . Further experiments such as SEM and TEM examination of LID cleaned surfaces should be conducted to determine what changes take place in the laser irradiated surface.

Simple Defect Model

In order to quantitatively analyze the defect mediated adsorption, a simple model was developed. As shown in Figure 1, we assume that the defect density and contaminant adsorption on the surface is uniform and that there is a single threshold laser intensity necessary for desorption. The assumption of a threshold intensity is a good approximation for a process which is undoubtedly governed by an activation energy whether it is strictly thermal or has some component of bond selective excitation. In addition, comparison of the desorption energy for H_2O on CaF_2, for example, with the available laser energy shows that two

photons of 2.8 μm are necessary for each H_2O molecule desorbed. The LID is thus highly nonlinear in the laser intensity and can be reasonably approximated by an intensity threshold. Above the threshold, all adsorbed molecules are assumed to be desorbed. Using this model, the desorption fluence, ψ, is proportional to the irradiated area abo the threshold intensity. For a gaussian beam, this become.

$$\Psi = m\pi r_{TH}^2$$
$$\Phi_{TH} = \Phi_o e^{-r_{TH}^2/\rho^2}$$
$$\Psi = m\pi\rho^2[\ln\Phi_o - \ln\Phi_{TH}]$$

If the desorbed fluence is plotted as a function of the natural logarithm of the axial energy density, Φ_o, the slope of the resulting straight line yields information on the defect density and size. The zero desorption intercept is the threshold intensity for the LID process.

An example of LID data for H_2O on etched CaF_2 using the HF laser (D_{1/e^2} = 380 μm) in a 1/1 experiment is given in Figure 2. The large data scatter indicates that this model is not applicable on the scale of several mm (the spacing between irradiated sites is 1 mm). If we similarly plot the data for a N/1 experiment for the same system, but use the cumulative desorbed H_2O fluence, we obtain a much improved signal to noise ratio as shown in Figure 3. Similar graphs have been plotted for many sites on CaF_2, both (100) and (111), BaF_2 and NaCl as shown in Figures 4, 5, 6 and 7. Although there is evidence of the site to site data scatter

shown in Figure 2, the curves tend to group naturally into several types. As indicated by the site coordinates, given in mm, similar sites occur in areas separated by up to a centimeter. In some curves, e.g., Figure 4, two distinct straight lines are evident, implying an initial desorption from defects with a relatively low threshold intensity and subsequent appearance of a second type of defect with a higher threshold. Occasionally one site will show an unusually high LID signal. For example, sites 5,15 and 7,0 in Figure 5 and 6 respectively lie signficantly above the remaining data. In each case the anomalous curves are approximately parallel to but offset vertically from the other curves. A possible explanation is the occurrence of a particularly large, lower threshold desorption site within the initial irradiated area. If such defects are uncommon, e.g. foreign particles, they are not accounted for using the proposed model. A large signal will result on the first but not on subsequent shots if a large signal will result on the first but not on subsequent shots if a large desorption site falls within the initially irradiated area.

In the absence of measurements at intensities near the indicated threshold and other gaps in the data, we have not attempted to draw any quantitative conclusions from either the measured thresholds or the density factors. What is remarkable is that the measured curves are so simple, implying in most cases, one or more types of defect sites uniformly distributed over an area several hundred microns in diameter.

A comparison with the previously reported data [1] shows that the 1/1 LID signal measured on CaF_2 (100) was more uniform from site to site and that the signals were more than an order of magnitude larger. The initially measured CaF_2 samples were polished and supplied by a different vendor. Independent damage measurements [5] of the two types of samples showed consistently lower damage thresholds for the material reported in reference 1. Poor quality, low damage threshold, high LID fluence surfaces are reproducibly bad from site to site, whereas good quality, high damage threshold surfaces exhibit low average LID fluences but large site to site variations. These observations are consistent with the proposed defect model.

Wavelength Dependence of LID

As shown in the previous paper [1], the desorption efficiency of the DF laser for H_2O was less than the observed for the HF laser, but the disparity was not as large as would be expected on the basis of the absorption coefficients of H_2O at 2.7 and 3.8 μm. As shown in Table 1, H_2O absorbs strongly in the 2.7 μm region and virtually not at all at 3.8 μm [6]. This seeming contradiction is also seen in the few points in Figures 3, 5, 6 and 7 where N/1 data for the DF and CO_2 lasers does not differ significantly from the HF LID data. There are several explanations which should be explored. The simplest is that the particular HF laser wavelengths used in this experiment do not effectively couple to the adsorbed OH bonds. The dominant spectral components

in the HF laser are 2.795 μm (34%); 2.71, 2.835, and 2.635 μm (20% each). The spectrum of H_2O adsorbed on CaF_2 powders [3] shows a broad spectral feature centered at 2.12 μm and extendeding from approximately 2.7 to 3.3 μm attributed to hydrogen bonded H_2O and a sharp absorption line at 2.72 μm ascribed to strongly held free H_2O molecules. In no case was there any absorption observed near 3.8 μm. An alternative explanation is that several contaminant species are co-adsorbed. As shown in Table 1, C-H bonds absorb in the DF laser region and C-C bonds in the CO_2 laser region. As alcohol is frequently used as a polishing vehicle and in the etching process for the surface preparation of the tested materials, it is reasonable to assume that some fraction of the adsorbed and surface occluded material is alcohol.

Sequential desorption measurements of CH_3 and H_2O were made at both HF and DF wavelengths. It was observed that on no site was one contaminant observed in the absence of the other. The ratios of desorbed fluence for first irradiation/second irradiation for the two components are given in Table 2. At 3.8 μm, the ratio of desorbed fluence for H_2O or CH_3 remains approximately the same whether H_2O or CH_3 is measured first. In contrast, similar measurements at the HF wavelengths yield a large change in ratio with change in observation order. A comparison of N/1 LID of the various suspect contaminants at closely spaced sites could quantify these apparent differences.

There is some evidence of cumulative heating effects for N/1 LID measurements in CaF_2 at 10.6 μm where the substrate is a bulk absorber. Water continues to be desorbed on sequential shots even when the energy density and therefore the irradiated area above threshold is fixed. An estimated temperature rise of at least several hundred ^{o}C due to the bulk absorption would lower the effective LID threshold in the heated area. As the area heated by bulk absorption and the substrate temperature increases, the LID also increases even for the same effective laser spot size. What is surprising in these experiments is the relatively high damage threshold observed in spite of the high bulk absorption. We were unable to damage the etched CaF_2 (111) in N/1 experiments up to 150 J/cm^2 measured for etched (111) NaCl (Fig. 7). This result emphasizes the importance of surface defect absorption versus bulk absorption in determining the laser damage theshold.

Conclusions

We have shown that for the surfaces considered, i.e., CaF_2, BaF_2, and NaCl, LID cleaning provides passivation for subsequent H_2O adsorption. These materials are representative of the ionic crystals used for high power infrared optics. The LID signal initially observed is, therefore, probably associated with adsorption of H_2O and other contaminants at native defects in the surface such as scratches, cracks, grain boundaries, etch pits, pores, etc. A simple defect model can explain the laser pulse energy dependence

of the LID fluence if measurements are made at a single site (N/1). Site to site LID measurements can differ by orders or magnitude, but some areas on the order of mm^2 show similar behavior, suggesting the possibility of using LID for nondestructive mapping of contaminant concentrations. A series of experiments involving the measurement of LID as a function of wavelength and multiple species at a single site imply that contaminants other than H_2O may significantly influence laser damage of these surfaces.

Acknowledgments

The authors are pleased to acknowledge the support of the Office of Naval Research Special Research Opportunities Program and Navy Independent Research Funding.

References

[1] J. O. Porteus, W. N. Faith, and S. D. Allen, this conference, 1981;

S. D. Allen, J. O. Porteus and W. N. Faith, Appl. Phys. Lett. 41, 416 (1982).

[2a] Absorbing Substrates:

L. P. Levine, J. F. Ready and E. Bernal G., J. Appl. Phys. 38, 331 (1967).

H. F. Winters and E. J. Kay, Appl. Phys. 43, 789 (1972).

P. A. Temple, D. K. Burge, and J. M. Bennett, NBS Special Publ. 462, 195 (1976).

R. Gauthier and C. Guittard, Phys. Status Solidi A 38, 477 (1976).

[2b] Low Absorption Substrates:

J. Heidberg, H. Stein, E. Riehl, and A. Nestmann, Z. Phys. Chem. Neue. Folge. 121, 145 (1980).

T. J. Chuang, J. Chem. Phys. 76, 3828 (1982).

[3] P. B. Barraclough and P. G. Hall, Surf. Sci. 46, 393 (1974), J. Chem. Soc. Faraday Trans. 171, 2266 (1975).

[4] S. D. Allen, M. Braunstein, C. Giuliano and V. Wang, NBS Special Publication 414, 66 (1974).

[5] J. O. Porteus, unpublished results.

[6] J. D. Roberts and M. C. Caserio, "Basic Principles of Organic Chemistry", W. A. Benjamin, NY (1965).

TABLE 1

COMPARISON OF H_2O AND HYDROCARBON SEQUENTIAL LID ON CaF_2 (100)

$\lambda(\mu M)$	CH_3/H_2O	H_2O/CH_3
3.8	0.4	2.4
2.8	0.3	14

Table 1. Ratio of desorbed H_2O and CH_3 fluence for first irradiation/second irradiation on the same site at both HF and DF wavelengths.

TABLE 2

CHROMOPHORE	ABSORPTION BANDS	LASER	EXAMPLES
O-H	2.7 - 2.8	HF	WATER, ALCOHOLS
O-H (HYDROGEN BONDED)	2.9 - 3.1	HF	WATER, ALCOHOLS
C-H	3.0 - 3.7	DF	HYDROCARBON ALCOHOLS
C-O	7.7 - 11.0	CO_2	ALCOHOLS
C-C	8.0 - 12.0	CO_2	HYDROCARBONS

Table 2. Absorption bands of suspected contaminants on optically polished and/or etched surfaces.

FIGURE CAPTIONS

Fig. 1 Schematic diagram of the defect density model used. $I_2 = 2I_1$, ρ is the $1/e^2$ radius of the gaussian beam, and $I_{threshold}$ is the minimum intensity at which desorption takes place from the surface defects.

Fig. 2 LID fluence of mass 18 (H_2O) as a function of axial energy density for a 1/1 experiment on etched (100) CaF_2. D_{1/e^2} = 380 μm at HF.

Fig. 3 Cumulative LID fluence of mass 18 (H_2O) as a function of axial energy density for a N/1 experiment using the same system as Fig. 2. Each irradiated site is designed by its coordinates in mm.

Fig. 4 Cumulative LID fluence of mass 18 (H_2O) as a function of axial energy density for an N/1 experiment on (100) CaF_2. D_{1/e^2} = 380 m at HF and DF. Irradiated sites are designated by their coordinates in mm.

Fig. 5 Cumulative LID fluence of mass 18 (H_2O) as a function of axial energy density for an N/1 experiment on (111) BaF_2. D_{1/e^2} = 380 μm at HF and DF. Irradiated sites are designated by their coordinates in mm.

Fig. 6 Cumulative LID fluence of mass 18 (H_2O) as a function of axial energy density for an N/1 experiment on (111) BaF_2. D_{1/e^2} = 380 μm at HF and CO_2. Irradiated sites are designated by their coordinates in mm.

Fig. 7 Cumulative LID fluence of mass 18 (H_2O) as a function of axial energy density for an N/1 experiment on (100) NaCl. D_{1/e^2} = 380 μm at HF and CO_2. Irradiated sites are designated by their coordinates in mm. (Back surface damage at the CO_2 wavelength is indiated by the CO_2 notation on two graphs.)

Fig. 8 Cumulative LID fluence of mass 18 (H_2O) as a function of axial energy density for an N/1 experiment on an SiO film on CaF_2. D_{1/e^2} = 380 μm at HF. Irradiated sites are designated by their coordinates in mm.

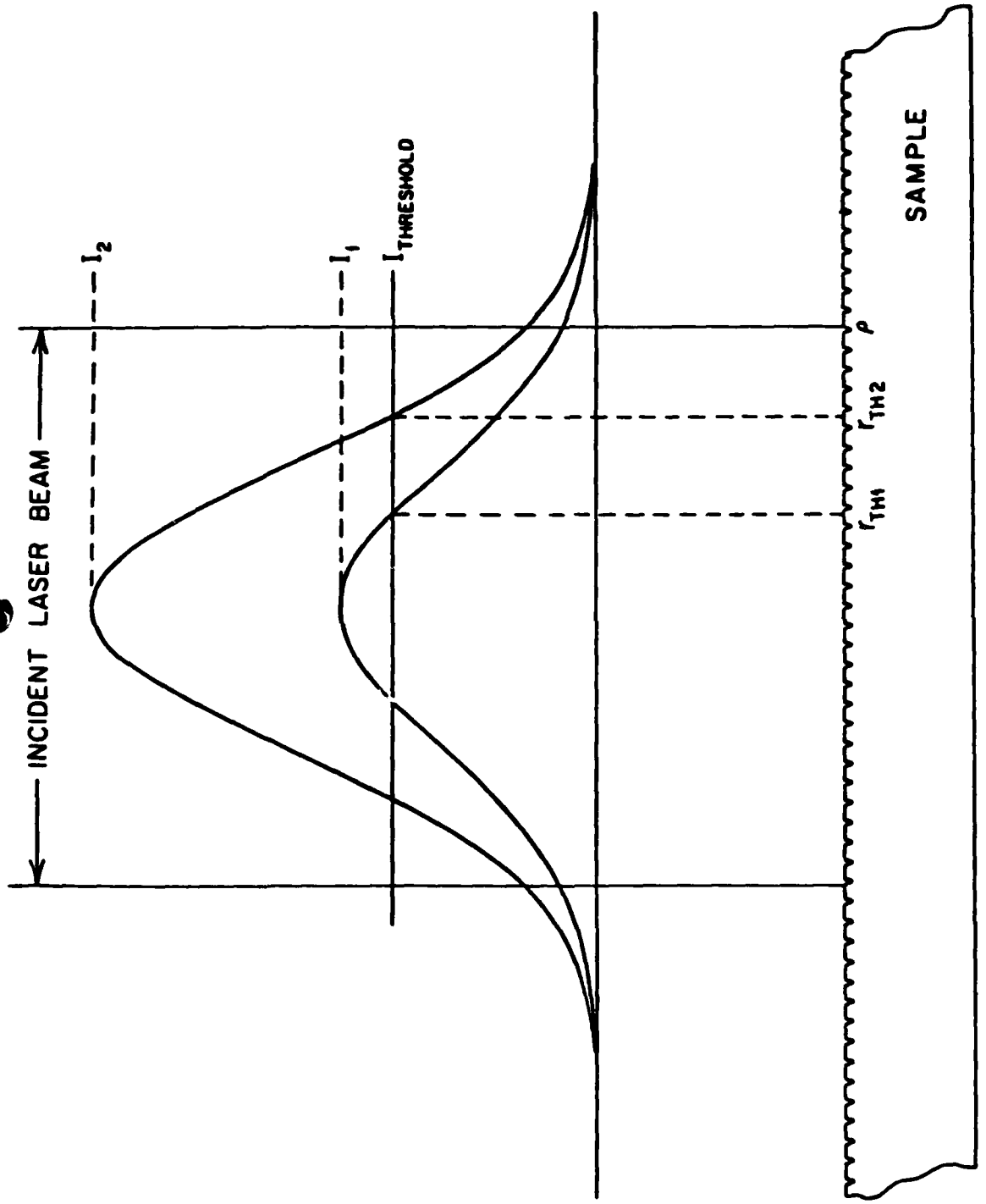

FIGURE 1

FIGURE 2

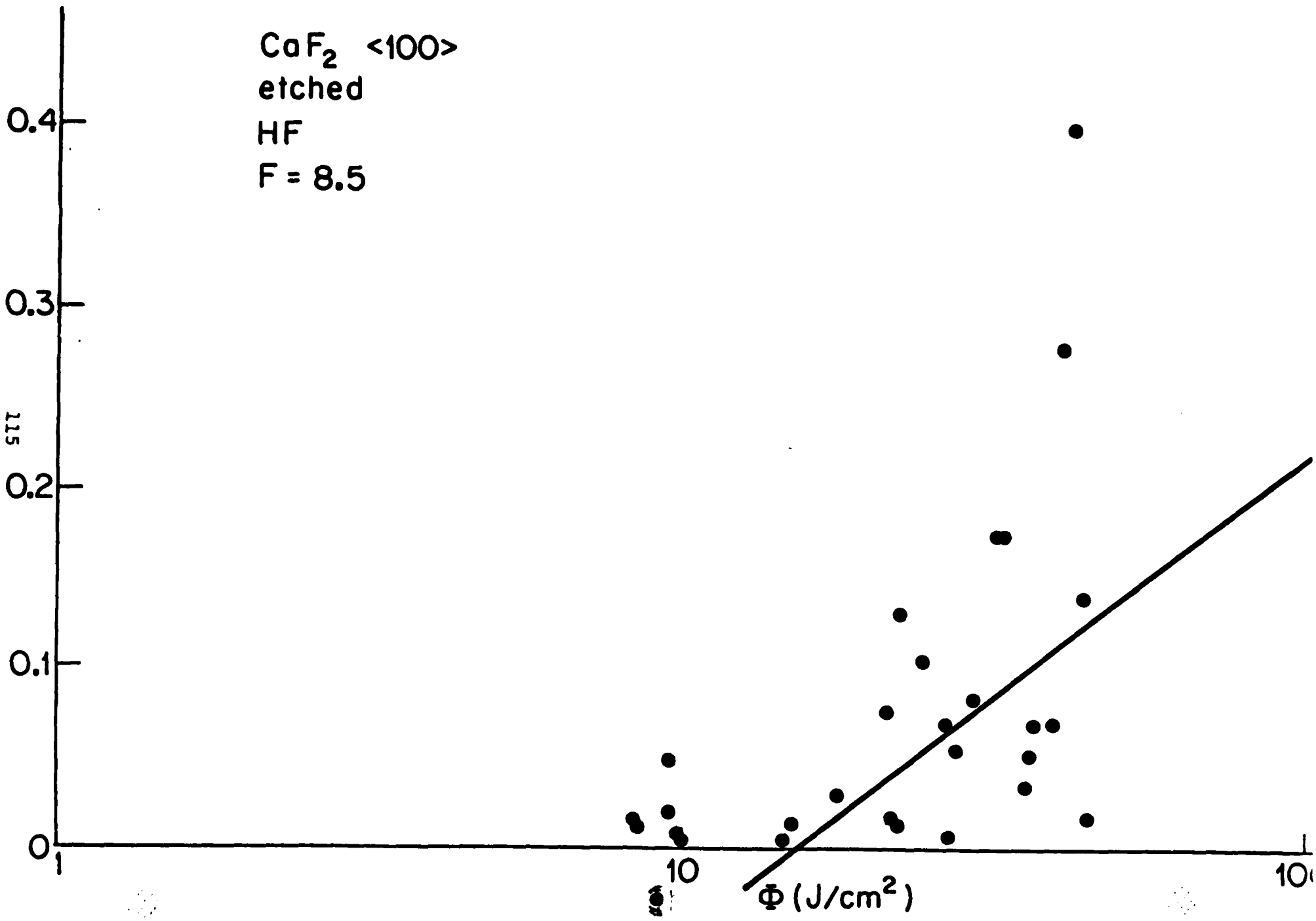

FIGURE 3

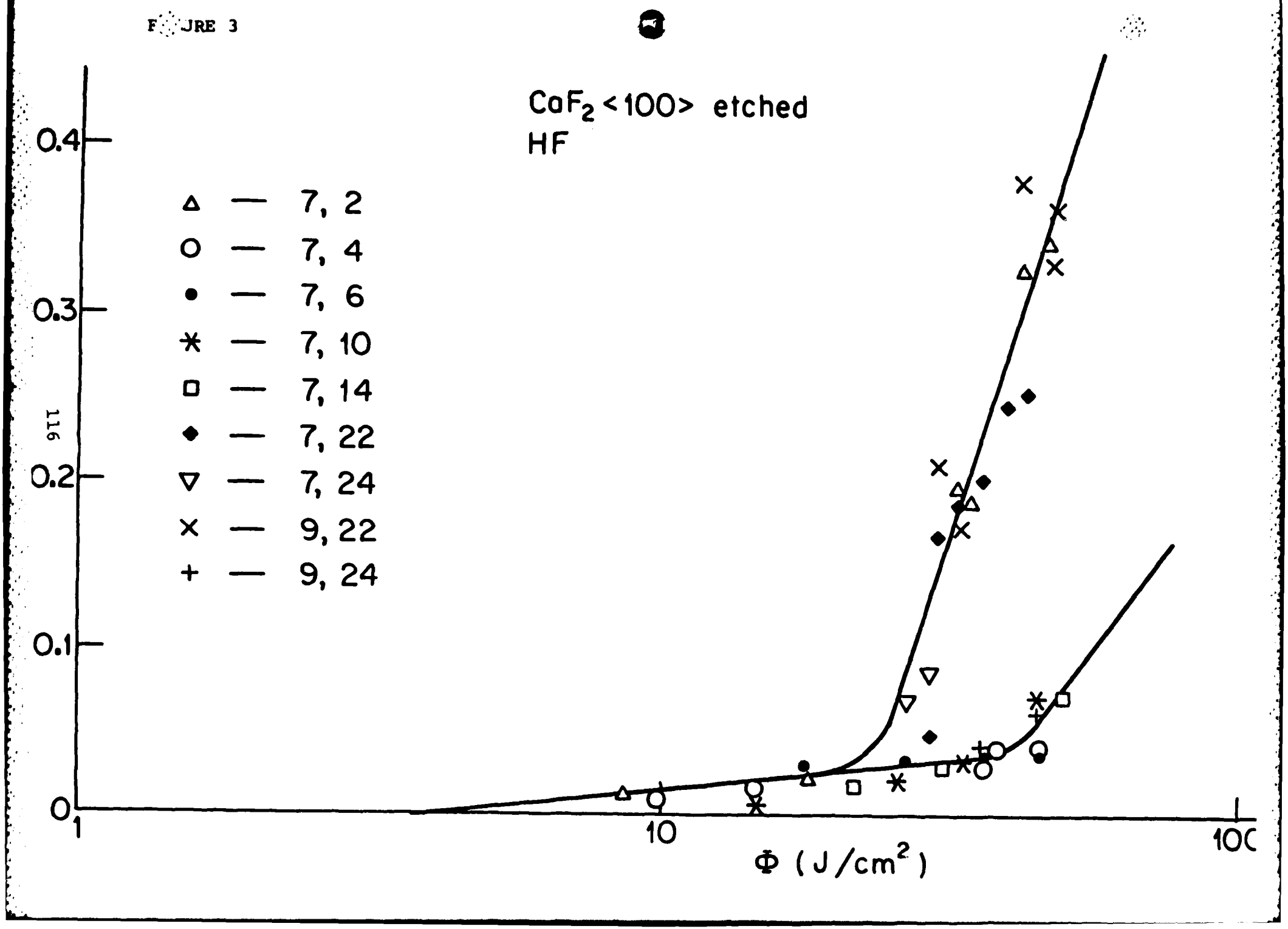
CaF_2 <100> etched
HF
△ — 7, 2
○ — 7, 4
● — 7, 6
✳ — 7, 10
□ — 7, 14
◆ — 7, 22
▽ — 7, 24
× — 9, 22
+ — 9, 24
0.4
0.3
0.2
0.1
0
1
10
100
Φ (J/cm²)
1116

FIGURE 4

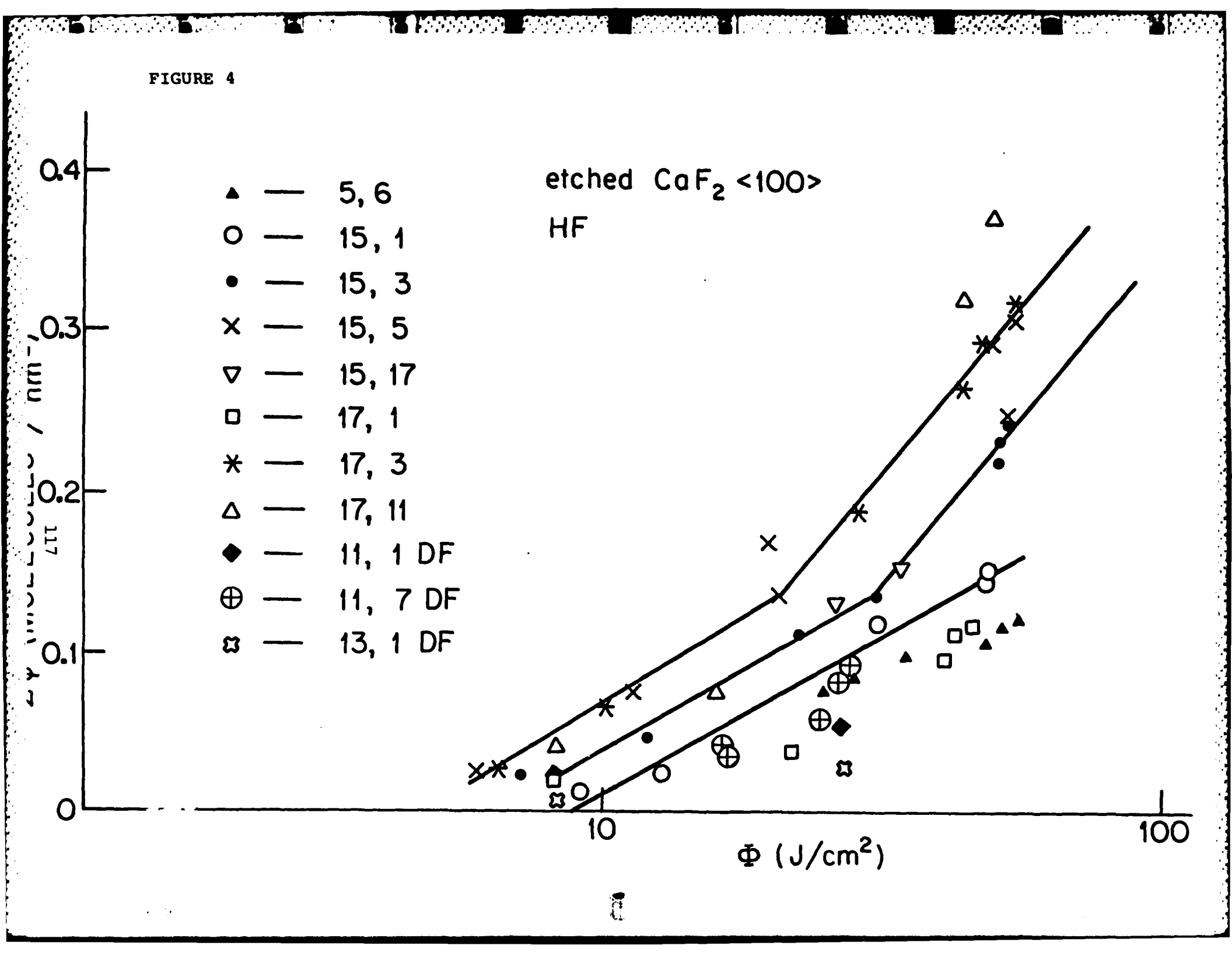
etched CaF_2 <100>
HF
▲ — 5, 6
○ — 15, 1
● — 15, 3
× — 15, 5
▽ — 15, 17
□ — 17, 1
✳ — 17, 3
△ — 17, 11
◆ — 11, 1 DF
⊕ — 11, 7 DF
✡ — 13, 1 DF
0.4
0.3
0.2
0.1
0
10
100
Φ (J/cm²)

FIGURE 5

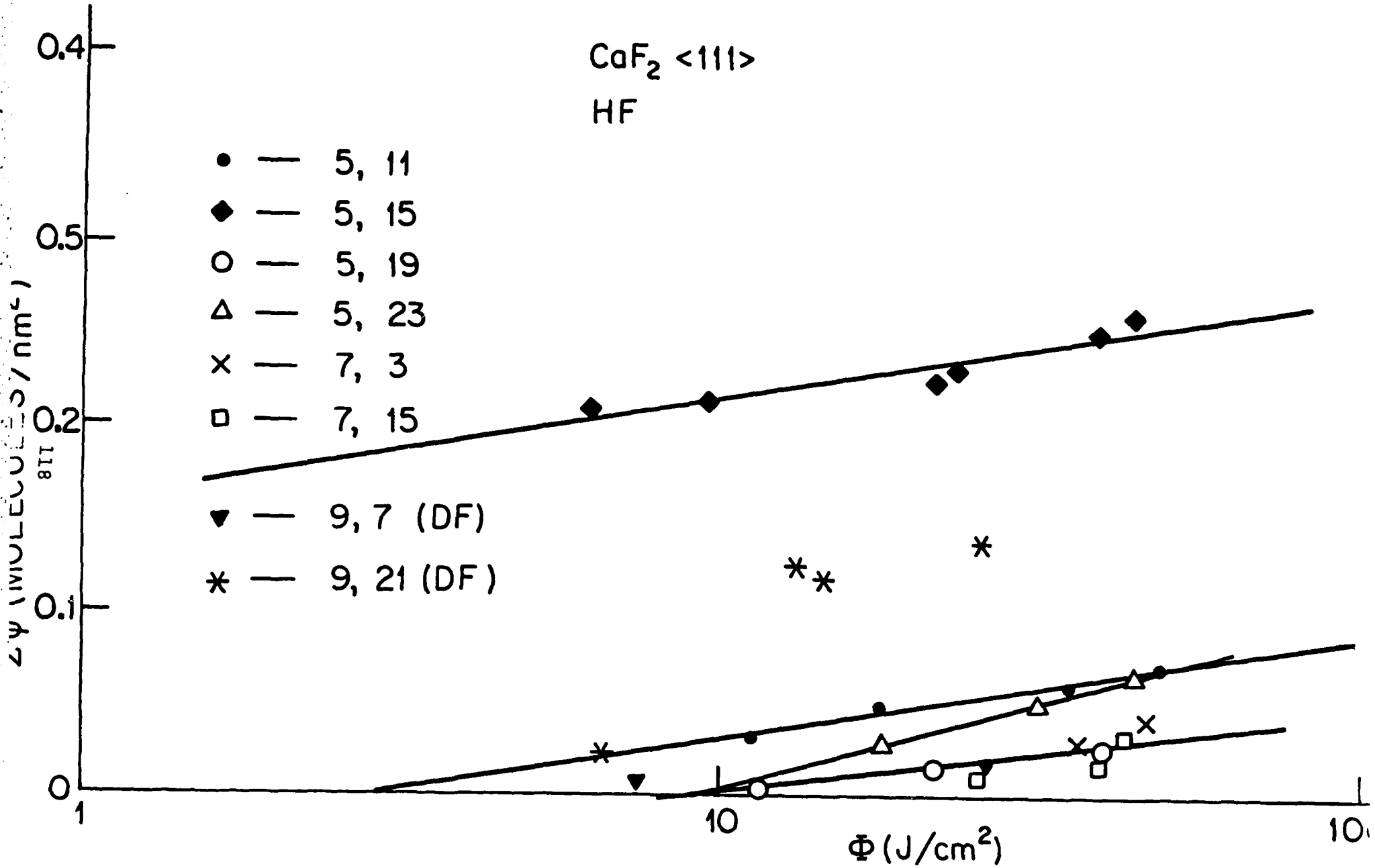
a
CaF_2 <111>
HF
• — 5, 11
◆ — 5, 15
○ — 5, 19
△ — 5, 23
× — 7, 3
□ — 7, 15
▼ — 9, 7 (DF)
* — 9, 21 (DF)
0.4
0.5
0.2
0.1
0
1
10
Φ (J/cm²)

FIGURE 6

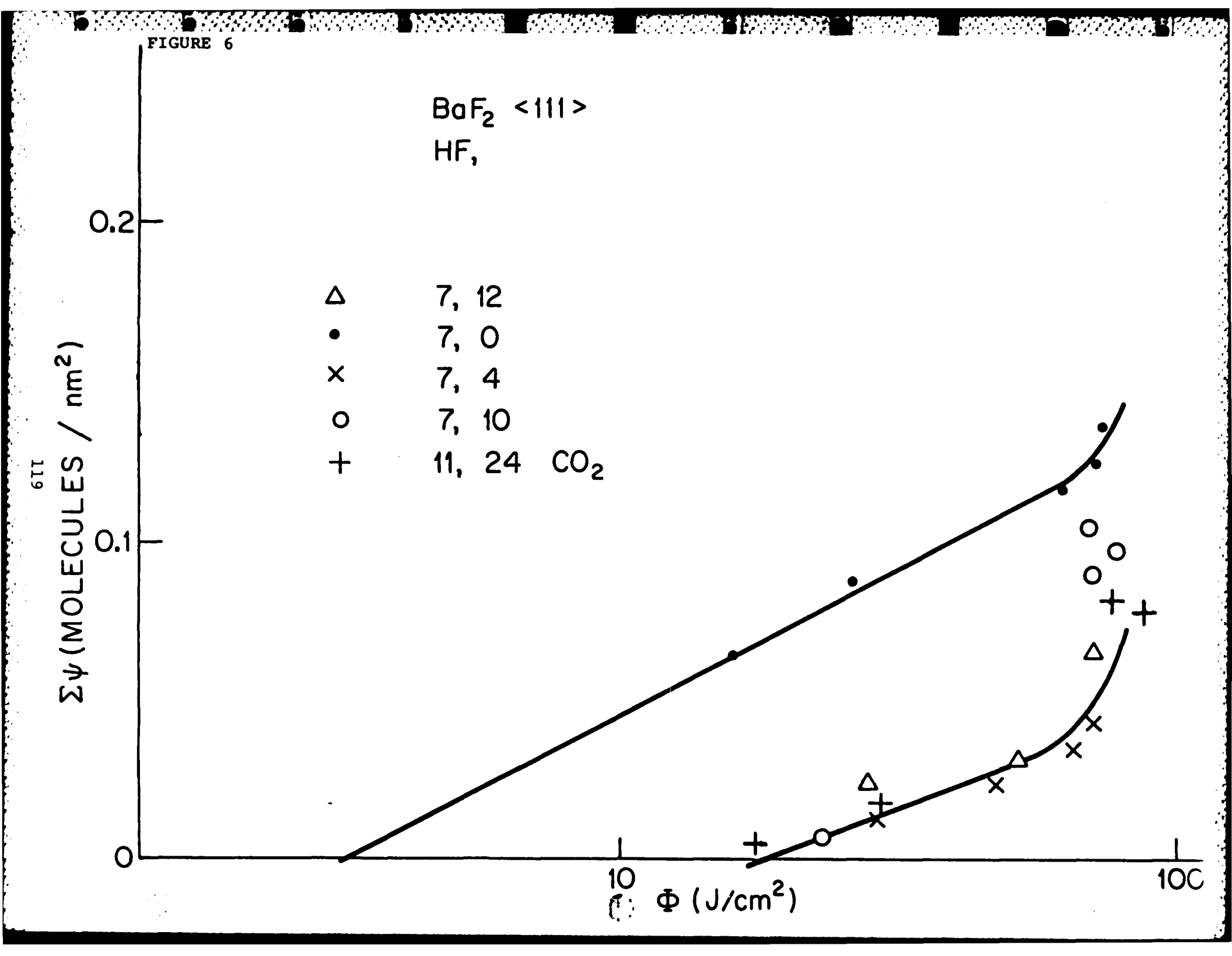
BaF2 <111>
HF,
△ 7, 12
• 7, 0
× 7, 4
o 7, 10
+ 11, 24 CO2
0.2
0.1
0
ΣΨ (MOLECULES / nm²)
10
Φ (J/cm²)
100

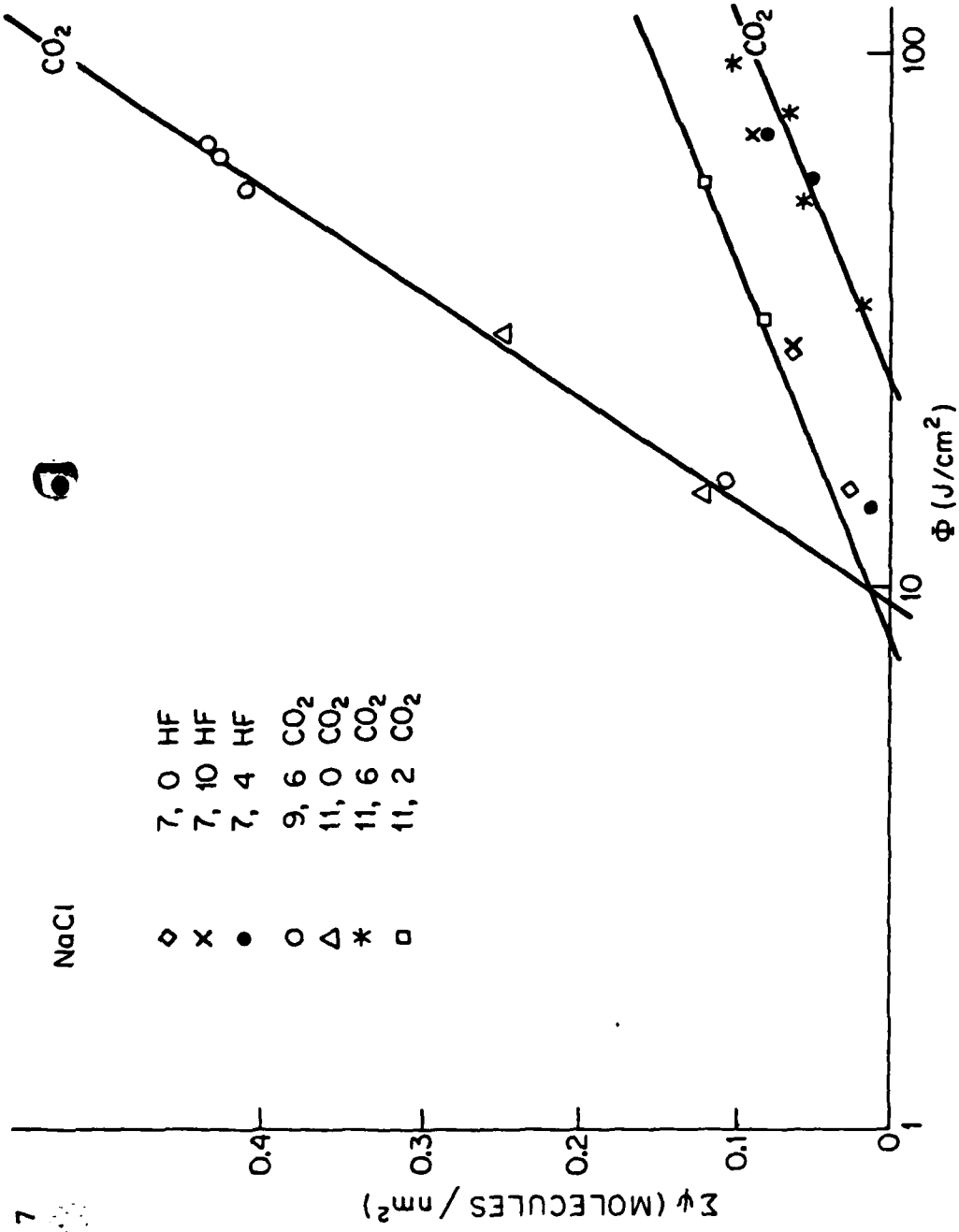
NaCl
◇ 7, 0 HF
× 7, 10 HF
● 7, 4 HF
○ 9, 6 CO_2
△ 11, 0 CO_2
* 11, 6 CO_2
□ 11, 2 CO_2
CO_2
CO_2
0.4
0.3
0.2
0.1
0
1
10
100
Φ (J/cm²)
Σψ (MOLECULES / nm²)

FIGURE 7

FIGURE 8

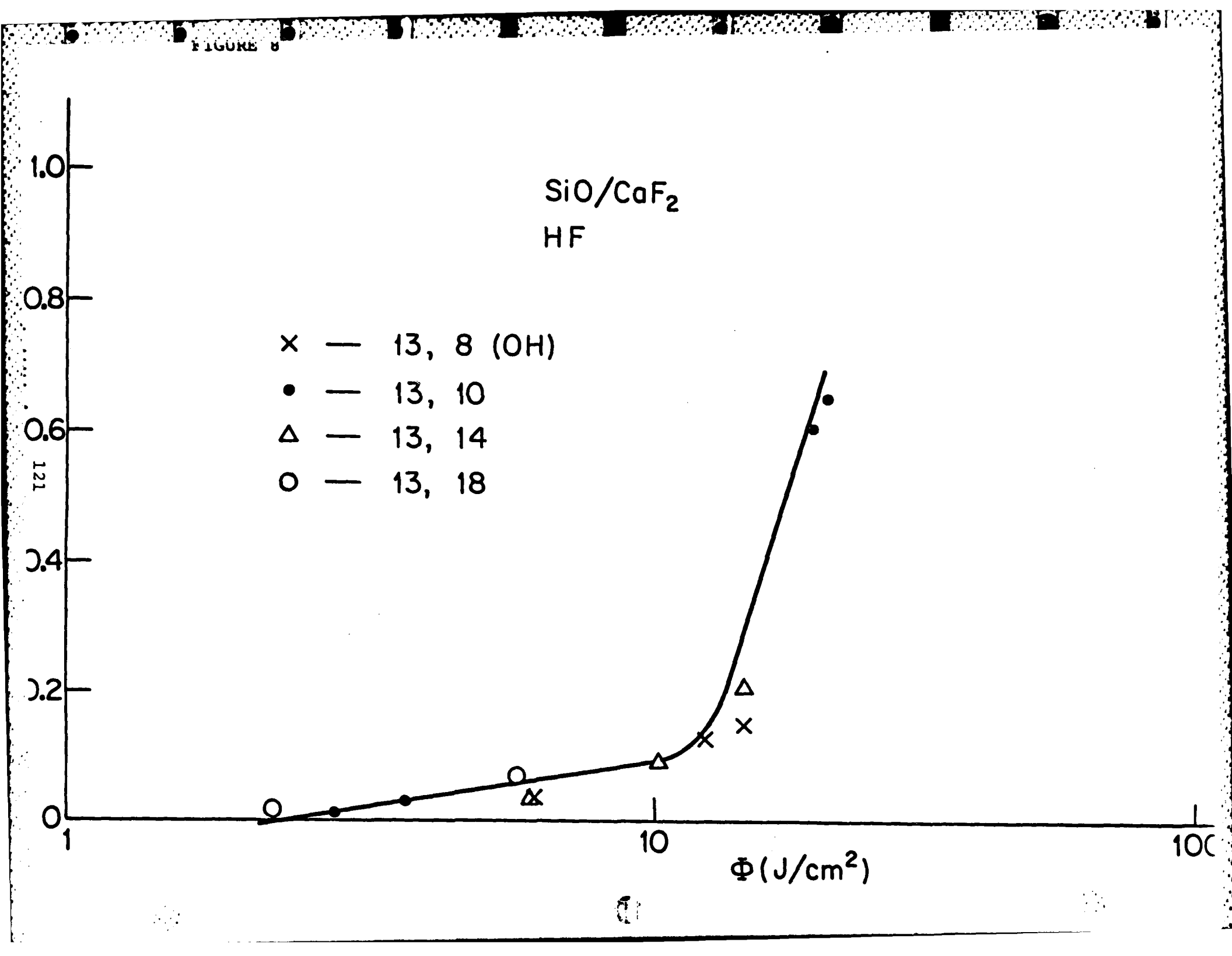

Chapter 7

Laser Mirror Operation at Cryogenic Temperature

D. L. Decker and V. A. Hodgkin

Michelson Laboratory, Physics Division
Naval Weapons Center
China Lake, CA 93555

Presented at the 13th Annual Symposium on Optical Materials for High Power Lasers
17 - 18 November 1981, Boulder, CO

Laser Mirror Operation at Cryogenic Temperatures*

D. L. Decker and V. A. Hodgkin

Michelson Laboratory, Physics Division
Naval Weapons Center, China Lake, California 93555

It has been suggested many times that operation of laser mirrors at low temperatures could result in significant performance improvements. Specifically for metal mirrors, the advantage perceived is in decreased absorption and increased thermal conductivity. For dielectric-enhanced mirrors, presumably a similar advantage would be present in lowering both the absorption of the initial metal film and perhaps lowering absorption in the dielectric films as well. From an engineering point of view, this proposition is not entirely academic, at least for space applications, where entirely passive methods of cooling could be employed.

This paper presents experimental absorptance vs wavelength and temperature data over the range from 1 to 10 μm and from room temperature to 80°K. Included in this study are silver samples prepared by different techniques including diamond single-point machining. Also included are similar data for a multilayer dielectric mirror. Theoretical interpretation of the performance of both mirror types is made with recommendations for actual use.

Key words: absorption; bare metal surfaces; cryogenic temperatures; dielectric-enhanced mirror; Drude theory; laser mirrors.

Introduction

The decrease in infrared absorption and increase in thermal conductivity of metals as the temperature is lowered is a consequence of the increase in mean-free path of the conduction electrons of the metal as the electron-phonon collision frequency decreases [1].[1] However, to obtain these results, the metal must be very pure and well ordered so that electron collisions with lattice imperfections will be the only limiting effect at very low temperatures. This paper presents data which demonstrate for the first time that useful improvements in performance for practical metal mirror surfaces can be achieved at cryogenic temperatures. Data are presented for evaporated thin film and diamond-machined silver which show optical absorptance in agreement with simple theory at temperatures down to 80°K.

Theory

The Drude theory of free-electron optical absorption has been shown to provide an accurate model of optical behavior of silver and other "good" metals in the infrared [2]. This is true not only at room temperatures but also at both elevated and cryogenic temperatures [3]. The complex dielectric constant $\varepsilon_1 + i\varepsilon_2$ is simply related to the plasma frequency, ω_p, and the electron relaxation time, τ [4]:

$$\varepsilon_1 = 1 - \omega_p^2/(\omega^2 + 1/\tau^2) \qquad (1)$$

$$\varepsilon_2 = \omega_p^2/(\omega^2 + 1/\tau^2)\omega\tau \quad . \qquad (2)$$

The plasma frequency and relaxation time can be related to other macro- and microscopic material parameters (cgs units),

*Work supported by the Defense Advanced Research Projects Agency.
[1]Numbers in brackets indicate the literature references at the end of the paper.

$$\omega_p^2 = 4\pi Ne^2/m^* \tag{3a}$$

$$\tau = m^*\sigma/Ne^2 \quad , \tag{3b}$$

where N is the electron concentration, m^* an effective electron mass, e the electronic charge, and σ the d.c. conductivity. The reflectance is simply given by Fresnel's relationship:

$$R = |(\tilde{\varepsilon}^{1/2} - 1)/(\tilde{\varepsilon}^{1/2} + 1)|^2 \quad . \tag{4}$$

If $(\omega_p\tau)^2 >> (\omega\tau)^2 >> 1$, which is true for silver, copper, and gold at near- and mid-IR wavelengths, then

$$R \cong 1 - 2/\omega_p\tau \quad . \tag{5}$$

If we assume that all incident light is either specularly reflected or absorbed, the absorptance A is simply 1 - R. The absorptance is then given by the following approximate expression:

$$A \cong 2/\omega_p\tau \quad . \tag{6}$$

The primary temperature dependence of the absorptance arises through the change in relaxation time with temperature. This dependence can be further described from changes in the macroscopic variable, σ, the d.c. conductivity. Figure 1 illustrates schematically the temperature dependence of $1/\sigma$, the electrical resistivity [1]. At temperatures on the order of the Debye temperature, T_D, $1/\sigma \sim T$. At very low temperatures, $1/\sigma \sim T^5$. For impure metals, the high temperature performance is unchanged, but at low temperatures, $T < T_D$, $1/\sigma$ approaches a minimum, "residual" value $1/\sigma_R$. To obtain significant benefit from cooling a metal mirror, the metal must be very pure and well ordered; this allows a small residual resistivity so that departure from linear behavior will occur only at very low temperatures. If we substitute eq (3b) into (6) and assume that $1/\sigma = \rho_0 + \rho_1 T$, the explicit temperature dependence of A is obtained:

$$A(T) = \frac{\omega_p}{2\pi}(\rho_0 + \rho_1 T) \tag{7a}$$

$$= A_0 + A_1 T \tag{7b}$$

$$\cong A_1 T \quad ; \quad T \geq T_D/3 \quad . \tag{7c}$$

Table 1 gives values of Debye temperature, Drude theory parameters, and absorptance.

Table 1. Values of the Debye temperature, T_D, the electron relaxation time, τ, the plasma frequency, ω_p, the temperature derivative of the absorptance, A_1, and the absorptance, A, at 300 and 80°K for silver, copper, and aluminum. Values taken from a variety of sources in the open literature.

	T_D(°K)	τ(sec)	ω_p(sec^{-1})	A_1(°K^{-1})	A(300°K)	A(80°K)
Ag	220	3.6×10^{-14}	1.3×10^{-16}	1.5×10^{-5}	4.2×10^{-3}	0.9×10^{-3}
Cu	315	2.7	1.6	1.8	4.5	0.5
Al	396	0.8	2.2	4.2	11.2	2.0

Experiment

The absolute reflectance of precision diamond-machined and evaporated silver as well as a multilayer enhanced reflector tuned for 3.8 μm was determined using equipment previously described [3]. The temperature range examined extended from 80 to 450°K, and measurements were made at 2.7, 3.8, and 10.6 μm wavelength. The precision of these measurements was $\pm 5 \times 10^{-5}$, and the absolute accuracy was $\pm 5 \times 10^{-4}$ at all wavelengths. The quantity 1 - R is plotted in figures 2-4 as an inferred absorptance. Since no scatter correction has been made, the values 1 - R are an upper bound to the true absorptance. In figure 2, data are plotted for a very high quality precision diamond-machined surface of electroplated silver. At room temperature and lower, all data are in agreement within experimental uncertainty with Drude theory predictions. However, the slope of a line fit through the data taken in aggregate at each temperature is somewhat steeper than the Drude theory predicts. At 80°K the value of 1 - R is on the order of 10^{-3} or smaller, a value very similar to that achieved by state-of-the-art multilayer dielectric-enhanced reflectors at room temperature.

Similar results were obtained for evaporated silver deposited on polished silicon, plotted in figure 3. This is a surprising result, since the relatively large disorder present in the evaporated film [5] would be expected to produce a substantial departure from linearity at temperatures not far below room temperature. The measured values of 1 - R at 3.8 μm are considerably larger than expected for reasons unknown. The trend of the data taken in aggregate is again steeper than the Drude theory predictions, and at 80°K, again, values on the order of 10^{-3} are achieved.

The results for a four-pair ZnS/ThF_4 quarter-wave stack on evaporated silver deposited on polished fused quartz are plotted in figure 4. These data are in sharp contrast to the bare silver results and show very little temperature dependence. This stability is considerably different than previously reported on a sample of similar construction and materials upon cycling to elevated temperatures only [6].

Cryogenic Mirror Performance

The primary optical advantage to be gained by cryogenic mirror operation is the substantial reduction in absorption. Nearly an order of magnitude has been obtained by reducing the mirror temperature from 300 to 80°K. For many mirror substrate materials, there is also a substantial increase in thermal conductivity. Table 2 gives values of the ratio of thermal conductivity K at 80°K to that at 300°K for a variety of common or proposed substrate materials [7]. For the metal substrates, the increase is on the order of 1.5. Also advantageous is the increase in elastic moduli that most metals experience upon cooling, resulting in stiffer mirror structures.

Table 2. Ratio of the thermal conductivity at 80°K to that at 300°K for a variety of common mirror substrate materials.

	Ag	Cu	Al	Mo	Si	C(graphite)
$\frac{K_{80°K}}{K_{300°K}}$	1.2	1.6	1.8	1.6	9.3	0.8

Theoretically, both for pulsed and CW laser radiation, substantial increases in laser-induced damage thresholds for metals will occur. However, it is not at all obvious what effect cryogenic operation would have on localized defect-initiated damage [8]. If the mirror absorptance, thermal conductivity, K, and heat capacity, C, are assumed to be constant and not temperature dependent, then for a square pulse of duration τ, the melt threshold fluence, θ_m, is just [9]

$$\theta_m = \frac{(\pi KC)^{1/2}}{2A} (T_m - T_0)\tau^{1/2} \quad , \tag{8}$$

where T_m and T_0 are the melting and initial temperatures of the mirror material, respectively. The temperature dependence of the product KC is very small, from 80°K up to the melting point for silver, copper, and gold. The effect of the temperature dependence of A can be approximately taken into account by substituting into eq (8) the average value $(A_0 + A_m)/2$, computing the values A_0 and A_m using eq (7c). The following expression for the relative melt threshold is obtained from eq (8):

$$\frac{\theta_m(T_1)}{\theta_m(T_0)} = \frac{T_0 + T_m}{T_1 + T_m} \quad \frac{T_m - T_1}{T_m - T_0} \quad . \tag{9}$$

This expression is pulse-length independent and for silver yields the result:

$$\frac{\theta_m(80°K)}{\theta_m(300°K)} = 1.16 \times 1.23 = 1.43 \quad .$$

It can be seen then that the increase in melt threshold arises almost equally from the effects of the lower initial absorption and from the lower initial temperature of the mirror surface. A numerical solution to the one-dimensional heat flow equations with proper boundary conditions for A(T) yields a value of 14% higher than the value obtained above.

Summary

Measurements presented in this paper indicate that upon cooling the absorptance of a multilayer dielectric-enhanced mirror (ZnS/ThF_4) is changed only slightly. Earlier measurements indicated the possibility of larger variation, including irreversible alteration of the sample behavior upon temperature cycling. In either event, little is gained optically by cooling such a mirror. In contrast, cooling a bare metal mirror of silver, copper, or gold from room temperature to 80°K should, theoretically, decrease the absorptance about an order of magnitude. This prediction is verified experimentally for both evaporated thin film and diamond single-point machined silver. The absorptance of silver at 80°K is comparable to the room temperature absorptance of a state-of-the-art dielectric-enhanced reflector. Additional benefit is predicted for mirror performance from an increase in thermal conductivity of the mirror substrate. A theoretical prediction is also made of the increase in pulsed laser melt threshold resulting from cryogenic mirror operation. For a silver mirror, an increase of about 1.5 in the melt threshold would be expected at 80°K compared to room temperature. These improvements in performance may be attractive in the design of high power density laser systems, especially for space application where passive cooling could be employed.

References

[1] Kittel, C. Introduction to solid state physics, 5th ed, chapter 6. New York, NY: John Wiley & Sons; 1976.

[2] Bennett, H. E.; Bennett, J. M. Validity of the Drude theory for silver, gold, and aluminum in the infrared in optical properties and electronic structure of metals and alloys. Abelès, F., ed. North Holland: 1966. 175-188.

[3] Decker, D. L.; Hodgkin, V. A. Wavelength and temperature dependence of the absolute reflectance of metals at visible and infrared wavelengths. Bennett, H. E.; Glass, A. J.; Guenther, A. H.; Newnam, B. E., ed. Proceedings of the 12th annual symposium on optical materials for high power lasers; 1980 September 30-October 1; Boulder, CO. Nat. Bur. Stand. (U.S.) Spec. Publ. 620; 1981 October. 190-200.

[4] Stern, F. Elementary theory of the optical properties of solids in Advances in solid state physics, Vol. 15. Seitz, F.; Turnbull, D., ed. New York, NY: Academic Press; 1963. 344-347.

[5] Théye, M. Investigation of the optical properties of Au by means of thin semitransparent films. Phys. Rev. B 2; 3060; 1970.

[6] Decker, D. L. Temperature and wavelength dependence of the reflectance of multilayer dielectric mirrors for infrared laser applications. Glass, A. J.; Guenther, A. H., ed. Proceedings of the 7th annual symposium on optical materials for high power lasers; 1975 July 29-31; Boulder, CO. Nat. Bur. Stand. (U.S.) Spec. Publ. 435; 1976 April. 230-235.

[7] American Institute of Physics Handbook. New York: McGraw-Hill.

[8] Porteus, J. O.; Decker, D. L.; Faith, W. N.; Grandjean, D. J.; Seitel, S. C.; Soileau, M. J. Pulsed laser-induced melting of precision diamond-machined Cu, Ag, and Au at infrared wavelengths. IEEE J. Quantum Electron. QE-17; 2078; 1981.

[9] Bennett, H. E. Thermal distortion thresholds for optical trains handling high pulse powers. Glass, A. J.; Guenther, A. H., ed. Proceedings of the 8th annual symposium on optical materials for high power lasers; 1976 July 13-15; Boulder, CO. Nat. Bur. Stand. (U.S.) Spec. Publ. 462; 1976 December. 20.

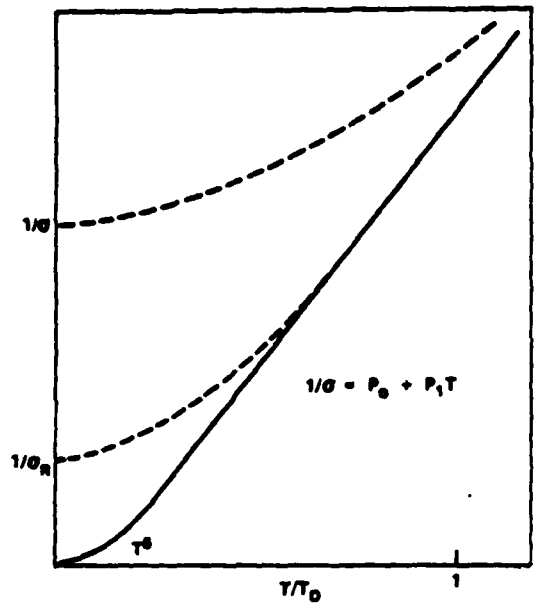

Figure 1. Schematic plot of the electrical resistivity, $1/\sigma$, vs the absolute temperature normalized to the Debye temperature for a metal. For a well-ordered, pure metal in the range above about $T_D/3$, the resistivity is linear with temperature. However, for less well-ordered or impure metals, significant departure from linearity will occur at temperatures ~ T_D, and at lower temperatures an asymptotic "residual" resistivity will be approached. In extreme cases, the residual resistivity will be perhaps only a factor of two smaller than the room temperature value.

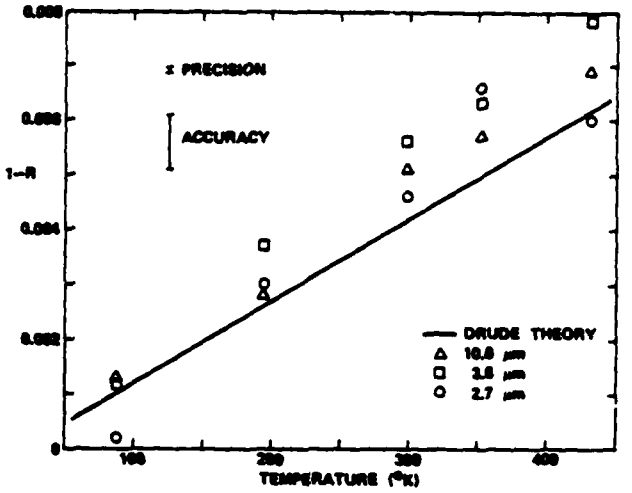

Figure 2. Plot of 1 - R vs absolute temperature for a diamond-machined silver surface at three wavelengths (2.7, 3.8, and 10.6 μm) compared with the Drude theory prediction using nonoptical input parameters.

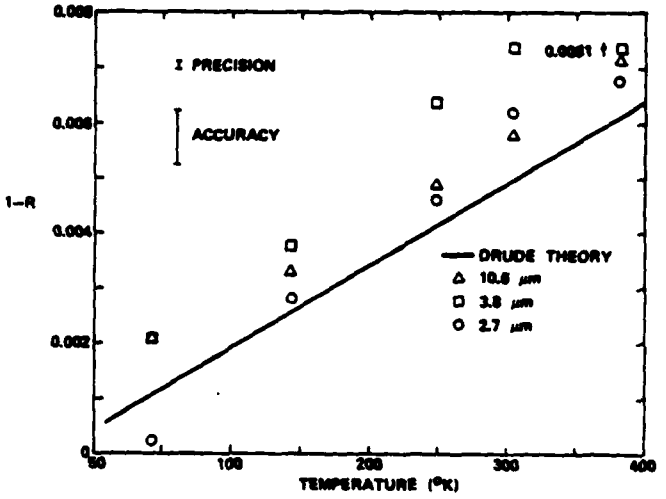

Figure 3. Plot of 1 - R vs absolute temperature for an evaporated thin film of silver deposited on polished single-crystal silicon. Data are shown at three wavelengths (2.7, 3.8, and 10.6 μm) compared with Drude theory predictions using nonoptical input parameters.

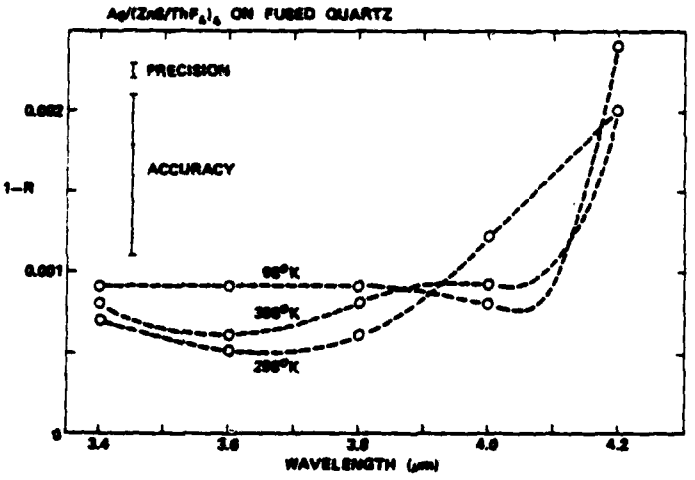

Figure 4. Plot of 1 - R vs wavelength for a multilayer ZnS/ThF_4 dielectric-enhanced silver reflector, tuned for 3.8 μm. Shown are data at three temperatures: 98, 298, and 398°K.

Chapter 8

Laser Damage to Metal Mirrors at Non-normal Incidence

D. L. Decker and J. O. Porteus

Michelson Laboratory, Physics Division
Naval Weapons Center
China Lake, CA 93555

Presented at the 13th Annual Symposium on Optical Materials for High Power Lasers
17 - 18 November 1981, Boulder, CO

Laser Damage to Metal Mirrors at Nonnormal Incidence*

D. L. Decker and J. O. Porteus

Michelson Laboratory, Physics Division
Naval Weapons Center, China Lake, California 93555

Virtually all laser damage experiments have been performed at normal incidence. However, many applications are for nonnormal incidence, and, obviously, it would be appropriate to characterize the surfaces with the intended geometry and polarization.

This paper presents damage threshold data on bare diamond-machined copper at 45-degree angle of incidence at 3.8 μm wavelength. Within experimental uncertainty, the melt threshold for p-polarization is identical to that obtained at normal incidence on the same surface. The thresnold for s-polarization is a factor of two larger. The experimental values are compared with theoretical melt threshold calculations and are found to be in reasonable agreement. The polarization dependence is seen to arise from the fundamental infrared optical properties of metals. The relationship between normal incidence and 45-degree incidence thresholds provides a valuable cross-check on the systematic errors in laser damage measurements.

Key words: laser-induced damage; melt threshold; metal mirrors; nonnormal incidence; optical absorptance.

Introduction

Pulsed laser-induced damage to metal mirrors is rather well understood theoretically [1,2].[1] There also exists reasonable agreement between theory and experimental data at normal incidence [2]. Very little has been done at nonnormal incidence, even though many nonnormal applications exist [3]. This paper presents data at 45-degree angle of incidence for p- and s-polarization, together with a theoretical interpretation which can be applied to arbitrary angles of incidence. It is shown that for s-polarization, large increases in damage threshold with increasing angles of incidence occur.

Theory

Pulsed laser damage in pure metals is thermal in origin, provided the pulse length is long compared to the electron relaxation time ($\sim 10^{-14}$ sec). On well-prepared metal surfaces, damage is ordinarily initiated by thermally induced stress, followed by melting as the pulse energy is increased [4]. At slightly higher pulse energies or in the presence of defects or inclusions, vaporization and plasma formation typically occur, resulting in more complicated effects [4]. If the irradiated area is sufficiently large and uniform, heat flow and momentum transfer directions are essentially normal to surface, independent of the incidence angle of laser irradiation.

In figure 1 incident radiation of intensity I_0 with either s- or p-polarization is incident upon a surface. The specularly reflected intensity is $I_0 R_{s(p)}$. R_s and R_p may be simply computed [5]:

$$R_s = \frac{a^2 + b^2 - 2a\cos\theta + \cos^2\theta}{a^2 + b^2 + 2a\cos\theta + \cos^2\theta} \tag{1}$$

$$R_p = R_s \frac{a^2 + b^2 - 2a\sin\theta\tan\theta + \sin^2\theta\tan^2\theta}{a^2 + b^2 + 2a\sin\theta\tan\theta + \sin^2\theta\tan^2\theta} \tag{2}$$

*Work supported by Navy Independent Research funds and by the Air Force Weapons Laboratory.
[1]Numbers in brackets indicate the literature references at the end of the paper.

where

$$a = \frac{n'k'}{n^2}\frac{1}{b} \quad ; \quad b^2 = \frac{-y + (y^2 - 4z)^{1/2}}{2}$$

$$y = \left(\frac{n'}{n}\right)^2 - \left(\frac{k'}{n}\right)^2 - \sin^2\theta \quad ; \quad z = -\left(\frac{n'k'}{n^2}\right)^2 \quad .$$

If all incident light is either specularly reflected or absorbed, then the absorptances A_s and A_p are just

$$A_s = 1 - R_s \tag{3}$$

and

$$A_p = 1 - R_p \quad . \tag{4}$$

For a metal at infrared wavelengths, $k' >> n' >> 1$ so that $A_s << 1$, $A_p << 1$. Figure 2 schematically illustrates the angle of incidence variation for this case. Particularly simple approximations for A_s and A_p can be derived:

$$A_s(\theta) \cong \frac{4n}{k^2}\cos\theta = A(0)\cos\theta \tag{5}$$

$$A_p(\theta) \cong \frac{A(0)}{\cos\theta} \quad ; \quad \theta < 70 \text{ deg} \quad . \tag{6}$$

At 45 degrees, the following expression can be obtained either from the above relationships or from an expansion of the Abelès condition, $R_p = R_s^2$,

$$A_s(45) = A(0)/\sqrt{2} \tag{7}$$

$$A_p(45) = \sqrt{2}\,A(0) \quad . \tag{8}$$

Figure 3 illustrates the far-field focus of a Gaussian laser beam with an angle of incidence θ of the sample plane to the beam axis. If the ratio of the focal spot size in the oblique plane to the depth of focus is small, the on-axis intensity in the oblique plane is just $I_o\cos\theta$. Laser-induced damage is reached when the energy per unit area absorbed from the laser pulse equals a threshold value. This value will be independent of angle of incidence. Hence,

$$A(\theta)T(\theta)\cos\theta = A(0)T(0) \quad ,$$

where T is the threshold fluence for a damage mechanism, e.g., melting. Therefore, the damage threshold fluence variation with incidence angle is just

$$T(\theta) = \frac{A(0)}{A(\theta)}\frac{T(0)}{\cos\theta} \quad . \tag{9}$$

Substituting eqs (5) and (6) in eq (9):

$$T_s(\theta) = \frac{T(0)}{\cos^2\theta} \tag{10}$$

$$T_p(\theta) = T(0) \quad ; \quad \theta < 70 \text{ deg} \quad . \tag{11}$$

Beyond an angle of incidence of 70 degrees, $T_p(\theta)$ increases very slowly reaching a value of slightly over 2T(0) at θ = 88 degrees. Table 1 gives computed values of A_s, A_p, T_s, and T_p for selected angles of incidence for copper at 3.8 μm wavelength using eqs (1)-(4),(9).

Table 1. Computed values of A_s, A_p, $T_s(\theta)/T(0)$, and $T_p(\theta)/T(0)$ for copper at 3.8 μm wavelength: n = 1.20, k = 25.0

θ	A_s	A_p	$T_s(\theta)/T(0)$	$T_p(\theta)/T(0)$
0	.0076	.0076	1.00	1.00
30	.0066	.0088	1.33	1.00
45	.0054	.0108	2.00	1.00
60	.0038	.0151	4.00	1.00
70	.0026	.0219	8.55	0.99
80	.0013	.0411	33.7	1.06
88	.0003	.0908	726.0	2.40

At 45 degrees, the theoretical thresholds are

$$T_s(45) = 2T(0) \tag{12}$$

$$T_p(45) = T(0) \quad . \tag{13}$$

For pure copper at 3.8 μm and a 100 nsec pulse length, the computed melt threshold (peak on-axis fluence) is 245 J/cm^2 [2]. Hence, the predicted s- and p-thresholds at 45 degrees are

$$T_s(45) = 490 \text{ J/cm}^2$$

$$T_p(45) = 245 \text{ J/cm}^2 \quad .$$

Experiment

The Naval Weapons Center experimental layout and procedures for laser-induced damage assessment have been previously described [2]. All damage measurements were performed in a vacuum of 0.3 torr (40 Pa). For nonnormal incidence, the sample is tilted appropriately. With the laser output polarized vertically, the sample configuration shown in figure 4 will then yield s-polarized irradiation. The sample is rotated 90 degrees about the axis of the incoming beam to achieve the other polarization. A Lumonics TE HF/DF laser producing 100 nsec pulses was employed. With a 5-in. focal length lens, the $1/e^2$ focal spot diameter was 56 μm. A 1.52-in.-diameter OFHC copper sample was precision diamond single-point machined and analyzed both at normal incidence and at 45 degrees. Figure 5 shows multi-threshold results for this sample at normal incidence. The measured melt threshold of 191 J/cm^2 is somewhat higher than previously reported, but the agreement is well within stated experimental absolute uncertainty of ±10%. In figure 6, very similar results were obtained for p-polarization with a measured melt threshold of 197 J/cm^2. Note that slip thresholds are virtually identical also. The thresholds for s-polarization are shown in figure 7. All thresholds are much larger, melt occurring at 358 J/cm^2, which is in the ratio of 1.9:1 to the normal incidence melt threshold. This ratio is not quite the 2:1 theoretically expected, but is well inside of the experimental uncertainty.

To compare the experimental data just given with the theoretical melt threshold values given in that section, the theoretical values must be corrected for finite spot size effects. The ratio of melt threshold at finite spot radius T_r to that at an infinite radius T_∞ is approximately [2]:

$$\frac{T_r}{T_\infty} \cong \frac{\chi}{\tan^{-1}\chi} \quad , \tag{14}$$

where $\chi = \sqrt{32/\pi}\ \ell/r$, ℓ being the thermal diffusion depth and r the spot radius.

The normal incidence values have been previously corrected by the ratio T_r/T_∞; however, the extended nature of the nonnormal incidence spot must now be taken into account. The focal spot shape for nonnormal incidence is an ellipse with minor axis r and major axis r/cosθ. Correction ratios for T_r/T_∞ and $T_{\sqrt{2}r}/T_\infty$ are given in table 2. The latter ratio of course is appropriate to a spot of diameter equal to the major diameter of the ellipse at 45-degree angle of incidence. An average correction for the ellipse can be obtained from the last column of table 1, the geometric mean.

Table 2. Spot size corrections to melt threshold for Naval Weapons Center TE DF laser damage data for 45-degree angle of incidence

2r(μm)	ℓ(μm)	T_r/T_∞	$T_{\sqrt{2}r}/T_\infty$	$T_{\sqrt{2}r}/T_r$	$\sqrt{T_{\sqrt{2}r}/T_r}$
55.9	9.6	1.32	1.17	0.89	0.94

Table 3 gives the corrected theoretical values as well as the experimental values just given.

Table 3. Theoretical and experimental values of melt thresholds for 100 nsec pulse length, 3.8 μm radiation at normal and 45-degree angles of incidence. Fluence values are given in J/cm²

	T(0)	$T_s(45)$	$T_p(45)$
Experiment	191	358	197
Theory	245	461	230

Conclusion and Summary

The morphology of the melt damage observed at normal and 45-degree angles of incidence is very similar to that observed on other similar samples at normal incidence [2]. No peculiar morphology was present at nonnormal incidence, as can be seen from an inspection of figures 8-10. The 45-degree angle of incidence damage craters have an aspect ratio on average about 10% less than the expected $\sqrt{2}$:1, presumably as a consequence of asymmetrical heat flow. For the very small crater shown in figure 10, the aspect ratio is only about 3% smaller than expected. This small crater was formed just at threshold and shows no splatter. The most serious discrepancy exists between the measured and computed melt thresholds at normal incidence where the 22% difference lies considerably outside of experimental uncertainty. This has been previously reported and discussed [2]. However, the interrelationships between the measured normal and nonnormal incidence thresholds are excellent. The measured thresholds for s- and p-polarization have a ratio of 1.8:1, about 10% less than expected. The measured melt thresholds for normal incidence and for p-polarization at 45-degree angle of incidence agree within 3%.

Laser damage effects on metals at nonnormal incidence for pulse lengths long enough so that thermal effects dominate are controlled by the variation of optical properties with angle of incidence. In the infrared, where the optical absorptance of metals such as copper, silver, gold, or aluminum is small, the simple relationships between normal and nonnormal incidence absorptance given in this paper permit accurate prediction of nonnormal incidence thresholds which is independent of optical constants. These relationships are particularly useful in providing a check for internal consistency in analyzing laser damage data. The strong increase in the thresholds for s-polarization has laser system design implications and may be a key effect in the design of very high fluence devices.

References

[1] Sparks, M.; Loh, E., Jr. Temperature dependence of absorptance in laser damage of metallic mirrors: one point melting. J. Opt. Soc. Am. 69; 847; 1979.

[2] Porteus, J. O.; Decker, D. L.; Faith, W. N.; Grandjean, D. J.; Seitel, S. C.; Soileau, M. J. Pulsed laser-induced melting of precision diamond-machined Cu, Ag, and Au at infrared wavelengths. IEEE J. Quantum Electron. QE-17; 2078; 1981.

[3] Hayden, J. J.; Liberman, I. Measurements at 10.6 μm of damage threshold in germanium, copper, sodium chloride, and other materials at levels up to 10^{10} W/cm^2. Glass, A. J.; Guenther, A. H., ed. Proceedings of the 8th annual symposium on optical materials for high power lasers; 1976 July 13-15; Boulder, CO. Nat. Bur. Stand. (U.S.) Spec. Publ. 462; 1976 December. 173-180.

[4] Porteus, J. O.; Fountain, C. W.; Jernigan, J. L.; Faith, W. N.; Bennett, H. E. Pulsed-laser stress phenomena on highly reflecting metal and alloy surfaces. Glass, A. J.; Guenther, A. H., ed. Proceedings of the 9th annual symposium on optical materials for high power lasers; 1977 October 4-6; Boulder, CO. Nat. Bur. Stand. (U.S.) Spec. Publ. 509; 1977 December. 204-214.

[5] Tousey, R. On calculating optical constants from reflection coefficients. J. Opt. Soc. Am. 29; 235; 1939.

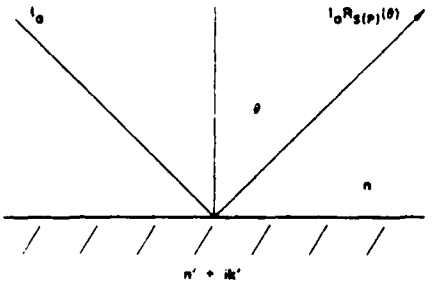

igure 1. Schematic diagram of radiation of intensity I_0 incident upon a surface. The specularly reflected beam has intensity $I_0R_{s(p)}$. The reflectance is a function of the angle of incidence, θ, polarization direction, and optical constants of the substrate n' and k', and external media, n.

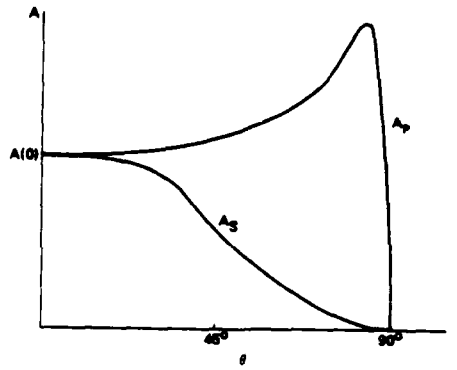

Figure 2. Plot of the angular dependence of the s- and p-absorptance of a metal in the infrared.

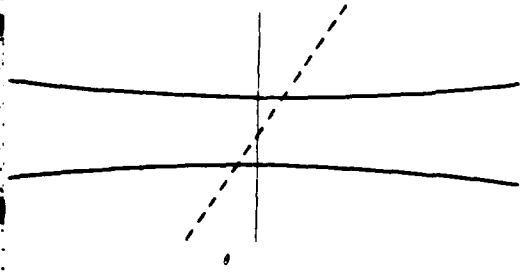

igure 3. Illustration of the far-field focus of a Gaussian laser beam with a sample surface oriented at angle θ to a plane perpendicular to the beam axis.

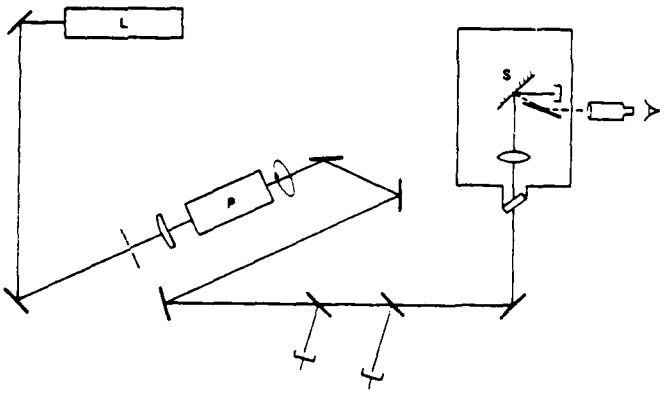

Figure 4. Experimental layout for nonnormal incidence laser-induced damage. With a laser polarization perpendicular to the plane of the drawing, the sample orientation shown will yield s-polarization. To obtain p-polarization, the sample is rotated about the beam axis by 90 degrees.

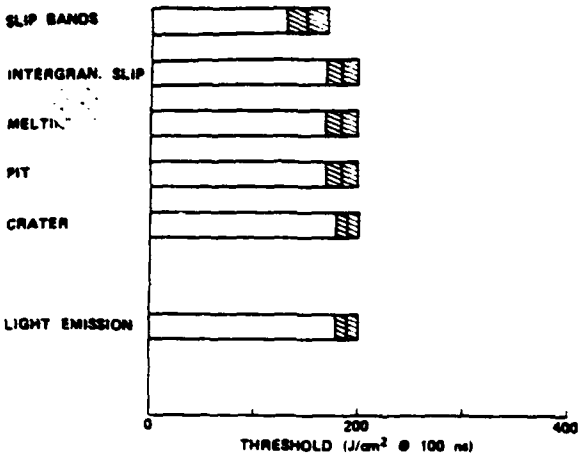

Figure 5. Multithreshold laser damage data for a diamond-machined OFHC copper surface using 100 nsec OF laser pulses. The threshold values plotted are peak on-axis fluences in J/cm^2.

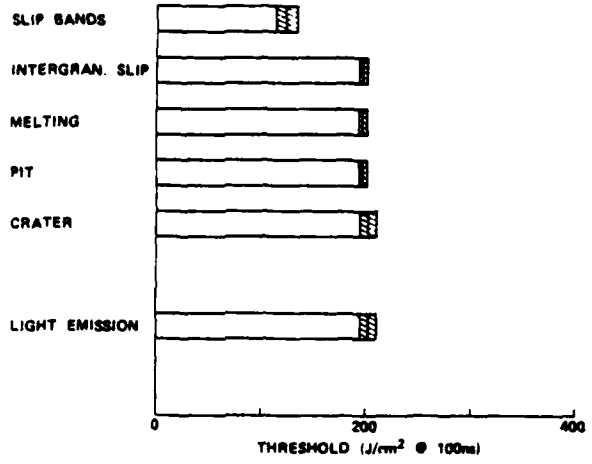

Figure 6. Multithreshold laser damage data for the copper sample shown in Fig. 5, but with an angle of incidence of 45 degrees and for p-polarization.

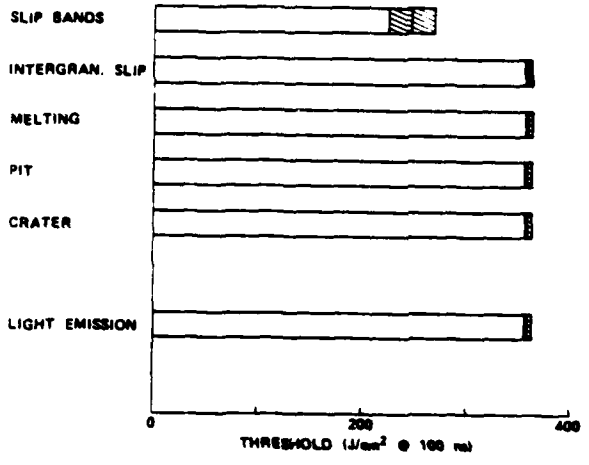

Figure 7. Multithreshold laser damage data for the same copper sample shown in Fig. 6, but with s-polarization.

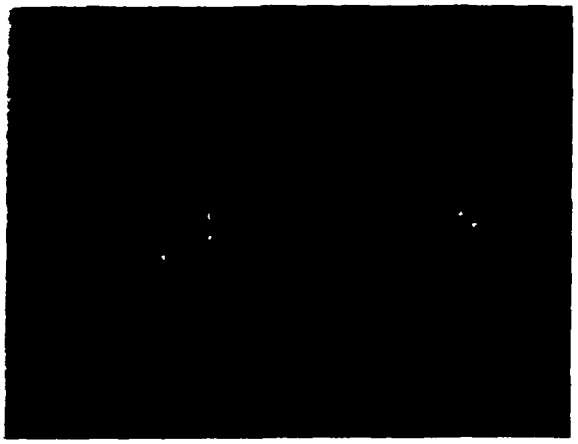

Figure 8. Nomarski micrograph of two damage sites on the diamond-machined OFHC copper sample from which the multithreshold data in Figs. 5-7 were taken. These two sites were damaged at normal incidence. The larger crater is 120 μm in diameter.

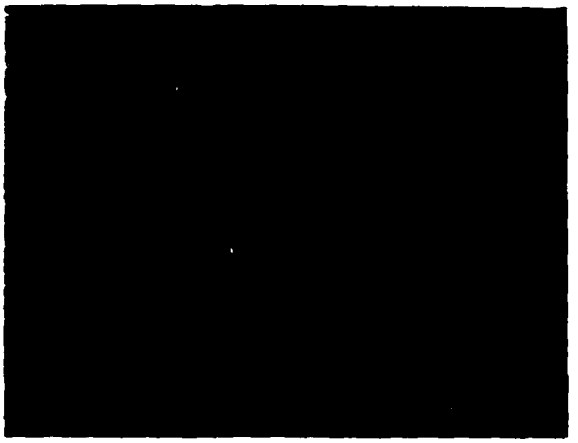

Figure 9. Nomarski micrograph of two damage sites on the same copper sample discussed in Fig. 8, irradiated at 45-degree angle of incidence and with o-polarization. The major axis of the larger crater is about 100 μm.

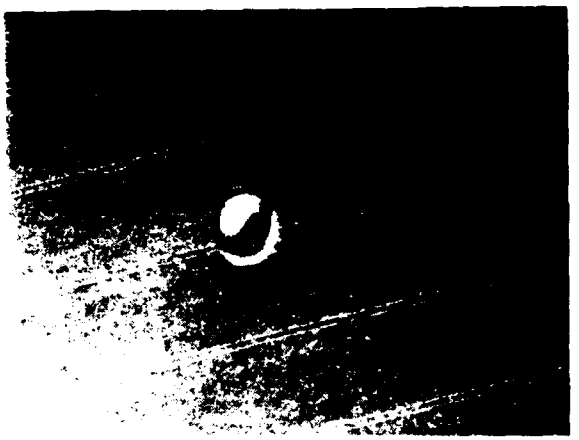

Figure 10. Higher magnification Nomarski micrograph of the small damage site snown in Fig. 9. This melt crater has a major axis of about 30 μm and was formed just at threshold.

Chapter 9

Thin-Film Absorption Measurements Using Laser Calorimetry

P. A. Temple

Michelson Laboratory, Physics Division
Naval Weapons Center
China Lake, CA 93555

Thin-Film Absorptance Measurements Using Laser Calorimetry

P. A. Temple
Michelson Laboratory, Physics Division
Naval Weapons Center, China Lake, California 93555

INTRODUCTION

Laser calorimetry has been used for several years as a method for measuring the absorptive loss in materials in both bulk and thin-film form. Two recent review articles on bulk absorption coefficient measurements in low-absorption, transparent materials were written by Skolnik (1) and Hordvik (2). Skolnik includes a table showing bulk absorption coefficients as low as 10^{-6} cm^{-1}. The technique is not limited to low absorption materials nor to those wavelengths where intense laser lines are available. In the work by Bos and Lynch (3), calorimetry was used to measure the absorption of chromium and two chromium alloys over the spectral range from 0.24 to 14.0 μm at liquid-helium temperatures.

Calorimetry has the advantage of simplicity and high sensitivity. The fundamental quantity measured is the absorptance, A, where

$$A = \frac{\text{absorbed energy}}{\text{incident energy}} \quad . \tag{1}$$

With optical materials, laser calorimetry is generally used to measure samples with absorptances of 1×10^{-2} and less. Figure 1 is a schematic of a typical laser calorimeter. In this apparatus, the sample is heated by a laser beam of constant intensity for a period of time sufficient to raise the temperature of the sample above ambient. The laser is then turned off, and the sample slowly returns to thermal equilibrium with its surroundings. Both the laser power and sample temperature are recorded on a strip-chart recorder. Several analysis techniques have been described in the literature. Figure 2 shows schematically

five sample temperature-vs-time curves. In technique (a) Pinnow and Rich (4) placed the sample in a laser cavity to take advantage of high intercavity power, allowed it to come to thermal equilibrium, and abruptly turned the laser off and observed the cooling curve. In technique (b) Allen et al. (5) irradiated the sample for 4 min and, using computer modeling, determined the absorptance by measuring the temperature rise at the 4-min point. Technique (c), called the rate method, has been used by various workers and is probably the most common analysis technique (1,2). The three-slope method, shown in (d), is not unlike the rate technique shown in (c), but it has the advantage of not requiring the sample to be initially in thermal equilibrium with its surroundings (6). Finally, technique (e), described by Decker and Temple (7), is a truly adiabatic technique where the sample enclosure is temperature controlled and is caused to follow the temperature of the sample as it is heated by the laser. This technique overcomes some of the temperature-gradient problems of the previous methods and is easily calibrated electrically.

There are a number of instrumental considerations involved in accurately determining the absorptance (8). Probably the most serious of these is that of temperature nonuniformity in the sample during irradiation. In the usual analysis, it is assumed that the rate of temperature increase is uniform throughout the sample. As discussed by Bernal G. (9), this is correct only if the sample thermal diffusivity is large and the heat losses are small. Only techniques (b), where a theoretical correction is made, or (e), where the sample is allowed to come to thermal equilibrium with itself, are free of this problem.

A second experimental consideration which is often neglected for both bare and coated samples is that of substrate interference effects. In any calorimetric technique using transparent substrates, the sample will have a rear surface from which the beam must emerge and from which the beam will be partially

reflected. Because of the long coherence length of laser radiation, the substrate may act as an added thin film of some unknown thickness. This will cause a substantial uncertainty in the transmittance of the substrate-film system and in the electric-field distribution within both the substrate and any films present. In order to avoid this undesirable situation, we are forced to defeat laser coherence effects in the substrate. Figure 3 shows three ways of accomplishing this. All three methods result in the same average electric-field intensity distribution in the various regions of the sample. In the first case, the substrate is slightly wedged and the beam is quite large. The wedge causes the substrate to go through several cycles in optical thickness. The second case uses a plane parallel substrate but a large diverging beam. The optical path length is different for various angles of incidence within the beam, causing a mixing similar to the previous case. In this case, tilting the sample slightly enhances the mixing. In the third case, a small-diameter beam is incident on a plane parallel sample at slightly off-normal incidence. Nonoverlap of beams on the entrance (or exit) surface assures us that no interference will exist within the substrate. This is essentially the classical incoherent-beam, multiple-bounce picture, and this model is used to calculate the effect of a real substrate in data given later in this chapter.

When these experimental considerations are taken into account, any of the calorimetric analysis techniques described above can be used to measure the absorptance of either uncoated or coated substrates. In this chapter, we are concerned with measuring the absorptive properties of a single-layer, thin film deposited on a highly transparent substrate.

SINGLE-LAYER FILMS

The most common way of determining the absorption properties of a material in thin-film form is to first measure the absorptance A_1 of a suitable substrate. A film of known thickness ℓ, usually a half-wave in optical thickness (OT), is then deposited on the substrate, and the absorptance A_2 is again measured. The film absorption coefficient β, where

$$\beta = \frac{(A_2 - A_1)}{\ell} \quad , \tag{2}$$

is then calculated. The variation in the electric field both throughout the film and from material to material is not accounted for in Eq. (2). Because of this, one typically finds that β measured when the sample is illuminated from the filmed side will be different from that measured when illuminated from the uncoated side. It is generally recognized that the increased absorption of the filmed substrate is due not only to the bulk of the film but also to the newly introduced film-substrate interface and the film-air interface, where there is a change in material type with possible stoichiometry problems, as well as residual cleaning compound, etc., which may lead to higher absorption. In addition, the work of McCloud (10) suggests that water migrates into the film system through pinholes and spreads out laterally into the interface regions. Donovan (11) has shown, by a nuclear resonance technique, that water is present in the film-substrate interface for discontinuous silicon films but is absent when the film is continuous. His work suggests that the interface layer in this system is at most a few hundred Å thick. In spite of the presence of interface absorption, nearly all thin-film, absorption-coefficient data reported in the literature have been calculated using Eq. (2), since it is a simple and convenient scheme for quickly characterizing coating materials.

A more complete analysis is possible by using a larger set of samples or, more elegantly, a single sample with a wedge-shaped film deposited on the incident face (12). In this technique a simple model of a film is assumed, where the bulk absorption coefficient of the film is constant throughout the thickness of the film and all the interface absorption occurs in infinitesimally thin sheets at the two film boundaries. Then, a minimum of two measurements, using $\lambda/4$ and $3\lambda/4$ OT (or $\lambda/2$ and 1λ OT) films, will give the bulk absorption coefficient of the film without interface absorption present. Two more measurements, one on the bare substrate and one on a $\lambda/2$ (or $3\lambda/4$ OT) coating, can be used to determine the contribution from the film-substrate interface and the air-film interface. This technique will now be described in detail.

WEDGED-FILM LASER CALORIMETRY

Figure 4 shows a sample with a beam normally incident from the left. The time average of the square of the electric field of the beam far from the sample is $< E_o^2 >$. Reflection of the beam from the various film and substrate interfaces causes a redistribution of electric field within the sample. The time average of the square of this field is $< E^2(z) >$, a quantity which varies sinusoidally in the vicinity of sample interfaces. For a sample of total thickness L including any films, Lambert's law can be written to give the absorptance as

$$A = \int_o^L \frac{n(z) < E^2(z) >}{n_o < E_o^2 >} \alpha(z) dz \qquad (3a)$$

$$= \int_o^L p(z)\alpha(z)dz \quad , \qquad (3b)$$

where $\alpha(z)$ and $n(z)$ are the absorption coefficient and the real part of the index of refraction, respectively, of the sample at the position z, and n_o is the index of the material outside the sample, which is normally air. $\alpha(z)$ is related to the extinction coefficient by $\alpha(z) = 4\pi k(z)/\lambda$.

The relative energy density, which contains the incident beam normalization factor, is p(z). The purpose of wedged-film laser calorimetry is to determine $\alpha(z)$ for the film and the film interfaces by using Eq. (3b), which relates the measured absorptance A and the calculable quantity p(z) to the material property $\alpha(z)$. Equation (3a) makes it clear that the contribution which any region in the sample makes to sample heating is proportional to $\alpha(z)$ in that region times the electric-field strength in that same region.

In order to make use of Eq. (3b), one assumes that the bulk absorption coefficient of the film α_f is constant throughout the film and is independent of film thickness. We also assume that all of the air-film interface absorption takes place in a thin sheet of material of absorption coefficient α_{af} and thickness Δ_{af}, and the film-substrate interface absorption takes place in a thin sheet of thickness Δ_{fs}, with absorption coefficient α_{fs}. Then the air-film and film-substrate interface absorption are characterized by the specific absorptances $a_{af} = \alpha_{af}\Delta_{af}$ and $a_{fs} = \alpha_{fs}\Delta_{fs}$. Finally, in calculating p(z), which will be described in the next section, we assume no absorptive attenuation of the illuminating beam in passing through the sample. In samples where $A < 10^{-2}$, this approximation is certainly acceptable. Without this simplification, knowledge of $\alpha(z)$ is necessary to calculate p(z), and the entire problem becomes more difficult.

Under these approximations, the absorptance of a single-layer film on a transparent substrate can be written as (13)

$$A = p_{af}a_{af} + \bar{p}_f\alpha_f\ell_f + p_{fs}a_{fs} + \bar{p}_sA_o \quad , \tag{4}$$

where $\bar{p}_f$ and $\bar{p}_s$ are the spatially averaged relative energy densities within the film and substrate, and A_o is the absorptance measured on the uncoated substrate. p_{af} and p_{fs} are the relative energy density at the air-film and film-substrate interfaces, respectively. As the film thickness is varied, a_{af}, α_f a_{fs}, and A_o

remain constant and A, ℓ_f, p_{af}, $\bar{p}_f$, p_{fs}, and $\bar{p}_s$ change. Of these A, A_o, and ℓ_f are the experimentally measured absorptances and physical film thickness. p_{af}, $\bar{p}_f$, p_{fs}, and $\bar{p}_s$ are calculated quantities. Values of p_{af}, $\bar{p}_f$, p_{fs}, and $\bar{p}_s$ for $\lambda/4$ and $\lambda/2$ thickness films are given in graphical form at the end of this chapter. By measuring the absorptances of an appropriate set of film thicknesses, we obtain a set of linearly independent equations which can be solved for α_f, a_{af}, and a_{fs}, the three coefficients which characterize a single film on a transparent substrate.

In order to use Eq. (4) to determine α_f, the bulk absorption of the film, one measures the absorptance of a pair of film thicknesses which have the same relative power densities at the interfaces, in the bulk of the film, and in the substrate. Such a pair consists of any two films which differ by $\lambda/2$ in optical thickness. Differentiating Eq. (4) and using absorptances from this pair of film thicknesses, we obtain

$$\alpha_f = \frac{(A_{t + \lambda/2} - A_t)}{\bar{p}_f \ell_{\lambda/2}} \quad , \tag{5}$$

where $\bar{p}_f$ is calculated for film thickness t. $\ell_{\lambda/2}$ is the physical thickness of a film of $\lambda/2$ OT. Like Eq. (2), two measurements are required; but in contrast to Eq. (2), this expression accounts for interface absorption and electric-field strength in the film and gives the bulk absorption coefficient of the thin-film coating.

A convenient sample configuration for this measurement is a sample one-half of which has been masked for part of the deposition. In this way, one side of a diameter has a coating of OT t while the other side has a coating of OT $t + \lambda/2$. While any thickness t will suffice, values of $\bar{p}_f$ for the $\lambda/2$-λ pair (or the $\lambda/4$-$3\lambda/4$ pair) are given here. When measuring the absorptances of these two coatings, the beam is aligned slightly off-center so that it passes

through one or the other of the coating halves. The use of one sample eliminates substrate-to-substrate and deposition-to-deposition variations which are present when two substrates and two depositions are needed to obtain the t and t + $\lambda/2$ samples.

With additional measurements on the bare substrate and on a $\lambda/4$ OT film, we can determine a_{af} and a_{fs}. The relative power densities at both interfaces, within the film, and within the substrate all change in going from a $\lambda/4$ OT film to a $\lambda/2$ OT film. This fact is utilized in the determination of a_{af} and a_{fs}. By rewriting Eq. (4) for these two cases (unprimed for $\lambda/2$ OT and primed for $\lambda/4$ OT) with all measured and/or calculated quantities on the right, including α_f which is determined by using Eq. (5), we have

$$a_{af}p_{af} + a_{fs}p_{fs} = [A - \bar{p}_f\alpha_f\ell_f - \bar{p}_sA_o] = [F] \tag{6a}$$

$$a_{af}p'_{af} + a_{fs}p'_{fs} = [A' - \bar{p}'_f\alpha_f\ell'_f - \bar{p}'_sA_o] = [F'] \quad , \tag{6b}$$

which have the solutions

$$a_{af} = \frac{[F]p'_{fs} - [F']p_{fs}}{p_{af}p'_{fs} - p'_{af}p_{fs}} \tag{7a}$$

$$a_{fs} = \frac{[F']p_{af} - [F]p'_{af}}{p_{af}p'_{fs} - p'_{af}p_{fs}} \quad . \tag{7b}$$

Figure 5 shows a convenient sample configuration for making this type of measurement. The maximum film thickness is $\sim 1\lambda$ OT, allowing measurement at the four regions required for obtaining A_o, $A_{1/4}$, $A_{1/2}$, and A_1. A small-diameter laser beam is used with the sample tilted slightly. The required thickness is found by moving the sample until the transmittance minimum or maximum is found. This type of sample is particularly useful when absorptances are to be measured at a variety of wavelengths, since precise $\lambda/4$, $\lambda/2$, and λ OT's can be found

for any wavelength. As in the case where two film thicknesses are present on the same substrate, this type of sample eliminates substrate-to-substrate and deposition-to-deposition variation present when three separate depositions are made to obtain the $\lambda/4$, $\lambda/2$, and λ OT films.

Figure 6, which is an example of this type of measurement (12,14), shows the absorptance measured on the bare CaF_2 substrate (shown at 0.0 film thickness) and at $\lambda/4$, $\lambda/2$, $3\lambda/4$, and λ OT positions of an As_2Se_3 wedged film. Measurements were made at 2.72 and 2.87 μm wavelength using a line-tuned HF CW gas laser. The substrate index is 1.42 and the film index is 2.6, which causes a $\lambda/2$ OT film to be ~ 0.5-μm thick. The values of α_f were calculated from the $\lambda/2$ and λ OT data (solid lines through data). The presence of water in the filmed substrate is evidenced by the higher absorptance as measured at 2.87 μm rather than at 2.72 μm. However, the bulk absorption coefficient of the film is quite low. The analysis of interface absorption indicates that nearly all the absorption is taking place at the film-substrate interface. Analysis of the bare substrate and $\lambda/2$ OT data and Eq. (2) gives a β of 14.60 cm^{-1}, which is ~ 35 times greater than α_f calculated by the wedged-film technique.

ELECTRIC-FIELD CONSIDERATIONS IN LASER CALORIMETRY

The technique and considerations in calculating p(z) for use in Eqs. (7a) and (7b) will now be described. The accurate determination of p(z) must take into consideration (1) the coherent interaction of a single beam with a dielectric interface and (2) the effect of the multiple (but incoherent) bounces the beam undergoes between the two faces of the sample.

A convenient method of making the first calculation was first given by Leurgans (15) and more recently detailed by DeBell (16). As originally described, the technique uses the Smith chart, but it is easily adapted to a computer or

even a hand calculator. Leurgans' method, which we will briefly describe, is restricted to normal-incidence, plane waves and lossless films. While only single films are of concern here, the general multilayer description will be given.

Figure 7 shows the layer-labeling system. The substrate is of index n_o, and the incident medium is of index n_k. The layers are labeled 1 through k-1 and are of physical thickness ℓ_1 to ℓ_{k-1}.

A right-traveling, normally incident plane wave of wavelength λ is represented by $\hat{E}^+ = E^+ e^{i(\omega t - \delta)}$, where $\delta = 2\pi nz/\lambda$. At a dielectric boundary, the partially reflected left-going field is given by

$$\hat{E}^- = E^+ \hat{\rho}\, e^{i(\omega t + \delta)} \quad ,$$

where the reflection coefficient $\hat{\rho}$ is complex. Now, in general,

$$\hat{\rho}(z) = |\hat{\rho}(z)| e^{i(2\delta + \phi)} \quad ,$$

within any given layer. In the lossless case, $|\hat{\rho}(z)|$ is constant within a layer and $\hat{\rho}$ only changes in phase through the layer. To calculate $\hat{\rho}$ across a boundary, we use the boundary condition requiring continuity of E_{tan} and H_{tan}. This is done using the reduced admittance, $\hat{y}(z)$,

$$\hat{y}(z) = \frac{\hat{H}(z)}{n\hat{E}(z)} \quad .$$

The boundary condition then requires that

$$\hat{y}_{i+1}(z_b) n_{i+1} = \hat{y}_i(z_b) n_i \quad ,$$

where z_b is the position of the boundary between the i^{th} and $(i+1)^{th}$ layers. Finally, $\hat{y}(z)$ and $\hat{\rho}(z)$ are related by

$$\hat{\rho}_i(z) = \frac{1 - \hat{y}_i(z)}{1 + \hat{y}_i(z)} \quad ; \quad \hat{y}_i(z) = \frac{1 - \hat{\rho}_i(z)}{1 + \hat{\rho}_i(z)} \quad .$$

These expressions, along with the condition that there is no beam incident on the exit surface from the right, are sufficient to uniquely determine $\hat{\rho}(z)$.

The calculation begins within the substrate and proceeds from right to left. The procedure is:

(1) Realize that $\hat{\rho}_o = 0$ and $\hat{y}_o = 1$.

(2) Use $\hat{y}_1(0) = \hat{y}_o n_o/n_1$ to cross the substrate-film (#1) interface.

(3) Use $\hat{\rho}_1(0) = [1 - \hat{y}_1(0)]/[1 + \hat{y}_1(0)]$ to find $\hat{\rho}_1(0)$.

(4) Use $\hat{\rho}_1(z) = |\hat{\rho}_1(0)|e^{i2\delta}$ to find $\hat{\rho}_1(z)$ in the first film.

(5) Use $\hat{y}_1(z_1) = [1 - \hat{\rho}_1(z_1)]/[1 + \hat{\rho}_1(z_1)]$ and

(6) $\hat{y}_2(z_1) = \hat{y}_1(z_1)n_1/n_2$ to find $\hat{y}_2(z_1)$.

(7) Now proceed as at step (3) above to find $\hat{\rho}_2(z)$, etc. In the work by Leurgans and DeBell, the calculation was used to determine the reflectance R of the stack, which is given by $R = \hat{\rho}_k\hat{\rho}_k^*$.

Having found $\hat{\rho}(z)$ throughout the system by the method of Leurgans, we will now calculate the electric-field strengths throughout the layered system. At any point z in the i^{th} layer, the net field is

$$\hat{E}_i(z) = \hat{E}_i^+(z) + \hat{E}_i^-(z) = [1 + \hat{\rho}_i(z)]\hat{E}^+(z) \quad .$$

The time average of the square of the field is given by

$$< E^2(z) > = \frac{1}{T}\int_o^T \frac{[\hat{E}_i(z) + \hat{E}_i^*(z)]^2}{2}\, dt = \frac{E_{imax}^{+2}}{2}[1 + \hat{\rho}_i(z)][1 + \hat{\rho}_i^*(z)] \quad ,$$

or, finally,

$$< E_i^2(z) > = < E_i^{+2} > [1 + \hat{\rho}_i(z)][1 + \hat{\rho}_i^*(z)] \quad . \qquad (8)$$

While $< E^2(z) >$ in general varies throughout a layer, $< E_i^{+2} >$ is constant in any given layer. Using the continuity of E_{tan} across a boundary, we derive the recursion relation

$$< E_i^{+2} > = < E_{i+1}^{+2} > \frac{[1 + \hat{\rho}_{i+1}(z_{i+1})][1 + \hat{\rho}_{i+1}^*(z_{i+1})]}{[1 + \hat{\rho}_i(z_{i+1})][1 + \hat{\rho}_i^*(z_{i+1})]} \quad , \qquad (9)$$

where the numerator is evaluated just to the left of the $(i+1)^{th}$ boundary and the denominator just to the right of it. Knowing ρ and using the recursion relation, we can now determine the electric-field distribution throughout the system.

The starting point in calculating the set of $< E_i^{+2} >$ is within the incident medium where the right-traveling field is $< E_k^{+2} >$, a known quantity. Equation (9) is used to find $< E_i^{+2} >$ for successive layers to the right of the incident medium. Equation (8) is used to determine $< E_i^2(z) >$. Finally, the relative energy density is

$$p_i(z) = \frac{n_i < E_i^2(z) >}{n_k < E_k^{+2} >} \quad .$$

This value does not take into account the multiple bounces which the beam undergoes between the two faces of the sample; this will be done next.

Figure 8 shows the right- and left-going beams within and to the right of the substrate. These are expressed in terms of the incident field $< E_{inc}^2 >$ and the first and second surface reflectance and transmittance of the coated sample, R_1, R_2 and T_1, T_2 (calculable from Leurgans' method); n_s is the substrate index.

When using Eq. (3), we must include the contribution of the field of each of the individual beams in Fig. 8. Since there is no beam overlap and therefore no interference, this can be done by adding all of the right-going beams to form an effective right-going beam and all the left-going beams to form an effective left-going beam. These values are

$$< E_R^2 > = \frac{< E_{inc}^2 > T_1}{n_s(1 - R_1R_2)} \tag{10a}$$

$$< E_L^2 > = \frac{< E_{inc}^2 > T_1R_2}{n_s(1 - R_1R_2)} \quad . \tag{10b}$$

To calculate p(z) in the region near the exit surface of the sample, the right-going field $< E_R^2 >$ is used as the starting value in the recursion relation Eq. (9). This and Eq. (8) are used to calculate $< E^2(z) >$. The average value of $< E^2 >$ within the substrate is the sum of Eqs. (10a) and (10b):

$$< E_{subst}^2 > = \frac{< E_{inc}^2 > T_1(1 + R_1)}{n_s(1 - R_1R_2)} \quad . \tag{11}$$

To calculate p(z) in the region near the entrance surface, we add the field resulting from the incident beam $< E_{inc}^2 >$ to the field resulting from the left-going beam $< E_L^2 >$. This is done since, while the transmittance of a lossless filmed surface is the same when illuminated from either side, the electric-field distribution is not. This is illustrated in Fig. 9, where the values of $< E(z)^2 > / < E_{inc}^2 >$ (solid lines) and p(z) (dashed lines) are shown for a single layer of material of index 3.0 and $\lambda/4$ OT is deposited on the exit surface of a substrate of index 1.5. A film of this thickness and index has a high reflectance and accentuates the various effects just described. The line labeled 1 is the value of $< E^2(z) > / < E_{inc}^2 >$ resulting from the incident beam encountering the entrance surface of the substrate. Lines 2 and 3 are the net right- and left-traveling beams $< E_R^2 > / < E_{inc}^2 >$ and $< E_L^2 > / < E_{inc}^2 >$, respectively. Line 4 is the value of $< E^2(z) > / < E_{inc}^2 >$ in the vicinity of the exit surface of the substrate. Line 5 is the value of $< E^2(z) > / < E_{inc}^2 >$ near the entrance surface due to the left-traveling beam. The total relative field intensity near the entrance surface is the sum of lines 1 and 5, and the total within the bulk is the sum of lines 2 and 3. The values of p(z) are then these sums multiplied by n_s/n_o. It is this

value of p(z), which includes all substrate multibounce effects, that is to be used in Eq. (3).

ENTRANCE VS EXIT SURFACE FILMS

Figure 10 shows the value of $< E^2 > / < E_{inc}^2 >$ at the entrance surface of the substrate, within the bulk of the substrate, at the film-substrate interface, the average value within the film, and at the air-film interface for an exit surface film, all as functions of film thickness. This graph shows how the fields gradually change with changing film thickness, causing each region in the system to contribute a different proportion to the measured absorptance as the film thickness changes.

The three significant regions of the substrate are the central or bulk region and the two interfaces, shown as regions 4, 5, and 3, respectively, in Fig. 10. Also in Fig. 10 we see that these three quantities change relative to each other as film thickness changes. For example, a $\lambda/2$ OT film causes nearly equal weighting, while a $\lambda/4$ OT film accentuates the incident surface and the bulk over the exit surface. Without knowing the values of $\alpha(z)$ throughout the substrate and in particular at the interfaces, it is not possible to properly account for the substrate contribution for an exit surface film.

Figure 11 is similar to Fig. 10, except now the film is on the entrance surface. In this case, $< E^2 > / < E_{inc}^2 >$ for the two interfaces and in the bulk of the substrate (i.e., at 3, 5, and 4) maintain a nearly constant ratio to each other for all film thicknesses. A careful inspection shows that the ratio between the bulk and the exit surface values of p is identically constant and that the ratio between the bulk and the film-substrate interface value of p is constant to within $\sim$ 2% over the thickness range shown. This is an important advantage in analysis, since now the substrate can be treated as a single entity whose contribution is directly proportional to the transmittance of the entrance surface of

the sample. We do not need prior knowledge of $\alpha(z)$ for the substrate as we would in the exit surface analysis. It is this property of entrance surface films which permits us to account for the substrate contribution with the single term $\bar{p}_s A_o$ in Eq. (4).

EXPERIMENTAL DETERMINATION OF α_f, a_{af}, AND a_{fs}

Several values of relative energy density ρ are needed in the analysis of two-thickness films using Eq. (5) or of wedge-shaped films using Eqs. (7a) and (7b). In Figs. 12-17 are shown plots of relative energy densities for substrates illuminated at normal incidence from the film side for $\lambda/4$ and $\lambda/2$ OT films. These calculations include substrate multibounce effects. All the figures are families of curves for substrates ranging in index from 1.0 to 4.0 by steps of 0.2. The film index also ranges from 1.0 to 4.0 and is given as the abscissa. The corresponding relative energy density is shown as the ordinate.

Figure 12 uses Eq. (11) and shows $\bar{p}_s$, the average substrate relative power density for $\lambda/4$ OT film. The value of $\bar{p}_s$ for $3\lambda/4$, $5\lambda/4$, ... OT films are identical to that for the $\lambda/4$ OT film. The value of $\bar{p}_s$ for a bare substrate and for $\lambda/2$, λ, ... OT films are identically 1.0 for all film and substrate indices and are not shown graphically.

Figures 13-15 show p_{af}, $\bar{p}_f$, and p_{fs}, the air film, average in the film, and film-substrate relative power density for a $\lambda/4$ OT film. As above, these same values apply to a $3\lambda/4$, $5\lambda/4$, etc. OT film. Figure 16 shows p_{af} and p_{fs} for films of $\lambda/2$, λ, ... thickness. Figure 17 shows $\bar{p}_f$ for $\lambda/2$, λ, ... OT films.

In evaluating a sample, the values of p_{af}, $\bar{p}_f$, p_{fs}, and $\bar{p}_s$ for the applicable substrate and film index are extracted from Figs. 12-17. If only the bulk absorption coefficient of the film is to be determined, then the absorptance for $\lambda/2$

and 1λ films are measured calorimetrically, and Eq. (5) is used, along with the value of $\bar{p}_f$ from Fig. 17, to find α_f.

If the interface absorptances are to be determined, then the absorptance of the bare substrate and a λ/4 OT film must be measured, in addition to the λ/2 and 1λ OT films. The values of p_{af}, $\bar{p}_f$, p_{fs}, and $\bar{p}_s$ for λ/4, λ/2, and λ OT films are taken from Figs. 12-17. Then, Eqs. (7a) and (7b) are used to determine a_{af} and a_{fs}.

REFERENCES

1. L. Skolnik, in Optical Properties of Highly Transparent Solids, edited by S. S. Mitra and B. Bendow (Plenum, New York, 1975), pp. 405-533.
2. A. Hordvik, Appl. Opt. 16, 2827 (1977).
3. L. W. Bos and D. W. Lynch, Phys. Rev. B 2, 4567 (1970).
4. D. A. Pinnow and T. C. Rich, Appl. Opt. 12, 984 (1973).
5. T. H. Allen, J. H. Apfel, and C. K. Carniglia, in Laser Induced Damage in in Optical Materials: 1978, edited by A. J. Glass and A. H. Guenther (NBS, Washington, DC, 1978), NBS Spec. Publ. 541, pp. 33-36.
6. M. J. Hass, J. W. Davisson, P. H. Klein, and L. L. Boyer, J. Appl. Phys. 45, 3959 (1974).
7. D. L. Decker and P. A. Temple, in Laser Induced Damage in Optical Materials: 1977, edited by A. J. Glass and A. H. Guenther (NBS, Washington, DC, 1977), NBS Spec. Publ. 509, pp. 281-285.
8. P. A. Temple, in Optical Thin Films (SPIE Vol. 325, Bellingham, WA, 1982), pp. 156-162.
9. E. Bernal G., Appl. Opt. 14, 314 (1975).
10. H. A. Macleod and D. Richmond, Thin Solid Films 37, 163 (1976).
11. T. M. Donovan, P. A. Temple, Shiu-Chin Wu, and T. A. Tombrello, in Laser Induced Damage in Optical Materials: 1979, edited by H. E. Bennett, A. J. Glass, A. H. Guenther, and B. E. Newnam (NBS, Washington, DC 1980), NBS Spec. Publ. 568, pp. 237-246.
12. P. A. Temple, Appl. Phys. Lett. 34, 677 (1979).
13. The last term in this expression has a further approximation which is discussed in the section on entrance vs exit surface films.

14. P. A. Temple, D. L. Decker, T. M. Donovan, and J. W. Bethke, in Laser Induced Damage in Optical Materials: 1978, edited by A. J. Glass and A. H. Guenther (NBS, Washington, DC, 1978), pp. 37-42.

15. P. J. Leurgans, J. Opt. Soc. Am. 41, 714 (1951).

16. G. W. DeBell, in Optical Coatings II (SPIE Vol. 140, Bellingham, WA, 1978), pp. 2-15.

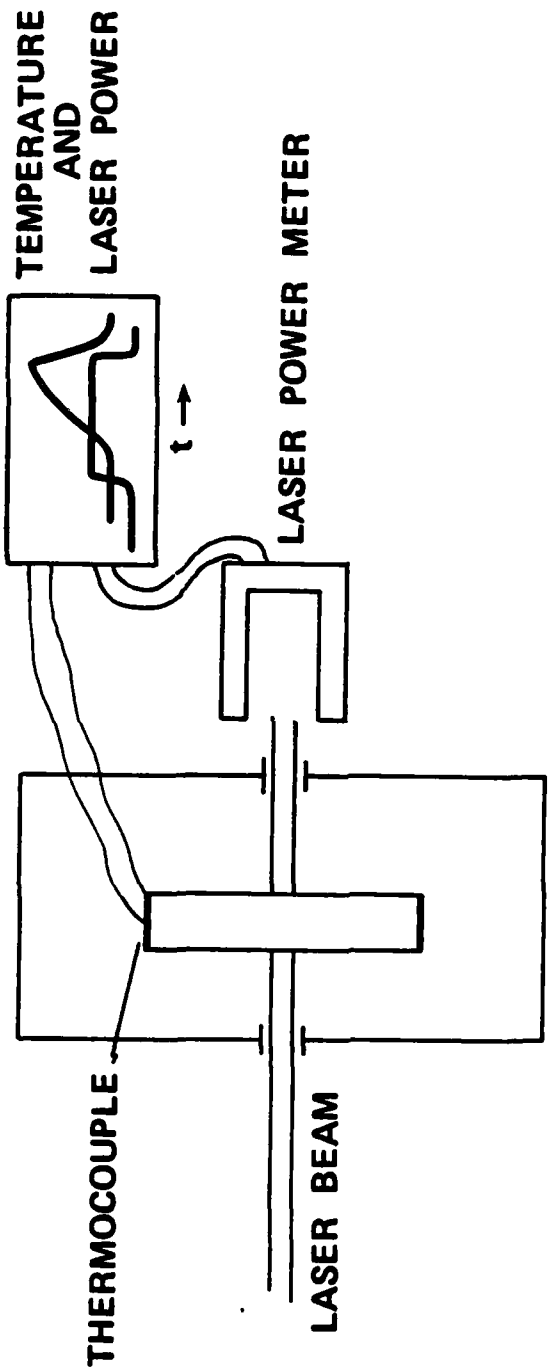

FIG. 1. Typical laser rate calorimeter.

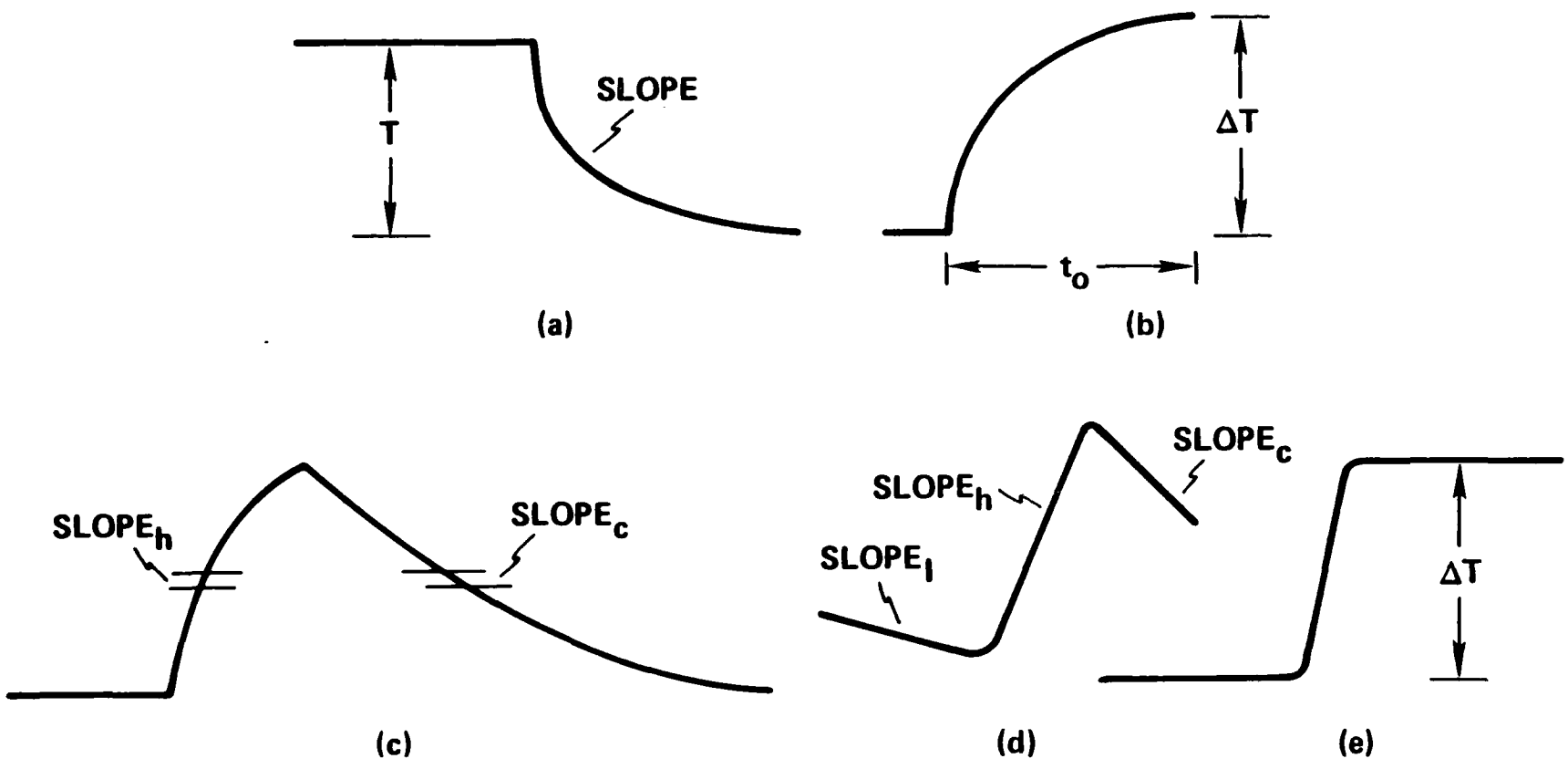

FIG. 2. Sample temperature as a function of time for five temperature-vs-time analysis schemes. The techniques are discussed in the text.

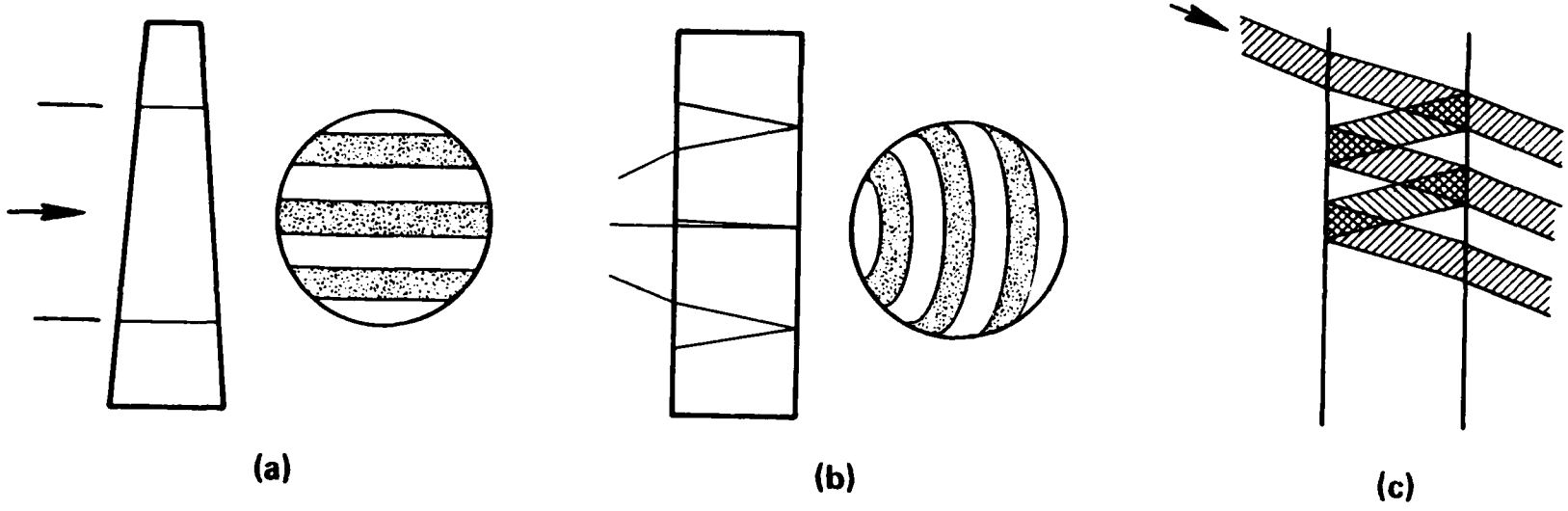

FIG. 3. Three techniques for defeating laser coherence effects in a substrate. (a) Wedged substrate and a large parallel beam, (b) plane parallel substrate and divergent beam, tilted sample shown, (c) plane parallel sample using small beam at nonnormal angle of incidence to avoid overlap.

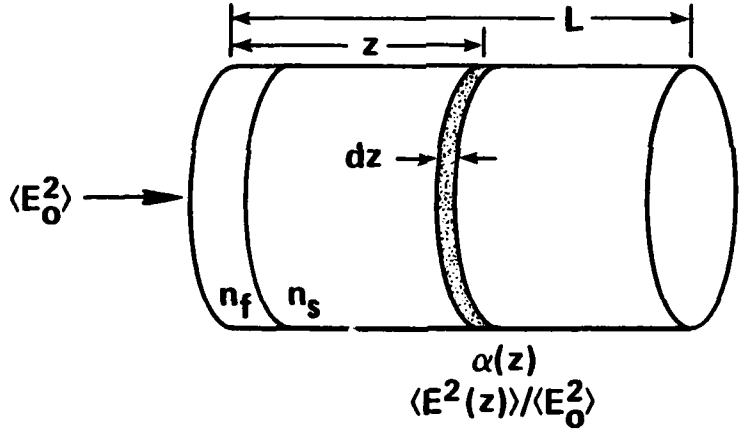

FIG. 4. Configuration for calculating the absorptance of a sample as per Eq. (3).

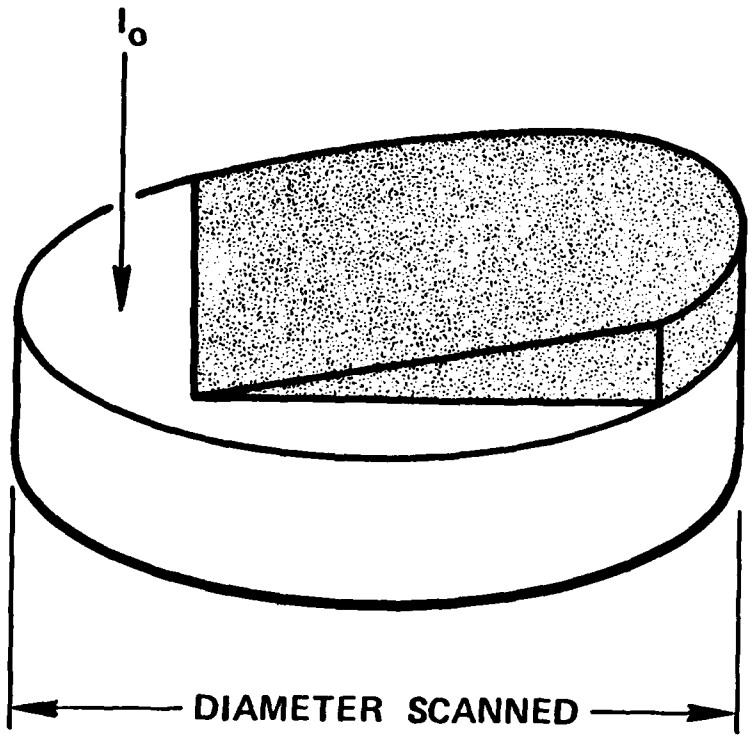

FIG. 5. Wedged-film sample used to obtain film bulk and interface absorption for single-layer films. The film varies from zero to $\sim 1\lambda$ OT.

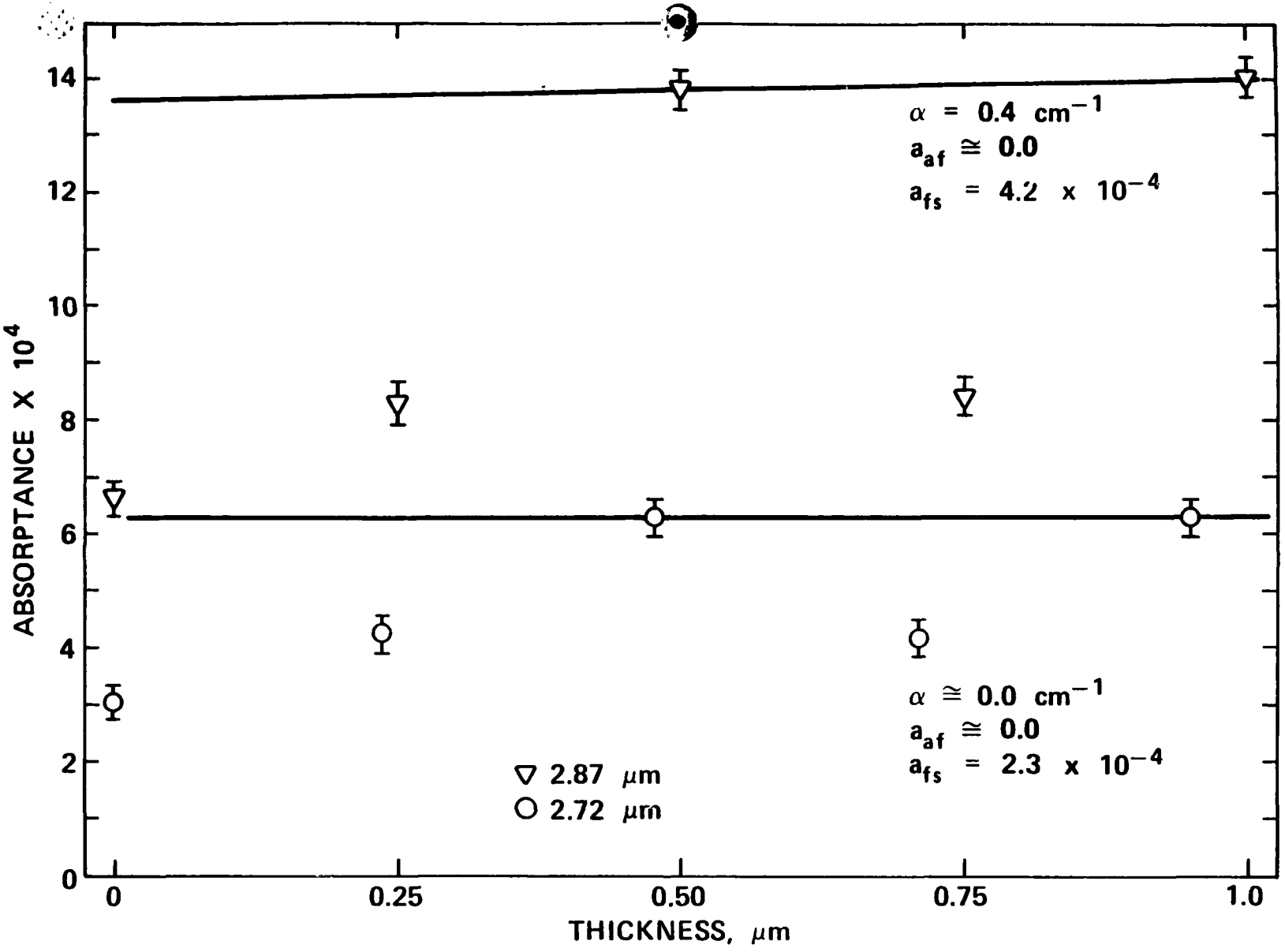

FIG. 6. The absorptance of an entrance surface film on As_2Se_3 on a CaF_2 substrate measured at two wavelengths and at λ/4, λ/2, 3λ/4, and λ OT. The two data points at 0.0 μm thickness are bare substrate absorptances A_o. The two lines have been drawn through λ/2 and λ OT data points. The λ/4 and 3λ/4 data points have lower absorptances because of reduced p_{fs} for these thicknesses.

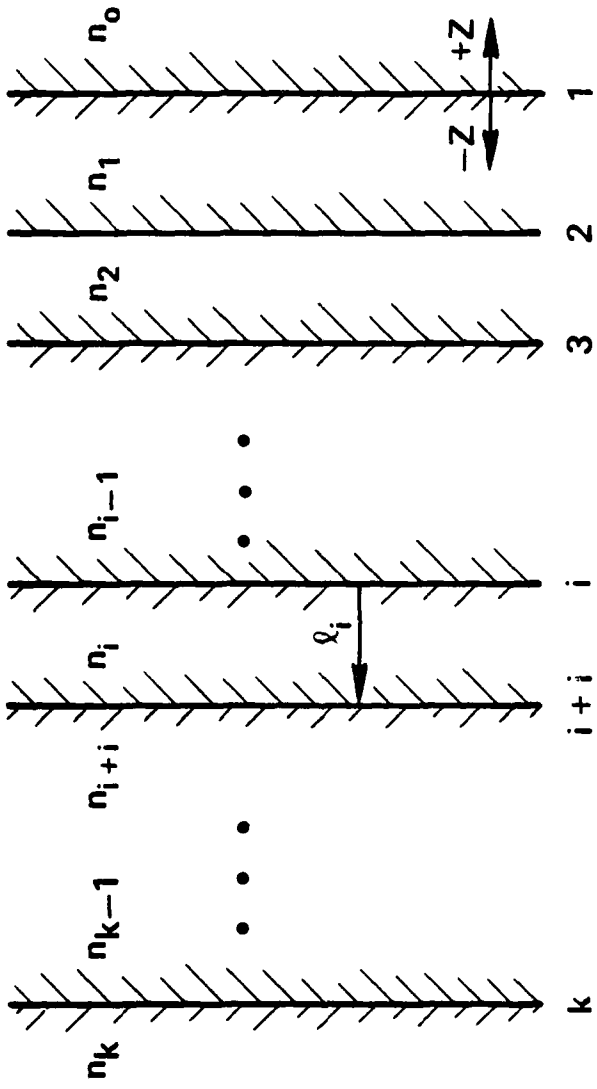

FIG. 7. The layer-labeling system for a thin-film stack.

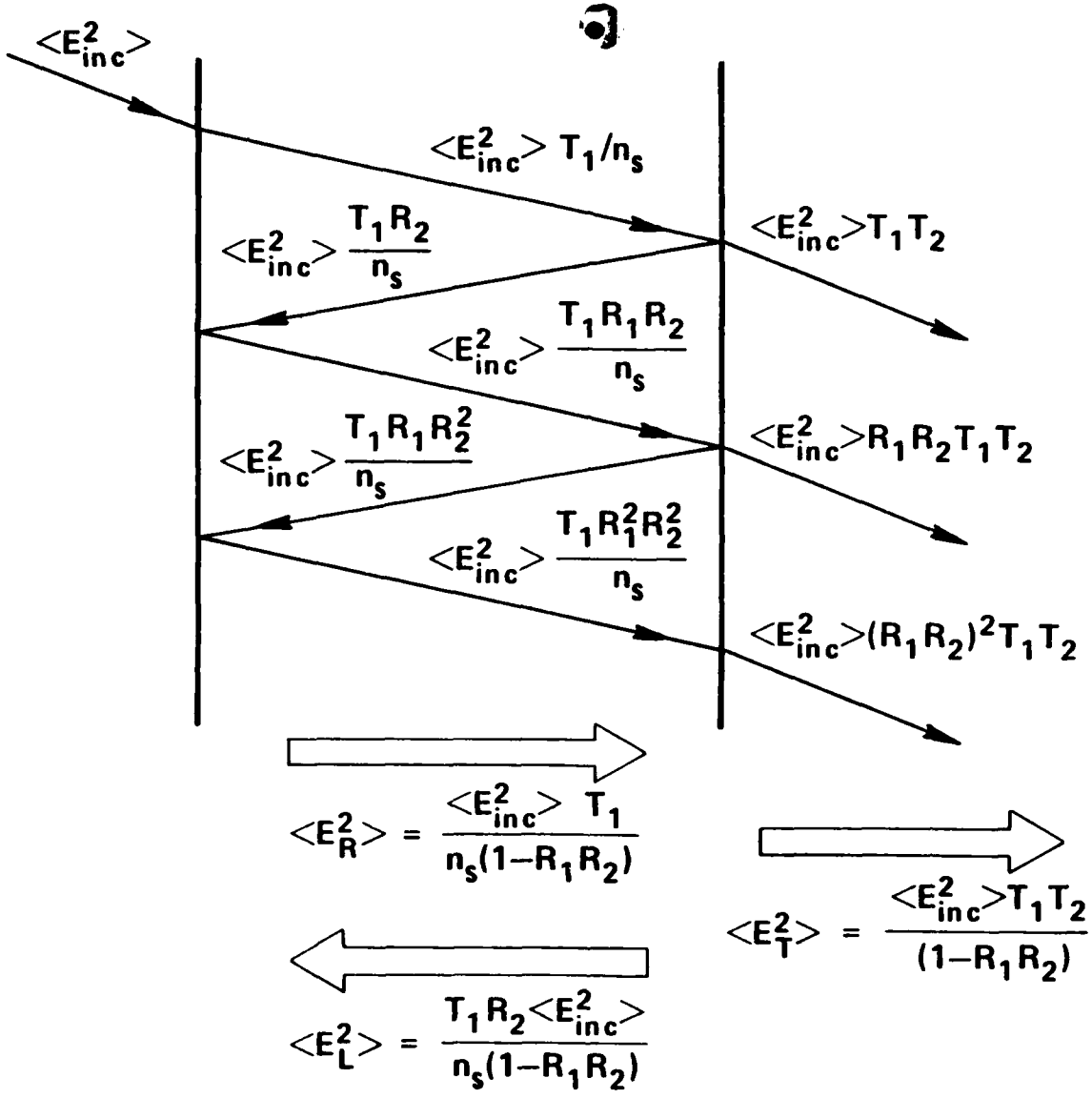

FIG. 8. The electric field intensities within a substrate for multiple bounces of nonoverlapping beams. The entrance surface has reflectance R_1 and the exit surface R_2. Assumed are $T_1 = 1 - R_1$ and $T_2 = 1 - R_2$.

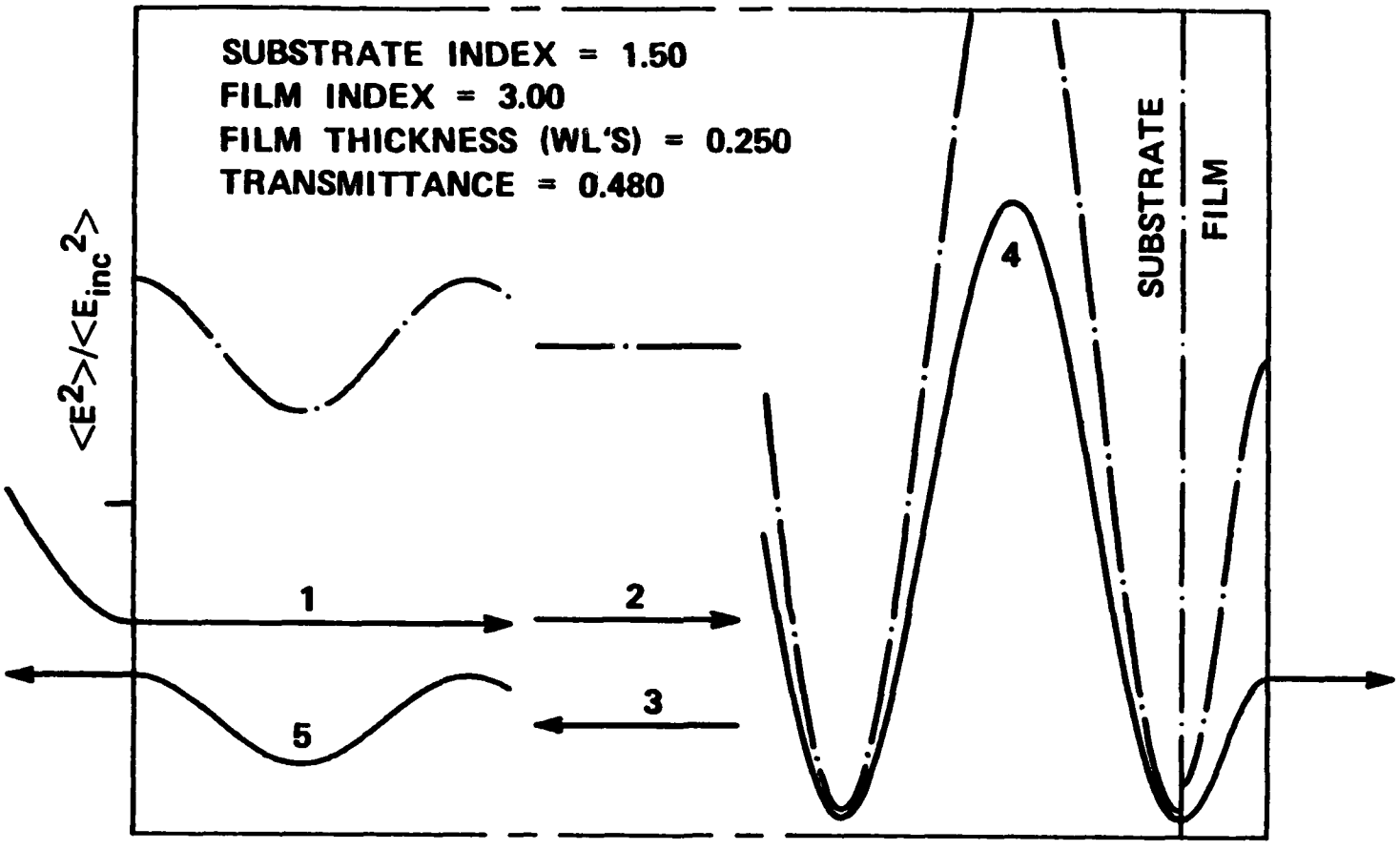

FIG. 9. The relative electric field intensity (solid) and relative energy density (dashed) for a $\lambda/4$ exit surface film. Line 1 is the incident beam, $< E_{inc}^2 > T_1/n_s$, while lines 2 and 3 are $< E_R^2 >$ and $< E_L^2 >$, all shown in Fig. 8. Line 4 is the coherent combination of 2 and 3 near the exit surface where the beams overlap; 5 is the coherent combination of 2 and 3 less 1 near the entrance surface. The dashed lines are n_s/n_o times 1 plus 5, 2 plus 3, and 4 at the entrance surface, in the central region, and near the exit surface, respectively.

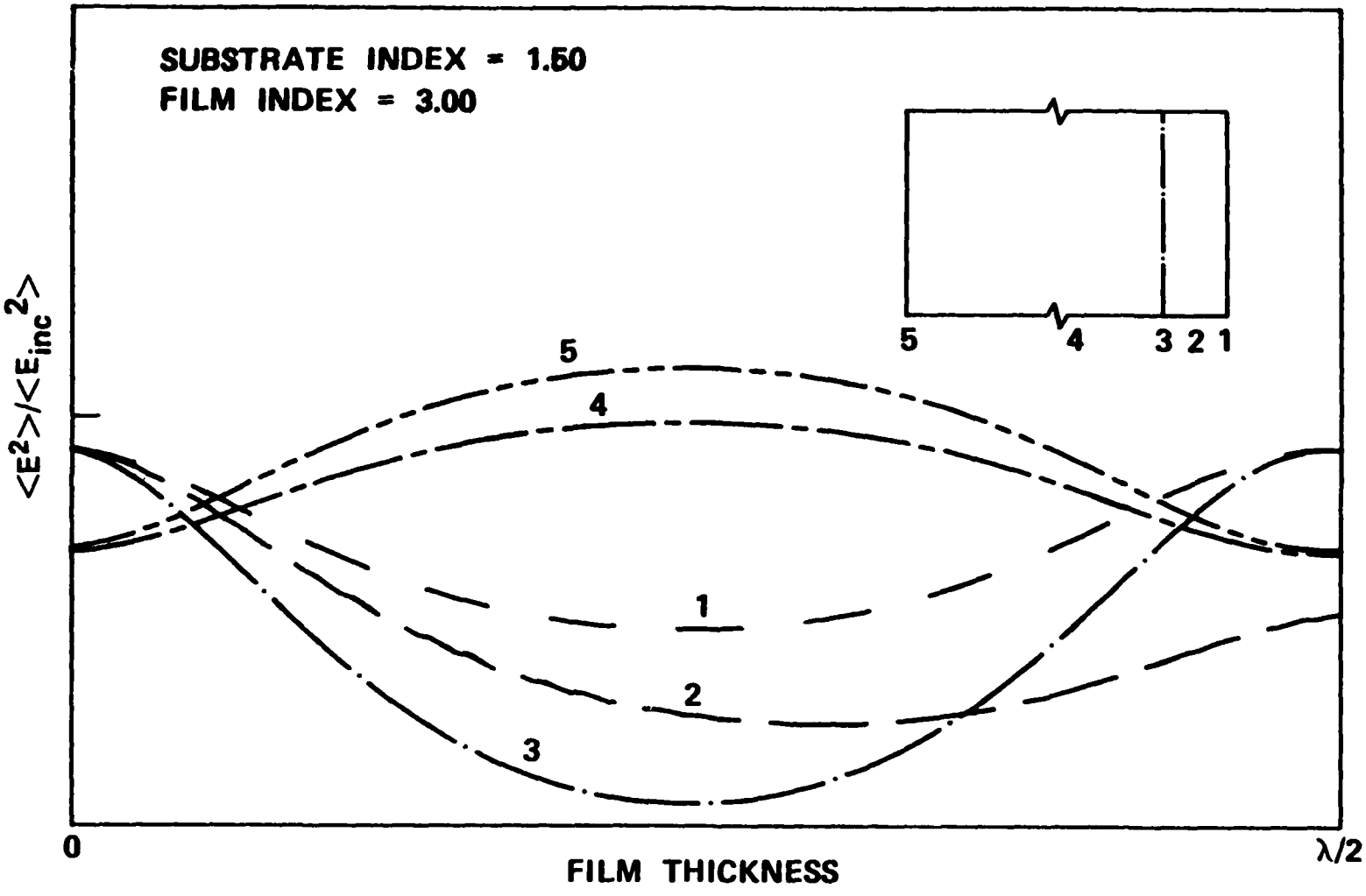

FIG. 10. The value of $< E^2 > / < E_{inc}^2 >$ for five regions in a single-layer exit surface film. The film thickness varies from zero to λ/2 OT.

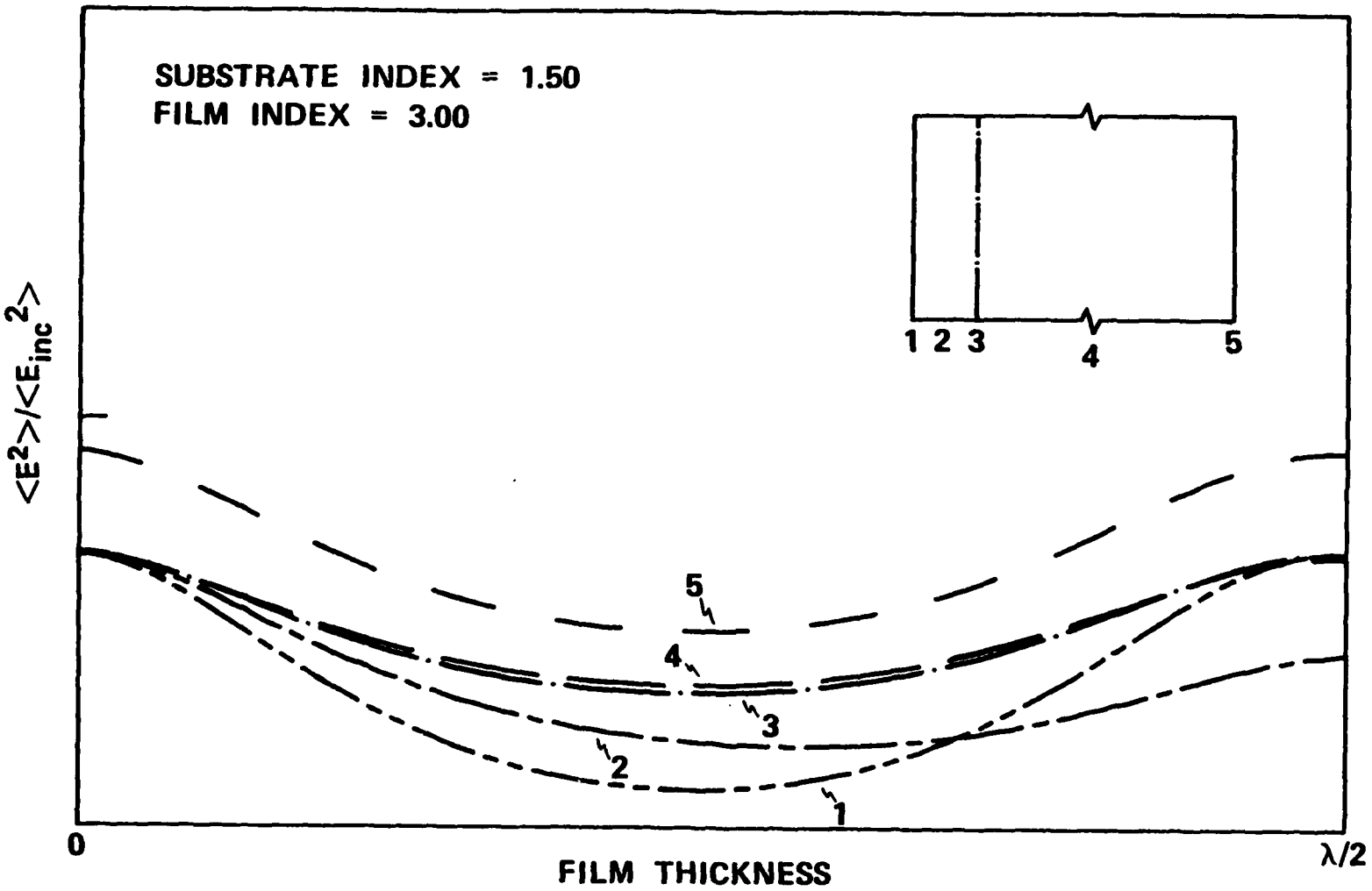

FIG. 11. The value of $< E^2 > / < E_{inc}^2 >$ for five regions in a single-layer entrance surface film. The film thickness varies from zero to $\lambda/2$ OT.

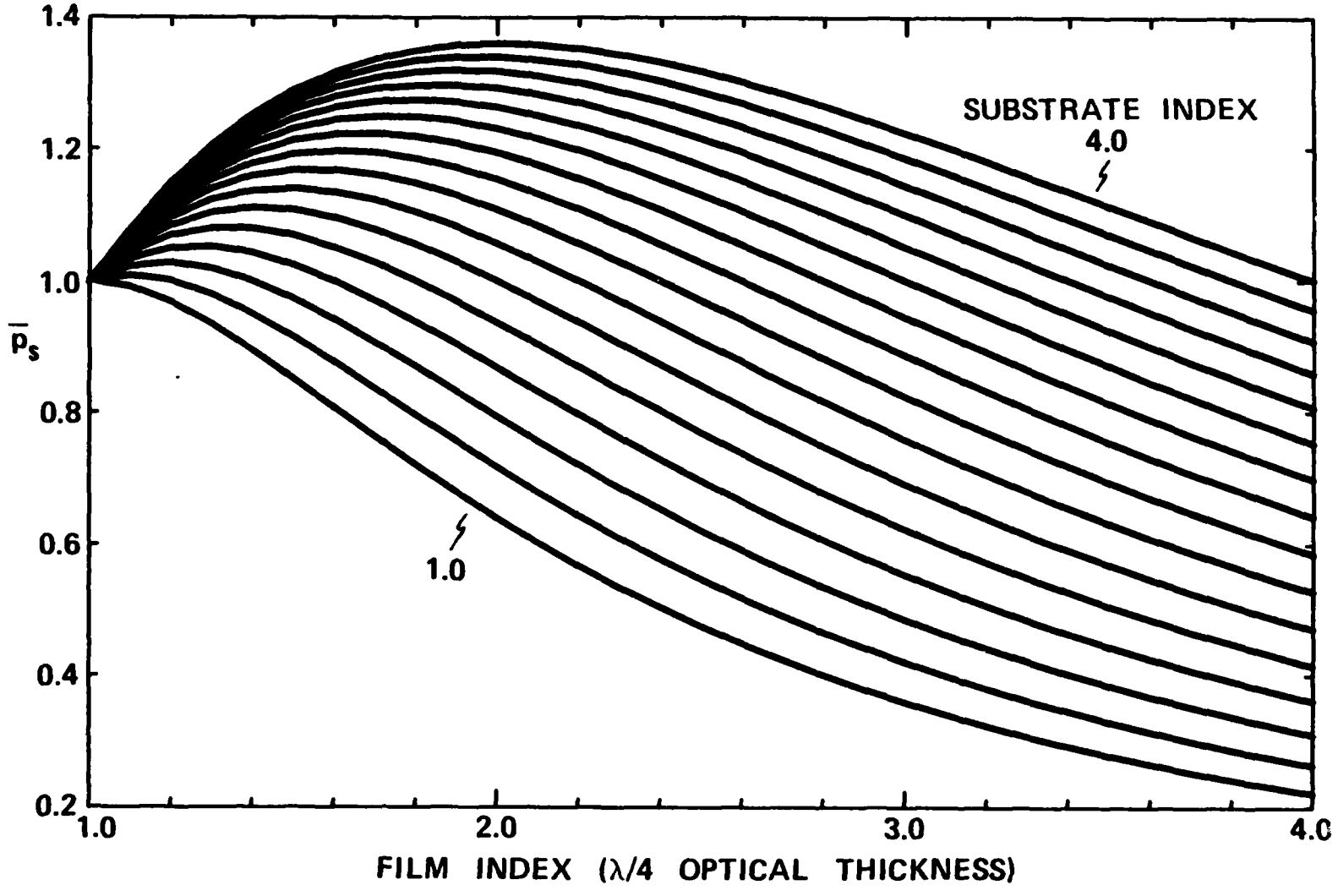

FIG. 12. The average relative energy density $\bar{p}_s$ within the bulk of a substrate with a $\lambda/4$, $3\lambda/4$, ... film on the entrance surface.

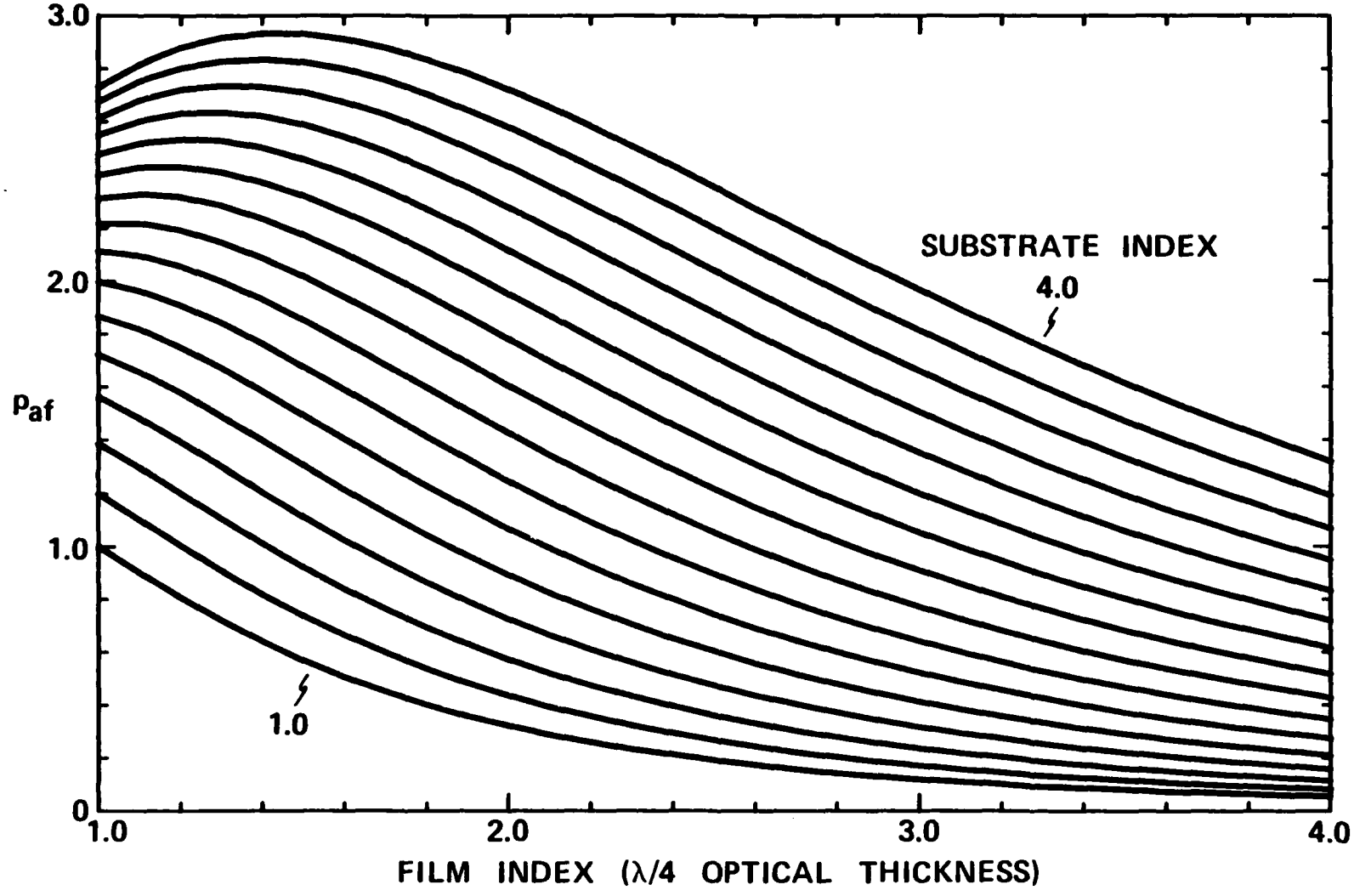

FIG. 13. The relative energy density p_{af} at the air-film interface for an entrance surface film of $\lambda/4$, $3\lambda/4$, ... OT.

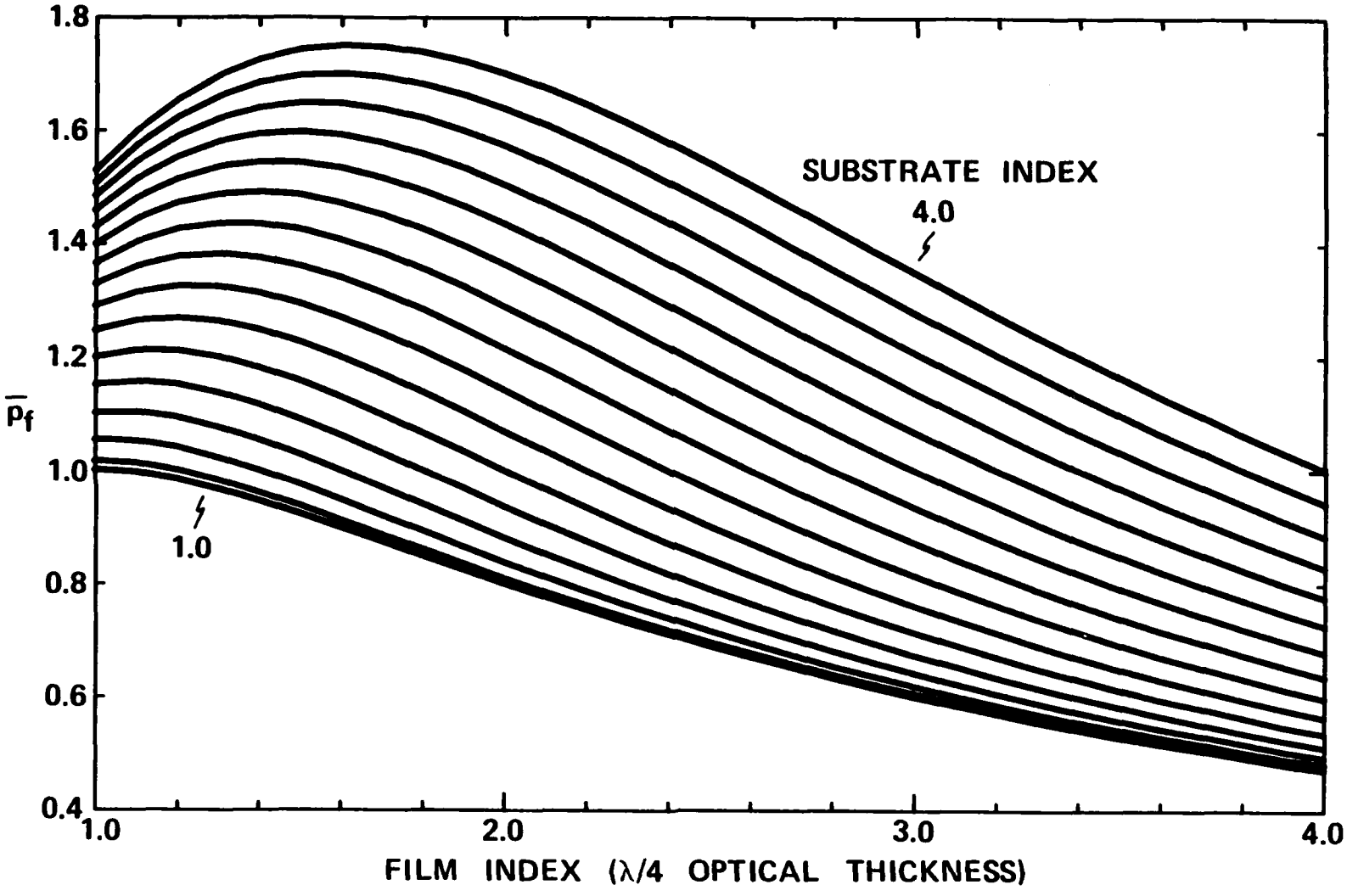

FIG. 14. The average relative energy density $\bar{p}_f$ within the bulk of an entrance surface film of λ/4, 3λ/4, ... OT.

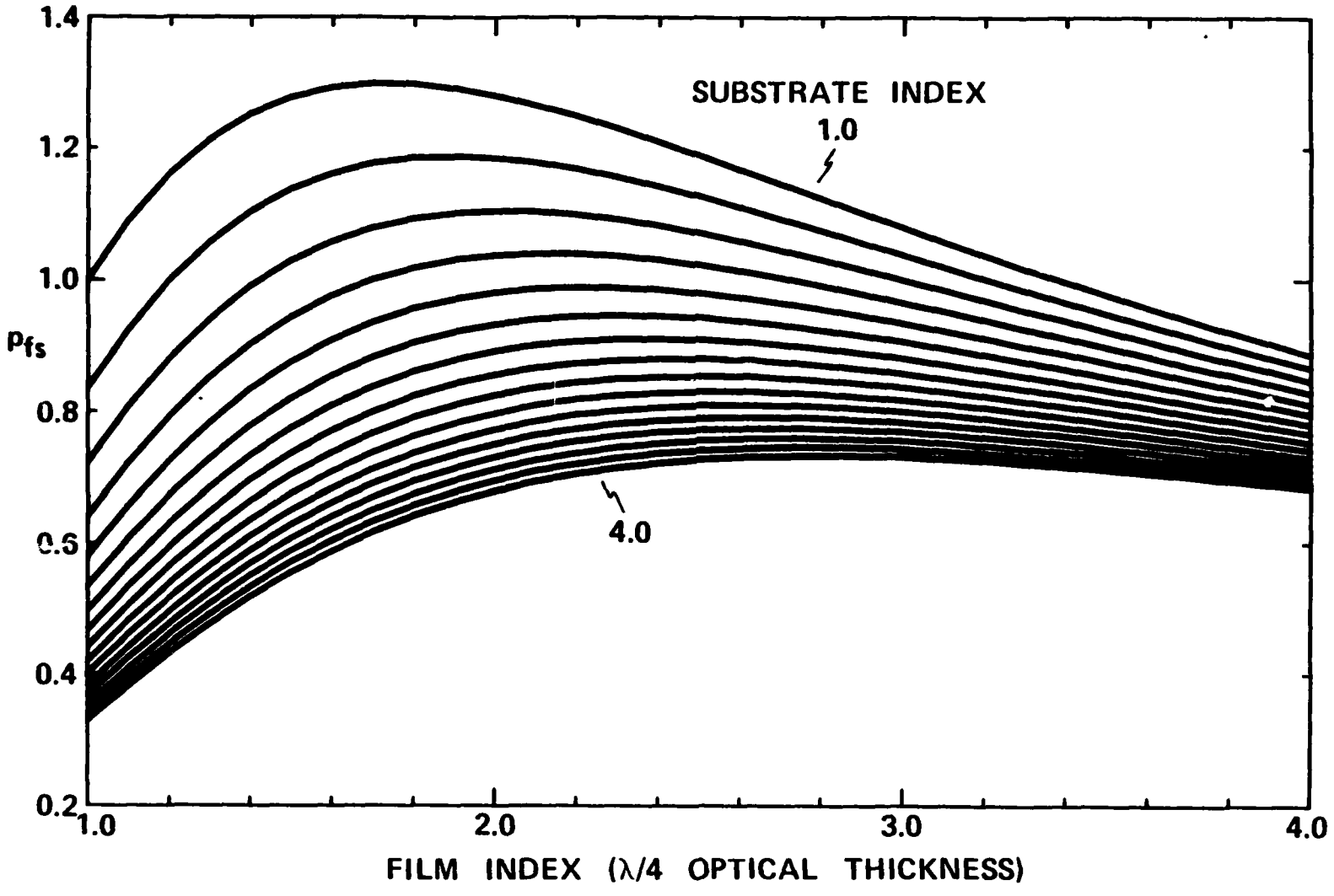

FIG. 15. The relative energy density p_{fs} at the film-substrate interface for an entrance surface film of $\lambda/4$, $3\lambda/4$, ... OT.

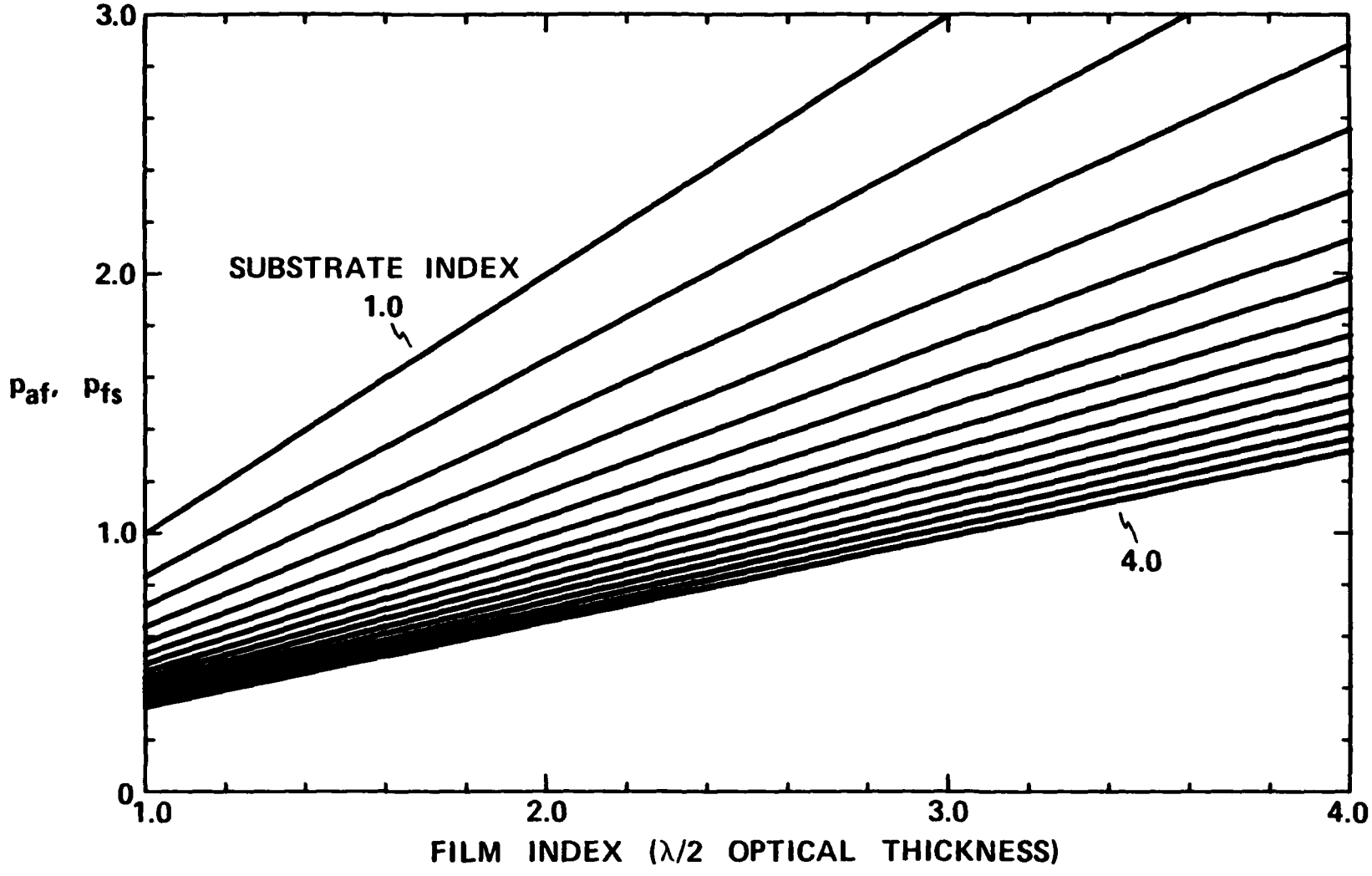

FIG. 16. The relative energy density at the air-film p_{af} and the film-substrate p_{fs} interface for an entrance surface film of $\lambda/2$, λ, ... OT.

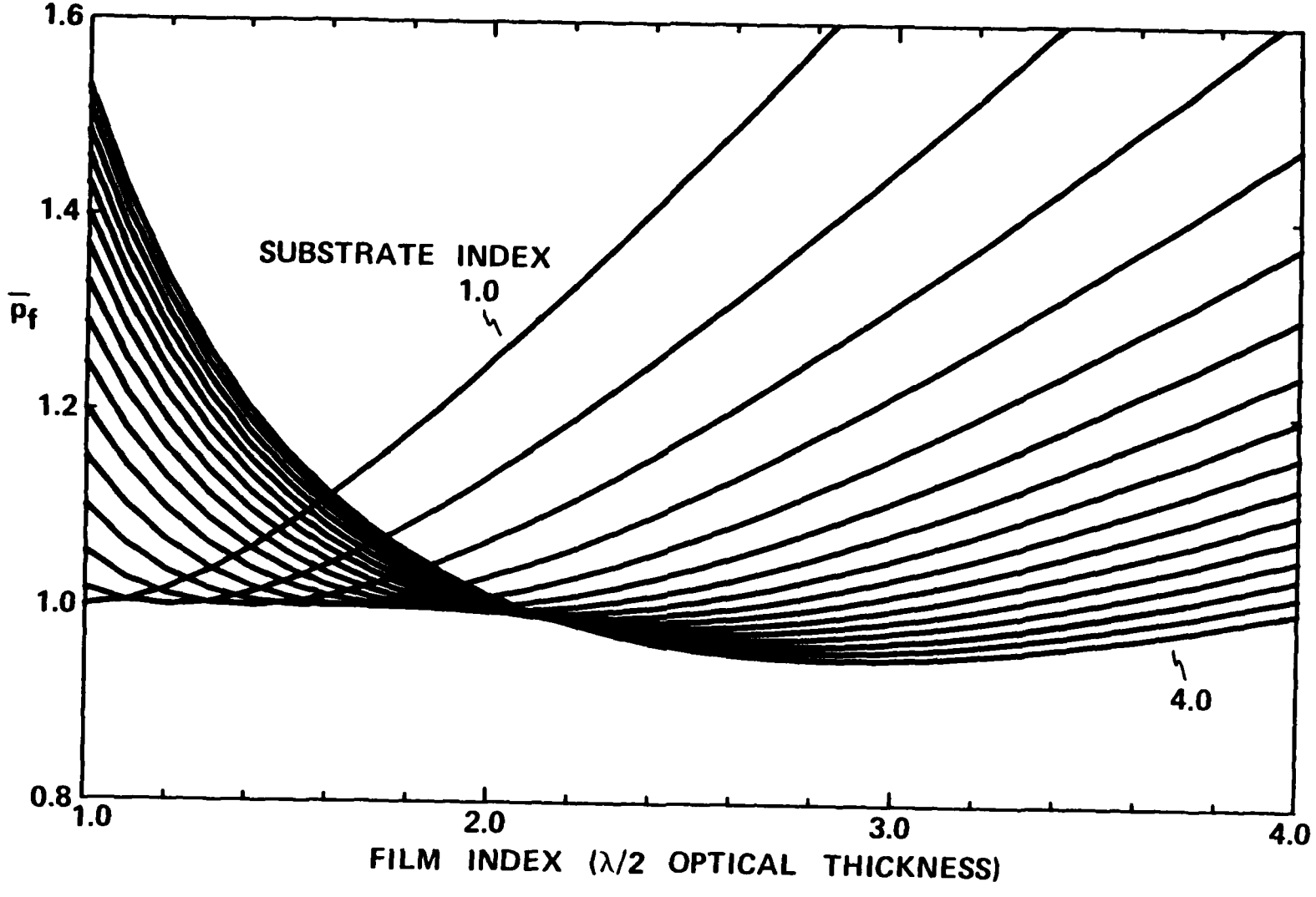

FIG. 17. The average relative energy density $\bar{p}_f$ within the bulk of an entrance surface film of $\lambda/2$, λ, ... OT.

Chapter 10

Replication Technique for Determining the Microroughness of Large or Unusually Shaped Optics

D. L. Gourley and H. E. Gourley

System Sciences Group
389 San Benito Way
San Franaisco , CA 94127

J. M. Bennett

Michelson Laboratory, Physics Division
Naval Weapons Center
China Lake, CA 93555

Replication technique for determining the microroughness of large or unusually shaped optics

Darrell L. Gourley and Helen E. Gourley

System Sciences Group, 389 San Benito Way, San Francisco, California 94127

Jean M. Bennett

Michelson Laboratory, Physics Division, Naval Weapons Center, China Lake, California 93555

(Received

A two-stage replication technique has been developed that will enable microroughness measurements to be made on large or unusually shaped optics that cannot be measured using existing techniques. A small, first-stage replica of room-temperature-vulcanizing (RTV) silicone rubber is made of one or more parts of the surface. This material exactly replicates surface details and separates easily from most glass and metal optics. A second-stage epoxy replica is then made from the first-stage replica. It also preserves surface details and can be easily separated from the first-stage replica. The epoxy replica can be aluminized for Nomarski microscope examination, interferometric or scattering measurements, and can also be profiled with a diamond stylus probe. Examples are given of various types of surfaces and their

replicas. Surface profiles are also shown of two masters and their replicas. This two-stage replication technique has been found to give excellent replication of surface detail, along with adequate preservation of surface flatness and a minimum lateral dimensional change, 0.3%. It is thus an excellent method for sampling small surface areas of large optics.

INTRODUCTION

Replication techniques have been used for many years to duplicate optical surfaces or entire optical-mechanical assemblies.[1,2] Some of the first high quality replicas were of large infrared diffraction gratings produced by David Richardson of Bausch and Lomb. The measured resolution of these gratings was somewhat better than that of the originals because roughness in the bottoms of the grating grooves on the master produced by the ruling diamond was transferred to the outer surface on the replica, and the groove bottoms on the replica were smooth. The measured resolution of one of these diffraction gratings exceeded the Rayleigh theoretical limit and approached the more stringent Abbe theoretical value.[3]

The conventional method for making replicas is to coat the master with a thin liquid or water-soluble parting layer and evaporate a thick layer of aluminum (or other reflecting material) onto the master. The master is then removed from the coating chamber and a thin layer of epoxy is added, followed by a backing plate of nearly the same shape as the master. The thickness of the epoxy layer is kept small to minimize dimensional changes that might occur during curing of the epoxy. After the epoxy has completely cured, the replica is separated from the master at the parting layer, hopefully not damaging the master, and the residue from the parting layer is removed.

The process described above requires that the master be placed in a vacuum chamber so that the parting layer and the aluminum coating that will form the reflecting surface for the replica can be applied. In the present application we desired a method for replicating the microroughness of small portions of optics that were too large to fit into normal size vacuum chambers. Also, replicas of only small, selected portions of the surface were needed, so that it was not necessary to replicate the entire surface.

Previously, plastic tapes and/or liquids such as collodion have been used to replicate small areas of large optics. The tapes are pressed onto the surface or moistened with a softening agent and laid on the surface (to more readily duplicate surface detail). After drying, the tapes are stripped from the master and fastened down on microscope slides, put into a vacuum chamber, and silvered or aluminized. The resulting high reflecting replicas of the surface do indeed contain the microroughness surface details, but also artifacts — bubbles, cracks, and, most objectionable, they become badly curled and wrinkled making it very difficult to observe surface detail using an interferometer, Nomarski microscope, or scattered light measuring instrument. Furthermore, the replica cannot be profiled with a diamond stylus because the softness of the film amplifies oscillations in the electromechanical stylus pickup and creates an unacceptable instrumental noise level.

For these reasons we wanted to try another approach to produce a replica that (a) would faithfully duplicate the surface microroughness of the master, (b) did not introduce additional artifacts to be confused with the surface microroughness, (c) could be aluminized for scattered light measurements and inspection under the Nomarski microscope, and (d) could be profiled using a diamond stylus probe and very light loading. Furthermore, it was desirable to

preserve the shape of the master sufficiently so that the above-mentioned measurements could be made without tedious realignment of the sample. Of course, the master should not be damaged in any way during the replication process.

Based on the first author's extensive experience in making conventional replicas, several approaches to the problem were considered and various processes were tried. Without recounting the methods that did not work, we will only mention one method which proved quite satisfactory. We will first describe the replication method, then show Nomarski micrographs of the surfaces of several masters and their replicas, and finally give the results of surface profile measurements on the masters and replicas.

METHOD FOR MAKING REPLICAS

As with any type of replication process, it is very important to clean the surface of the master thoroughly and perform the entire replication process in a dust-free environment. Any dust, particulate matter, residual stains, or water marks will replicate just as well as the surface microroughness.

In order to ensure that the replica could be separated nondestructively from the master, it was decided to use a room-temperature-vulcanizing (RTV) silicone rubber as a first-stage replica. The rubber was poured directly onto the surface of the master without using a parting agent, and allowed to cure. It could then be easily peeled off without causing damage to the master. However, a very thin contamination layer remained which could be easily removed by standard cleaning procedures. Unfortunately, the silicone rubber was too soft for surface profiling, and aluminum vacuum evaporated onto the rubber surface crazed badly, producing a nonspecular finish. Therefore, a second-

stage replica was made of the silicone rubber replica using high temperature curing epoxy. After this second replica had cured, it could be easily separated from the silicone rubber. It was then aluminized for comparison of the surface microroughness with that of the master. The epoxy replica was also sufficiently hard that surface profiling was possible, although with not quite the height sensitivity that was possible with harder substrate materials.

For these tests, small-diameter masters were used so that the masters and replicas were the same size, approximately 1.5 inches in diameter. The low reflectance glass masters were also subsequently aluminized so that their surface details would be easier to see.

Relatively little attention was paid to preserving the surface flatness of the masters on the replicas. The silicone rubber first-stage replicas were formed in retaining plastic cups, or else simply poured onto the surface of the master, with a tape dam around the edge to contain the rubber. The epoxy for the second-stage replica was similarly contained. Also, the thicknesses of the replicas was large, 1 cm, so any shrinkage upon cooling would be enhanced. As a result, the second-stage replicas were many fringes convex. However, their flatness was adequate for Nomarski examination and surface profiling. If desirable, the flatness of the replicas could certainly be improved.

CHARACTERIZATION OF REPLICAS

Dimensional changes of the replicas relative to the masters were checked by measuring distances between scribed marks on two diameters of a diamond-turned copper master and its replica. It was found that there was a lateral dimensional change (increase) of approximately 0.3% on the replica relative to the master, probably caused by thermal expansion of the silicone rubber during

the high temperature curing of the epoxy. This change is much too small to affect measurements of surface microroughness.

For the replication tests, six different 1.52-inch-diameter masters were used: diamond-turned, oxygen-free, high conductivity copper, dual-abrasive polished molybdenum,[4] polished dense flint, polished float glass, polished pyrex, and supersmooth polished fused quartz. These masters represented types of microroughness found on most high quality optical surfaces; the magnitudes of the roughness varied from about 60 Å rms for the diamond-turned copper sample to under 5 Å rms for the supersmooth polished fused quartz.

Since the most important part of the study involved determining to what extent microroughness on the master was preserved on the replica, Nomarski micrographs were taken of corresponding places on the masters and replicas. Several of these are shown in Figs. 1-4. The diamond-turned surface shown in Figs. 1 and 2 contains the most surface detail. A careful inspection of the surfaces in the Nomarski microscope and the original Polaroid photographs revealed that apparently all the surface detail on the diamond-turned copper master was being preserved in the epoxy replica. The molybdenum surface in Fig. 3 is typical of the texture that might also be found on many polished glass surfaces, particularly softer ones that do not take such a smooth polish. The scratch shown in this figure is intended to provide a convenient reference point.

The smoother polished glass and fused quartz surfaces are essentially featureless except for dirt and occasional fine scratches. Thus, it is difficult to compare photographs of masters and replicas. Figure 4, taken of a polished float glass surface, is included to show that even fine scratches replicate with remarkable detail.

The Nomarski micrographs of masters and replicas show that sharp surface features, i.e., those having steep slopes, are well replicated. However, the question remains whether features with gradual slopes that are not observable under Nomarski illumination also replicate. To look for these features, surface profiles were made of masters and replicas using a Talystep surface profiling instrument that has a diamond stylus.[5] Figures 5 and 6 show two such sets of profiles. Since the 20X magnification of the microscope on the Talystep instrument is not adequate to show individual surface features such as are clearly evident in the 100X magnification of the Nomarski microscope, the profiles are from similar but not identical areas. Note that the profiles across the grooves on the master and replica of the diamond-turned surface have a very similar character. Also, the magnitudes of the roughnesses are similar. In this case, the slightly increased instrumental noise level on the replica profile is insignificant compared to the surface structure.

The profiles shown in Fig. 6 were made to determine exactly how smooth a surface could be and still have its microroughness faithfully replicated. The supersmooth polished fused quartz master had a roughness of well under 5 Å rms, as determined from surface profile measurements, and a minimum of surface waviness. The 60-μm-long surface profile thus well represents the microroughness of the master. In this case, the profile of the replica is markedly influenced by high frequency vibrations that are amplifications of the carrier frequency on the stylus pickup produced by the elastic epoxy. Note that the vibrations are also shown on the instrumental noise profile for the replica, made while the stylus was stationary. However, realizing that the vibrations are artifacts of the profiling system, the overall profile appears to have very little waviness. Hence, the epoxy replication technique appears to faithfully

replicate surface detail close to the limit for very smooth optical surfaces. We hope to make independent measurements of the surface profiles of these masters and replicas when the Mireau heterodyne interferometer[6] is delivered to China Lake. This instrument is noncontacting, has a lateral resolution $\sim$ 1 μm, and a height sensitivity $\sim$ 1 Å rms.

CONCLUSIONS

In summary, a two-stage replication technique has been developed that gives excellent replication of surface detail, provides adequate preservation of surface flatness, has lateral dimensional changes of approximately 0.3%, and can be used to sample small areas of large optics.

REFERENCES

1. Erwin G. Loewen, "Replication of Mirrors and Diffraction Gratings," Symposium on Optical Surface Technology, 12-14 April 1983, Garmisch, Germany.

2. H. M. Weissman, "Replicated Laser Scanning Components," SPIE Vol. 396, Proceedings of 1983 SPIE International Technical Conference, 18-22 April 1983, Geneva, Switzerland (Advances in Laser Scanning and Recording).

3. D. H. Rank and T. A. Wiggins, "Double Passing a Plane Grating," J. Opt. Soc. Am. 42, 983 (1952).

4. D. G. Ewing, J. W. Bender, and R. McGillicuddy, "Reduction and Elimination of Surface Texture on Molybdenum Optical Components," Proceedings of the Los Alamos Conference on Optics '81, D. H. Liebenberg, Ed., SPIE Vol. 288, The International Society for Optical Engineering, Bellingham, Washington, 1981, pp. 136-141.

5. J. M. Bennett and J. H. Dancy, "Stylus Profiling Instrument for Measuring Statistical Properties of Smooth Optical Surfaces," Appl. Opt. 20, 1785 (1981).

6. James C. Wyant, "Interferometric Optical Metrology: Basic Principles and New Systems," Laser Focus, Vol. 18, No. 5, pp. 65-71 (May 1982).

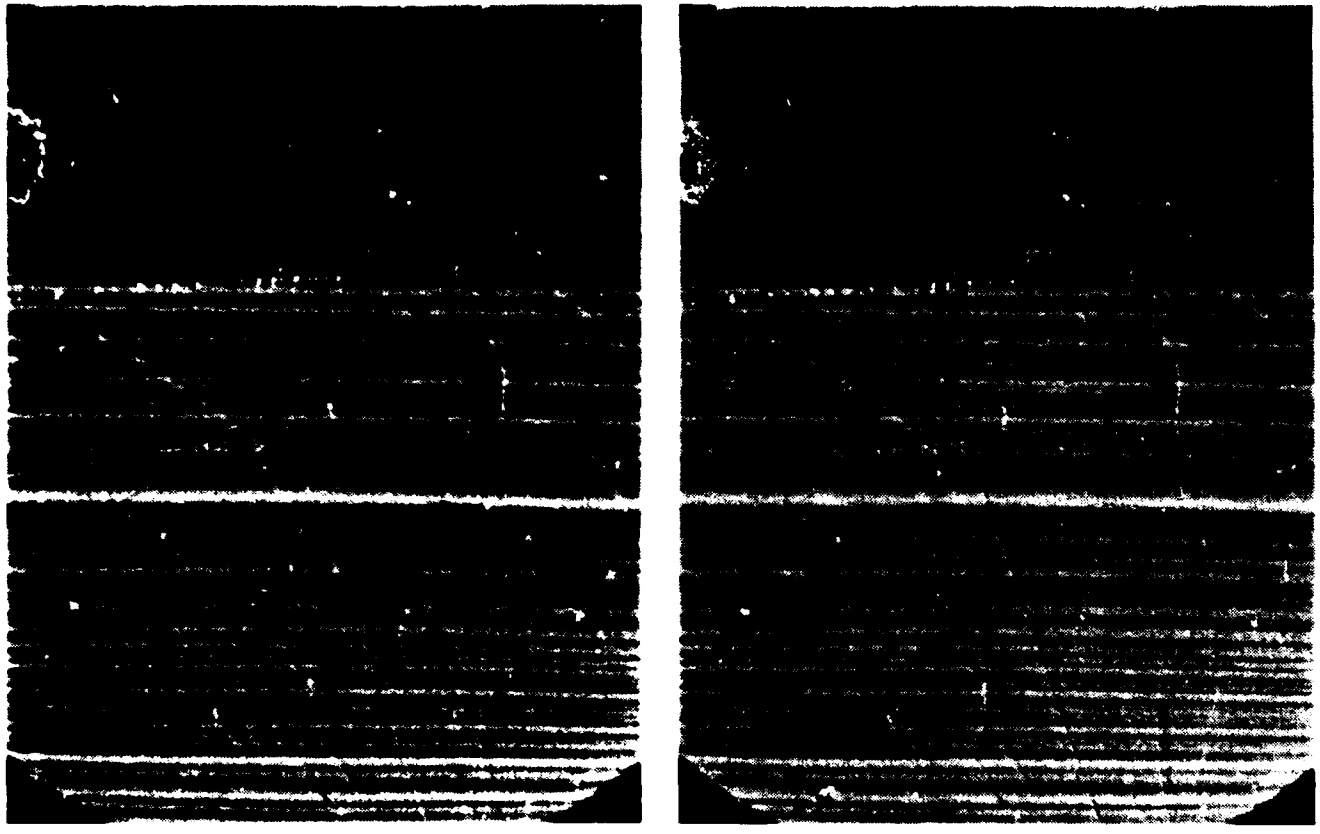

FIG. 1. Nomarski micrographs of master (left) and replica (right) of a diamond-turned OFHC copper surface.

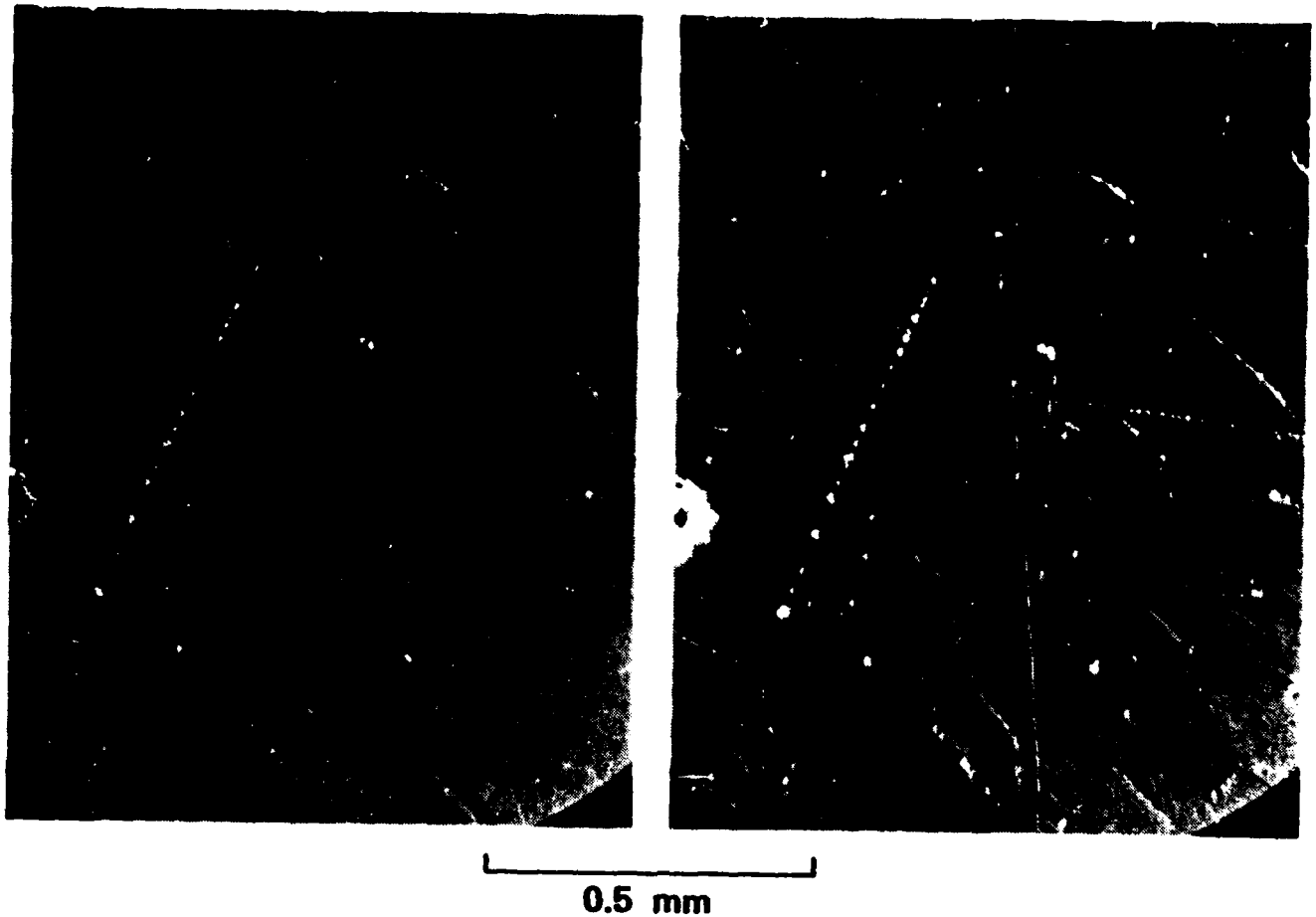

FIG. 2. Nomarski micrographs of master (left) and replica (right) of the same diamond-turned copper surface as in Fig. 1. The samples have been oriented in such a way as to eliminate the diamond-turning grooves.

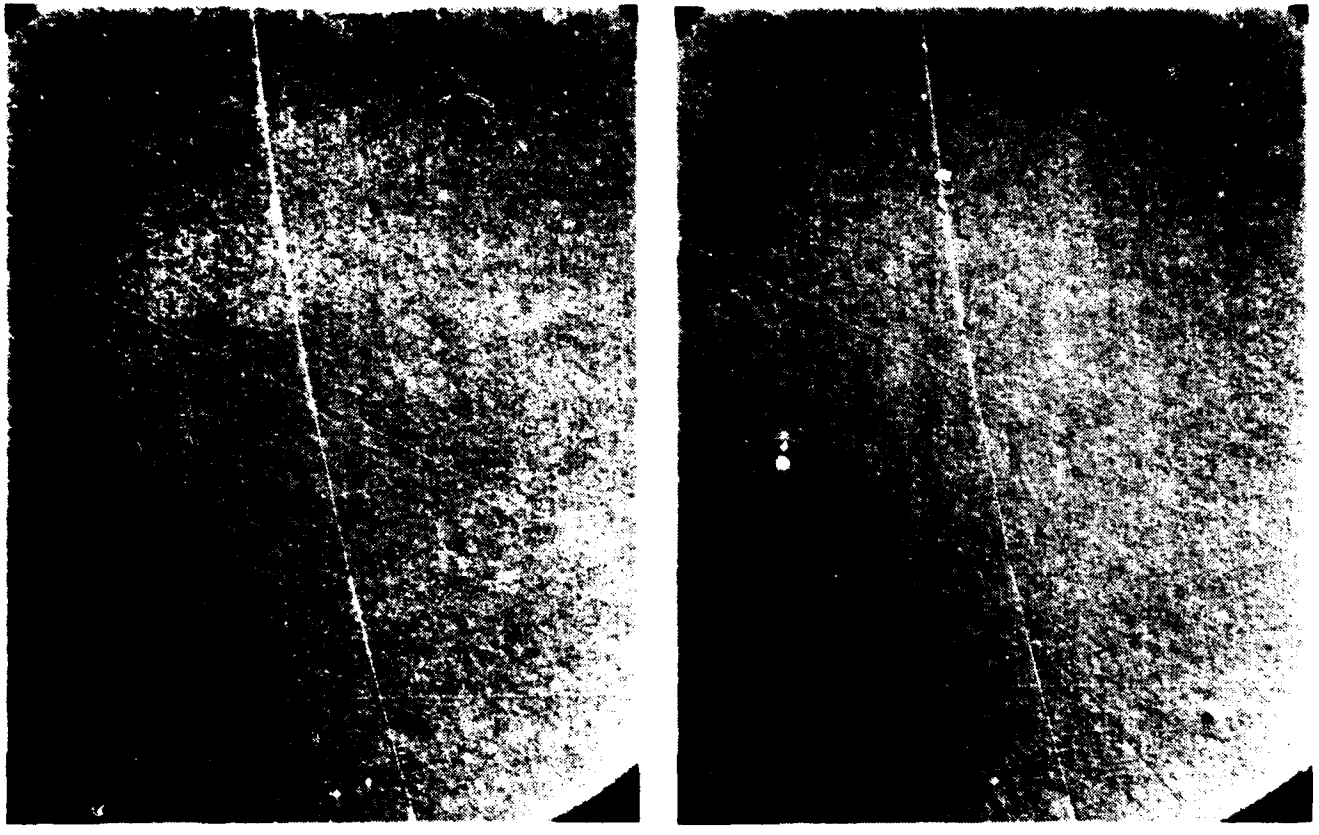

FIG. 3. Nomarski micrographs of master (left) and replica (right) of a dual-abrasive polished molybdenum surface. The scratch forms a convenient reference point.

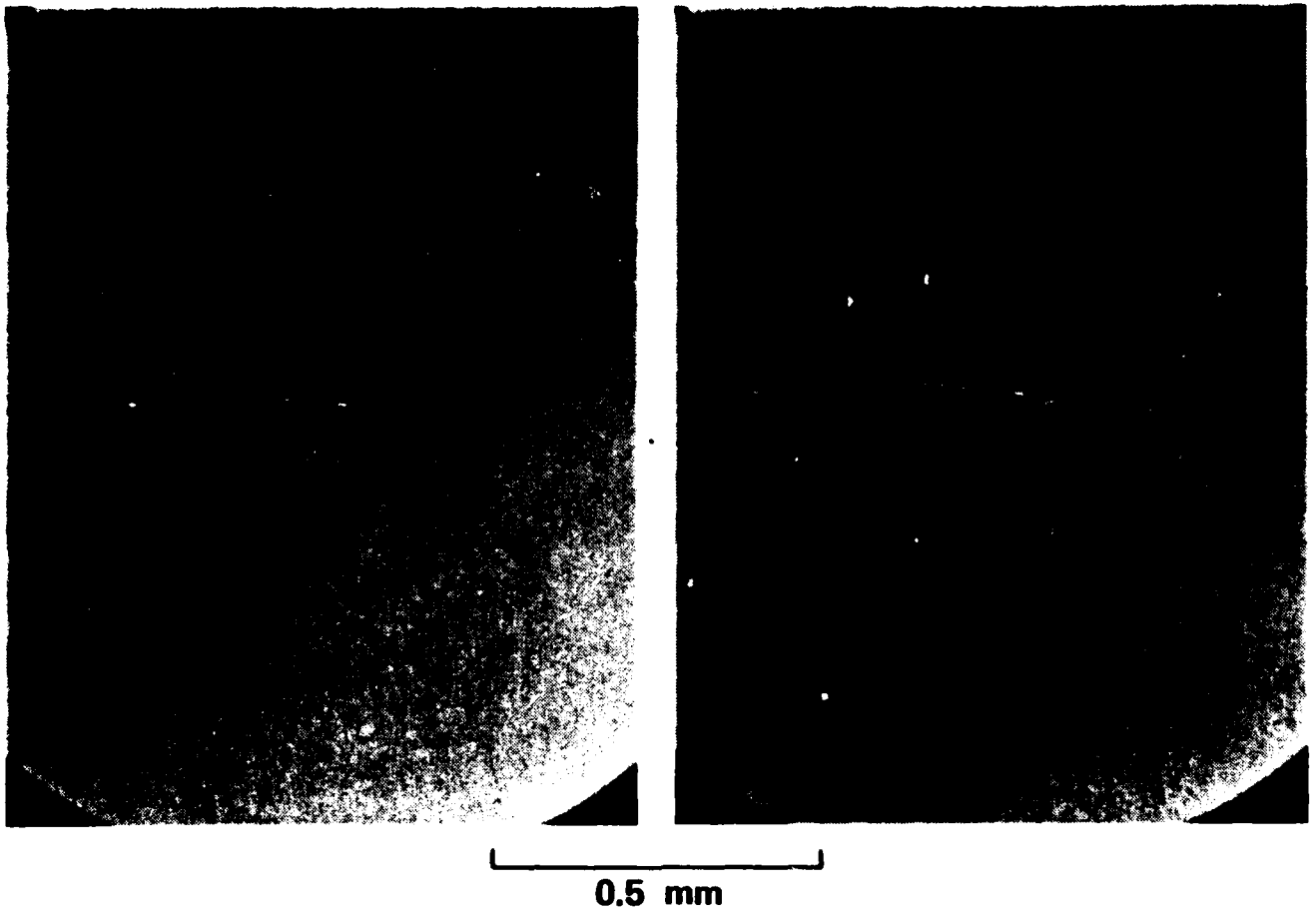

FIG. 4. Nomarski micrographs of master (left) and replica (right) of a polished float glass surface. The scratch marks are included as a reference point.

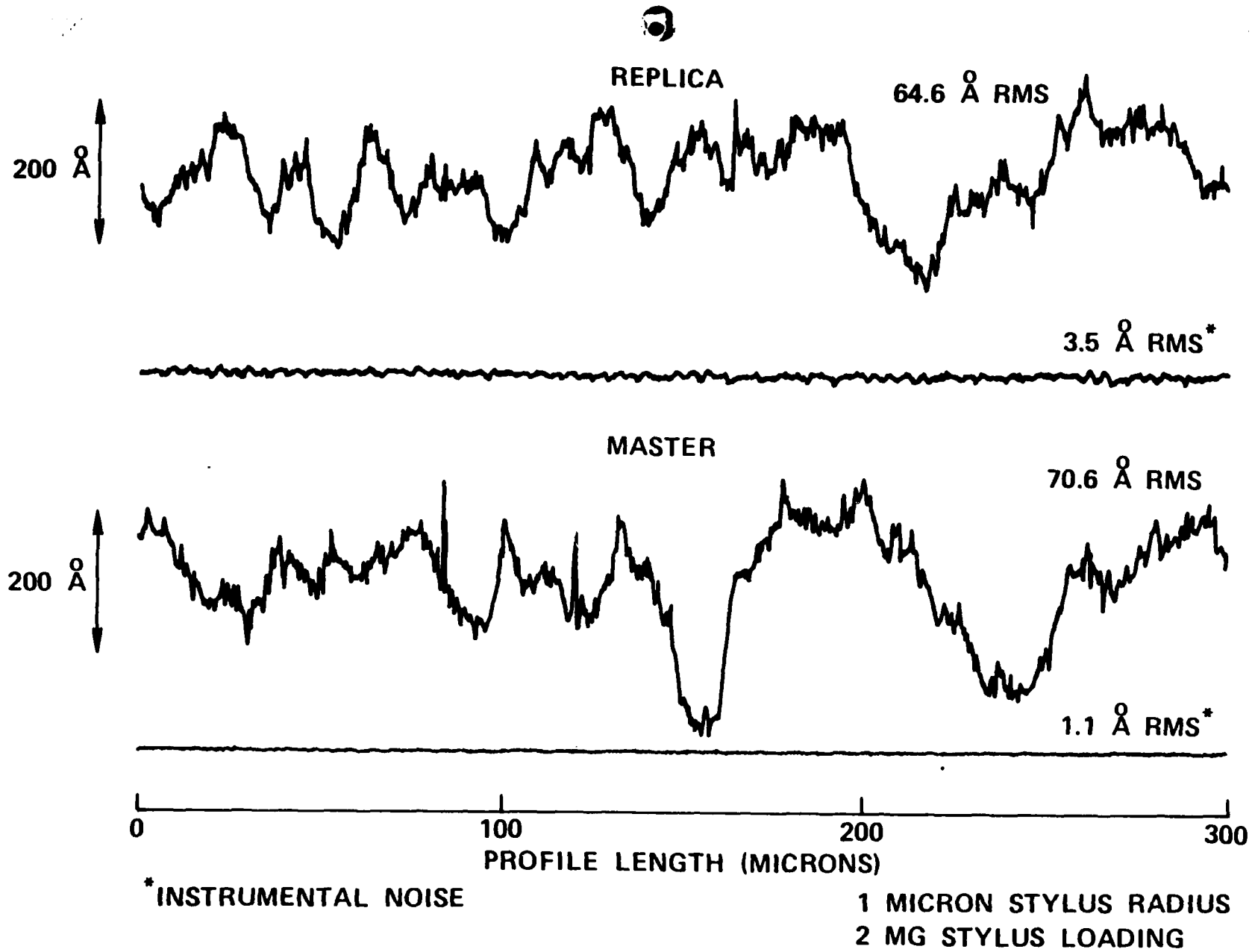

FIG. 5. Talystep surface profiles of a master and a replica of the same diamond-turned OFHC copper surface that was shown in Fig. 1. The surface profiles are taken perpendicular to the diamond-turning grooves.

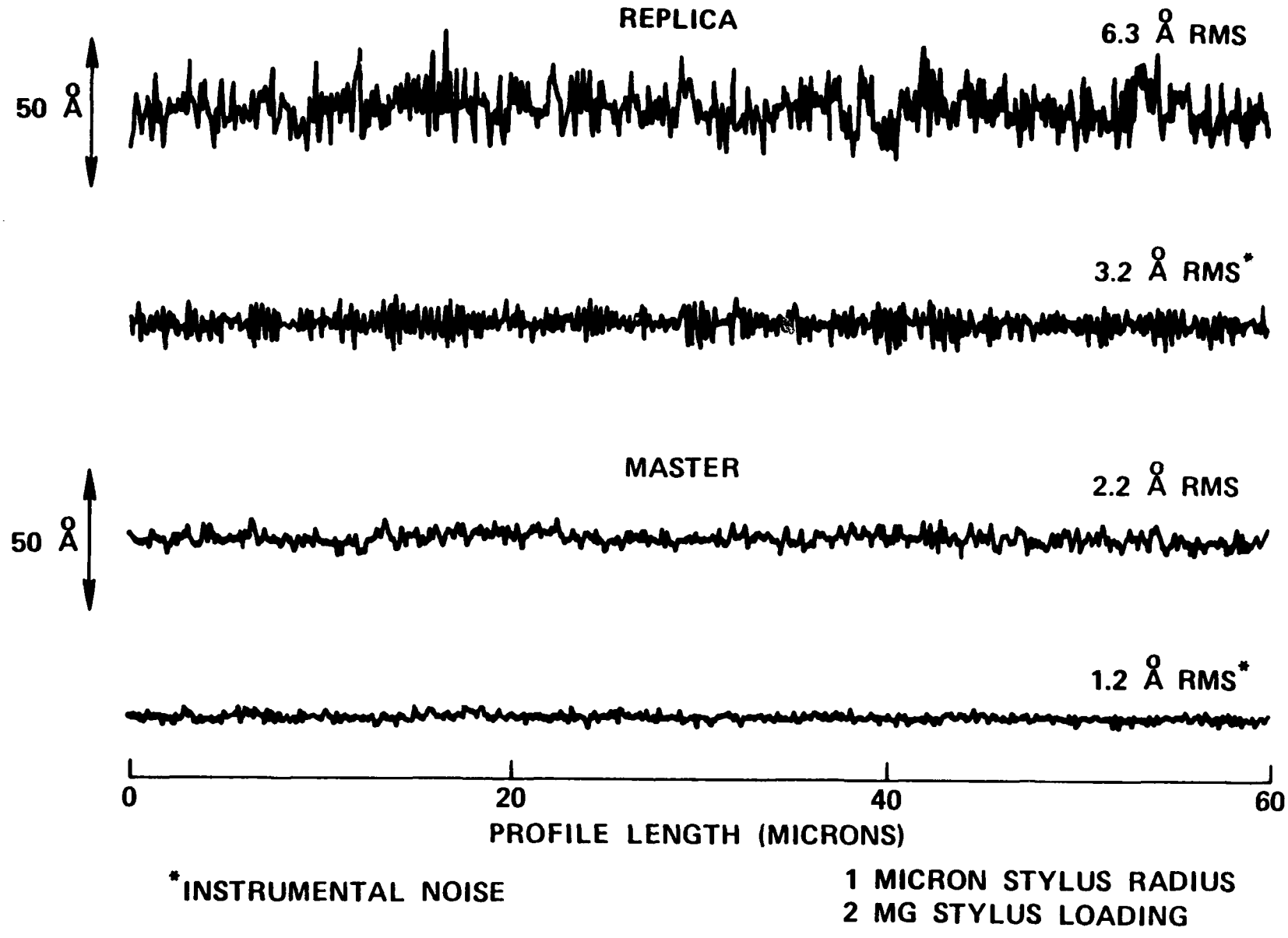

FIG. 6. Talystep surface profiles of a master and a replica of a supersmooth polished fused quartz surface. The instrumental noise is increased for the epoxy replica, as explained in the text.

Chapter 11

Low Scatter Molybdenum Surfaces

J. M. Bennett, P. C. Archibald, J. P. Rahn

Michelson Laboratory, Physics Division
Naval Weapons Center
China Lake, CA 93555

A Klugman

Northrop Research and Technology Center
Palos Verdes, CA 90274

Low scatter molybdenum surfaces

J. M. Bennett, P. C. Archibald, J. P. Rahn

Physics Division, Michelson Laboratory, Naval Weapons Center,
China Lake, California 93555

A. Klugman

Northrop Research and Technology Center, Palos Verdes, California 90274

(Received

Molybdenum (Mo) mirrors are being used in high power infrared lasers and would be ideal for lasers operating in the visible and ultraviolet if lower scatter surfaces could be produced. Surfaces prepared by two novel techniques have been found to be smoother and have lower scatter than conventionally polished material, which has a surface texture that profiles the grain structure of the bulk material. A dual-abrasive polishing technique has been found to produce surfaces that show almost no surface grain relief, have scattering levels as little as one-seventh that of conventionally polished Mo, and roughnesses as small as 15 Å rms, measured from surface profiles. Sputtering a layer of Mo onto a previously polished Mo surface and then polishing the sputtered layer produces a surface that is very similar to that of polished glass in profile and scattering properties. Scattering levels approximately one-tenth that of conventionally polished bulk Mo and roughnesses approximately 13 Å rms have been measured on such surfaces. However, laser damage thresholds measured at 2.7 μm show that higher scatter, conventionally polished Mo surfaces have higher melt thresholds than do the lower scatter, dual-abrasive polished and sputtered Mo surfaces.

AD-A134 285 OPTICAL PROPERTIES OF METALS(U) UNIVERSITY OF SOUTHERN CALIFORNIA LOS ANGELES CENTER FOR LASER STUDIES M BASS ET AL. 15 JUL 83 N00014-79-C-0896 3/3

UNCLASSIFIED F/G 11/6 NL

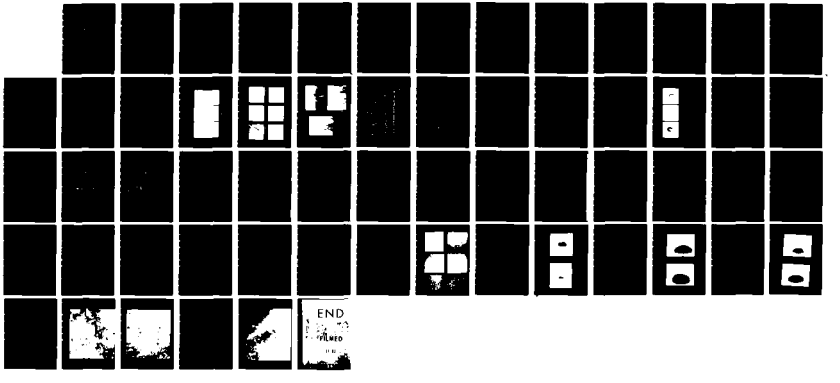

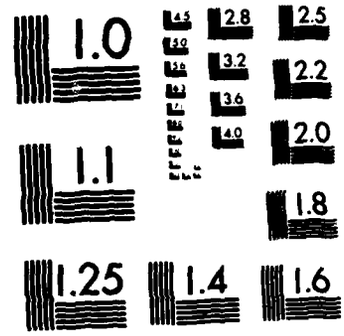

INTRODUCTION

Molybdenum (Mo) mirrors are being used in many high power infrared laser systems and are also candidates for lasers operating in the visible and ultraviolet spectral regions. However, a limiting factor is the scattered light from the mirror surfaces which degrades the laser system performance. It has been previously shown[1] that the surface finish obtainable on Mo mirrors polished by conventional techniques is directly related to the grain structure of the material. Normal polishing procedures which produce smooth, featureless surfaces on glass, fused quartz, silicon, and other materials accentuate the grain structure of the Mo. Depending on the type of stock and the previous metallurgical treatment, the polished surface may appear to have a uniform coarse or fine-grained structure, mixed or irregular grains, voids, or a combination of grain sizes and shapes. Any structure on the polished surface produces unwanted scattering, and thus much effort has been expended in developing polishing techniques that minimize or eliminate surface structure.

This paper will describe two promising new techniques that have been developed to produce low-scatter surfaces on Mo. The scattering and topography of these surfaces will be compared with that obtainable on the best conventionally polished Mo surfaces. Results of laser damage studies at 2.7 μm on various types of Mo surfaces will also be presented.

SURFACE PREPARATION

Conventional pitch polishing techniques have been used to produce scratch-free surfaces on bulk Mo, but with varying amounts of grain relief showing on the polished surface. An alternative polishing method, called the dual-abrasive technique, uses two sizes of abrasives simultaneously and can

produce surfaces that show much less grain relief, although some fine scratches and pits remain. Another approach is to sputter a fine-grained layer of Mo onto a conventionally polished surface and then polish the sputtered material. Nomarski micrographs of Mo surfaces produced by the three different techniques are shown in Fig. 1. The polishing methods are described below.

Conventional polishing

Low carbon, vacuum arc-cast bar or plate is the preferred material for polished Mo mirrors. This material is purer than the powder metallurgy product which can contain voids or inclusions of harder materials such as carbides that polish at different rates and, hence, produce a rougher surface. The polishing process to be described here is used at the Northrop Research and Technology Center in Palos Verdes, California. Figure 2 shows the appearance of a surface at different stages of the preparation. Molybdenum samples 1.5 inches in diameter are blocked in multiples of 7, 20, or other convenient number on an aluminum backing plate. Rough grinding is accomplished on a Strasbaugh Curve Generator using an 80-grit silicon carbide wheel. Fine grinding is done on a cast iron grinding tool using 22.5-μm-diameter alumina (aluminum oxide) abrasive followed by 9.5-μm alumina. A medium-hard pitch lap (145 to 150°F melting point) is used for polishing, with a slurry of 0.3-μm-diameter alumina powder. The consistency of the slurry is similar to that of heavy cream. From 18 to 24 hours are needed to completely polish out a 20-piece block. Speeds and weights are determined by the operator to maintain the optical figure. Since the optical figure of Mo changes very slowly, speed and weight do not have as much effect as they do on most other materials. An important transition occurs after about 10 hours of polishing

time, as shown in Figure 2. The ground appearance of the surface is disappearing, and the grain structure of the Mo is starting to appear. Further polishing removes the last of the grinding pits but also enhances the grain structure. Although all well-polished Mo surfaces exhibit grain structure to a greater or lesser extent, depending on the polishing time and the metallurgical processing of the material, improperly polished Mo can also show scratches or pits remaining from the grinding process (see Fig. 8 in ref. 1).

Several Mo samples polished as described above were included in the study, all of which showed grain structure similar to that in Fig. 1 (photo at left). In some cases the grain structure was more uniform than in others, and some surfaces showed very large grains interspersed with smaller grains. Measurements on three representative samples are included for comparison with samples prepared by other types of polishing.

Dual-abrasive polishing

The so-called dual-abrasive process has been developed by personnel at the Developmental Optics Facility (DOF) of International Laser Systems, Inc. in Albuquerque, New Mexico. Described in an article by Ewing *et al.*,[2] the process is similar to that discussed above in that the material, blocking, and grinding operations are similar, and a conventional pitch lap is used. The polishing abrasive, however, is a 50-50 mixture of 0.3- and 0.05-μm alumina (Linde A and Linde B, respectively) in a water slurry. For a block of seven 1.5-inch-diameter Mo samples prepared for this study, the samples were ground with 9-μm-diameter alumina for three hours, and then with 5-μm-diameter alumina for another two hours using a cast iron grinding tool and

tap water. The block was polished for 30 hours using the above-mentioned dual-abrasive slurry and a medium-soft pitch lap. Although a relatively long polishing time was used in this particular case, DOF personnel claim that in some cases polishing can be accomplished in a fraction of the time normally required, and even conventionally polished Mo surfaces can be quickly repolished to show considerably less surface texture.

Six of the group of seven specially prepared dual-abrasive polished samples had surface textures similar to that shown in the center photo of Fig. 1. There were a few pits, some very fine scratches, and a few larger scratches, but almost no indication of the Mo grain structure. The seventh sample had been damaged and showed many randomly oriented fine scratches. Other samples produced by dual-abrasive polishing and examined in this study had surface finishes that varied from ones showing fine scratches and pits, to one sample containing almost no visible scratches but with a very definite Mo grain structure. As will be discussed in the section on scattering, the near-angle scattering and also the total scattering for the dual-abrasive polished samples was much lower than that from conventionally polished Mo samples.

Polishing sputtered Mo on bulk Mo

An alternate technique for producing smooth Mo surfaces is to apply a thick layer of Mo which has a very fine grain structure to a polished Mo surface. Evaporation has not proved to be a satisfactory method for applying the surface layer since the thickness of material which can be deposited in a reasonable time is of the order of a few microns, much smaller than is needed

for repolishing. A high-speed sputtering technique has been developed[3] to sputter Mo at rates approximately 1 μm/min, so that layers of Mo up to several-hundred-microns thick can be deposited onto previously polished Mo surfaces. Examination of the sputtered layer in a transmission electron microscope showed that the grain size of the sputtered material is about 0.5 μm and that there is a very high defect density. X-ray data revealed a highly textured structure with oriented grains. No impurities could be detected in the layer using x-ray fluorescence techniques. Metallographic examination of the sputtered layer in cross section (Fig. 3) revealed that the fine-grain structure is accompanied by what appears to be some epitaxial growth from the bulk Mo, or the occurrence of a second phase.

The surfaces of the sputtered layers were too rough to use as is, so they were ground with 9.5-μm-diameter alumina, removing approximately 50 μm of material. (The thickness of the sputtered layer on these particular samples was 150 μm, but other samples were made with about 360 μm of sputtered material.) Following the grinding operation, the samples were polished using 0.3-μm-diameter alumina (Linde A). Polishing times were of the order of 18 hours, comparable to times used for polishing bulk Mo. Polished sputtered Mo surfaces prepared in the above manner are nearly featureless in Nomarski illumination, as shown in the right-hand photo of Fig. 1, and produce much less scattered light than conventionally polished bulk Mo (see section on scattering). Several polished sputtered samples were examined in this study. All had similar surface textures but somewhat different amounts of scattered light. The sample used here for comparison is the best of the group examined.

SURFACE ROUGHNESS AND SCATTERING

Figures 4 and 5 show 600- and 60-μm-long surface profiles, respectively, for the three different types of Mo for which Nomarski photos were shown in Fig. 1. These profiles were obtained with the Michelson Laboratory Talystep surface profiling instrument.[4] The profiles of the conventionally polished bulk Mo show the typical structure of the Mo grains which were polished at different rates and, hence, have a mesa-like or high-low carpet appearance. The roughness obtained from a profile at a particular spot on the surface is of course very dependent on the grain structure at that spot; for this reason, it is very difficult to obtain an ensemble average roughness for conventionally polished bulk Mo from surface profile measurements.

The profiles of the polished, sputtered Mo, on the other hand, look very similar to profiles of polished glass or fused quartz surfaces, with closely spaced surface features (autocovariance length approximately 1.0 μm) and no long-range waviness. The dual-abrasive polished samples have profiles that are intermediate between these two extremes, with some closely spaced features and only a hint of the Mo grain structure evident. These surfaces would be characterized by two roughness components -- a short-range roughness with an autocovariance length approximately 0.7 μm and a long-range waviness dependent on the residual structure of the Mo grains (autocovariance length, approximately 5 to 30 μm).

The question often arises: What profile length should be used to specify the roughness of a Mo surface? As has been pointed out by Church[5] and others, in general there is no one roughness value that can be assigned to a surface; the value depends on the bandwidth, or range of surface spatial wavelengths

that are included in the determination. Figure 6 illustrates this point. In the figure are plotted roughnesses measured for the three types of Mo using different profile lengths. The total profile length, 1000 μm, gives of course the largest roughness. If this total profile is broken up into smaller parts of approximately 10- and 100-μm lengths, respectively, and the average values of rms roughness are determined from these shorter lengths, the other data points in the figure will be obtained. It is clear that for conventionally polished bulk Mo the roughness value is critically dependent on the profile length, while there is almost no dependence for the polished sputtered Mo. Dual-abrasive polished bulk Mo is intermediate, and in this case the curve critically depends on the particular sample since there is a fairly wide variability in the surfaces of samples polished using this process. For comparison, the curve for polished fused quartz shows no dependence on surface spatial wavelength since there are no longer range surface waviness components on well-polished fused quartz.

The scattering from the different types of Mo varies both in magnitude and in angular distribution. For systems applications, one frequently wants to know the magnitude of light scattered into a particular angle or range of angles. However, the light scattered into a nearly hemispherical range of angles can be used as a general measure of surface quality. This so-called total integrated scattering (TIS) measurement[6] is a good method for characterizing polished glass surfaces and other surfaces that do not have longer spatial wavelength roughness components present. At Michelson Laboratory, the Optical Evaluation Facility[7] for measuring TIS contains an aluminized hemispherical collector (Coblentz sphere) that collects scattered light in

the angular range of 2.85 to 80 degrees from the specular direction. Light scattered at angles less than 2.85 degrees is not collected. For well-polished glass or fused quartz optics coated with reflecting films, this near-angle scattering amounts to only one or two percent of the total scattered light and is thus negligible. However, for polished Mo surfaces and in particular conventionally polished bulk Mo, this is no longer true. As shown in Fig. 7, as much as 60% of the total light scattered into a hemisphere can be scattered at angles less than 3 degrees. The near-angle scattering values were integrated from measurements made on an angular scattering apparatus[8] in the angular range 0.3 to 3 degrees in increments of 0.1 degree.

Polished sputtered Mo shows the least amount of near-angle scattering, and, in this respect, is most similar to glass or fused quartz optics. The dual-abrasive polished Mo also tends to have rather small amounts of near-angle scattering. However, conventionally polished bulk Mo can have large and variable amounts of near-angle scattered light, depending on the grain structure on the surface producing the scattering. Surface spatial wavelengths that produce scattering in the 0.3- to 2.85-degree angular range from the specular direction lie in the range of 13 to 100 μm when the surface is illuminated by normal incidence light of 6328 Å wavelength. This can be understood by referring to Fig. 8 which shows the scattering angles as a function of surface spatial wavelength plotted for the HeNe laser line of 6328 Å. This curve was calculated from the grating equation which determines the angular dependence of scattering by surface microirregularities; at normal incidence, the relation is $\sin\theta = \lambda/d$, where θ is the scattering angle, λ the illuminating wavelength, and d the surface spatial wavelength.

Near-angle scattering from the three types of Mo surfaces is photographically illustrated in Fig. 9 for angles out to about 2 degrees from the specular direction. Note the large difference in the amount of scattering from the different surfaces.

COMPARISON OF SURFACE ROUGHNESSES DETERMINED FROM PROFILE AND SCATTERED LIGHT MEASUREMENTS

It has been noted previously[1] that there is very poor correlation between the roughnesses of conventionally polished Mo surfaces measured using a surface profiling (stylus) instrument[4] and deduced from TIS measurements made using a Coblentz sphere type of instrument,[6,7] and invoking scalar scattering theory.[6] Some of this discrepancy is caused by the different range of surface spatial wavelengths sampled using the two different techniques, as mentioned in the preceding section and discussed more thoroughly in a forthcoming paper.[9]

In an attempt to determine how the roughness would compare when the surface spatial wavelength ranges of the two measuring techniques were comparable, we present Figs. 10 and 11. In Fig. 10 the roughness values, as open circles, have been determined from measurements made using the Coblentz sphere instrument (3- to 80-degree collection angles, corresponding to surface spatial wavelengths 0.6 to 13 μm) along with the scalar theory:[6]

$$\mathrm{TIS} \cong (4\pi\delta/\lambda)^2 \quad ,$$

where δ is the rms surface roughness and λ the illuminating wavelength. The open squares are the surface profile roughnesses determined from the

corresponding spatial wavelengths (0.6 to 13 μm). The open diamonds are roughnesses determined from the complete 1-mm-long profile. Measurements were made on approximately five different places on each sample. In Fig. 11 the situation is similar except that near-angle cumulative scattering (0.3 to 3 degrees) has also been included, increasing the surface spatial wavelength range from 0.6 to 100 μm. The profile lengths have been increased accordingly. It is seen that in both cases the profile roughnesses are consistently smaller than the corresponding scattered light roughnesses. Whether this is caused by incomplete statistics using the surface profiling instrument or a more fundamental reason is not clear at this time. The scattered light measurements sampled 19 different places on the surface, using a 1-mm-diameter krypton laser beam, wavelength 6471 Å. More work is clearly needed in this area.

LASER DAMAGE MEASUREMENTS AT 2.7 μm

Since Mo mirrors are used in many high power laser applications, it is of interest to see whether there are detectable differences in the amount of energy which the different types of polished surfaces can withstand. For this reason, selected samples of each type were tested using an HF laser (nominal wavelength 2.7 μm) with a 100-ns pulse length and 60-μm-diameter spot size. Plots of the multithreshold damage levels[10] are shown in Figs. 12 - 14, and the melt thresholds are listed in Table I. For comparison, the melt threshold of a Mo surface ground with 5-μm-diameter alumina is also shown. It is clear from Table I that although the polished sputtered Mo sample has the lowest scatter of the three, its melt threshold is also the lowest, while the highest scatter, conventionally polished bulk Mo sample has the highest damage threshold.

The extremely low threshold for the ground sample indicates that surface roughness and/or contaminants remaining from the grinding process can adversely affect the damage threshold in extreme cases. It is not clear whether the lower threshold for the polished, sputtered Mo is caused by poor heat transfer in the sputtered layer or between the sputtered layer and the bulk material, or to some other cause. However, it is clear that surface roughness alone is not the dominant factor in laser damage thresholds at 2.7 μm with 100-ns pulses.

CONCLUSIONS

In conclusion, Mo samples prepared by two novel techniques have been found to have much lower scattering levels than bulk material polished in the conventional manner. For example, polished sputtered Mo on bulk Mo can have a scattering level one-tenth that of the conventionally polished material. Profile roughnesses as low as 13 Å rms (for a 1-mm-long scan length) have been measured on such samples. A comparison of roughnesses determined from surface profiles and TIS using the same spatial wavelength ranges shows smaller values for the profile roughnesses for all samples. The reason for this discrepancy is not clear, but requires further study to determine if the difference is of a fundamental nature. Finally, the laser damage threshold was measured at HF wavelengths (2.7 μm) and found to be lower for the lower scatter materials than for rougher, conventionally polished Mo surfaces.

ACKNOWLEDGMENTS

The authors would like to thank John Bender of the Developmental Optics Facility for providing several Mo samples polished by the dual-abrasive

polishing process. The sputtered Mo was produced by Nils Laegreid and R. Knoll of Battelle Pacific Northwest Laboratories and polished by A. Klugman. Finally, J. O. Porteus, J. B. Franck, and W. N. Faith at the Naval Weapons Center performed the laser damage measurements.

Table I. Melt thresholds for various polished Mo samples at HF wavelengths (2.7 μm). Pulse length 100 ns; spot size 60 μm.

Sample	Melt threshold (J/cm^2)
Sputtered #1	31 ± 2
Bulk #B[a]	39 ± 6
Bulk #3[b]	44 ± 5
Ground, 5 μm Al_2O_3	9 ± 0.85

[a] Dual-abrasive polished

[b] Conventionally polished

REFERENCES

1. J. M. Bennett, S. M. Wong, and G. Krauss, "Relation Between the Optical and Metallurgical Properties of Polished Molybdenum Mirrors," Appl. Opt. 19, 3562-3584 (1980).

2. D. G. Ewing, J. W. Bender, and R. McGillicuddy, "Reduction and Elimination of Surface Texture on Molybdenum Optical Components," Proceedings of the Los Alamos Conference on Optics '81, D. H. Liebenberg, Ed., SPIE Vol. 288, The International Society for Optical Engineering, Bellingham, Washington, 1981, pp. 136-141.

3. J. L. Stanford, N. Laegreid, R. Knoll, and A. Klugman, "Sputtered Molybdenum for Thin Mirror Faceplate Refurbishment," Proceedings of the High Power Laser Optical Components Meeting, 19-20 November 1981, J. L. Stanford, Ed., Naval Weapons Center, China Lake, CA, 1983 (in press).

4. J. M. Bennett and J. H. Dancy, "Stylus Profiling Instrument for Measuring Statistical Properties of Smooth Optical Surfaces," Appl. Opt. 20, 1785-1802 (1981).

5. E. L. Church and J. M. Zavada, "Residual Surface Roughness of Diamond-Turned Optics," Appl. Opt. 14, 1788-1795 (1975).

6. H. E. Bennett, "Scattering Characteristics of Optical Materials," Opt. Engr. 17, 480-488 (1978).

7. P. C. Archibald and H. E. Bennett, "Scattering from Infrared Missile Domes," Opt. Engr. 17, 647-651 (1978).

8. J. M. Elson, J. P. Rahn, and J. M. Bennett, "Light Scattering from Multilayer Optics: Comparison of Theory and Experiment," Appl. Opt. 19, 669-679 (1980).

9. J. M. Elson, J. P. Rahn, and J. M. Bennett, "Relationship Between Total Integrated Scattering, Angular Scattering, and Correlation Length for Reflecting Single- and Multilayer-Coated Optics," Appl. Opt. (in press).

10. J. O. Porteus, D. L. Decker, W. N. Faith, D. J. Grandjean, S. C. Seitel, and M. J. Soileau, "Pulsed Laser-Induced Melting of Precision Diamond-Machined Cu, Ag, and Au at Infrared Wavelengths," IEEE J. Quantum Electron. QE-17, 2078-2085 (1981).

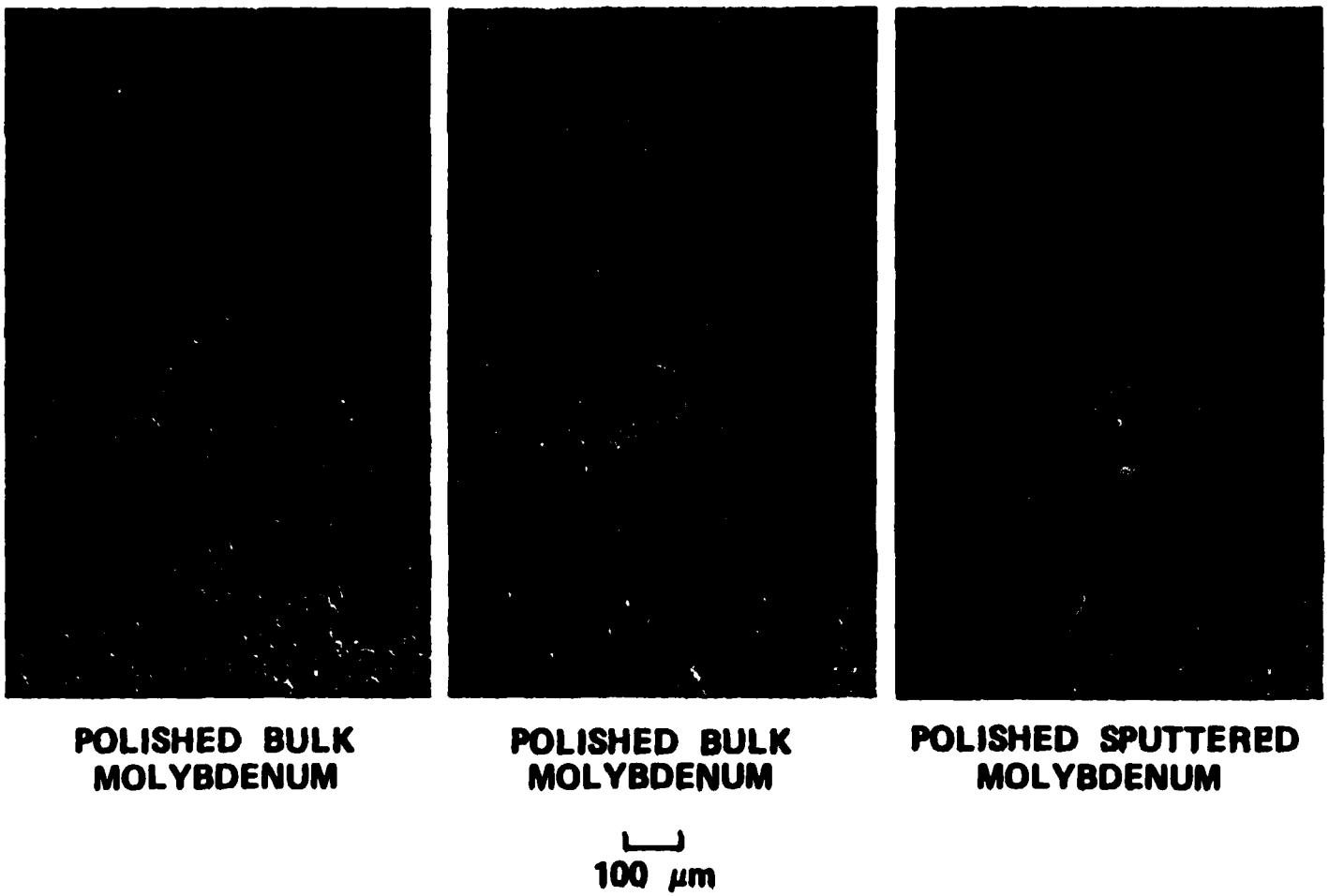

Fig. 1. Nomarski micrographs of three types of Mo surfaces: conventionally polished bulk Mo (left), dual-abrasive polished bulk Mo (center), and polished sputtered Mo (right).

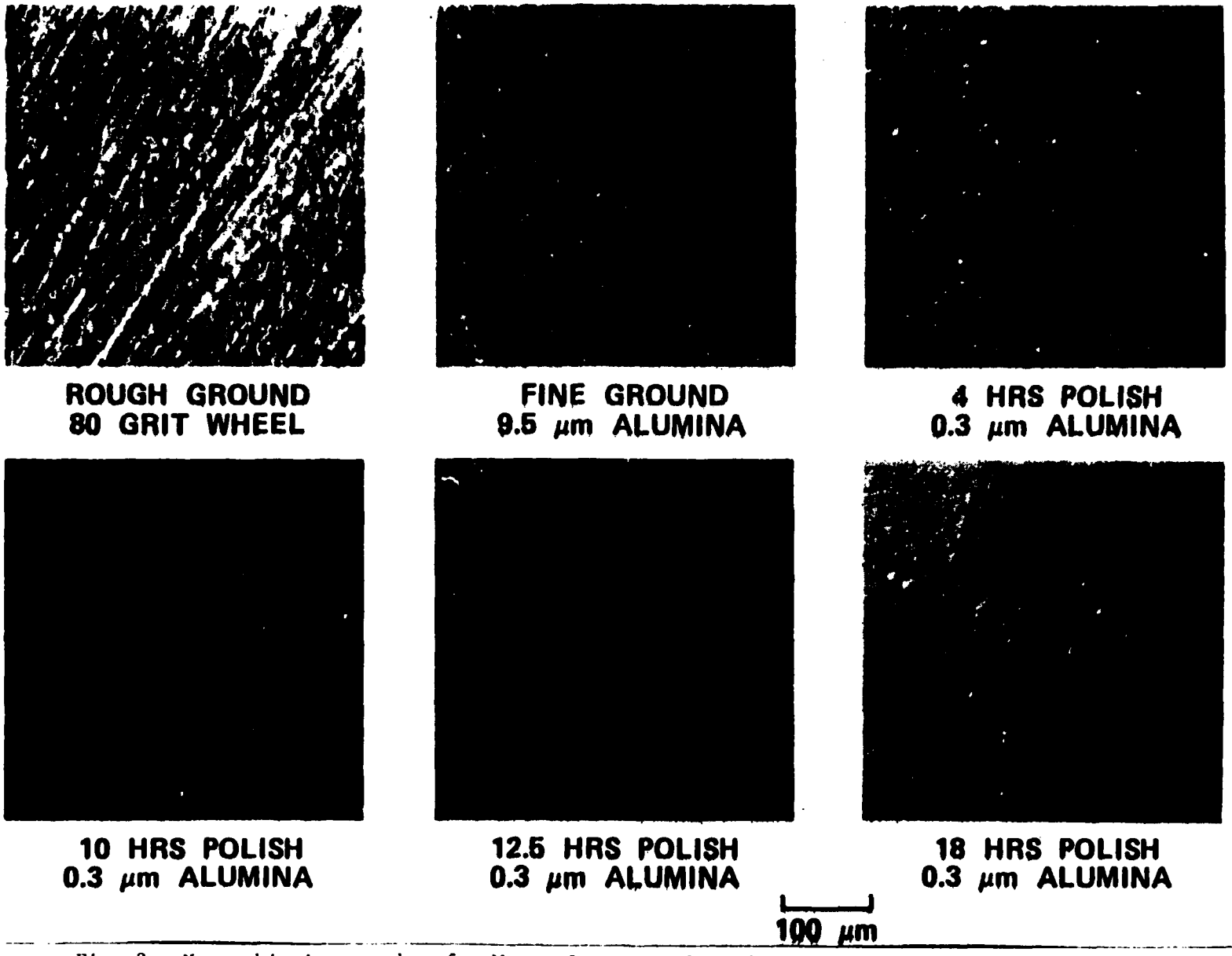

Fig. 2. Nomarski micrographs of a Mo surface at selected stages during the grinding and polishing process.

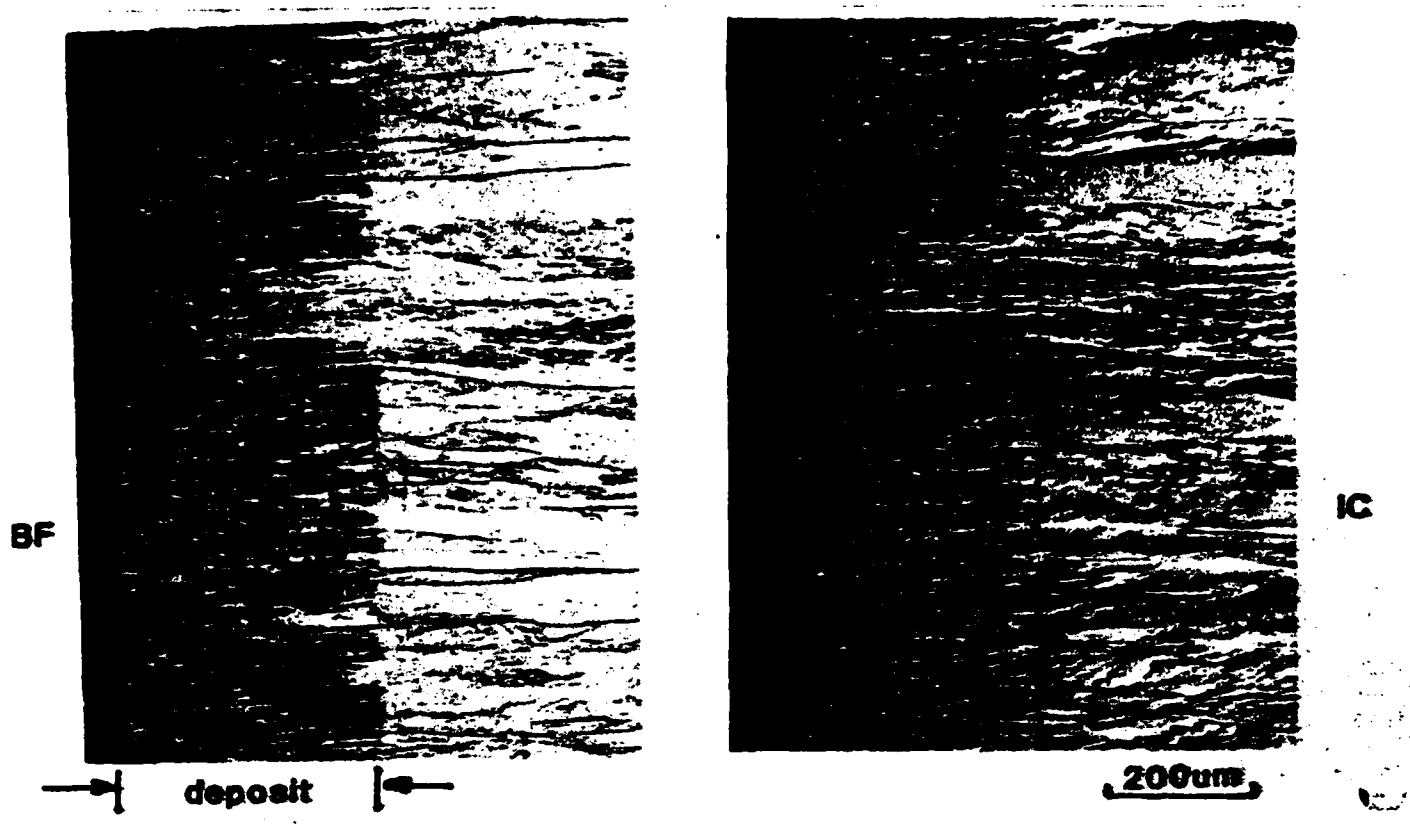

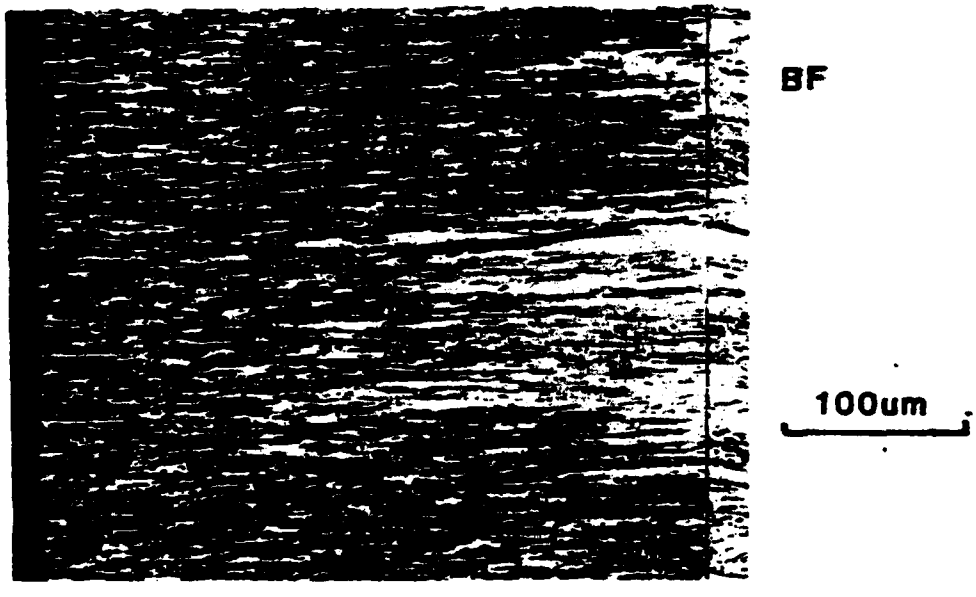

Fig. 3. Bright field and interference contrast (Nomarski) micrographs of a cross section of metallurgically polished and etched sputtered Mo deposited onto bulk Mo. The light contrast regions in the sputtered layer are apparently large epitaxial grains. (Photos courtesy of Nils Laegreid, Battelle Pacific Northwest Laboratories.)

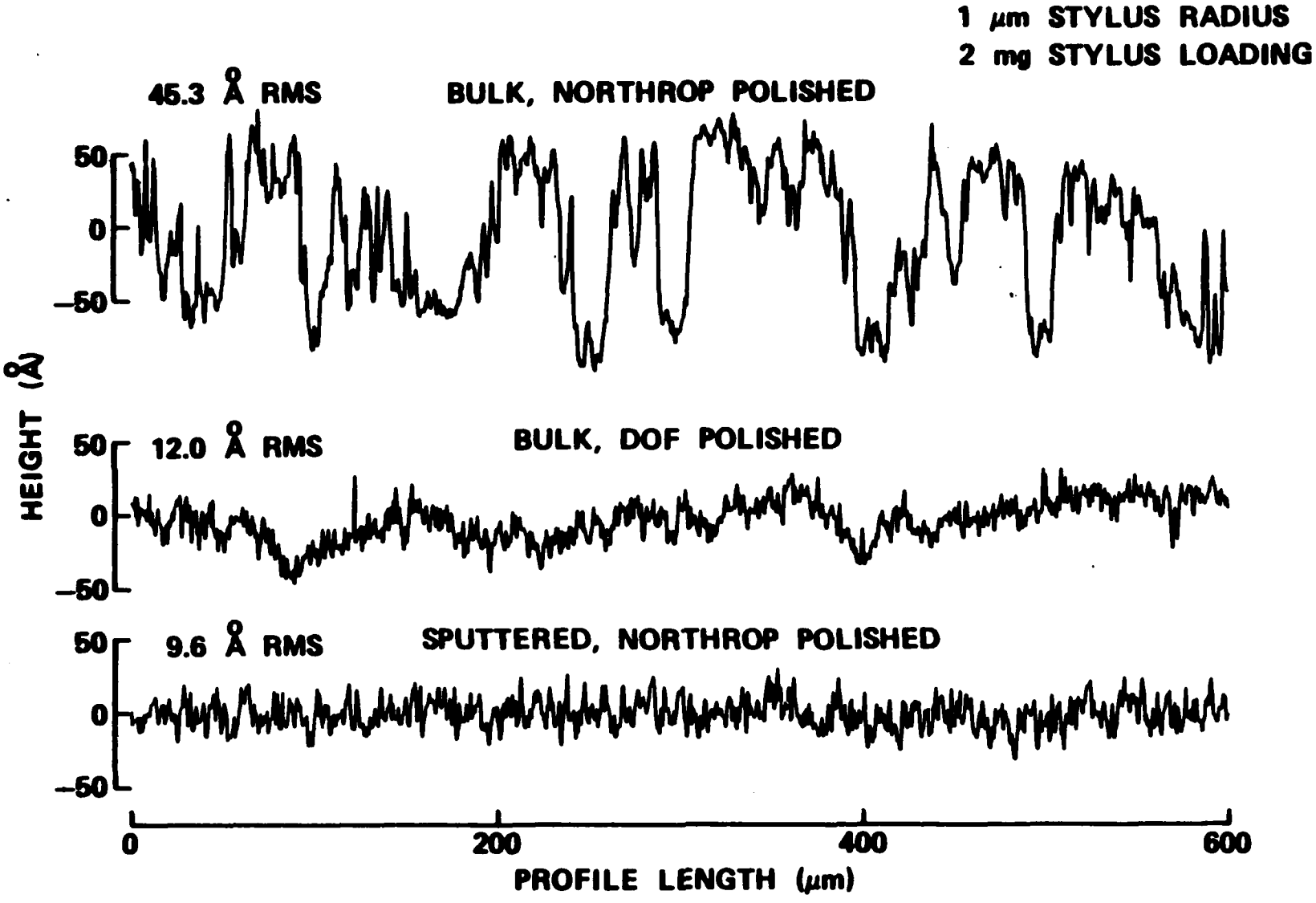

Fig. 4. Surface profiles of the three Mo surfaces shown in Fig. 1 for a profile length of 600 μm. Measured roughness values are shown at the left of the profiles.

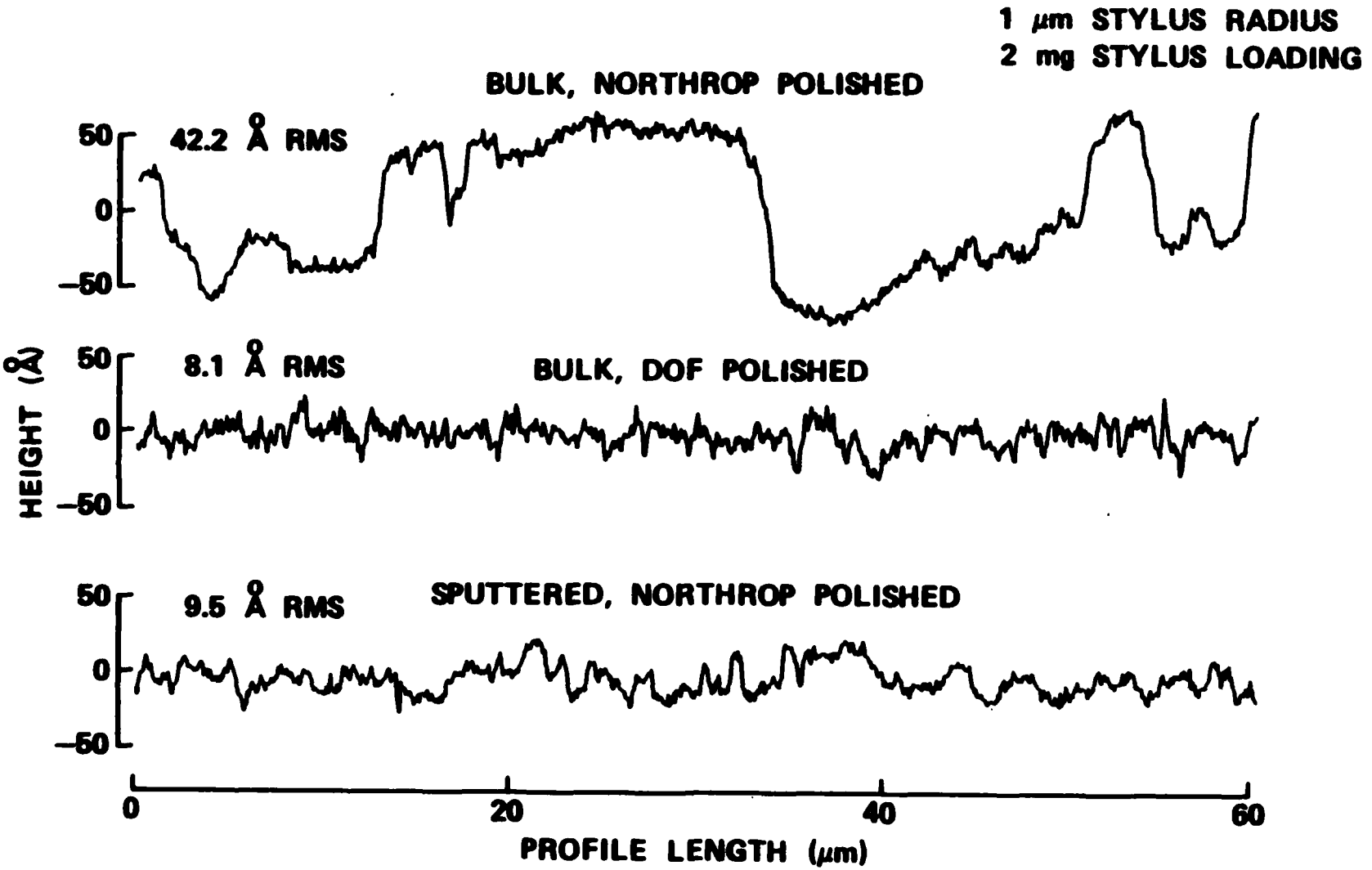

Fig. 5. Surface profiles of the three Mo surfaces shown in Fig. 1 for a profile length of 60 μm. Measured roughness values are shown at the left of the profiles.

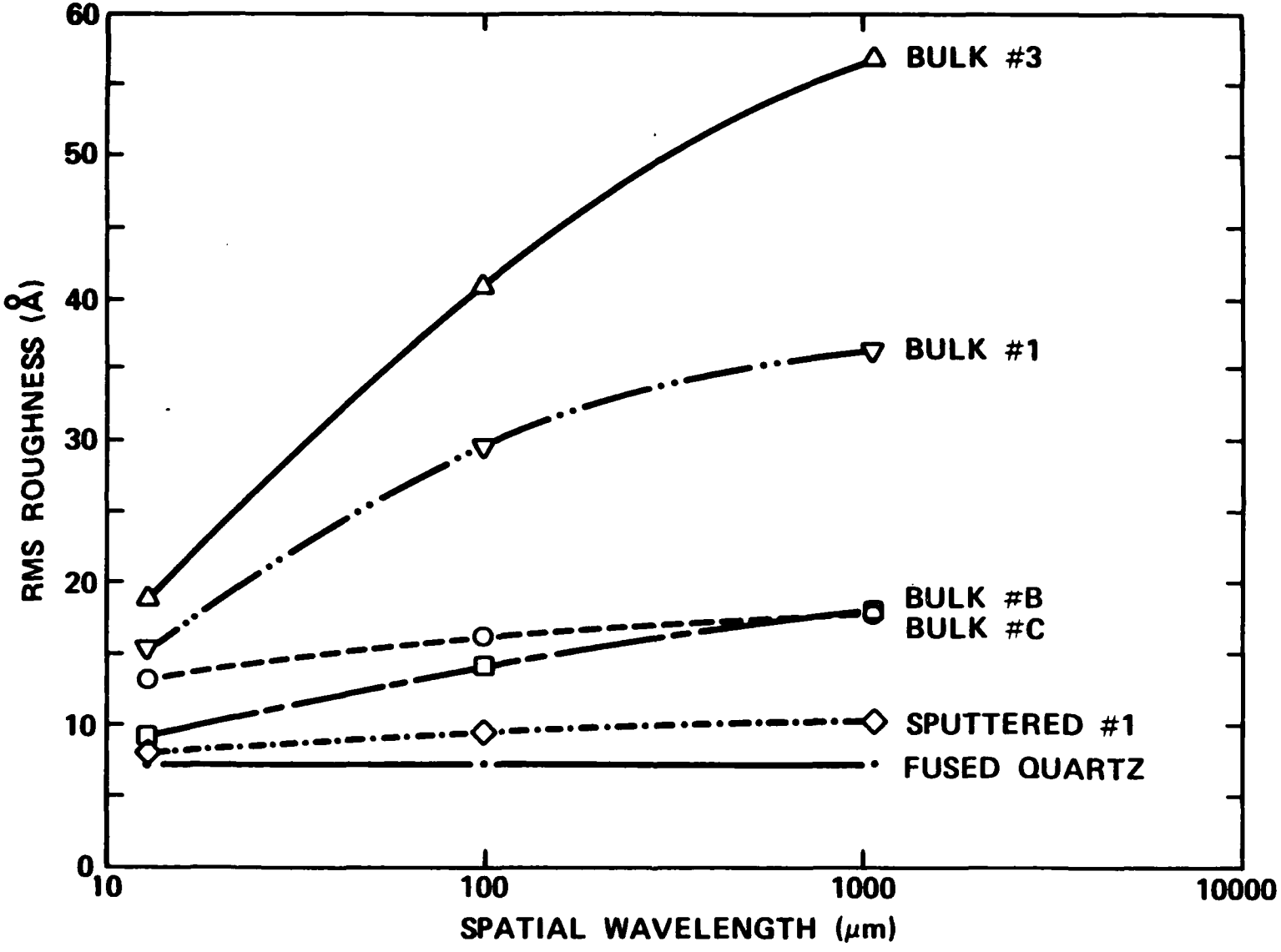

Fig. 6. Relation between rms roughness obtained from surface profile measurements and surface spatial wavelength for several Mo surfaces. Bulk #1 and Bulk #3 are conventionally polished Mo; Bulk #B and Bulk #C are dual-abrasive polished Mo; Sputtered #1 is polished sputtered Mo on bulk Mo. The curve for polished fused quartz is shown for comparison.

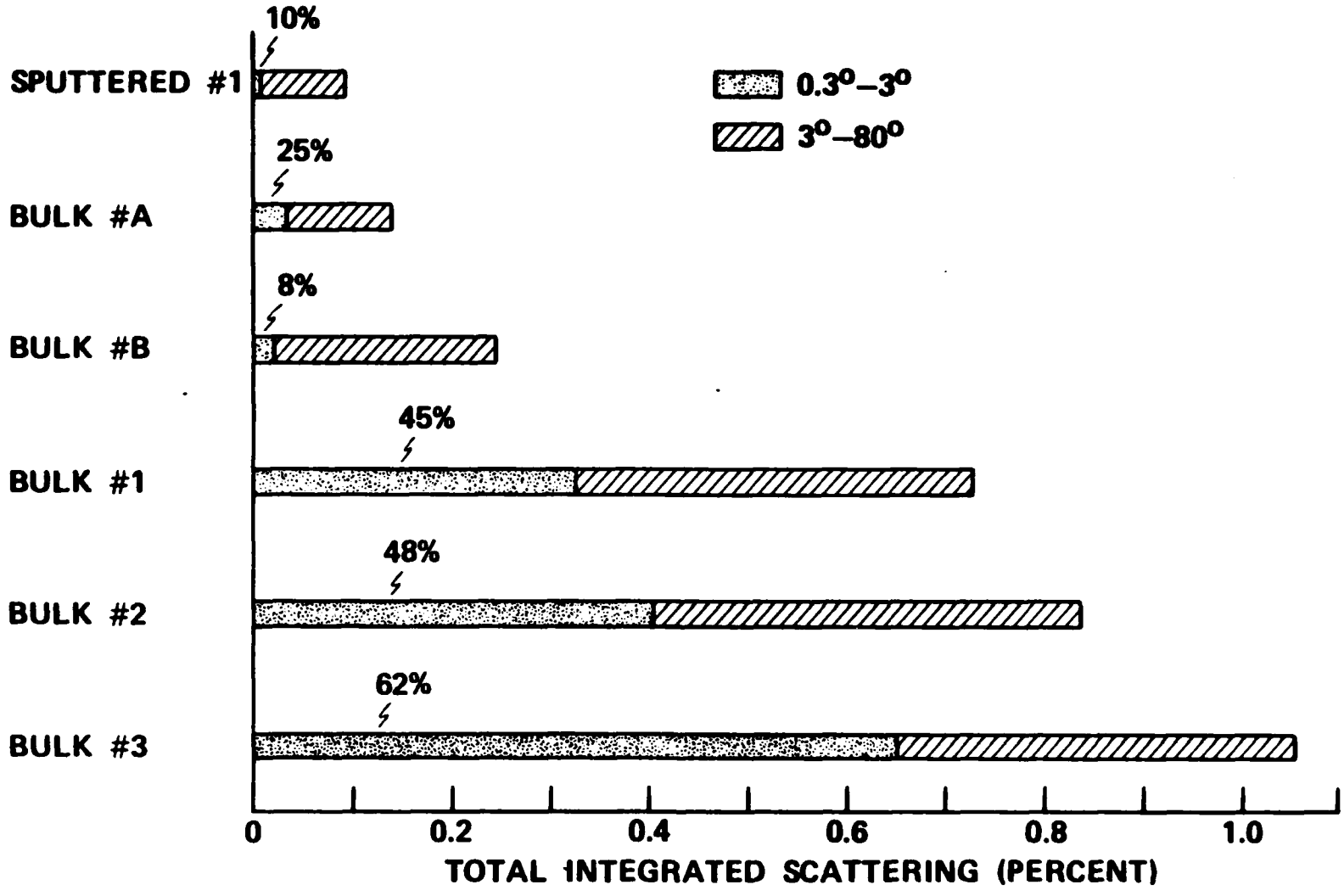

Fig. 7. Measured integrated scattering from several Mo surfaces. Values in the angular region 0.3 to 3 degrees were integrated from angular scattering measurements (Ref. 8), while the 3- to 80-degree values were measured directly. Bulk #1, #2, and #3 are conventionally polished Mo; Bulk #A and #B are dual-abrasive polished Mo; Sputtered #1 is polished sputtered Mo on bulk Mo.

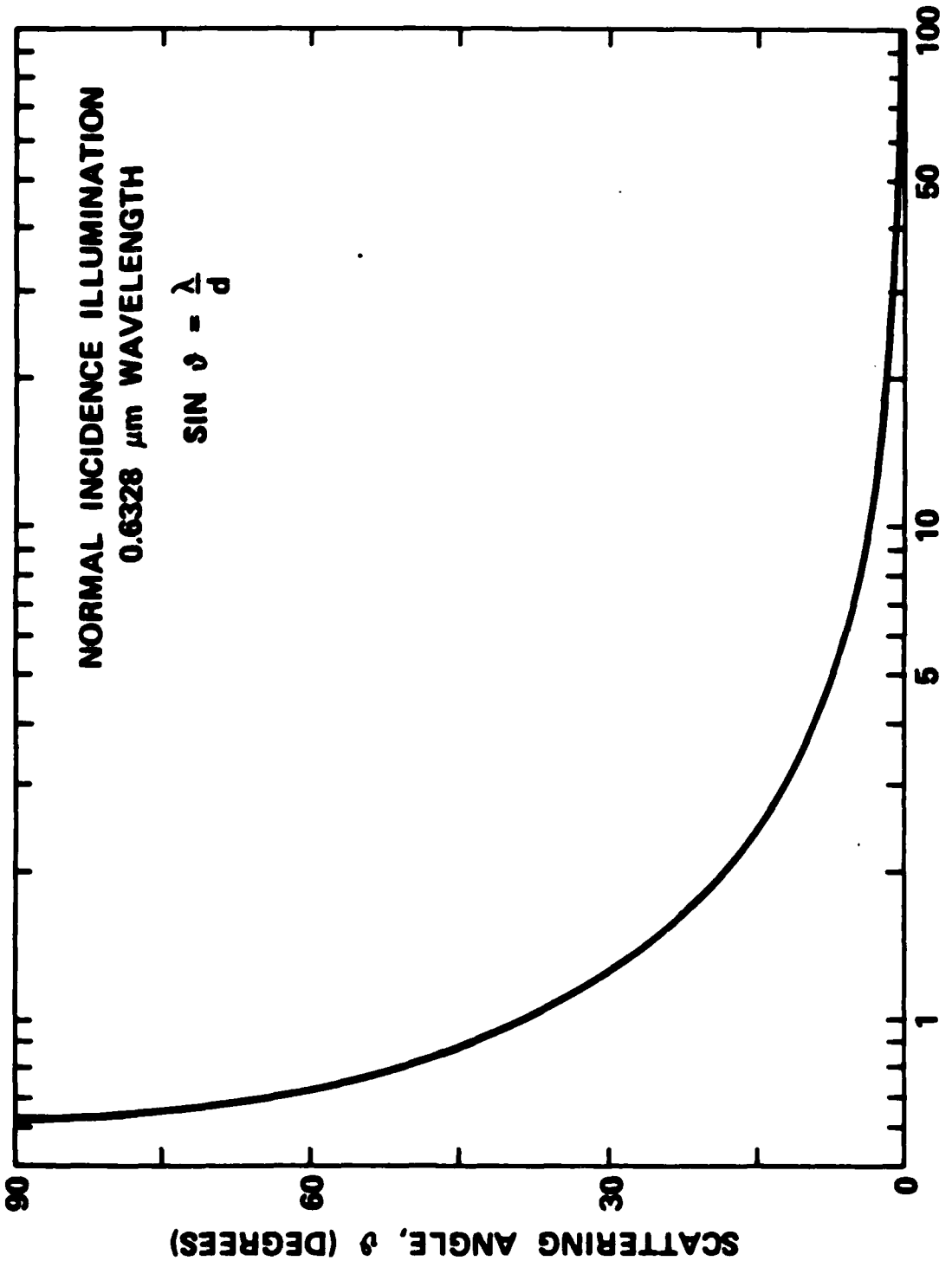

Fig. 8. Relation between the surface spatial wavelength and scattering angle for normally incident light of wavelength 6328 Å.

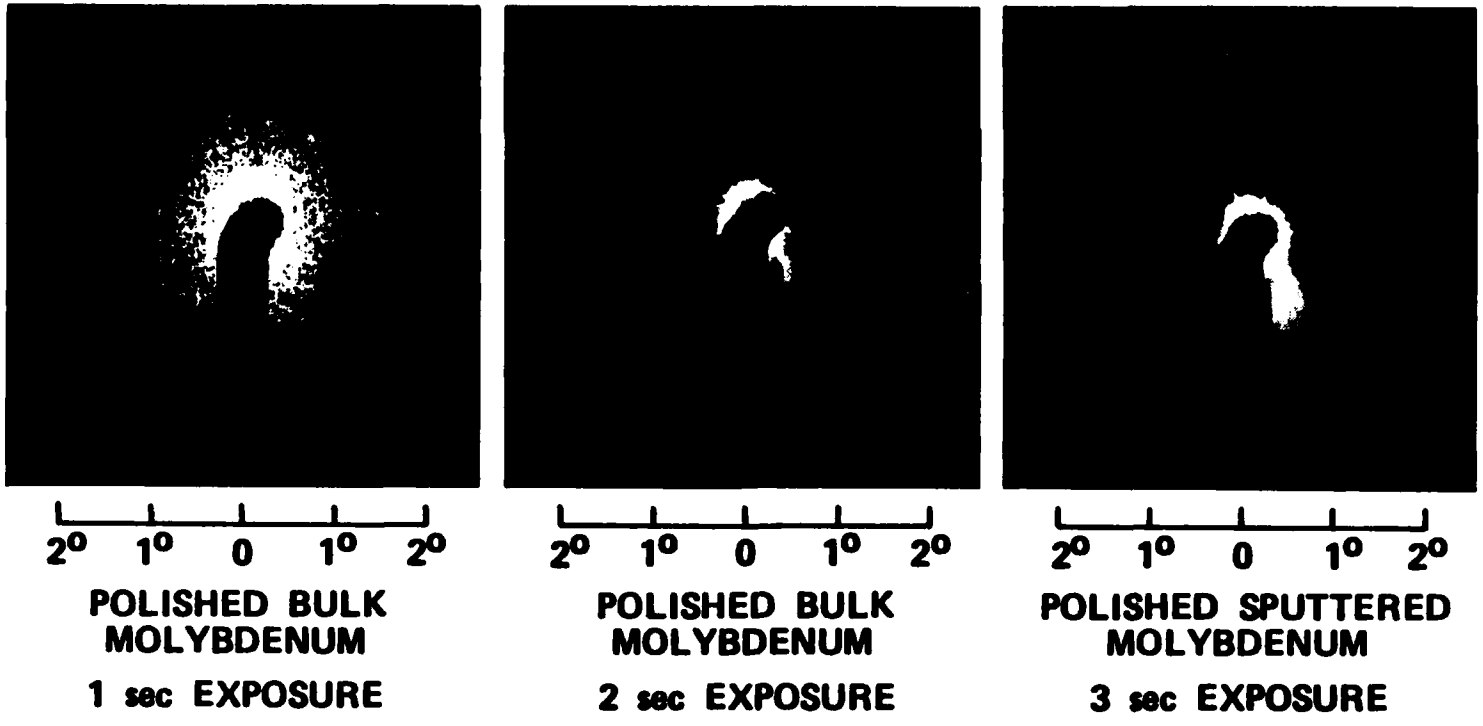

Fig. 9. Photographs of the near-angle scattering for the three Mo surfaces shown in Fig. 1.

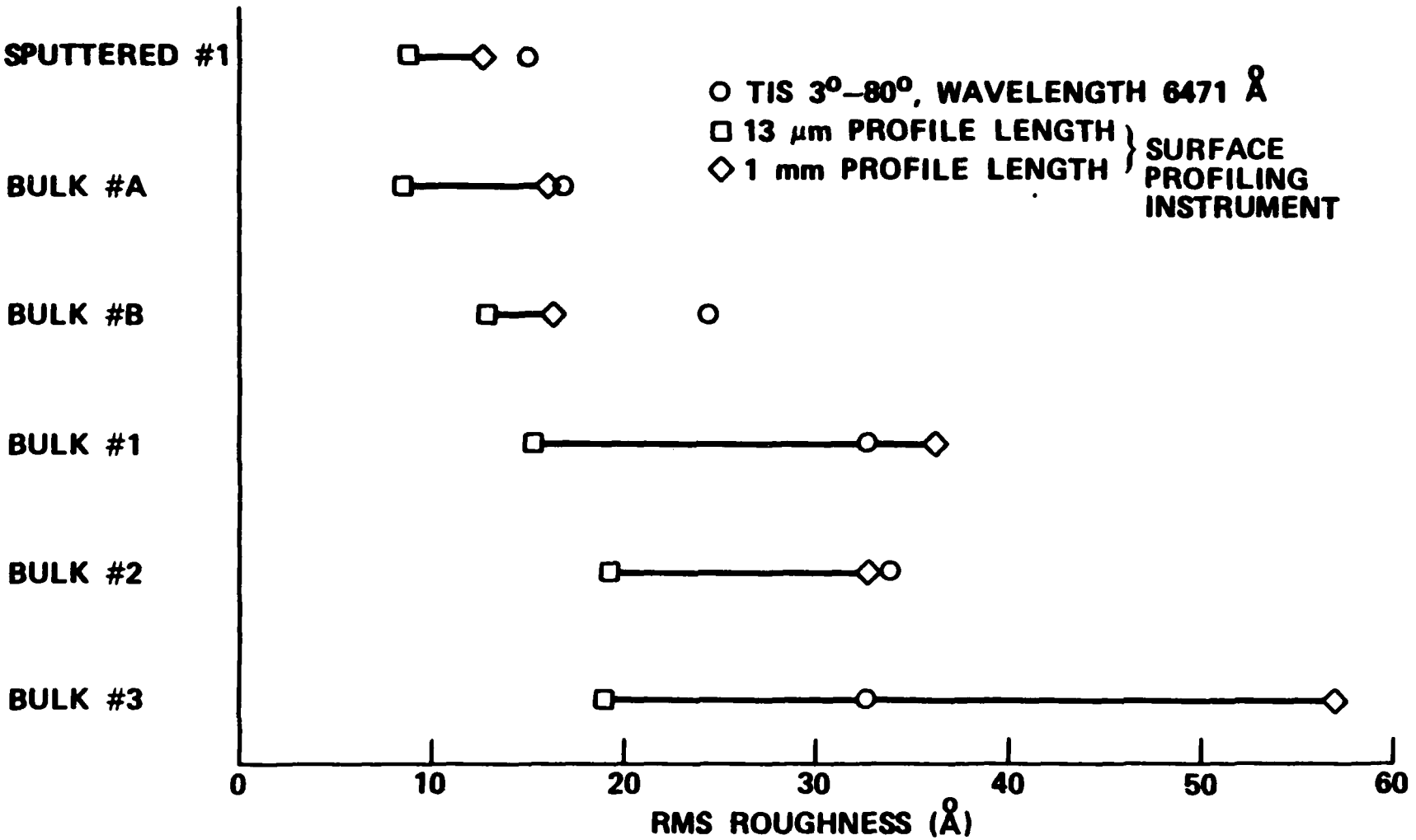

Fig. 10. Roughnesses of the same Mo surfaces as in Fig. 7 determined from scattered light (3- to 80-degree scattering angles) and profile measurements (13-μm and 1-mm profile lengths).

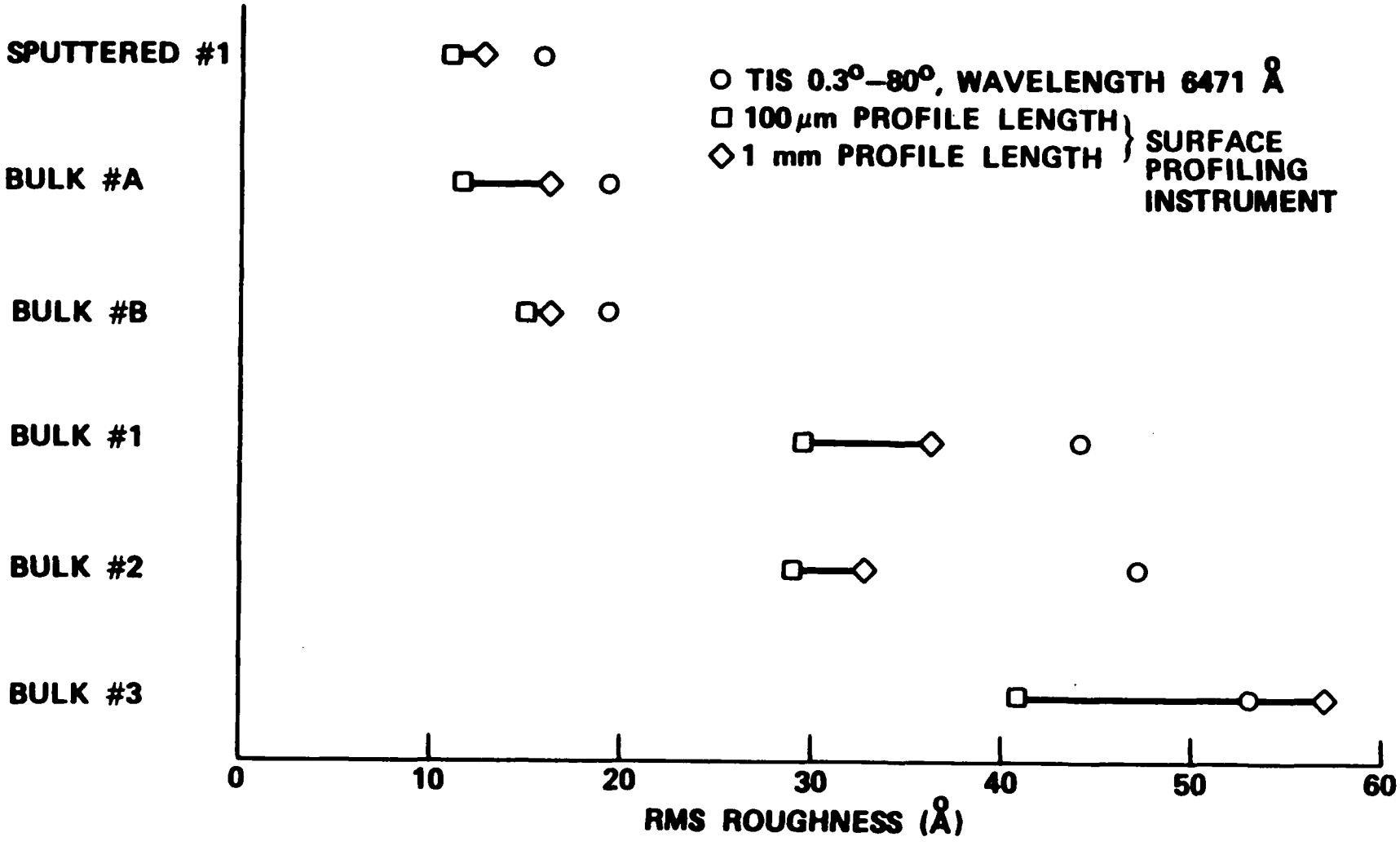

Fig. 11. Roughnesses of the same Mo surfaces as in Fig. 7 determined from scattered light (0.3- to 80-degree scattering angles) and profile measurements (100-μm and 1-mm profile lengths).

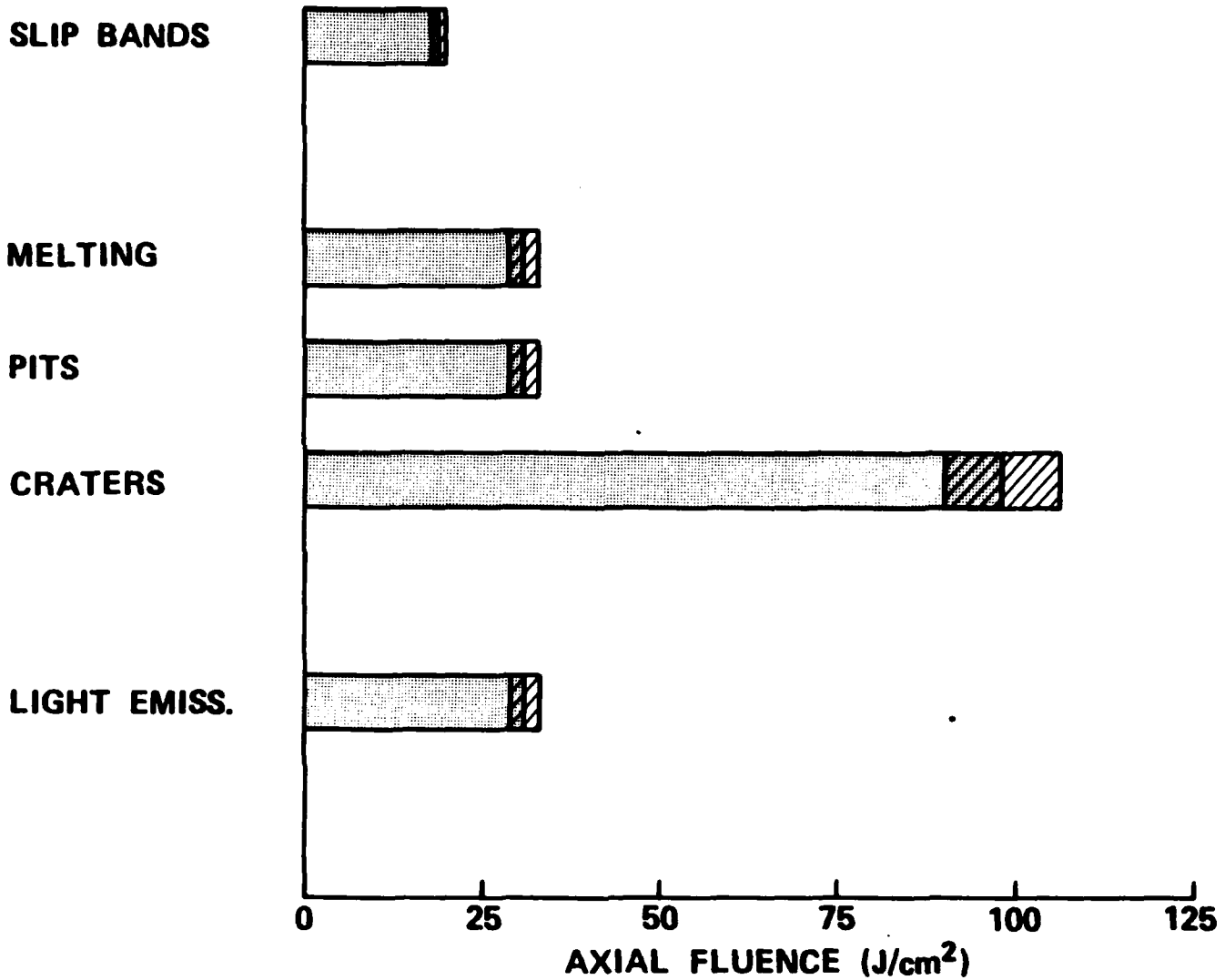

Fig. 12. Multithreshold damage levels at 2.7 μm for polished sputtered Mo #1 on bulk Mo.

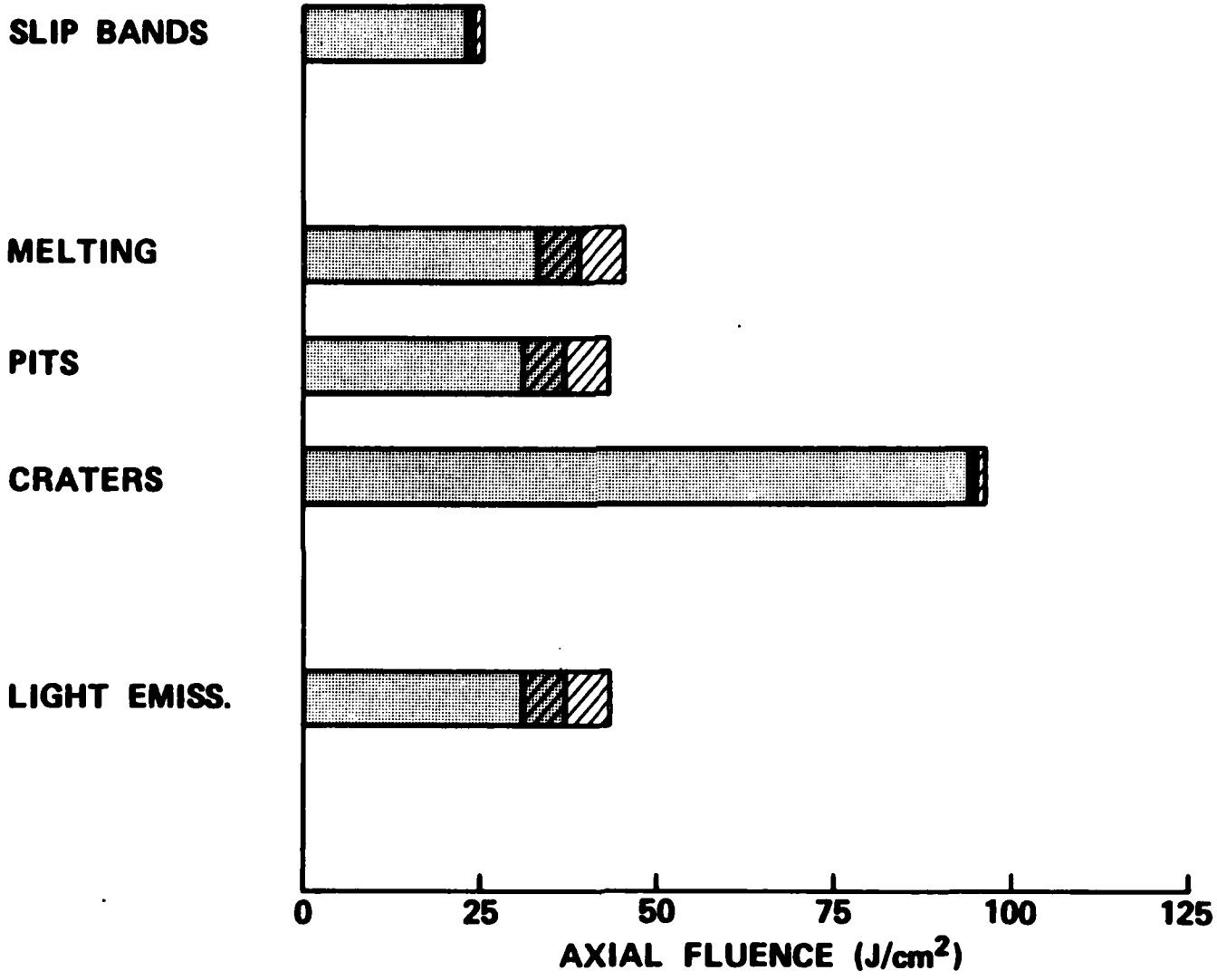

Fig. 13. Multithreshold damage levels at 2.7 μm for dual-abrasive polished Mo #B.

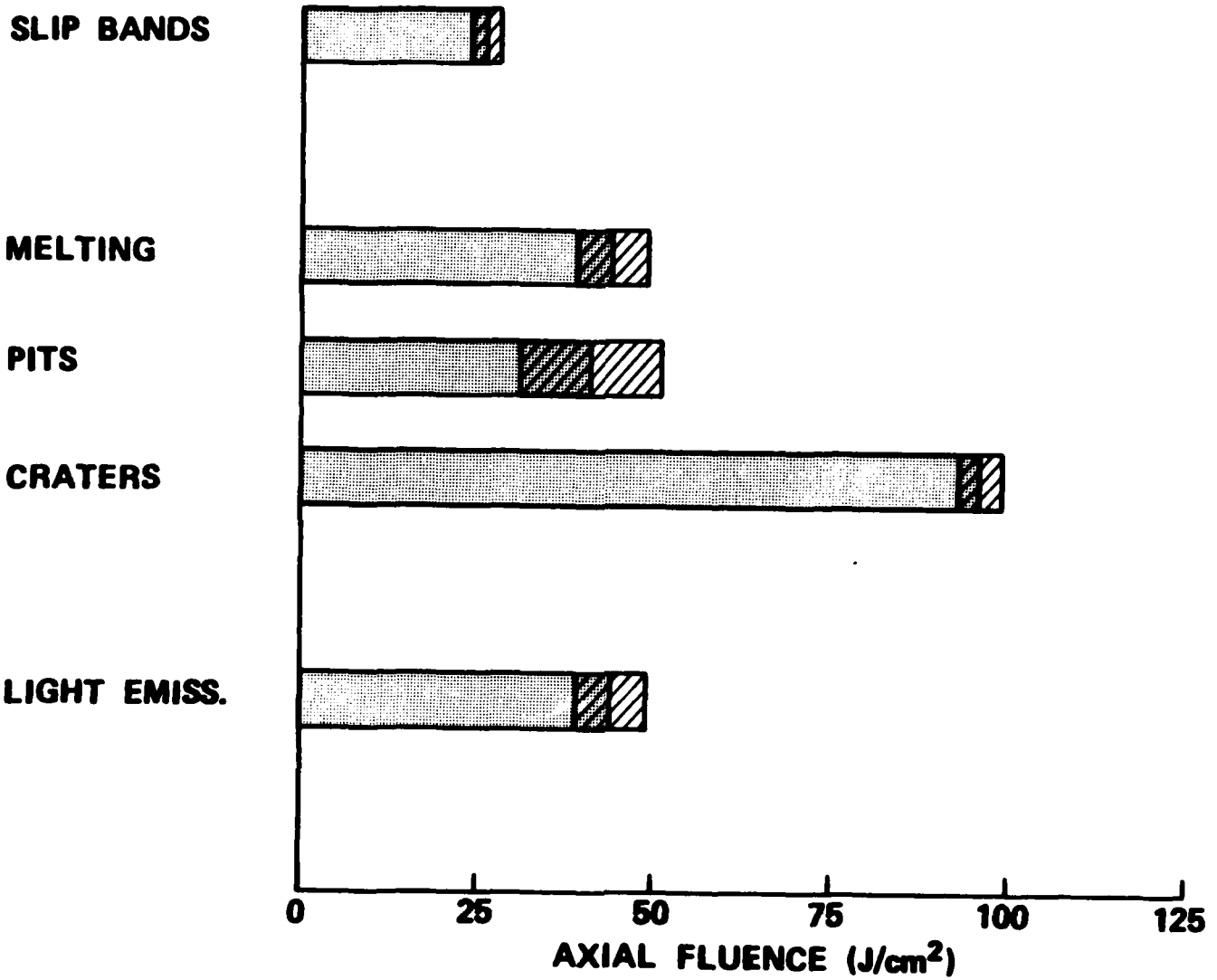

Fig. 14. Multithreshold damage levels at 2.7 μm for conventionally polished Mo #3.

Appendix A

Intensity Dependent Absorption and Laser Induced Damage to Metal Mirrors

Ph. D. Thesis

C. S. Lee

Department of Physics
University of Southern California
Los Angeles, CA 90089

INTENSITY-DEPENDENT ABSORPTION AND LASER-INDUCED DAMAGE TO METAL MIRRORS

by

CHUN-SHEU LEE

A Dissertation Presented to the
FACULTY OF THE GRADUATE SCHOOL
UNIVERSITY OF SOUTHERN CALIFORNIA
In Partial Fulfillment of the
Requirements for the Degree
DOCTOR OF PHILOSOPHY
(Physics)

May 1983

ABSTRACT

Repetitively pulsed laser calorimetry was used to measure the optical absorption as a function of incident light intensity and record the onset of multiple pulse irradiation-induced failure of several metal mirrors. The absorptance of copper and silver was found to increase with increasing light intensity at 1.06 μm. Two different physical mechanisms were considered: 1.) two-photon absorption processes and 2.) thermally induced effects. It was shown that the observed absorption change in metals with the incident light intensity is not a true intensity-dependent absorption (IDA) but caused by irradiation induced temperature changes.

A comparison of single and multiple pulse damage fluxes for diamond-turned oxygen-free high-conductivity (OFHC) copper, high quality silver and gold at 0.532, 1.06, and 10.6 μm shows opposite trends in spot-size dependence. The single pulse damage threshold decreases or remains constant with increasing spot size in the range of sizes used (50-250 μm) but the multiple pulse threshold increases. However, both have the same value in the limit of large spot size. The observed spot-size dependence of the single pulse damage threshold of the metal surfaces resembles that

observed for damage to thin films and the surfaces of transparent media where a defect-triggered breakdown process appears to be responsible for the nature of single-pulse damage. On the other hand, the unexpected spot-size dependence of the multiple-pulse (fatigue-like) damage threshold reported in this work is thought to be the result of the peaked Gaussian spatial distribution of the laser beams. A model based on cumulative plastic deformation resulting from laser-induced thermal stress is proposed to explain the properties of multiple-pulse failure. The thermal stress induced by a temperature gradient resulting from nonuniform laser heating of metal surfaces is greater for smaller spot-size Gaussian distributions than it is for larger spot sizes. By applying a linearized thermoelastic theory, the power density which will produce a thermal stress barely equal to the yield strength of the metal surface is linearly proportional to spot size. This result is in good agreement with the experimental data of the spot-size dependence of multiple pulse damage threshold.

CHAPTER 1

INTRODUCTION

The research described in this thesis was motivated by the need for more complete understanding of the interactions of light with metals. This need results from the basic physical questions involved and from the fact that metal mirrors are being used in high power laser systems. Some of the physical properties of metal reflectors which are considered in this work are 1.) optical absorption processes under irradiation by intense pulsed laser beams and 2.) laser-induced damage phenomenon. In the former case the optical absorptance was measured as a function of incident light intensity by laser calorimetry. This type of experiment was commonly performed to study nonlinear absorption processes in transparent materials [1]. In the latter case single and multiple pulse induced damage thresholds were measured as a function of the irradiated spot sizes. This was done because significant progress has been made in identifying the basic physical mechanisms responsible for damage in thin films and on the surfaces of transparent media through the study of spot-size dependence of damage thresholds [2-4].

Various phenomena which were not observable at low intensities are measurable under irradiation by high power laser

beams. For instance, harmonic generation [5-7], optical mixing [6-8], multiphoton absorption [9,10], etc. have been extensively studied in transparent materials such as semiconductors and optical insulators. In this thesis, repetitively pulsed laser calorimetry was used to measure the optical absorption of several metal mirrors as a function of incident light intensity at 1.06 μm. The results were that the measured optical absorptance increased as the incident light intensity increased. The increase in absorptance with increasing light intensity was reversible with respect to the light intensity unless catastrophic damage had occurred. This result was different from that observed in alkali-halides. In alkali-halides, there is a threshold intensity above which absorption increase with intensity becomes irreversible [11]. In other words, the absorption coefficient is larger for a site after being irradiated by laser pulses having intensity above the threshold value than before.

Absorptance was measured on several OFHC (oxygen-free, high conductivity) polycrystalline copper and high purity silver electroplated on OFHC Cu substrate. The surfaces of these specimens were either diamond-turned or mechanically polished. Studies were conducted using a Q-switched Nd:YAG laser operating in the TEM_{oo} mode at 1.06 μm. Oscillation was confined to a single longitudinal mode of pulse duration 22 nsec at FWHM. In the range of intensities below the level which will cause optical breakdown, the absorptance increases linearly with increasing light intensity. The observed dependence of the absorptance on

the light intensity may be due to two photon absorption (TPA) processes where by absorbing two photons simultaneously the electrons from the valance band may be promoted to above Fermi level or from the Fermi level to the next higher empty band. However, there is an apparent intensity dependence of optical absorption due to the temperature dependence of the absorption. In other words, any local temperature change introduced by the laser beam would change the effective absorptivity of the irradiated region. As a result of calculations of the temperature of the irradiated region during the pulse, the observed absorption increase can be fully explained by the absorption change due to the increased surface temperature. There is no significant dependence of the absorptance on the irradiated spot sizes ($\sim$100-250 μm) used in this work.

As the incident light intensity reaches a critical value, the irradiated site of the metal surface will always be destroyed during the very first pulse. This type of failure is always accompanied by a visible spark or flash. The intensity at which such catastrophic failure or breakdown takes place has been conventionally defined as the damage threshold. However, in contrast with single pulse damage, failure due to multiple pulse irradiation is frequently observed in the present work. This phenomenon is observed at intensities which are always lower than that required for single pulse damage. The number of pulses required to cause catastrophic failure was investigated at different intensities for several different irradiated spot

sizes. Consistent results show that the number of pulses needed to cause breakdown decreases as the incident power density increases.

A comparison of single and multiple pulse damage fluxes for several metal mirrors (e.g., Cu, Ag and Au) at 10.6, 1.06, and 0.532 μm show opposite trends in spot-size dependence. The single pulse damage threshold decreases or remains constant with increasing spot size in the range of sizes used (50-250 μm), but the multiple pulse threshold increases. However, both appear to have the same value in the limit of large spot size.

The damage morphology as observed with a Nomarski microscope shows that single pulse damage generally occurs at localized defect sites. On the other hand, the surface of a site after being irradiated for a large number of pulses without observation of a visible flash or spark as in conventional catastrophic damage has become roughened. In addition, it was observed that the degree of roughness induced by multiple pulse irradiation increases as the number of pulses increases. The observed spot-size dependence of the single pulse damage threshold of the metal surfaces resembles that observed for damage to thin films and the surfaces of transparent media reported in the literature [2-4]. The model suggested by DeShazer et al. [2] and which appears also to be valid for the metal mirrors assumes that the nature and distribution of surface defects determine the spot-size dependence of the damage threshold. In this model the probability of the laser beam striking an easily damaged defect will be greater for

larger spot sizes. For very small spot size there will be no defect present. Thus, the damage threshold of a particular surface will be high and due to an intrinsic damage mechanism for small spot sizes and low for large ones where easily damaged defects are encountered.

The trend in spot-size dependence of multiple pulse damage threshold was different from that observed in thin film damages [12] where the spot-size dependence was similar to that of single pulse damage. This suggests that multiple pulse damage to metal surfaces may be due to different physical processes. The multiple pulse irradiation-induced surface roughening indicates that the surface region was permanently deformed at a power density lower than that required for single-pulse catastrophic failure. Similar damage morphology was described by Porteus et al. [13] as slipband damage. They observed this phenomenon at power densities slightly below the ones required for single pulse catastrophic failure as it had been defined here. As discussed later in the work, the mechanism for single pulse slipband damage and multiple pulse surface roughening are related. It has been suggested that repetitive pulse irradiation will cause an accumulation of plastic deformation providing the yield strength of the surface is exceeded during each pulse [14]. Furthermore, such a cumulative effect may progressively deteriorate the surface quality eventually leading to premature catastrophic failure. The unexpected spot-size dependence of the N-pulse damage threshold reported in this thesis is thought to be the result of the peaked

Gaussian spatial distribution. The thermal stress induced by a temperature gradient resulting from nonuniform laser heating of metal surfaces is greater for smaller spot-size Gaussian beams than it is for larger spot sizes. By applying a linearized thermoelastic theory, the power density which produces a thermal stress barely equal to the yield strength of the surface has been derived in this work and is shown to be linearly dependent on spot size. This is consistent with the experimental observations of the spot size dependence of the multiple-pulse damage threshold.

In the 2nd Chapter, a brief review on mechanisms of optical absorption by metal surfaces is given. In Chapter 3, measurements of optical absorptance as a function of incident light intensity are described in detail. A model consistent with the experimental results is put forth. In Chapter 4, experiments to determine the spot-size dependence of single and multiple-pulse damage in several metal mirrors at 10.6, 1.06 and 0.532 μm are presented. In Chapter 5, a model for interpreting the unexpected spot-size dependence of the multiple-pulse damage threshold on metal surfaces is proposed. Finally, a brief summary and discussion of this thesis work is given in the last chapter.

Appendix B

Microstructural Properties of Diamond Turned Metal Mirrors

Ph. D. Thesis

H. H. Hurt

Department of Material Sciences
University of Southern California
Los Angeles, CA 90089

ABSTRACT

The diamond machined optical surface was investigated with the intention of correlating known optical properties of diamond machined surfaces with the microstructure and properties of the surface region. The generation of surfaces by machining is known to introduce subsurface deformation and localized heating of the surface, and diamond machining of optical surfaces creates similar effects on a much smaller scale. To illustrate the effect of various machining parameters on the surface produced, optical quality diamond machined surfaces were characterized. Methods included transmission electron microscopy, reflection electron diffraction and a novel method for determining the electrical conductivity of the deformed surface layer.

Differences in the surface structure were observed with changes in the tool top rake angle and with the initial hardness of the base material. All diamond machined surfaces were crystalline and showed no evidence of an amorphous Bielby layer. The damage introduced by the machining operation in producing the reflecting surface apparently extends one to two microns below the surface and results in a net residual tensile stress on the surface. The amount of deformation increases with increasing negative rake angle until -15 degrees where there is a drop in microhardness and other indications of induced recrystallization at the surface. Optical surfaces produced on Cu. by normal lapping methods appear to be far less deformed than any of the diamond machined surfaces.

Transmission electron micrographs show a periodic structure of extended subgrains along the machining direction. Transverse views of the sections show areas at the surface that are dislocation free which concurrs with earlier studies of dislocation anihilation at surfaces in deformed metals. The results of an in-depth investigation of the effect of the rake angle on the near surface dislocation structure are not available at the time of this writing.

The diamond machining process produces surfaces that not only have characteristic topography but also exhibit characteristic material properties in the near surface region due to the dynamic deformation processes of chip formation and tool-surface interaction. A definite recrystallization effect takes place between -10° and -15° rake angle and this corresponds to changes in the optical and physical properties previously observed in high negative rake angle machined surfaces. The deformation introduced by the process is slight, but is resolvable by high resolution TEM and RED.

INTRODUCTION

The nature of the optically polished surface has been a subject of conjecture and debate for several centuries. Hooke ( ) and Newton ( ) contended that polishing was actually a cutting process where surface material was removed by the sharp abrasive particles, the finer the abrasive the smaller the scratches on the surface until a specularly reflecting surface is obtained. The development of electron diffraction led researcers such as Bielby( ) to conclude that the mirror is produced by smearing the workpiece material across the surface, thereby filling the depressions and producing an amorphous layer 20 to 100Å thick. In recent years the amorphous Bielby layer has failed to make an appearance and Samuels ( ) and others have concluded that the original assumptions of Hooke and Newton were correct and that the polished surface is crystalline and is plastically deformed, the amount and depth of deformation dependent on the polishing conditions.

The metal cutting process as a method of reducing a workpiece to a given shape is of great importance in the manufacture of most items used in our modern technological society. A highly specialized derivative of normal machining, the diamond machining process for the production of metal mirror surfaces has reached an advanced state of development. To date, the focus of this development effort has been directed towards improving and characterizing the microtopography of the surface produced. This is because the optical scattering is related to the statistical properties of the surface roughness (1).

The development of high fluence laser diagnostics and other methods has resulted in a wealth of data on the surface and optical properties of diamond turned mirrors. From this data it has been determined that the diamond turned surface exhibits unique properties which are related to the machining conditions empirically only. Most interesting is anamalous non-Drude behavior(2). The Drude model for reflection in metals is based on the interaction of the incident electromagnetic fields with the "free" electrons of the conductor. When the mean free path of the electrons is shortened due to collisions, damping occurs and reduces the amount reflected. Although the primary mechanism is phonon-electron collisions, non-Drude behavior of certain diamond machined surfaces should be linked with the state of the near surface region of the material. To date the type and number of crystalline imperfections in this region due to the diamond machining process was undetermined.

As diamond machining is a micro-scale orthogonal machining process, current research in the fields of plasticity theory, metal cutting theory, friction in machining, and the mechanisms of the production of the surface have direct application. But consider that for normal machining of Cu, dimensions of interest are in thousandths of an inch and features are easily resolved. By contrast, in diamond machining a RMS surface roughness of 150Å and a finish depth of cut of 50μin are typical. This obviates specialized methods of examination, and equally sophisticated sample preparation methods

In this study the nature of the deformation introduced by the diamond machining process is investigated by several methods, the particular objective being to investigate the surface and near surface region by high resolution transmission electron microscopy (TEM). Specimen cross sections are prepared normal and transverse to the machining direction and also surface sections to establish the structural changes with respect to the orientation of the diamond cutting tool as it passes over the surface. Imaging of dislocation structure and density in the first few hundred Å of the surface that contribute to the optical reflection process is of particular importance.

Other methods of characterizing the surface include reflection electron diffraction (RED) to investigate the first 150Å of depth for crystal perfection and recrystallization effects at high negative tool rake angles. Surface microhardness is another sensitive technique as Cu. exhibits a high degree of work hardening and recrystallization softening. Other selected methods include X-ray diffraction for residual stress measurement and high resolution SEM and STEM of the diamond machined surface.

To provide data for the Drude model for the reflectivity of diamond machined optical surfaces, a specialized four point resistivity measurement apparatus is employed measuring the conductivity of a diamond machined taper section as a function of thickness. This gives an indication of the resistivity of the 2μ thick deformed surface layer produced by the machining operation.

The goal of this investigation is to develop a better understanding of the mechanisms of the production of an optical surface by the diamond machining method. By understanding the effect of the machining parameters on the surface produced, better microtopography with desired reflectance and laser damage properties can be realized.

FIGS.1 & 2

SURFACE MICROHARDNESS OF DIAMOND MACHINED SAMPLES

Two sets of OFHC copper samples were prepared the first having an undisturbed surface prior to the diamond machining process. The second group was deliberately prepared with a deformed surface by flycutting. Microhardness results are shown as a function of the tool top rake angle. Two indenter weights were used resulting in a depth of penetration of 2 μm for the 20g weight and 0.3 μm for the 1g. A scanning electron microscope was used to measure the indenter marks for the 1g test. The indenter marks were scattered widely to sample several grains.

The data for the 20g weight indicates a drop in hardness between the -10° and -15° rake angles. The data with the 1g weight indicates an increasing hardness with increasing negative rake angle.

SURFACE HARDNESS OF DIAMOND MACHINED SAMPLES

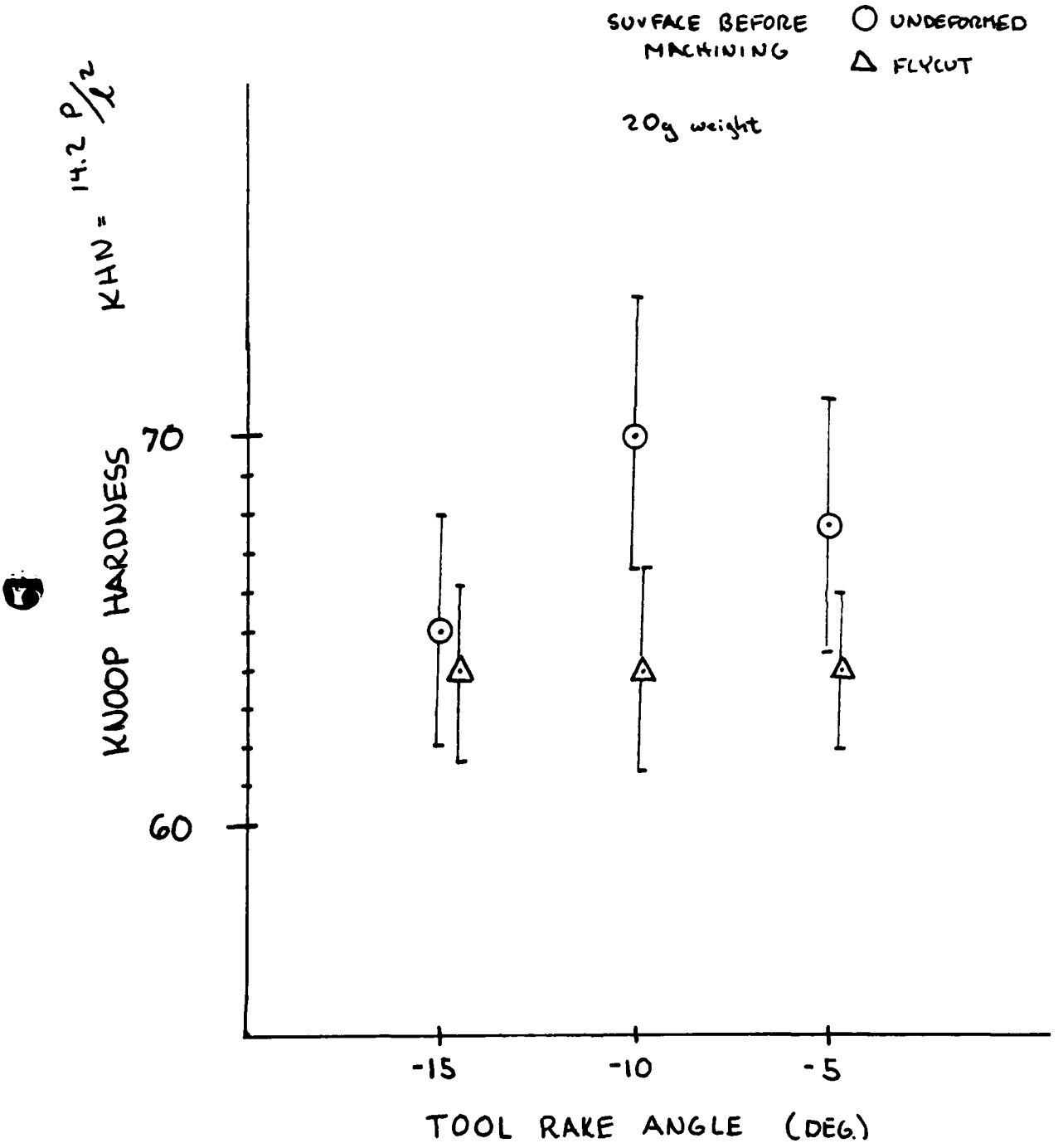

SURFACE MICROHARDNESS

Surface before diamond machining

○ undeformed

△ flycut

1g indenter weight

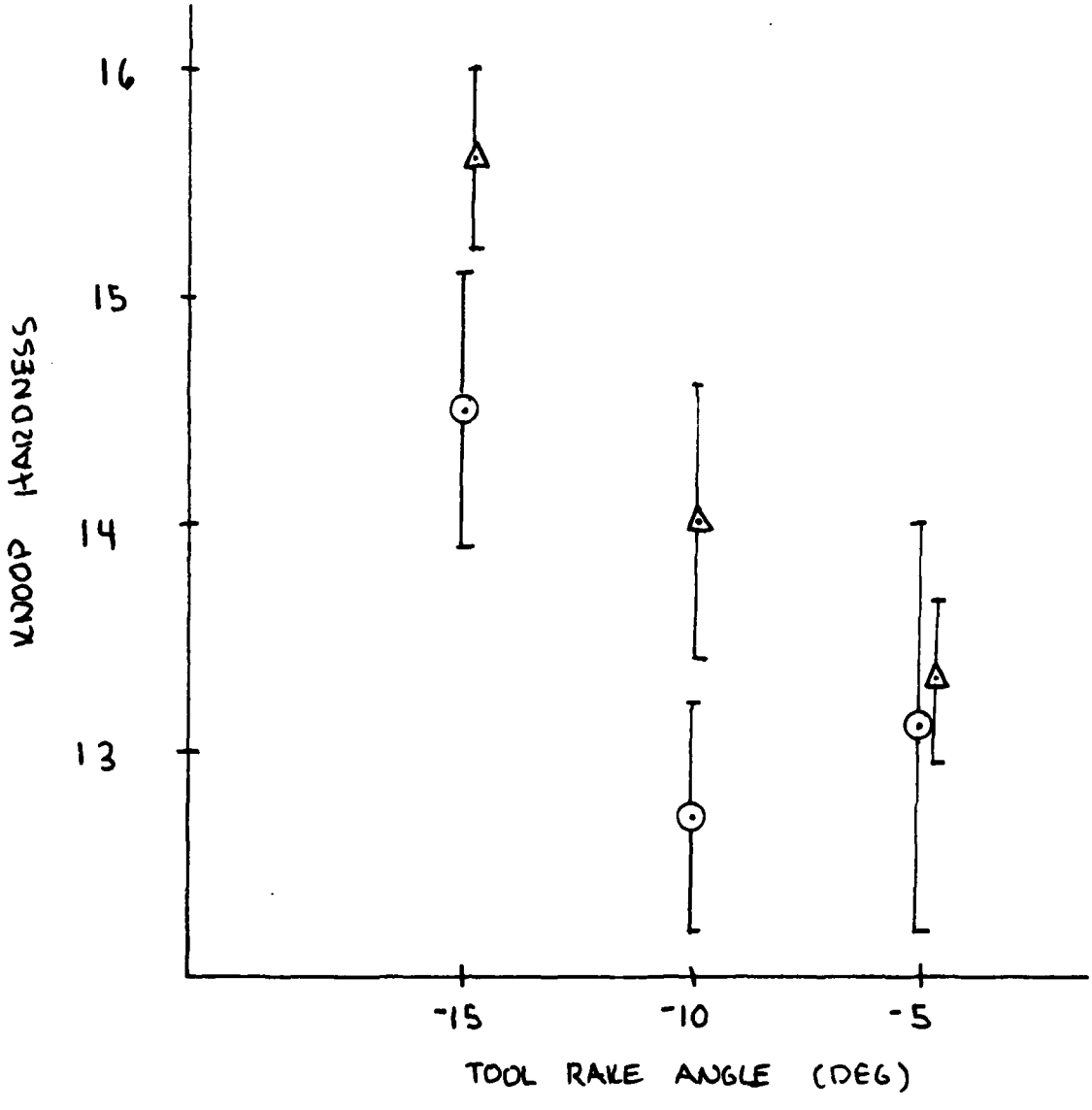

FIG.3

TEM REPLICAS OF THE DIAMOND MACHINED SURFACE

UNDEFORMED SURFACE BEFORE DIAMOND MACHINING

FLYCUT SURF.

RAKE ANGLE

-5°

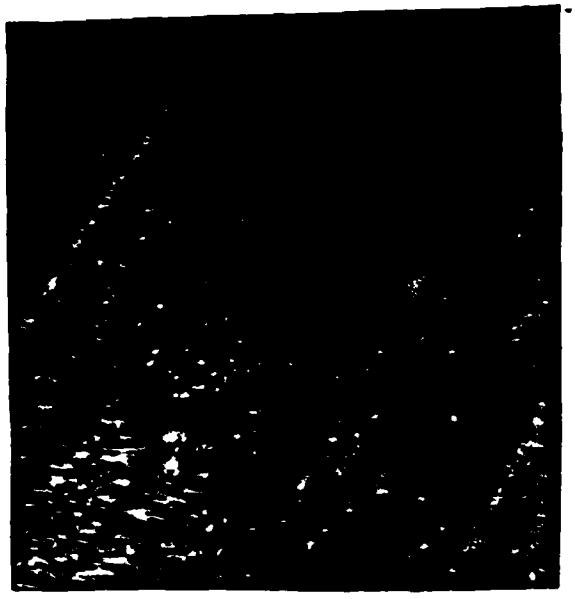

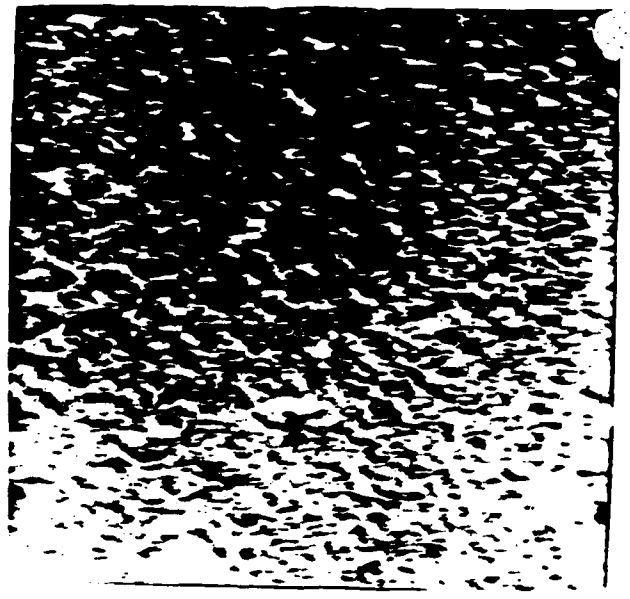

-10°

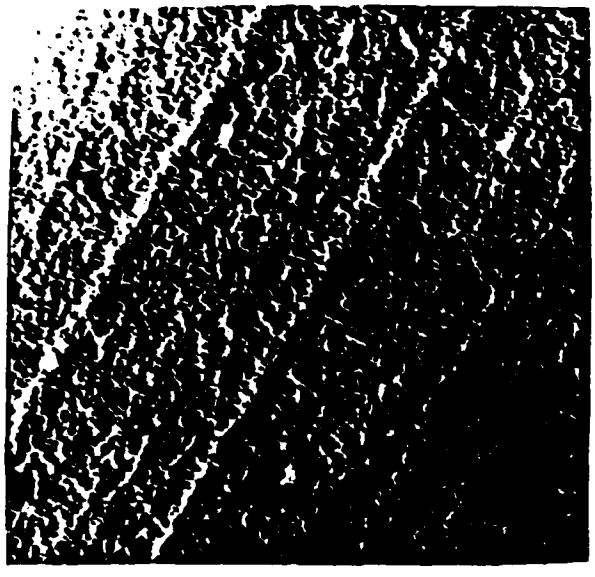

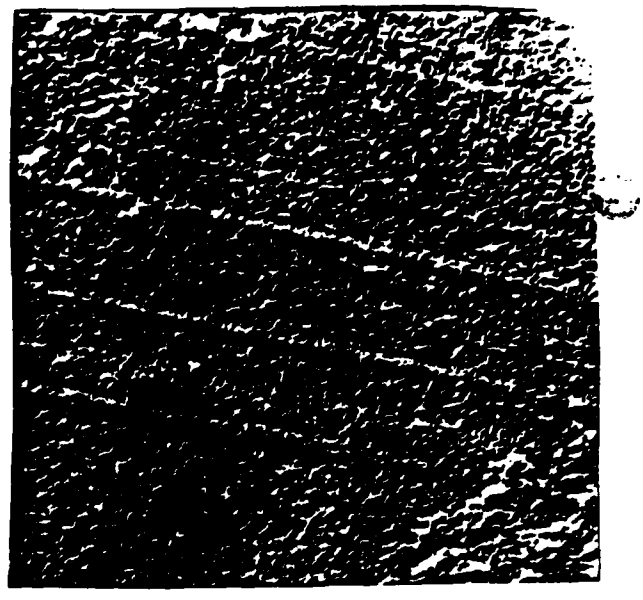

-15°

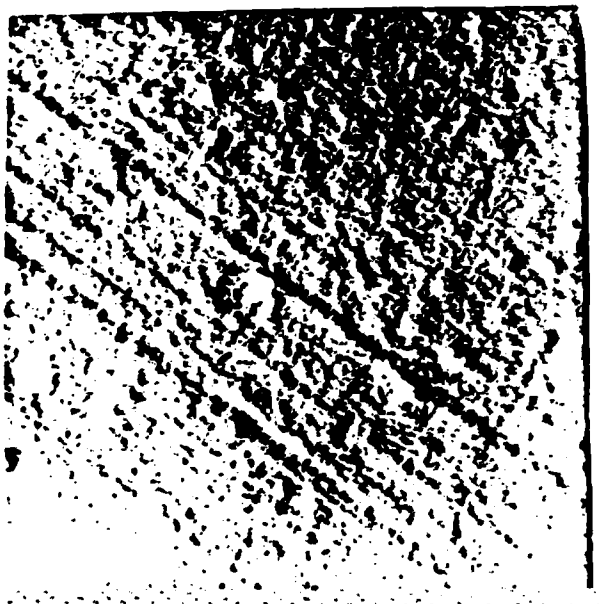

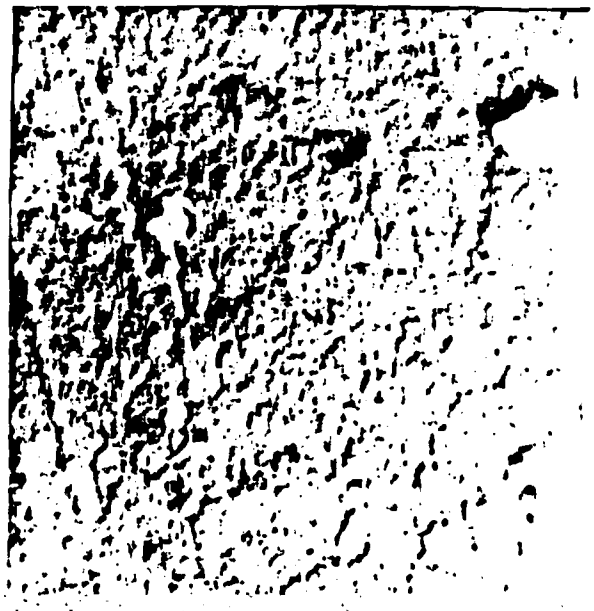

FIGS. 4 & 5

REFLECTION ELECTRON DIFFRACTION PATTERNS

Fig.4: Starting material OFHC Cu. electropolished. Shows that the starting material has some degree of cold work.

Fig.5: Lapped surface prepared at NWC. Ring pattern is typical of polished metal surfaces caused by random crystallite orientation at the abraided surface.

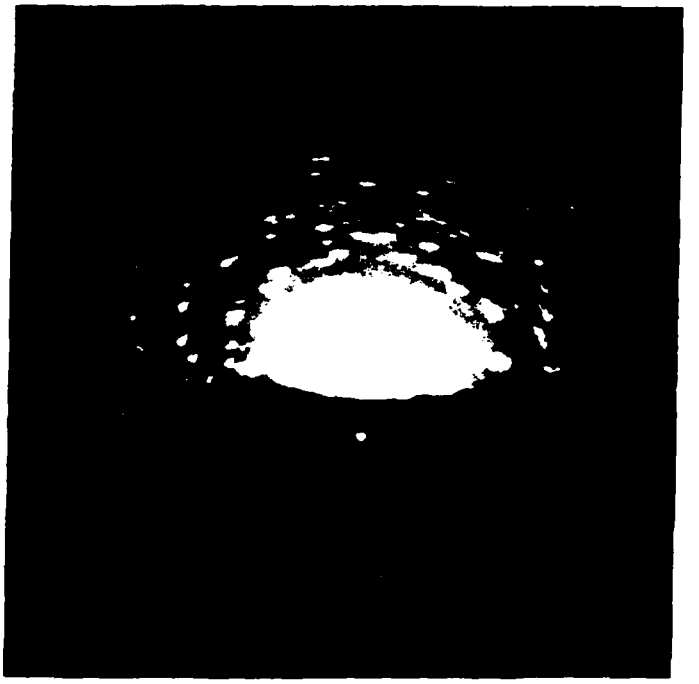

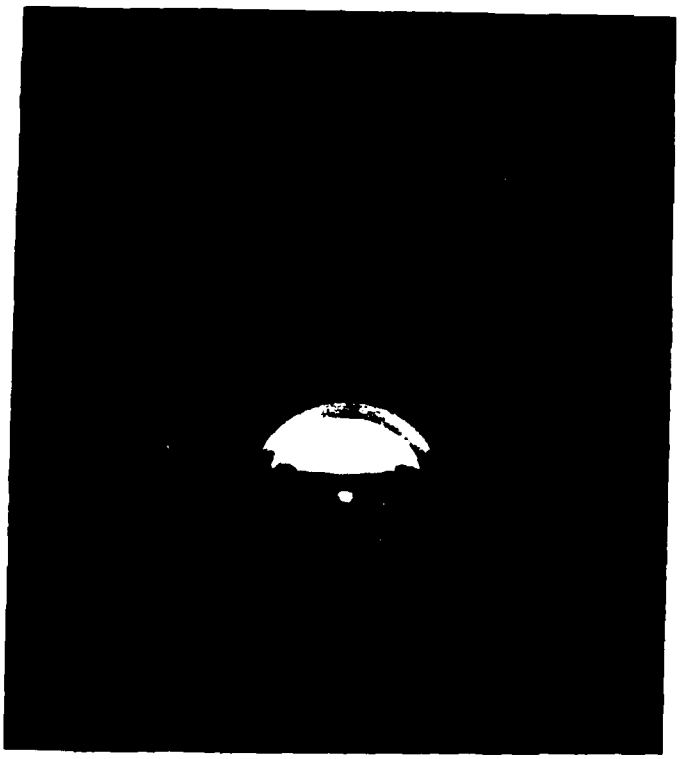

FIGS. 6 & 7

RED PATTERNS OF DIAMOND MACHINED SURFACES

Fig.6: Lapped sample increased magnification to show detail. Figs. 6-9 same mag.

Fig.7: Diamond machined at -5° rake angle. Note that the rings are more diffuse than the lapped sample indicating a decrease in atomic ordering (increase in cold work damage). The information depth for RED is approximately 100Å for this case.

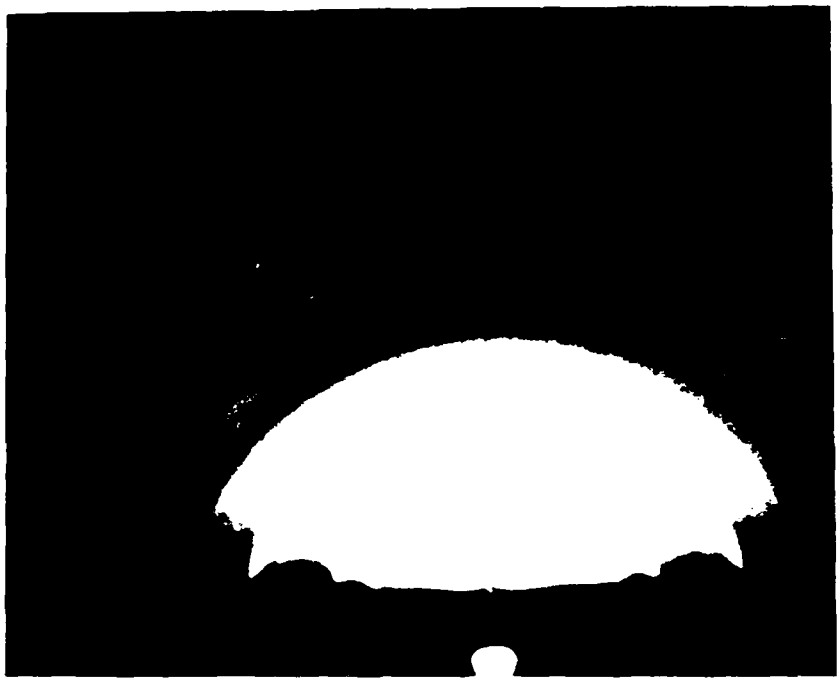

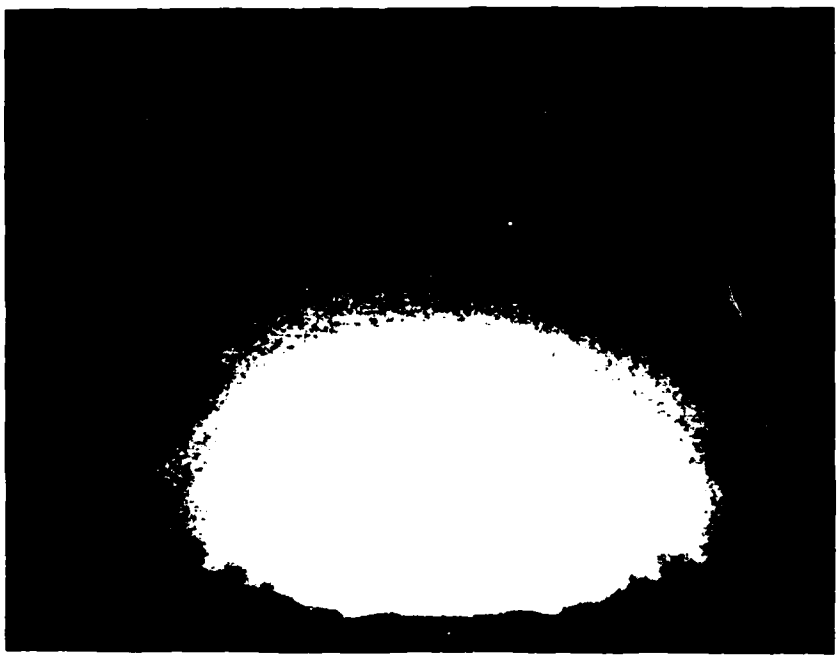

FIGS. 8 & 9

RED PATTERNS OF THE DIAMOND MACHINED SURFACE

Fig. 8: Diamond machined at -10° rake angle. Shows a further decrease in ordering and a more damaged surface.

Fig. 9: Diamond machined at -15° rake angle. Note the several bands of spotty rings indicating preffered recrystallization.

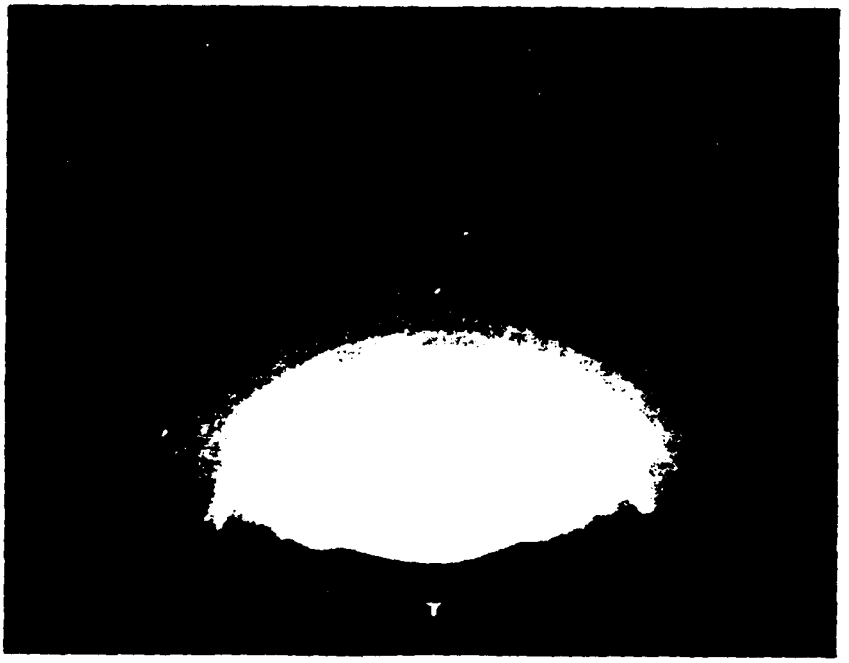

FIGS. 10 & 11

TEM MICROGRAPHS OF THE DIAMOND MACHINED SURFACE

Fig.10: View is looking down at the diamond machined surface machined at -10° rake angle. Note the extended subgrain structure in the direction of machining. The feed is approximately the width of the micrograph.

Fig.11: Increased mag. to show detail.

FIG.12

TEM MICROGRAPH OF TRANSVERSE SECTION OF D.M. SAMPLE

By cladding the diamond machined surface, TEM cross sections could be prepared. The boundary between the sample and the Cu. cladding is dashed in, the cladding being at the top. Note the banded dislocation structure and the regions of low dislocation density at the surface.